Atomic layer deposition of vanadium oxides for lithium-ion batteries

Kobe Geryl

Supervisor: Prof. Christophe Detavernier
Counsellors: Felix Mattelaer, Geert Rampelberg

Master's dissertation submitted in order to obtain the academic degree of
Master of Science in Engineering Physics

WE04
Chairman: Prof. dr. Paul Matthys
Faculty of Engineering and Architecture
Academic year 2013-2014

UNIVERSITEIT
GENT

Atomic layer deposition of vanadium oxides for lithium-ion batteries

Kobe Geryl

Supervisor: Prof. Christophe Detavernier
Counsellors: Felix Mattelaer, Geert Rampelberg

Master's dissertation submitted in order to obtain the academic degree of
Master of Science in Engineering Physics

WE04
Chairman: Prof. dr. Paul Matthys
Faculty of Engineering and Architecture
Academic year 2013-2014

UNIVERSITEIT
GENT

Acknowledgements

If someone would ask me to compare my master's thesis with a lithium-ion battery - not that such an absurd question would ever be posed - then I would reply that I'm probably the lithium ions, as I performed the work. 29 ALD processes, 108 in-situ XRD anneals, 52 electrochemical tests and roughly 120 pages, a worthy end of 5 years studying Engineering Physics.

But a lithium ion by itself is nothing more than just another element in Mendeleev's table. Before it can achieve something, it requires 2 electrodes. Therefore, special thanks go out to Geert and Felix. Thank you both for starting me up in semester 1 and 2, for guiding me and answering my questions. Thanks for all your time, for the help with the different set-ups, with the ALD processes, with the interpretation of the stubborn vanadium oxides who tend to crystallize in unexpected ways, for the answers to all my electrochemical questions, for starting up some procedures and for the many hours of correcting this work.

Quite often, a solid electrolyte interface is formed, very useful in a lithium-ion battery because of its stabilizing influence and because of its ionic conductivity, helping the lithium ions in doing their work. My SEI would be all the helpful people in S1. Thanks to Kilian, Mathias and Nico for XPS, to Olivier for the help with the SEM, to Shaoren for resolving ALD 1 problems, to Ranjith for the Pt ALD process, to Wouter for AFM, to Thomas, Kilian and Shaoren for the warm welcome in their office and to everyone else for the nice atmosphere in CoCooN.

I would also like to thank my promotor, prof. dr. Detavernier, who - I guess - has to be the packaging of the lithium-ion battery in this story, since he keeps everyone together. Thank you for giving me the opportunity to study this interesting topic and for the trust and freedom in this intellectual journey.

And last, but not least, a lithium ion needs an electrolyte. My parents, my sister and my friends are definitely my electrolyte, since they have been supporting me every step of the way. Thank you for believing in me, for the listening ears or welcome distraction whenever needed.

Kobe Geryl, June 2014

Reprints and permissions

Gent, 02/06/2014

Kobe Geryl

Outline

Atomic layer deposition of vanadium oxides for lithium-ion batteries

Kobe Geryl
Master's dissertation submitted in order to obtain the academic degree of
MASTER OF SCIENCE IN ENGINEERING PHYSICS
Academic year 2013-2014
Promotor: Prof. Dr. Christophe Detavernier
Counsellors: Geert Rampelberg and Felix Mattelaer

Faculty of Engineering and Architecture
Ghent University
Department of Solid State Sciences
Chairman: Prof. Dr. Paul Matthys

Content

The opportunities of combining nanotechnology and synthesis of lithium-ion batteries are described in chapter 1, where an introduction to vanadium oxides is given as well. Chapter 2 theoretically describes ALD and techniques for characterisation of thin films, which are applied in chapter 3 on ALD deposited films of vanadium oxide. By variating annealing conditions, 6 different vanadium oxide phases are obtained, which can be tested electrochemically. The fundamentals of electrochemistry and a description of the used procedures and techniques is given in chapter 4. Chapter 5 contains a discussion of the experimental results on the different vanadium oxide phases. Finally, chapter 6 describes coating of a three dimensional substrate as an example system to discuss the opportunities of ALD for lithium-ion batteries.

Keywords

Atomic layer deposition, thin films, vanadium oxide, annealing, lithium-ion batteries, electrode

Atomic layer deposition of vanadium oxides for lithium-ion batteries

Kobe Geryl

Supervisor(s): Prof. dr. Christophe Detavernier
Counsellors: Felix Mattelaer, Geert Rampelberg

Abstract— **Synthesis of electrodes for lithium-ion batteries with nanotechnology could lead to batteries with improved power density. In this work, thin films of vanadium oxide were deposited with atomic layer deposition, because of its ability to deposit uniform layers conformally. Post-deposition annealing conditions were investigated to allow formation of different vanadium oxides. A systematical electrochemical study of the obtained phases was carried out to investigate the possibilities for application in lithium-ion batteries. Subsequently, a 3 dimensional substrate was coated with vanadium oxide by ALD to examine the opportunities of combining ALD with electrode synthesis.**

Keywords— **Atomic layer deposition, lithium-ion battery, annealing, vanadium oxide**

I. INTRODUCTION

Research in development of improved rechargeable lithium-ion batteries has recently been focusing on nanostructures as electrode material, since they could potentially combine high energy and power density. The improved power density with respect to classical electrodes is caused by the increased surface area and shorter Li^+ diffusion lengths[1]. Among the various techniques for synthesis of nanostructures, atomic layer deposition (ALD) shows great promise because of its capability to deposit uniform films on three-dimensional structures conformally.

In this work, ALD was applied for the deposition of vanadium oxide thin films, for application as electrode in lithium-ion batteries (LIB). Compared to $LiCoO_2$, which is the most popular cathode material, vanadium oxide has a much higher specific capacity[2]. Other advantages of vanadium oxide are low cost, abundance, easy synthesis and tunable oxidation state[3].

The as-deposited vanadium oxide films were annealed to allow crystallisation and formation of different oxide phases. By means of electrochemical testing, the best candidates for application as electrode material were identified.

II. DEPOSITION AND PHASE CONTROL OF VANADIUM OXIDE FILMS

A. Experimental methods

Two ALD processes were used for the deposition of amorphous thin films of vanadium oxide, as described by Rampelberg et al.[4] Both processes used Tetrakis[ethylmethylamino]-vanadium (TEMAV) as vanadium precursor and respectively water or ozone as oxygen precursor. Three substrates were examined, i.e. a silicon wafer with thermally grown SiO_2 layer of 100 nm and substrates with sputtered top-layer of TiN (48 nm) and Pt (80nm).

XRR was performed to determine the film thickness. However, on the TiN and Pt substrates, this technique proved unreliable because of the high roughness and multilayer structure of the substrates. Therefore, a relation between XRF counts of vanadium and XRR thickness was established from the samples deposited on SiO_2. This relation allowed to obtain the thickness for samples on Pt and TiN. Cross SEM images confirmed the results obtained by the XRR-XRF relation.

The amorphous films were examined by XPS. As the different oxidation states of vanadium oxide give rise to a shift in energy of the characteristic X-rays[5], XPS allowed to determine the oxidation state of the amorphous thin films. The measured spectrum indicated that the amorphous vanadium oxide films contain contributions of V^{4+} and V^{5+}.

Phase formation of the amorphous films deposited by the two ALD processes was studied by means of an in-situ XRD (ISXRD) setup, allowing measurement of the XRD spectrum while controlling the temperature and ambient conditions of the sample. In this work, the temperature was increased by 0.25°C/s. The ISXRD uses a leak tight chamber containing 2 X-ray transparent Kapton-foil windows, which was purged to vacuum (5.10^{-2} mbar) before a certain gas is supplied to the chamber. Thus, the ISXRD setup allows to control the ambient conditions in which a sample was annealed. In this study, a mass flow controller (MFC) was used to superimpose a well determined flow of oxygen to a constant flow of helium. By adjusting the oxygen flow, the partial pressure of oxygen in the chamber was varied from 1 Pa to 50 Pa, in five steps. Furthermore, an anneal in air was performed.

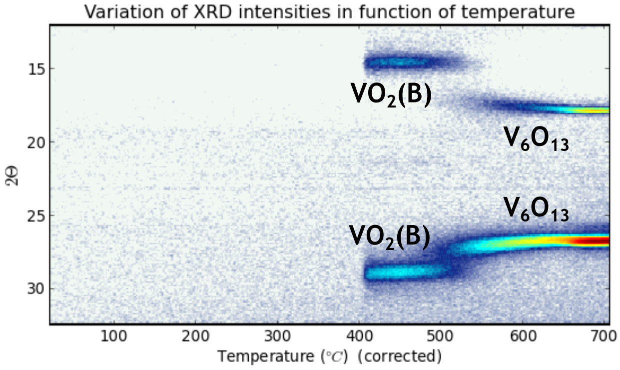

Fig. 1. ISXRD anneal of an amorphous film deposited by the O_3 based ALD process on SiO_2 substrate, in 3.6 Pa O_2.

E-mail: Kobe.Geryl@UGent.be .

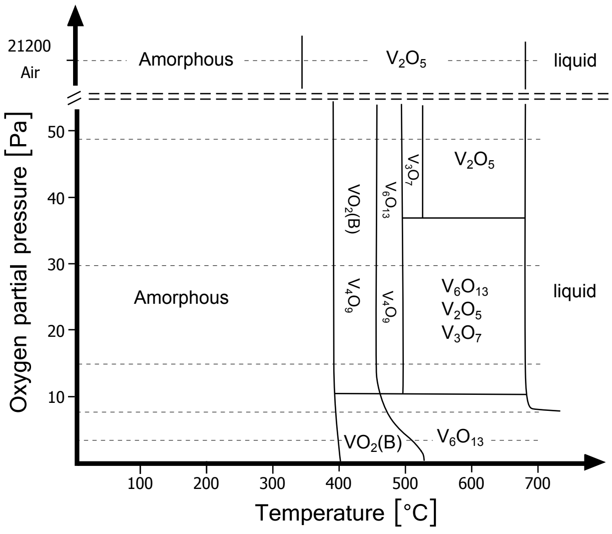

Fig. 2. Formation diagram of amorphous vanadium oxide deposited by the O_3 process on SiO_2. The dotted lines indicate the oxygen partial pressure of the different measurements.

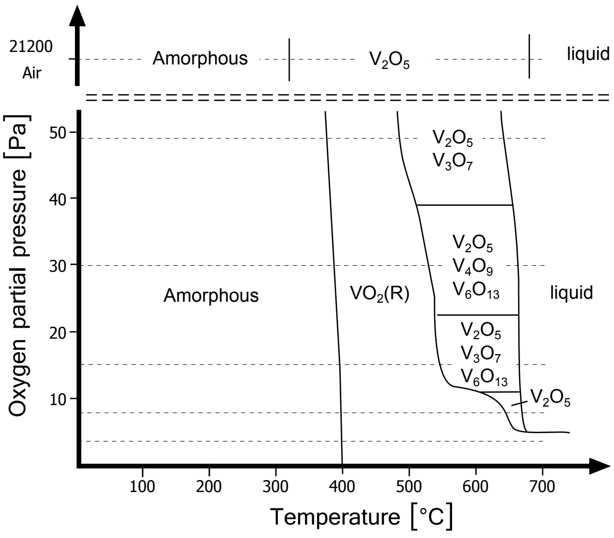

Fig. 3. Formation diagram of amorphous vanadium oxide deposited by the H_2O process on SiO_2. The dotted lines indicate the oxygen partial pressure of the different measurements.

B. *Results and discussion*

As an example, an ISXRD measurement of the amorphous vanadium oxide film on SiO_2, annealed in an atmosphere containing a partial pressure of 3.6 Pa oxygen, is shown in figure 1. Formation of VO_2(B) and V_6O_{13} is observed at approximately 400 °C and 520 °C. .

The results of the phase formation under variating atmospheric conditions are summarised in 'formation diagrams'. Figure 2 and 3 show the formation diagram for the amorphous films deposited with the ozone and water based ALD processes on SiO_2. The observed phases are all part of the V_nO_{2n+1} series (with n=2, 3, 4 and 6), which have an oxidation state between 4+ and 5+, indicating that the oxidation state of the amorphous film limits the phases that can be reached by annealing. Furthermore, it is observed that the phases containing more oxygen are formed for higher partial pressures of O_2, as oxygen is more easily absorbed into the layer. For instance, annealing in air results in V_2O_5 while annealing in 3.7 Pa O_2 results in VO_2(R) and VO_2(B). The formation diagrams also indicate that the layers deposited by the two processes are not equal. The difference of crystallization in oxygen deficient atmosphere, to VO_2(B) and VO_2(R), can be understood by the difference in density between the films deposited with both processes. It was observed that more XRF counts per unit thickness are measured for a film deposited with the H_2O process, indicating that the amorphous film by the H_2O process has a higher density, compared to the film deposited by the O_3 process. This translates to crystallization in the high density phase VO_2(R) (4.67 g/cm^3)[6] for H_2O based depositions and to the low density phase VO_2(B) (4.03 g/cm^3)[6] for O_3 based depositions.

Similar annealing studies were performed for thin films deposited with both ALD processes on TiN and Pt substrates. The results illustrated that the phase formation is substrate dependent. In general, the preferential formation of VO_2(R) and VO_2(B) was retrieved, but less phases were formed and less mixed phase regions were observed for films on TiN and Pt. In the case of the TiN substrate, the annealing was limited to formation of VO_2(R) and VO_2(B), for all controlled oxygen deficient atmospheres, while annealing in air resulted in formation of V_2O_5, preceded by other phases of the V_nO_{2n+1} series. A possible explanation could be that the SiO_2 substrate acts as a secondary source of oxygen, apart from the supply from the atmosphere, while the Pt substrate is neutral and the TiN layer behaves as an oxygen drain, considering formation of TiO_2(A) and TiO_2(R) was observed during annealing at approximately 400 °C and 600 °C. Furthermore, if the formation of TiO_2(R) occurred in the presence of a VO_2(R) layer, a shift in the XRD peak of VO_2(R) could be observed. As both rutile phases have nearly identical lattices, it is possible that a mixed rutile phase of titanium oxide and vanadium oxide was formed.

The various phases, formed upon annealing, were studied for application in lithium-ion batteries. Since the conductivity of vanadium oxide is low, a current conducting layer must be present underneath the vanadium oxide. For this reason, the films deposited on the platinum substrate were studied electrochemically. On the platinum substrate, single phase regions of all six phases were encountered, such that electrochemical tests of all oxides in the V_nO_{2n+1} series could be carried out.

III. ELECTROCHEMICAL TESTING OF VO_x

A. *Experimental methods*

Three electrochemical procedures were applied on the various vanadium oxide films, allowing comparison between the 6 different phases. Additionally, three regions of the $Li_xV_2O_5$-system were examined: cycling within the α-ϵ-δ phases (2.9 - 4 V vs. Li/Li$^+$), or within the γ (2.0 - 4 V vs. Li/Li$^+$) or ω phase (1.5 - 4.0 V vs. Li/Li$^+$). The different phases of the

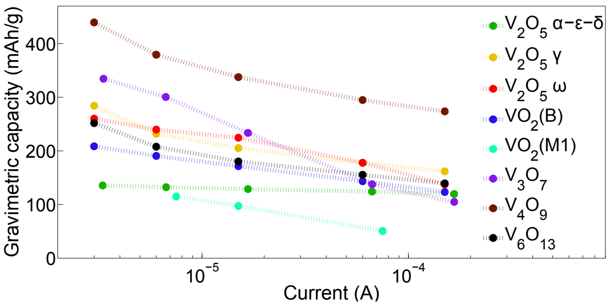

Fig. 4. Total capacity of discharge with respect to applied current for the different vanadium oxides.

$Li_xV_2O_5$ system allow intercalation of 1, 2 and 3 lithium ions, respectively[7].

The 3 electrochemical procedures consisted of a cyclic voltammetry (CV) measurement at a scan rate of 0.01 V/s, followed by a galvanostatic charge/discharge (CD) at different current densities, approximately 1C, 2C, 5C, 20C and 50C. Finally, a cyclability experiment was conducted, which consisted of 50 cycles galvanostatic charge/discharge at approximately 2C. The measurements were carried out in a 3 electrode test cell with a Metrohm PGSTAT302N and PGSTAT204 galvanostat/potentiostat, in an argon-filled glovebox with oxygen and water concentration below 1 ppm. As reference and counter electrode, a lithium strip (99.9% pure, Sigma Aldrich) was utilised and 1M $LiClO_4$ in PC solvent (io-li-tec, 99%) was used as electrolyte.

B. *Results and discussion*

CV measurements yielded information regarding the characteristic potential of the lithium intercalation processes. Comparison between the different vanadium oxides revealed that the peaks in the voltammogram of several oxides showed good resemblance, which could be explained by similarities between the lattices of the different vanadium oxides and thus comparable lithium insertion mechanisms, based on similar studies for other systems[8,9]. More specifically, a peak at 2.5 V vs. Li/Li^+ was present in the voltammogram of VO_2(B), which was also retrieved for V_4O_9, V_6O_{13} and V_3O_7 and to lower extent for VO_2(M1). A second remarkable agreement was found at 2.27 V vs. Li/Li^+ for V_3O_7 and γ-V_2O_5. Thus, CV granted an experimental proof that the different oxides of the V_nO_{2n+1} series are strongly related, as theoretically described by Katzke et al.[10]

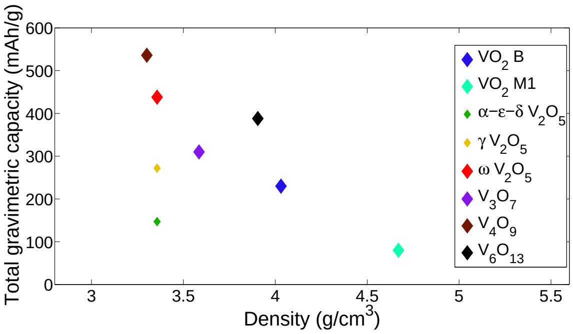

Fig. 5. Observation of the relation between total capacity and density.

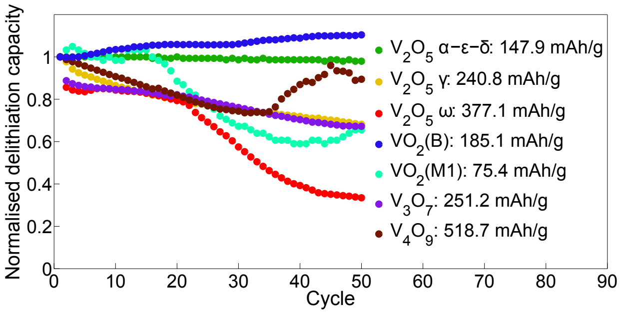

Fig. 6. Normalised capacity evolution with increased cycling, the initial capacity is given in the legend.

Total capacity and rate capability was obtained by CD measurements. Figure 4 shows the discharge capacity obtained for the various vanadium oxides at different currents. V_4O_9 clearly outperforms the other vanadium oxides, an initial charge and discharge capacity of 536 mAh/g and 440 mAh/g were obtained. The second highest capacity value was obtained for V_3O_7 when a current of 3 μA was applied, but due to low rate capability, only 30% was retrieved at a current of 175 μA. The rate capability of the other vanadium oxides was observed to be comparable, except for α-ϵ-δ V_2O_5, which barely suffered a decrease in capacity in the investigated current domain. The current limits were not yet reached for this electrode and can be further examined by CD experiments at higher C-rates.

An interesting relation between the capacity and density was observed, see figure 5. More lithium ions could be inserted in vanadium oxides with lower density, which can be explained by the presence of more voids and interstitial spaces. This relation could be valid to some extent for other materials and could be used as a preliminary indication on possibly interesting structures.

For application in rechargeable LIB, it is crucial that the material can withstand multiple charge/discharge cycles without suffering capacity loss. This is tested by the cyclability experiment, of which the results are displayed in figure 6. Only 2 of the considered electrodes show good behaviour with respect to cycling, VO_2(B) and α-ϵ-δ V_2O_5, since a severe capacity loss is observed for the other phases after 50 cycles. The conspicuous behaviour of V_4O_9, VO_2(M1) and ω-V_2O_5 is caused by unwanted side-reactions, which could be identified as substrate related. By means of XRD, the formation of $LiCl_4$ on the surface of these samples was identified. For V_3O_7, γ-V_2O_5 and the first 30 cycles of V_4O_9, a comparable degree of capacity loss is observed.

The cyclability experiment allows to conclude that VO_2(B) and α-ϵ-δ V_2O_5 are the most promising candidates for application as electrode in LIB, unless the capacity loss problems associated with the other phases can be resolved. More specifically, based on figure 4, VO_2(B) should be considered if small currents are involved because of its higher initial capac-

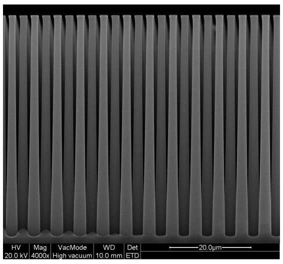

Fig. 7. SEM image of the silicon nanopillars.

ity, while α-ϵ-δ V_2O_5 is the better candidate for applications with higher current because of of its good rate capability.

Several lithiated samples were characterised with XPS, AFM, XRD and SEM. The most important conclusions could be drawn by the SEM measurements, which allowed to determine the volume expansion upon lithiation for 2 samples. A value of approximately 25% was obtained. As several authors relate expansion to capacity loss[11,12], it might prove to be interesting to perform a more thorough comparison of the volume expansion upon lithiation of the different phases and investigate if this expansion could be reduced.

IV. V_2O_5 COATED NANOPILLARS

The choice of ALD for the deposition of the thin films was governed by the intrinsic ability of ALD to deposit layers of uniform thickness on three dimensional substrates. In this work, three dimensional silicon nanopillars were used as example, with total surface area increased by a factor 15.5. A platinum layer was deposited with ALD on the surface of the pillars as current collector, after which the ALD processes for vanadium oxide films were applied. The conformity of the deposited layer was examined by EDX. By extended exposure to both precursors, the conformity of the deposited layer was successfully enhanced. Subsequent annealing caused the amorphous vanadium oxide film to crystallize to V_2O_5, such that electrochemical testing in the α-ϵ-δ V_2O_5 region could be carried out. CD measurements revealed a reduced rate capability, which could possibly be caused by limited supply of the electrolyte. Cyclability testing of the nanopillars confirmed the promising behaviour of α-ϵ-δ V_2O_5, obtained on flat surfaces.

V. CONCLUSION

Amorphous vanadium oxide films, deposited by two ALD processes, have been successfully crystallised into 6 different phases (VO_2(B), VO_2(M1), V_2O_5, V_3O_7, V_4O_9 and V_6O_{13}), by annealing in an atmosphere with controlled oxygen content. The 6 oxides have been compared electrochemically for application as electrode material in LIB, resulting in VO_2(B) and α-ϵ-δ V_2O_5 as best candidates for low current and high current applications respectively. Finally, a three dimensional structure has been coated with V_2O_5 to illustrate the possibilities of ALD in development of nanostructured electrodes.

REFERENCES

[1] X. Rui, D. Sim, C. Xu, W. Liu, H. Tan, K. Wong, H. H. Hng, T. M. Lim, and Q. Yan, “One-pot synthesis of carbon-coated VO_2(B) nanobelts for high-rate lithium storage,” *RSC Adv.*, vol. 2, pp. 1174–1180, 2012.

[2] M. Rahman, J.-Z. Wang, N. H. Idris, Z. Chen, and H. Liu, “Enhanced lithium storage in a VO_2(B)-multiwall carbon nanotube microsheet composite prepared via an in situ hydrothermal process,” *Electrochimica Acta*, vol. 56, no. 2, pp. 693 – 699, 2010.

[3] N. Ganganagappa and A. Siddaramanna, “One step synthesis of monoclinic VO_2(B) bundles of nanorods: Cathode for Li ion battery,” *Materials Characterization*, vol. 68, no. 0, pp. 58–62, 2012.

[4] G. Rampelberg, M. Schaekers, K. Martens, Q. Xie, D. Deduytsche, B. D. Schutter, N. Blasco, J. Kittl, and C. Detavernier, “Semiconductor-metal transition in thin VO_2 films grown by ozone based atomic layer deposition,” *Applied Physics Letters*, vol. 98, pp. 162902–162904, 2011.

[5] G. Silversmit, D. Depla, H. Poelman, G. B. Marin, and R. D. Gryse, “Determination of the V2p XPS binding energies for different vanadium oxidation states (V5+ to V0+),” *Journal of Electron Spectroscopy and Related Phenomena*, vol. 135, no. 2, pp. 167 – 175, 2004.

[6] C. Leroux, G. Nihoul, and G. Van Tendeloo, “From VO_2(B) to VO_2(R): Theoretical structures of VO_2 polymorphs and in situ electron microscopy,” *Phys. Rev. B*, vol. 57, pp. 5111–5121, Mar 1998.

[7] C. Delmas, H. Cognac-Auradou, J. Cocciantelli, M. Menetrier, and J. Doumerc, “The $Li_xV_2O_5$ system: An overview of the structure modifications induced by the lithium intercalation,” *Solid State Ionics*, vol. 69, no. 3, pp. 257–264, 1994.

[8] A. C. Gorren, A. J. Kungl, K. Schmidt, E. R. Werner, and B. Mayer, “Electrochemistry of pterin cofactors and inhibitors of nitric oxide synthase,” *Nitric Oxide*, vol. 5, no. 2, pp. 176 – 186, 2001.

[9] M. Hourani and A. Wieckowski, “Single crystal electrochemistry of rhodium: Anion effects and order/disorder transitions of clean and silver coated rh (111) surfaces,” *Journal of Electroanalytical Chemistry and Interfacial Electrochemistry*, vol. 244, no. 1, pp. 147 – 161, 1988.

[10] H. Katzke, P. Toledano, and W. Depmeier, “Theory of morphotropic transformations in vanadium oxides,” *Phys. Rev. B*, vol. 68, p. 024109, Jul 2003.

[11] P. C. Hayes and S. H. Algie, *Process Principles in Minerals and Materials Production*. Hayes Publishing, 1993.

[12] K. West, B. Zachau-Christiansen, M. Ostergard, and T. Jacobsen, “Vanadium oxides as electrode materials for rechargeable lithium cells,” *Journal of Power Sources*, vol. 20, no. 1, pp. 165 – 172, 1987. 3rd International Meeting on Lithium Batteries.

Atomaire laag depositie van vanadium oxiden voor lithium-ion batterijen

Kobe Geryl

Supervisor(s): Prof. dr. Christophe Detavernier
Counsellors: Felix Mattelaer, Geert Rampelberg

Abstract—**Synthese van elektroden voor lithium-ion batterijen met behulp van nanotechnologie kan mogelijks leiden tot batterijen met verbeterde vermogensdichtheid. In dit werk werden dunne lagen gedeponeerd met atomaire laag depositie (ALD), omwille van de mogelijkheid om uniforme lagen af te zetten op conforme wijze. Nadien werd de invloed van bepaalde parameters bij thermische behandeling onderzocht, met als doel verschillende vanadium oxide fasen te vormen. Door middel van een systematische elektrochemische studie werd nagegaan of de verkregen fasen toepasbaar zijn als elektrode voor lithium-ion batterijen. Tot slot werd een driedimensionaal substraat gecoat met vanadium oxide met behulp van ALD, om de kansen te onderzoeken van het combineren van ALD en synthese van elektroden.**

Keywords— **Atomaire laag depositie, lithium-ion batterij, thermische behandeling, vanadium oxide**

I. INLEIDING

Recent onderzoek naar verbeterde herlaadbare lithium-ion batterijen spitst zich toe op nanostructuren als elektrode, aangezien deze structuren mogelijks een hoge energie- en vermogensdichtheid kunnen combineren. De verhoogde vermogensdichtheid ten opzichte van klassieke elektroden wordt veroorzaakt door het groter oppervlak en de kortere diffusielengte van de Li^+ ionen[1]. Er bestaan verscheidene technieken voor het deponeren van dunne lagen. Een daarvan is ALD, veelbelovend omwille van de mogelijkheid om uniforme lagen af te zetten op conforme wijze op driedimensionale structuren.

In dit werk werd ALD toegepast voor het deponeren van dunne vanadium oxide lagen voor toepassingen als elektrode in lithium-ion batterijen (LIB). Vanadium oxide heeft een hogere specifieke capaciteit dan $LiCoO_2$[2], het populairste kathodemateriaal. Bijkomende voordelen van vanadium oxide zijn lage kostprijs, overvloed, eenvoudige verwerking en een wijzigbare oxidatietoestand[3].

De gedeponeerde vanadium oxide lagen werden thermisch behandeld om kristallisatie en fasevorming tot verschillende oxide fasen mogelijk te maken. Door middel van elektrochemische proeven werden deze vergeleken, om zo het beste materiaal te selecteren voor toepassingen als elektrode.

II. DEPOSITIE EN FASE CONTROLE VAN VANADIUM OXIDE LAGEN

A. Experimentele methoden

Twee ALD processen werden gebruikt voor de depositie van amorfe vanadium oxide lagen, zoals beschreven door Rampelberg et al.[4] Beide processen maakten gebruik van Tetrakis[ethylmethylamino]vanadium (TEMAV) als vanadium precursor en water of ozon werd gebruikt als zuurstof precursor. Drie substraten werden onderzocht; een silicium wafer met 100 nm thermisch gegroeide SiO_2 laag en substraten met gesputterde top-laag TiN (48 nm) en Pt (80 nm).

XRR werd gebruikt om de laagdikte te bepalen. Op de TiN en Pt substraten was deze techniek echter niet toepasbaar, omwille van de hoge ruwheid en gelaagde structuur. Bijgevolg werd een relatie opgesteld tussen het aantal vanadium tellen bij XRF en de laagdikte, bepaald door XRR, voor de lagen op SiO_2. Deze relatie liet toe om de laagdikte van de gedeponeerde lagen op Pt en TiN te bepalen. SEM beelden van de doorsnede van verschillende stalen bevestigden de voorspellingen op basis van de XRR-XRF relatie.

De amorfe lagen werden onderzocht met XPS. Aangezien de verscheidene oxidatietoestanden van vanadium een verschuiving in de energie van de karakteristieke X-stralen teweegbrengen, kan XPS gebruikt worden om de oxidatietoestand te bepalen[5]. XPS toonde aan dat de oxidatietoestand van de amorfe vanadium oxide lagen bestond uit een opmenging van V^{4+} en V^{5+}.

Fasevorming van de amorfe lagen, gedeponeerd met de twee beschouwde ALD processen, werd bestudeerd met behulp van in-situ XRD. Deze techniek liet toe het XRD spectrum te meten terwijl de temperatuur en omgeving van het staal gewijzigd werd. De temperatuur werd verhoogd met 0.25 °C/s. De ISXRD opstelling maakt gebruik van een afgesloten kamer waarin 2 Kapton vensters bevestigd werden, die transparant zijn voor X-stralen. De kamer werd eerst naar vacuum gebracht (5.10^{-2} mbar), waarna vervolgens een gas door de kamer werd gepompt. Op deze wijze laat de ISXRD

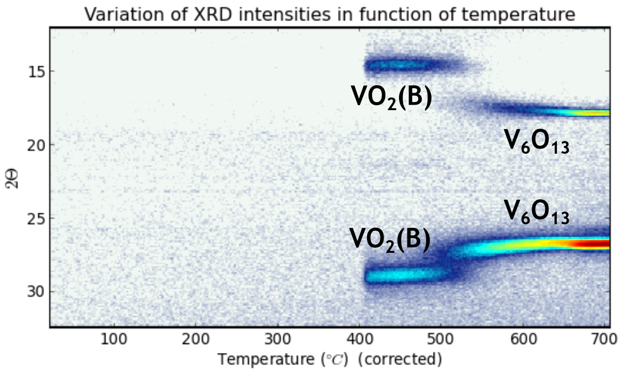

Fig. 1. ISXRD meting op een amorfe film, gedeponeerd met het O_3 ALD proces op SiO_2, in 3.6 Pa O_2.

E-mail: Kobe.Geryl@UGent.be .

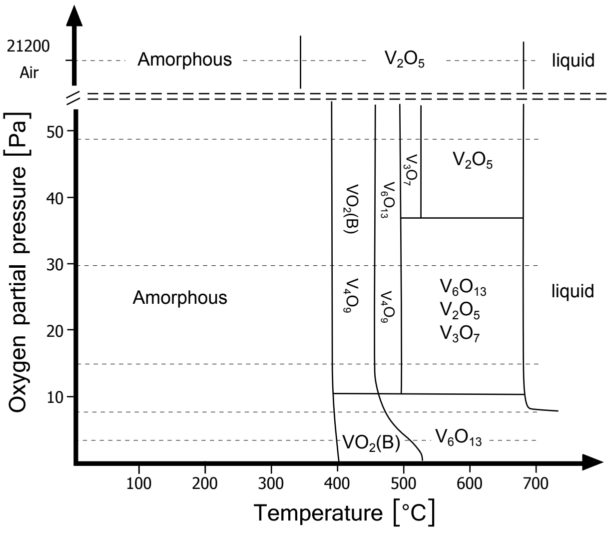

Fig. 2. Vormingsdiagram van amorf vanadium oxide op SiO_2 met het O_3 proces. De stippellijnen tonen de partieeldruk zuurstof van de verschillende metingen.

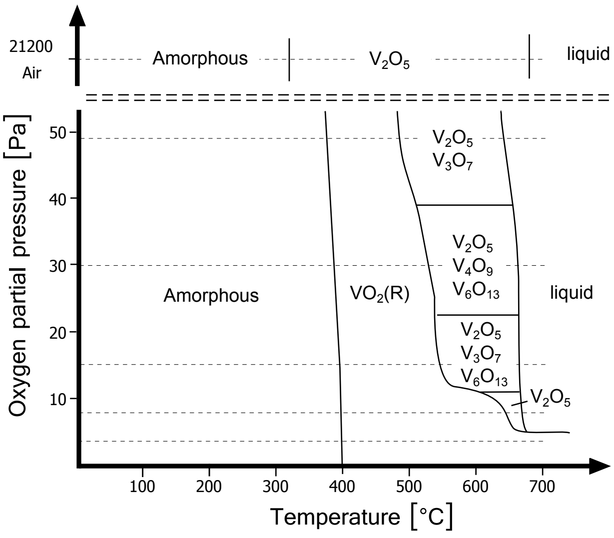

Fig. 3. Vormingsdiagram van amorf vanadium oxide op SiO_2 met het H_2O proces. De stippellijnen tonen de partieeldruk zuurstof van de verschillende metingen.

opstelling toe om de omgeving te wijzigen waarin het staal thermisch behandeld werd. Met behulp van een 'mass flow controller' (MFC) werd een welbepaalde hoeveelheid zuurstof toegevoegd aan een constante stroom heliumgas. Door de hoeveelheid zuurstof aan te passen kon de partieeldruk van zuurstof gewijzigd worden van 1 Pa tot 50 Pa. Nadien werd een staal in zuivere lucht opgewarmd.

B. Resultaten en discussie

Een ISXRD meting van een amorfe vanadium oxide laag op SiO_2, thermisch behandeld in een atmosfeer met partieeldruk zuurstof van 3.6 Pa, wordt getoond in figuur 1. De vorming van $VO_2(B)$ en V_6O_{13} werd vastgesteld op 400 °C en 520 °C.

De resultaten van de fasevorming bij wijzigende partieeldruk zuurstof in de omgeving worden samengevat in 'vormingsdiagrammen'. Figuren 2 en 3 tonen het vormingsdiagram van de amorfe lagen op SiO_2. De optredende vanadium oxide fasen zijn allen onderdeel van de V_nO_{2n+1} reeks (met n=2, 3, 4 en 6) met oxidatiegetal tussen 4+ en 5+, wat erop wijst dat het oxidatiegetal van de amorfe laag beperkingen oplegt aan de bereikbare fasen tijdens thermische behandeling. Bovendien werd vastgesteld dat zuurstofrijke fasen gevormd werden bij hogere partieeldruk zuurstof, waarbij absorptie van zuurstof uit de atmosfeer eenvoudiger wordt. Zo leidde thermisch behandelen in zuivere lucht tot V_2O_5, terwijl $VO_2(R)$ en $VO_2(B)$ bereikt werden in 3.7 Pa zuurstof. De vormingsdiagrammen tonen ook aan dat de gedeponeerde lagen niet identiek zijn. Het verschil in kristallisatie naar $VO_2(R)$ en $VO_2(B)$ kan begrepen worden door het verschil in densiteit tussen de lagen afgezet met beide processen. Op basis van XRF werd vastgesteld dat meer vanadium atomen per dikte eenheid aanwezig zijn in de laag die met het water proces gedeponeerd werd, wat erop wijst dat de densiteit van deze laag hoger is. Als gevolg kristalliseert een laag, gedeponeerd met het H_2O proces, in $VO_2(R)$ met hoge densiteit ($4.67\ g/cm^3$)[6] en zorgt het O3 proces voor kristallisatie tot $VO_2(B)$($4.03\ g/cm^3$)[6].

Een vergelijkbare studie werd uitgevoerd voor de thermische behandeling van lagen gedeponeerd op TiN en Pt substraten. De resultaten hiervan wezen erop dat de fasevorming beïnvloedt wordt door het substraat. De preferentiële vorming van $VO_2(R)$ en $VO_2(B)$ werd teruggevonden, maar verder werden voor deze substraten werden minder gebieden met gemengde fasevorming waargenomen. In het geval van TiN was de fasevorming tot 50 Pa zuurstof gelimiteerd tot $VO_2(R)$ en $VO_2(B)$. Thermische behandeling in lucht leidde tot V_2O_5, voorafgegaan door andere fasen uit de V_nO_{2n+1} reeks. Een mogelijke verklaring is dat SiO_2 als bijkomstige zuurstofbron optreedt, naast zuurstoftoevoer uit de atmosfeer, terwijl Pt hierin neutraal is en TiN zuurstof afvoert, gelet op de geobserveerde vorming van $TiO_2(A)$ en $TiO_2(R)$ vanaf 400 °C en 600 °C. Indien de vorming van $TiO_2(R)$ gebeurde in nabijheid van $VO_2(R)$ werd een verschuiving van de XRD piek van $VO_2(R)$ waargenomen. Aangezien beide rutiel fasen uit een nagenoeg identiek rooster bestaan, kan dit erop wijzen dat er een mengfase van titanium oxide en vanadium oxide gevormd werd.

De verscheidene fasen die waargenomen werden tijdens de thermische behandeling, werden bestudeerd met het oog op toepassing in lithium-ion batterijen. Gezien de geleidbaarheid van vanadium oxide onvoldoende is, dient een stroomgeleidende laag aanwezig te zijn onder het oxide. Om deze reden werden denkel de deposities op het platina substraat elektrochemisch bestudeerd. Het was bovendien mogelijk zuivere fasen van de 6 oxiden te vormen op platina, zodat alle zes de elementen uit de V_nO_{2n+1} reeks getest konden worden

III. Electrochemische proeven op VO_x

A. Experimentele methoden

Drie elektrochemische procedures werden toegepast op de vanadium oxide lagen om vergelijking tussen de zes fasen mo-

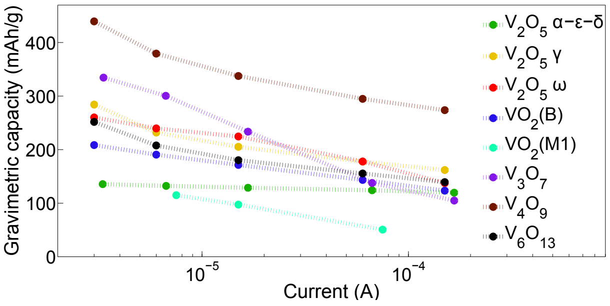

Fig. 4. Totale capaciteit bij ontladen vergeleken met de aangelegde stroom vooor de verschillende vanadium oxiden.

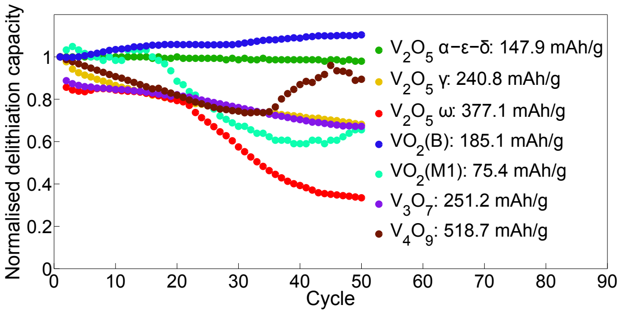

Fig. 6. Evolutie van de genormaliseerde capaciteit na meerdere cycli.

gelijk te maken. Bovendien werden drie gebieden van het $Li_xV_2O_5$ systeem onderzocht, namelijk de α-ϵ-δ fasen (2.9 - 4 V vs. Li/Li$^+$), of de γ fase (2.0 - 4 V vs. Li/Li$^+$) of ω fase (1.5 - 4 V vs. Li/Li$^+$). Deze laten absorptie toe van respectievelijk 1, 2 of 3 lithium ionen.

De 3 elektrochemische procedures bestonden uit een 'cyclic voltammetry' (CV) meting aan een scansnelheid van 0.01 V/s, gevolgd door een reeks galvanostatisch opladen/ontladen (CD, eng: charge/discharge) metingen aan een stroom van ongeveer 1C, 2C, 5C, 20C en 50C. Tot slot werd de herlaadbaarheid onderzocht door middel van 50 cycli galvanostatisch opladen/ontladen aan ongeveer 2C. De metingen werden uitgevoerd in een 3 elektroden test cell met een Metrohm PGSTAT 302N en PGSTAT204 galvanostat/potentiostat in een handschoenkast gevuld met argon, met zuurstof en water concentratie kleiner dan 1 ppm. Als referentie- en tweede elektrode werd een lithium strip gebruikt (99.9% zuiver, Sigma Aldrich) en 1M $LiClO_4$ in PC solvent (io-li-tec, 99%) werd gebruikt als elektrolyt.

B. Resultaten en discussie

De CV metingen toonden de karakteristieke potentiaal van de lithium intercalatieprocessen. Vergelijking tussen de verscheidene vanadium oxiden toonde aan dat de pieken in het voltammogram van meerdere oxiden opvallende gelijkenissen vertoonden, wat kon verklaard worden door gelijkenissen in de roosters van de verschillende vanadium oxiden, gebaseerd op vergelijkbare studies op andere systemen[8,9]. Meer specifiek werd een piek op 2.5 V vs. Li/Li$^+$ waargenomen in het voltmamogram van VO_2(B) die ook zichtbaar was bij V_4O_9, V_6O_{13} en V_3O_7 en met mindere mate in VO_2(M1). Een tweede opvallende gelijkenis werd gevonden bij 2.27 V vs. Li/Li$^+$ voor V_3O_7 en γ-V_2O_5. Op deze wijze leverde CV experimenteel bewijs dat de verschillende fasen van de V_nO_{2n+1} reeks sterk gerelateerd zijn, zoals theoretisch beschreven door Katzke et al.[10]

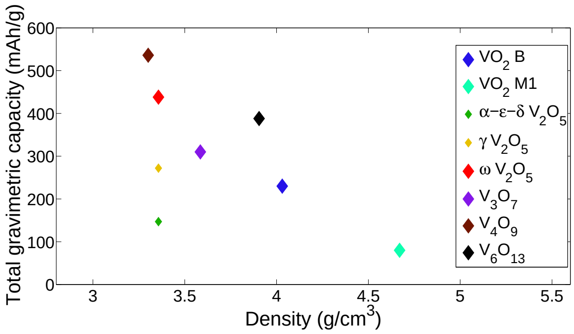

Fig. 5. Vaststelling van het verband tussen totale capaciteit en densiteit.

De totale capaciteit en afhankelijkheid van de stroom werd verkregen door CD metingen. Figuur 4 toont de capaciteit bij ontladen voor de verscheidene vanadium oxiden aan verschillende stroomsterktes. V_4O_9 onderscheidt zich van de andere oxiden, een initiële capaciteit bij opladen en ontladen van 536 mAh/g en 440 mAh/g werd bereikt. De op een na hoogste waarde werd bereikt voor V_3O_7 bij een stroom van 3 μA, bij een stroom van 175 μA werd echter maar 30% van deze waarde gemeten. De stroomafhankelijkheid van de andere vanadium oxiden was vergelijkbaar, behalve voor α-ϵ-δ V_2O_5, dat amper capaciteitsverlies vertoonde bij toenemende stroom. De limiet werd voor deze elektrode nog niet bereikt en kan verder onderzocht worden met CD experimenten aan hogere C-waarden.

Een interessante relatie tussen capaciteit en densiteit werd vastgesteld, zie figuur 5. Bij een lagere densiteit is het materiaal in staat meer lithium ionen op te nemen, wat kan verklaard worden door de aanwezigheid van meer lege ruimtes en interstitiële plaatsen. Deze relatie is mogelijks tot op zekere hoogte geldig voor andere materialen en zou als aanwijzing kunnen worden gebruikt om potentieel interessante structuren op te sporen.

Voor toepassingen in LIB is het cruciaal dat de elektroden meerdere cycli opladen/ontladen kunnen weerstaan zonder capaciteitsverlies. Dit werd getest door de herlaadbaarheidsexperimenten, waarvan de resultaten in figuur 6 zijn weergegeven. Slechts 2 van de beschouwde elektroden vertonen veelbelovend gedrag, VO_2(B) en α-ϵ-δ V_2O_5, aangezien ernstig capaciteitsverlies werd vastgesteld bij de andere fasen na 50 cycli. Het opvallende gedrag van V_4O_9, VO_2(M1) en ω-V_2O_5 werd veroorzaakt door ongewenste zij-reacties, die konden verklaard worden als reacties met het substraat. Door middel van XRD werd de afzetting van $LiCl_4$ geïdentificeerd. Voor V_3O_7, γ-V_2O_5 en de eerste 30 cycli van V_4O_9 werd een gelijkaardige mate van capaciteitsverlies vastgesteld.

De proeven inzake herlaadbaarheid laten toe te besluiten dat VO_2(B) en α-ϵ-δ V_2O_5 de meest veelbelovende kandida-

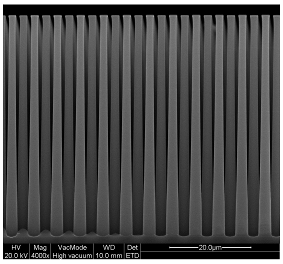

Fig. 7. SEM afbeelding van de silicium nanopilaren.

ten zijn voor toepassingen als elektrode in LIB, tenzij het verlies aan capaciteit bij herladen van de andere fasen kan opgelost worden. Meer specifiek kan men op basis van figuur 4 stellen dat VO_2(B) de beste optie is wanneer kleine stromen nodig zijn, terwijl α-ϵ-δ V_2O_5 het beste materiaal is voor toepassingen met grotere stromen.

Meerdere gelithieerde stalen werden gekarakteriseerd met XPS, AFM, XRD en SEM. De belangrijkste conclusies werden getrokken uit de SEM metingen, die toelieten om de volume-expansie ten gevolge van lithium absorptie te bepalen voor 2 stalen. Een waarde van om en bij de 25% werd bekomen. Aangezien meerdere auteurs expansie in verband brengen met capaciteitsverlies[11,12], is het mogelijks nuttig een meer diepgaande studie uit te voeren op de verschillende fasen met betrekking tot expansie en mogelijke limiterende factoren.

IV. Nanopilaren gecoat met V_2O_5

De keuze voor ALD bij de depositie van dunne films werd bepaald door de intrinsieke mogelijkheid van ALD om uniforme lagen af te zetten op conforme wijze op driedimensionale substraten. Als voorbeeld werden driedimensionale silicium nanopilaren gebruikt in dit werk, met oppervlak verhoogd met een factor 15.5. Een stroomgeleidende platina laag werd afgezet op dit oppervlak met ALD. Nadien werd vanadium oxide gedeponeerd met de 2 beschouwde ALD processen. De conformiteit van de afgezette laag werd onderzocht met EDX. De blootstelling aan beide precursoren werd met succes verlengd om de conformiteit te verhogen. Nadien werd de amorfe laag thermisch behandeld om kristallisatie tot V_2O_5 mogelijk te maken, zodat het staal elektrochemisch getest kon worden in de α-ϵ-δ V_2O_5 fase. CD metingen wezen op een grotere afhankelijkheid van capaciteit ten opzichte van de opgelegde stroom, mogelijks verklaard door een gelimiteerde toevoer van lithium ionen door het elektrolyt. Verder werd de uitstekende herlaadbaarheid van α-ϵ-δ V_2O_5 bevestigd op de nanopilaren.

V. Conclusie

Amorfe lagen van vanadium oxide, afgezet met 2 ALD processen, werden succesvol gekristalliseerd tot 6 verschillende fasen (VO_2(B), VO_2(M1), V_2O_5, V_3O_7, V_4O_9 en V_6O_{13}), door middel van thermisch behandelen in een atmosfeer met gecontroleerde hoeveelheid zuurstof. De 6 oxiden werden elektrochemisch vergeleken met het oog op toepassing als elektrode in LIB, wat erop wees dat VO_2(B) en α-ϵ-δ V_2O_5 de beste kandidaten zijn voor toepassingen met lage en hoge stroom. Bovendien werd een driedimensionale structuur gecoat met V_2O_5 om de mogelijkheden aan te tonen van ALD in de ontwikkeling van elektroden op nanostructuur.

Referenties

[1] X. Rui, D. Sim, C. Xu, W. Liu, H. Tan, K. Wong, H. H. Hng, T. M. Lim, and Q. Yan, “One-pot synthesis of carbon-coated VO_2(B) nanobelts for high-rate lithium storage,” *RSC Adv.*, vol. 2, pp. 1174–1180, 2012.

[2] M. Rahman, J.-Z. Wang, N. H. Idris, Z. Chen, and H. Liu, “Enhanced lithium storage in a VO_2(B)-multiwall carbon nanotube microsheet composite prepared via an in situ hydrothermal process,” *Electrochimica Acta*, vol. 56, no. 2, pp. 693 – 699, 2010.

[3] N. Ganganagappa and A. Siddaramanna, “One step synthesis of monoclinic VO_2(B) bundles of nanorods: Cathode for Li ion battery,” *Materials Characterization*, vol. 68, no. 0, pp. 58–62, 2012.

[4] G. Rampelberg, M. Schaekers, K. Martens, Q. Xie, D. Deduytsche, B. D. Schutter, N. Blasco, J. Kittl, and C. Detavernier, “Semiconductor-metal transition in thin VO_2 films grown by ozone based atomic layer deposition,” *Applied Physics Letters*, vol. 98, pp. 162902–162904, 2011.

[5] G. Silversmit, D. Depla, H. Poelman, G. B. Marin, and R. D. Gryse, “Determination of the V2p XPS binding energies for different vanadium oxidation states (V5+ to V0+),” *Journal of Electron Spectroscopy and Related Phenomena*, vol. 135, no. 2, pp. 167 – 175, 2004.

[6] C. Leroux, G. Nihoul, and G. Van Tendeloo, “From VO_2(B) to VO_2(R): Theoretical structures of VO_2 polymorphs and in situ electron microscopy,” *Phys. Rev. B*, vol. 57, pp. 5111–5121, Mar 1998.

[7] C. Delmas, H. Cognac-Auradou, J. Cocciantelli, M. Menetrier, and J. Doumerc, “The $Li_xV_2O_5$ system: An overview of the structure modifications induced by the lithium intercalation,” *Solid State Ionics*, vol. 69, no. 3, pp. 257–264, 1994.

[8] A. C. Gorren, A. J. Kungl, K. Schmidt, E. R. Werner, and B. Mayer, “Electrochemistry of pterin cofactors and inhibitors of nitric oxide synthase,” *Nitric Oxide*, vol. 5, no. 2, pp. 176 – 186, 2001.

[9] M. Hourani and A. Wieckowski, “Single crystal electrochemistry of rhodium: Anion effects and order/disorder transitions of clean and silver coated rh (111) surfaces,” *Journal of Electroanalytical Chemistry and Interfacial Electrochemistry*, vol. 244, no. 1, pp. 147 – 161, 1988.

[10] H. Katzke, P. Toledano, and W. Depmeier, “Theory of morphotropic transformations in vanadium oxides,” *Phys. Rev. B*, vol. 68, p. 024109, Jul 2003.

[11] P. C. Hayes and S. H. Algie, *Process Principles in Minerals and Materials Production*. Hayes Publishing, 1993.

[12] K. West, B. Zachau-Christiansen, M. Ostergard, and T. Jacobsen, “Vanadium oxides as electrode materials for rechargeable lithium cells,” *Journal of Power Sources*, vol. 20, no. 1, pp. 165 – 172, 1987. 3rd International Meeting on Lithium Batteries.

Contents

List of abbreviations

AB	Acetylene Black
AC	Alternating Current
AFM	Atomic Force Microscopy
ALD	Atomic Layer Deposition
BSE	Backscattered Electrons
CB	Carbon Black
CD	Charge/Discharge
CE	Counter Electrode
CV	Cyclic Voltammetry
CVD	Chemical Vapour Deposition
DC	Direct Current
EDS	Energy Dispersive X-ray Spectroscopy
EDX	Energy Dispersive X-ray Spectroscopy
EIS	Electric Impedance Spectroscopy
ESCA	Electron Spectroscopy for Chemical Analysis
GPC	Growth per Cycle
HOMO	Highest Occupied Molecular Orbital
ISXRD	In-Situ X-ray Diffraction
LIB	Lithium-Ion Battery
LUMO	Lowest Unoccupied Molecular Orbital
MFC	Mass Flow Controller
MW-CNT	Multi Wall Carbon Nanotubes
R_q	Root Mean Square Roughness
RE	Reference Electrode
S	Sense Electrode
sccm	Standard Cubic Centimeters per Minute (cm^3/min)
SCE	Standard Calomel Electrode
SE	Secondary Electrons
SEI	Solid Electrolyte Interface
SEM	Scanning Electron Microscopy
SHE	Standard Hydrogen Electrode
TEMAV	Tetrakis[ethylmethylamino]vanadium

TMA	Trimethylaluminium
VO_x	Vanadium Oxides
WE	Working Electrode
XPS	X-ray Photoelectron Spectroscopy
XRD	X-ray Diffraction
XRF	X-ray Fluorescence
XRR	X-ray Reflectivitiy

1

Introduction

1.1 Batteries for the future

In 2010, the worldwide amount of vehicles in operation exceeded 1 billion[1]. Nearly all those vehicles combust traditional fossil-based fuels and emit greenhouse gases, adding up to an important contribution of the global emission. For the U.S., transportation was responsible for 27% of the emitted greenhouse gases in 2011[2]. Electric vehicles, using the energy produced by electrochemical reactions in batteries or fuel cells could offer a solution for this environmental problem, though the technologies are not yet at the required level[3]. Figure 1.1 indicates the requirements for (hybrid) electric vehicles with respect to the current technologies.

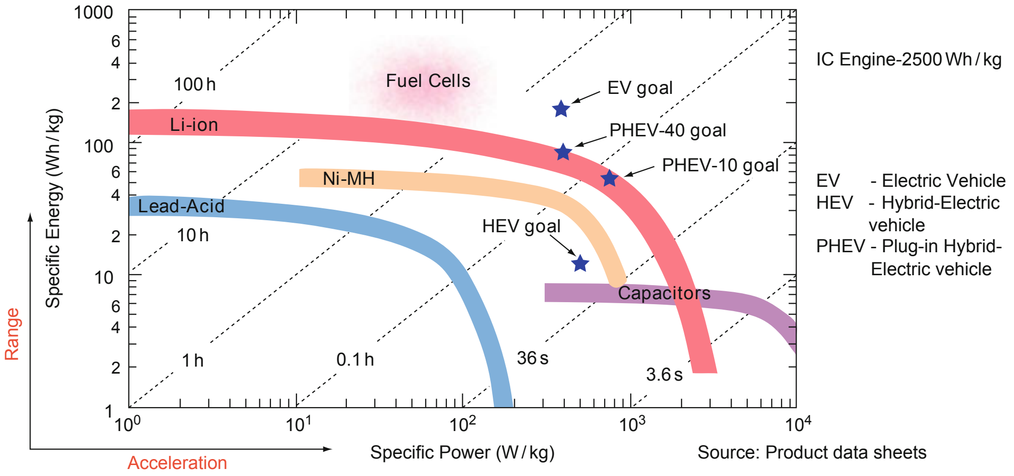

Source: Product data sheets

Figure 1.1: Ragone plot, indicating the relationship between specific energy and specific power for different technologies. The requirements for (plug-in hybrid) electric vehicles are given (from[3]).

This work focuses on lithium-ion batteries. The specific energy of a lithium-ion battery (LIB) is directly influenced by the capacity of the two electrodes, determined by the number of lithium ions that can be reversibly inserted and extracted from the electrode host[4]. The capacity of an electrode depends on the output current. For high currents, a loss of capacity occurs because of the diffusion limited nature of the lithium intercalation process[5]. As a result, a trade-off between energy and power exists. For high power applications (such as electric vehicles), the output current needs to be sufficiently high, resulting in a decrease in capacity.

This can be countered by limiting the length over which the lithium ions have to travel, by using thin films as intercalation electrode. The reversible insertion of lithium will then be dominated by fast surface reactions[6]. Downsizing the intercalation host to a thin film directly leads to a lower total capacity, since less material is available for the lithium ions to intercalate. However, this can be countered by applying the thin films on the surface of three-dimensional nanostructures. Such structures with high surface area can combine the advantage of rapid surface interactions instead of diffusion limited processes, with sufficiently high capacities. Atomic layer deposition (ALD) is a technique that allows uniform deposition of thin films on three-dimensional structures[7], which makes it an ideal tool for this work.

Downsizing of the electrodes to nanoscale dimensions opens the door to another domain of research with respect to LIB, i.e. the development of an all solid battery of microscopic dimensions. Such a solid state LIB would allow on-chip implementation of the energy source. In combination with an energy harvester, the latter can open the door to self-sustainable chip systems. These would mainly have applications in the medical sector, for example for human implants[8]. For such applications, the safety concerns would be critical. As the solid state LIB does not require the flammable solvents needed for the liquid electrolyte used in wet-cell chemistry, it scores very well with regard to safety, making it very promising for applications. On top of that, the solid state LIB does not require scaling of the nanotechnology to macroscopic dimensions, as is the case for electric vehicles, such that this might prove to be a more feasible goal.

1.2 Vanadium oxides

In this work, ALD deposited thin films of vanadium oxide will be examined as possible electrode material for lithium-ion batteries. A short introduction to vanadium oxides is given.

Vanadium forms many compounds with oxygen, with different optical and chemical properties. Among the vanadium oxides, V_2O_5 and VO_2 are most widely used in applications. Vanadium has oxidation states between 2+ and 5+. Depending on the oxidation state, 4 principal vanadium oxides are formed[9], see table 1.1.

Table 1.1: The existing valence states of vanadium and corresponding principal oxide.[9]

Oxidation state	Principal phase structure
V^{2+}	VO
V^{3+}	V_2O_3
V^{4+}	VO_2
V^{5+}	V_2O_5

Next to the four principal oxides, various other phases exist, which can be divided into 2 main groups with general formula V_nO_{2n-1} or V_nO_{2n+1}[9]. The oxides in the first group are called the Magnéli phases. Their structure is based on a V_2O_5 lattice with missing oxygen planes (121). Nearly all oxides in the Magnéli series exhibit a metal-insulator transition, of which the temperature is influenced by the stoichiometry[10]. The second group (V_nO_{2n+1}) contains V_3O_7, V_4O_9 and V_6O_{13}, with valence state in between VO_2 and V_2O_5[9]. These oxides will be studied in this work.

1.2.1 V_2O_5

Vanadium pentoxide (V_2O_5) is one of the more stable vanadium oxide phases. V_2O_5 films are used as optical filters, reflectance mirrors or smart windows[9]. Another application being investigated is the use of V_2O_5 as tunable emitting surface for temperature control of space vehicles[9]. Its structure consists of two-dimensional layers[11]. As a result, V_2O_5 is a good host for lithium ions as intercalation compound. The building block of V_2O_5 is a deformed octahedral VO_6[9]. Adjacent octahedral share an oxide anion and form layers. Between those layers, a weak Vanderwaals interaction is present.

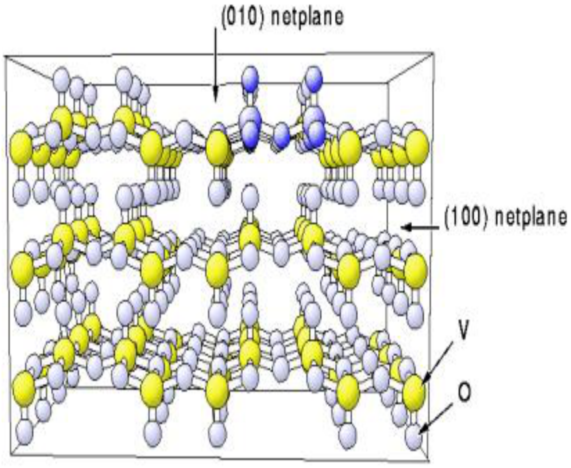

Figure 1.2: Representation of the layered structure in V_2O_5 (from[9]).

1.2.2 VO_2

Four VO_2 phase structures exist, VO_2(M1), VO_2(R), VO_2(B) and VO_2(A)[12]. They are all based on a BCC lattice with vanadium in the octahedral sites. The mutual orientation of the fourfold axis divides the VO_2 phases in two groups. The octahedral are aligned in VO_2(B) and VO_2(A) and perpendicular in VO_2(M1) and VO_2(R). As a consequence, the oxides in these two groups have very distinctive structures and densities[13].

Table 1.2: The density of the VO_2 phases[13]

VO_2-phase	Density (g/cm^3)
VO_2(R)	4.67
VO_2(M1)	4.67
VO_2(B)	4.031
VO_2(A)	4.035

The rutile VO_2(R) phase only differs slightly from the VO_2(M1) phase, which contains a zigzag-type pairing distortion of vanadium ions along the rutile *c*-axis[14], see figure 1.3. The rutile phase is metallic and the monoclinic (M1) structure is semiconducting. A transition between VO_2(R) and VO_2(M1) is observed at 68 °C, resulting in a change from metal to semiconductor. This transition is the main reason for research on VO_2, for possible applications as optical filter, switching device, memory material or thermochromic windows[12]. A second monoclinic VO_2 phase exists, $VO_2(M_2)$, which is only stable for doped VO_2 [15].

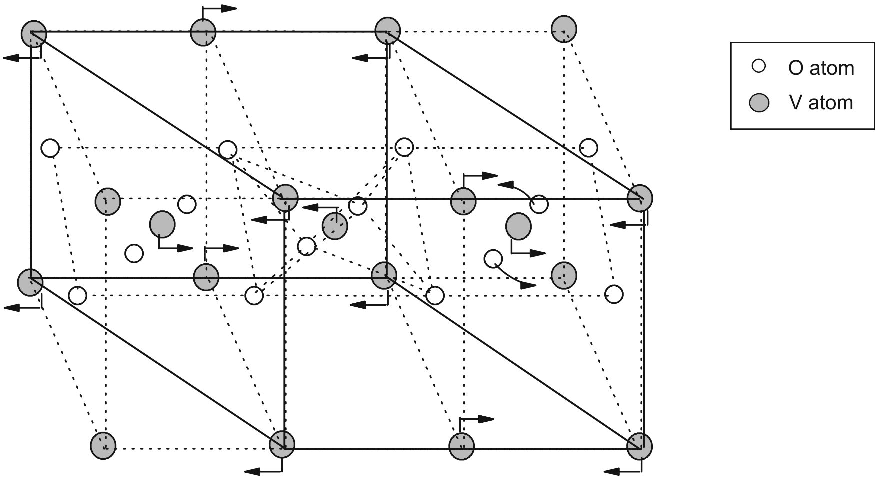

Figure 1.3: Indication of the distortion from the high-temperature rutile (R) tetragonal phase to the low-temperature monoclinic (M1) phase (from[14]).

1.2.3 Relation between the different vanadium oxides

In the BCC lattice of VO_2(B), vacancies are present on the octahedral interstices. When these vacancies are ordered, they can create stable structures. Leroux et al. demonstrates how ordering of vacancies leads to V_4O_9 [13]. In the same work, the existence of striking similarities between VO_2(B) and V_6O_{13} is reported. Both phases differ only in the connection between adjacent octahedra.

Katzke et al. reports that the V_nO_{2n-1} and V_nO_{2n+1} series can be interpreted as sequences of lock-in commensurate phases[16]. The limit lock-in structure for the 2 series would be VO_2(R) and VO_2(B), respectively. Thus, the Magnéli phases are related to VO_2(M1), which explains the existence of the typical metal to insulator transition in all of these phases. For the V_nO_{2n+1} series, the parent structure is FCC VO and all phases in the series are considered as oxygen deficient FCC structures with ordered vacancies, deduced from the parent structure. The threefold orthorhombic structure, V_2O_5, corresponds to the parent structure with respective concentrations of vanadium (x_V) and oxygen (x_O) of $x_V = 1/3$ and $x_O = 5/6$. In a similar way, V_6O_{13} is obtained for $x_V = 1/3$ and $x_O = 13/18$. V_3O_7 and VO_2(B) are formed by $x_V = 0.3$ and $x_O = 0.7$ or $x_V = 1/3$ and $x_O = 2/3$. Figure 1.4 illustrates how symmetry-breaking mechanisms of FCC VO lead to the different phases.

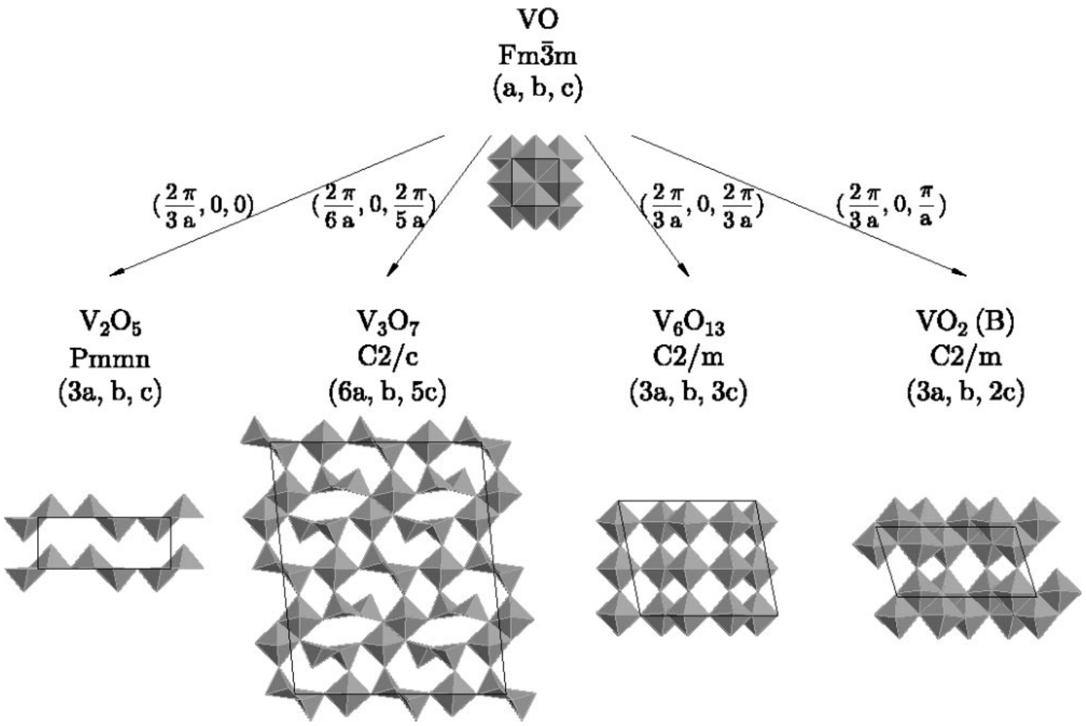

Figure 1.4: Illustration of the relation between the phases of the V_nO_{2n+1} series, symmetry-breaking mechanisms from the cubic VO structure give rise to the different phases (from[16]).

Manthiram et al. confirms that the oxides of the V_nO_{2n+1} series are related to each other since they are all shear structures derived from a hypothetical VO_3 with the ReO3 structure[17]. West et al.[18] states that V_6O_{13} can be regarded as an intermediate phase between VO_2(B) and V_2O_5. Figure 1.5 shows how the lattice of V_6O_{13} can be decomposed into the two structures to which it is related.

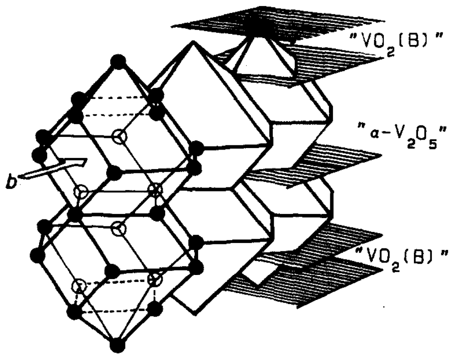

Figure 1.5: A stack of VO_2(B) and V_2O_5 sheets, joined at octahedra corners form the V_6O_{13} structure (from[18]).

1.2.4 The VO_x phase diagram

Figure 1.6 displays the V-O phase diagram for a condensed system (0.1 MPa). The oxides that are treated in this work are situated between atomic percent oxygen of 66.6 % and 71.4 %, corresponding with VO_2 and V_2O_5.

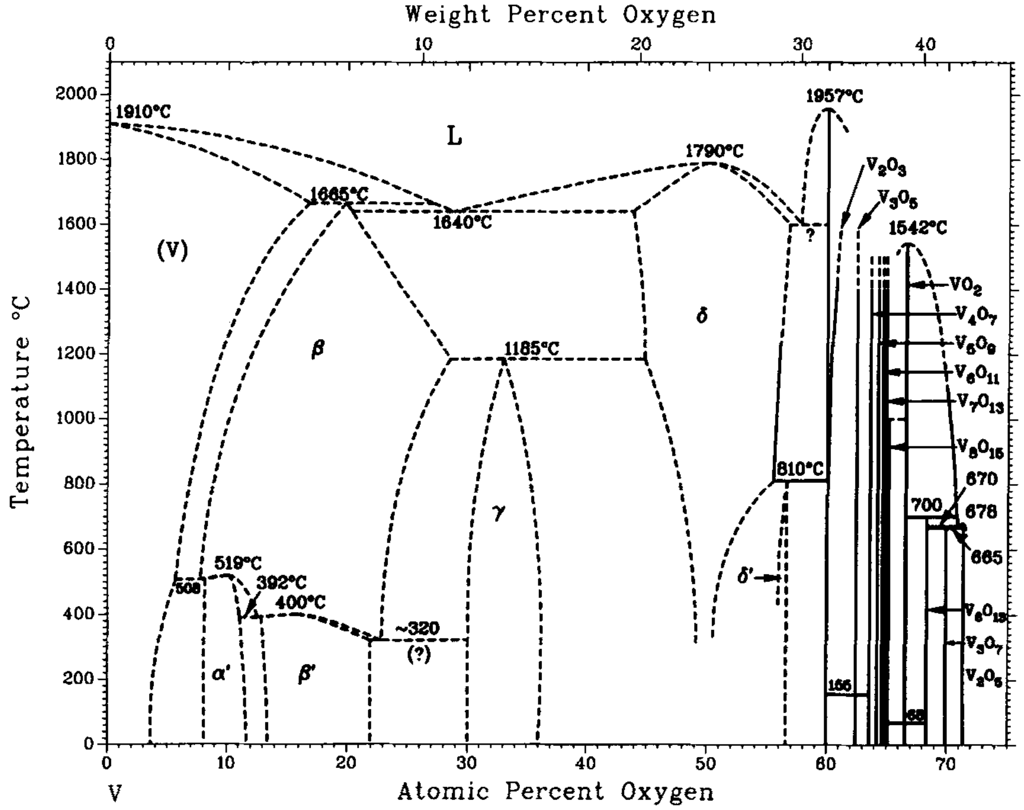

Figure 1.6: Phase diagram of the equilibrium solid phases of the V-O system at a hydrostatic pressure of 0.1 MPa (from[19]).

2

Atomic layer deposition and characterization of thin films

2.1 Atomic layer deposition

Many techniques are available for deposition of thin films, such as physical vapour deposition, sol-gel deposition, electrochemical deposition, etc. One of those techniques is atomic layer deposition (ALD). Atomic layer deposition is a vapour-phase deposition technique, consisting of (at least) two self-terminating solid-gas interactions. Figure 2.1 shows a schematic representation of an ALD process. The example treated here uses trimethylaluminium (TMA) and water as precursors to deposit an Al_2O_3 layer.

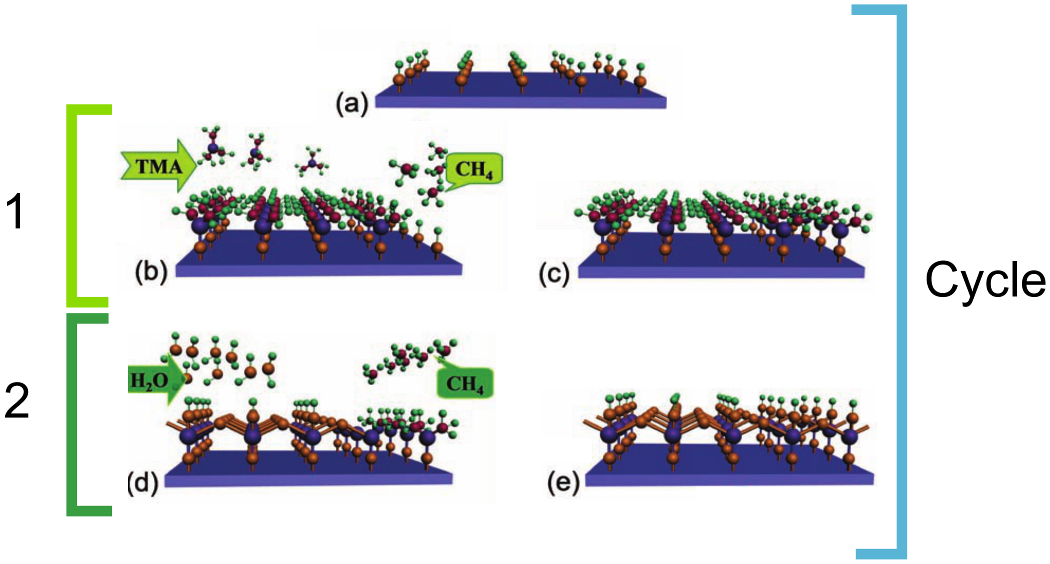

Figure 2.1: Representation of an ALD process, using TMA and water precursors to deposit an Al_2O_3 layer, redrawn from[7].

a) In the case of a vacuum-type set-up, one places the sample in a vacuum chamber with pressure of approximately 10^{-6} mbar.
b) The first precursor gas is released into the chamber. This gas reacts with the surface groups of the sample in a self-saturating manner, such that one monolayer of the first precursor can be deposited on the surface of the substrate. In this example, TMA is released and a reaction with the hydroxyl groups of the surface takes place. CH_4 molecules are formed as

reaction product.

c) The chamber is purged to high vacuum, meaning that no gases are left in the chamber. The leftover TMA molecules and the CH_4 are removed completely.
d) The second precursor gas can then be released into the chamber. This gas reacts chemically with binding groups or ligands of the first precursor. In this example, a H_2O precursor is applied. The hydrogen reacts with CH_3 molecules on the surface with formation of CH_4 as reaction product and the OH binds on the surface.
e) The chamber is purged for a sufficiently long to allow the pressure to decrease to the base pressure, thus removing all gases from the chamber.

After the fifth step, one monolayer of material is deposited onto the sample and the surface is formed by hydroxyl groups once again, allowing the next cycle to start. These steps are repeated for several cycles to grow a thin film. The film thickness can be easily controlled down to the monolayer level (∼Å) in ALD processes by adjusting the number of take place.

ALD is strongly related to chemical vapour deposition (CVD) where the two precursor gases are simultaneously available inside the reaction chamber, leading to a continuous growth. When there is insufficient pumping between two pulses in an ALD process, CVD reactions can occur.

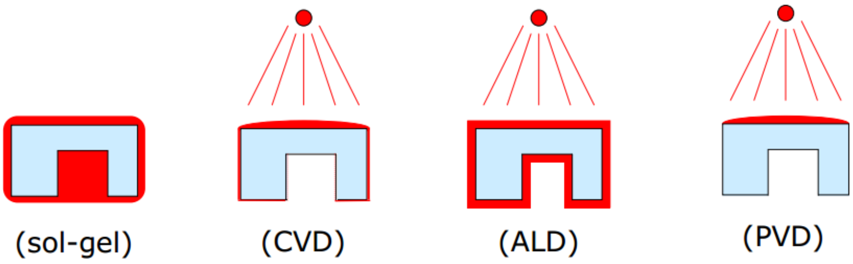

Figure 2.2: Comparison of 4 deposition techniques with respect to uniformity of the deposited layer (from[20]).

An advantage of ALD is that the growth of the film can be controlled monolayer by monolayer and that the reactions are self-terminating. As a result, three dimensional materials can be coated uniformly, if the precursor pulses are long enough, see figure 2.2. The main disadvantage of atomic layer deposition is the slow growth rate, because of the need to purge to high vacuum between two pulses. This limits the practical use of this technique to depositions up to several hundreds of nanometers. For thicker films in the order of micrometers, other techniques such as sputtering or CVD are better suited.

2.2 X-ray diffraction

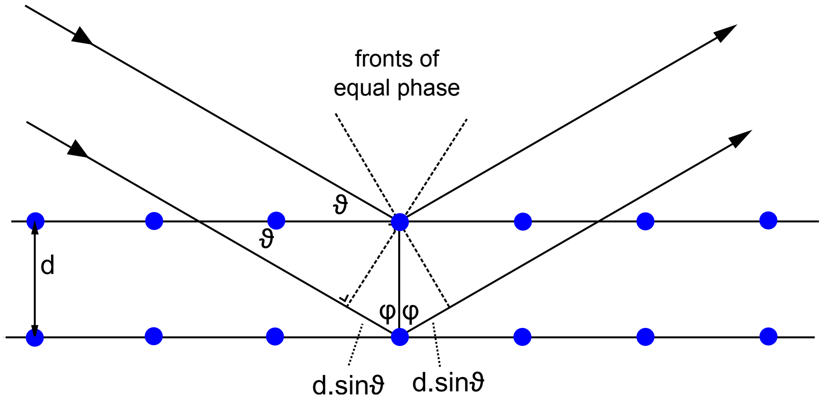

Figure 2.3: Illustration of positive interference of diffracted X-rays at parallel atomic planes.

In X-ray diffraction (XRD), a monochromatic X-ray bundle is incident onto the sample as schematically represented in figure 2.3, causing the X-rays to be reflected on parallel planes of atoms[21]. The intensity is measured outside of the sample. The measured spectrum shows peaks where positive interference is occurring. This means that the differences in path length of numerous rays is a multiple of the wavelength, $\Delta x = k\lambda : k \in \mathbb{N}$. Figure 2.3 illustrates that the difference in path length equals $2dsin(\theta)$, which leads to the following equation, known as the law of Bragg.

$$2d\sin(\theta) = k\lambda \tag{2.1}$$

In Bragg's Law, λ is the wavelength of the X-ray bundle and θ is the angle for positive interference, i.e. peaks in the XRD spectrum. These two values are known, which means that d, the spacing between two atomic layers, can be calculated easily, next to a factor k. Only the spacing between two atomic layers which are parallel to the surface of the sample can be determined. However, samples often contain grains with various orientation (or powders are used), such that different atomic layers are oriented parallel to the surface. As a consequence, the spacing of various interatomic distances will yield peaks in the XRD spectrum, at different values of θ. This shows how the crystallographic structure can be examined by use of XRD. In practice, one compares a measured XRD spectrum with a database, containing the theoretical or measured XRD spectra of many phase structures.

2.3 X-ray reflectivity

X-ray reflectivity (XRR), also referred to as X-ray reflectometry, is a non destructive X-ray based technique that can be used to determine the thickness, density and surface roughness of thin films[22].

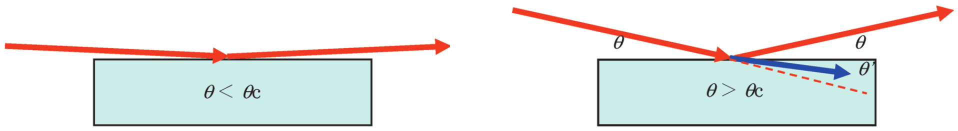

Figure 2.4: Total reflection for $\theta < \theta_c$ (left) and partially transmitted x-ray for $\theta > \theta_c$ (right) (from[22]).

A monochromatic X-ray source irradiates the sample under small angles θ, where θ is the angle between the incident X-ray bundle and the surface of the sample. The reflected intensity is measured with a detector in mirror configuration, thus with angle between detector and surface equal to θ. X-rays are electromagnetic waves for which the refractive index of materials is slightly less than one. Therefore, a critical angle θ_c exists. X-rays with incident angle $\theta < \theta_c$ will be reflected completely. For an incident angle $\theta > \theta_c$, the wave will be partially transmitted into the thin film, see figure 2.4. This gives rise to an interference pattern, as schematically depicted in figure 2.5. If the difference in path length between reflected and transmitted ray is a multiple of the wavelength, positive interference will occur. According to Bragg's law (equation 2.1), the incident angle is related to the distance between the reflecting planes. Thus, the principles of XRR and XRD are similar. In XRD, interatomic spacing is measured, while XRR allows determination of film thickness. As the investigated length is larger in XRR, smaller angles are required.

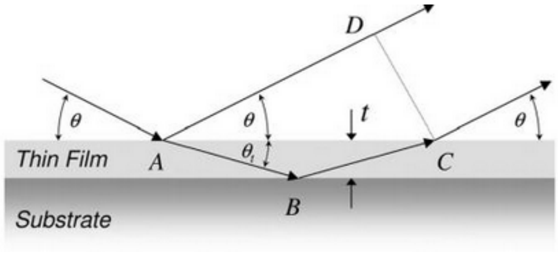

Figure 2.5: Schematical representation of the path of an X-ray inside the material (from[23]).

The complex refractive index of a substance is given by $n = 1 - \delta - i\beta$. In this equation, n is the refractive index, δ depends on the wavelength of the X-ray, the density and composition of the material and β is related to the absorption coefficient, according to $\beta = \lambda\mu/4\pi$. The critical angle for total reflection is given by

$$\theta_c = \sqrt{2\delta} \tag{2.2}$$

As a consequence, the density of the thin film can be calculated from the critical angle θ_c. For larger angles, a periodic oscillation is retrieved in the reflected intensity. These oscillations are often called Kiessig fringes, as they were discovered by Kiessig[24]. The oscillation is related to the film thickness according to

$$cos\left(4\pi d/\sqrt{sin^2\theta - 2\delta}\right) \tag{2.3}$$

Figure 2.6 illustrates the influence of film thickness (left) and density (right) on an XRR spectrum. The oscillations in intensity have a shorter period for thicker films and have a smaller amplitude for films with lower density.

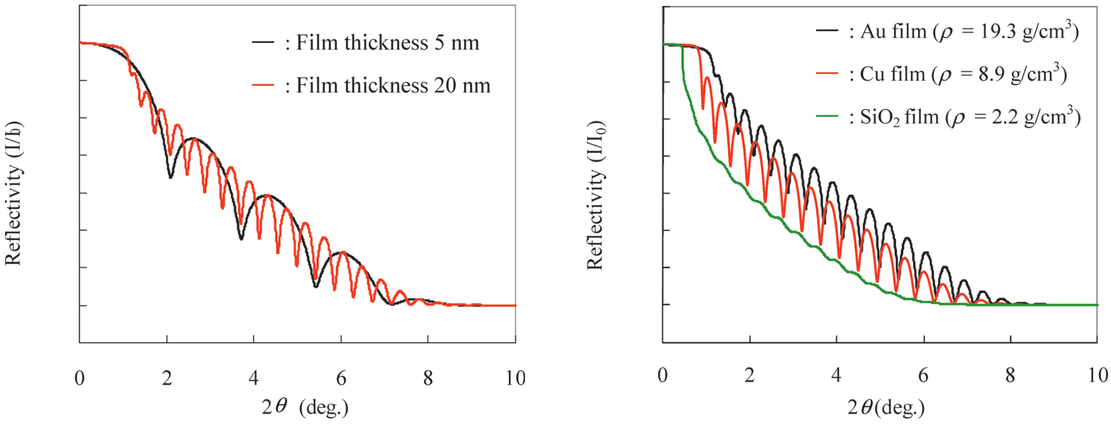

Figure 2.6: Illustration of the influence of film thickness (left) and density (right) on the XRR pattern (from[22]).

2.4 X-ray fluorescence and energy dispersive X-ray spectroscopy

X-ray fluorescence (XRF) is a technique that yields quantitative information regarding the elemental composition of the examined sample. The sample is bombarded with high energetic X-rays, with sufficient energy to ionize atoms. If an atom is ionized, an electron is removed from its shell. When an electron of an inner shell is kicked out, the atom is not in the most stable configuration after ionization. An electron of an outer shell will fill the gap left by the electron kicked out of the inner shell. In doing so, this electron goes to a lower energy state, thus it has to emit energy. This can be achieved by emitting a secondary electron, also known as Auger electron, or by emitting a secondary or fluorescent photon.

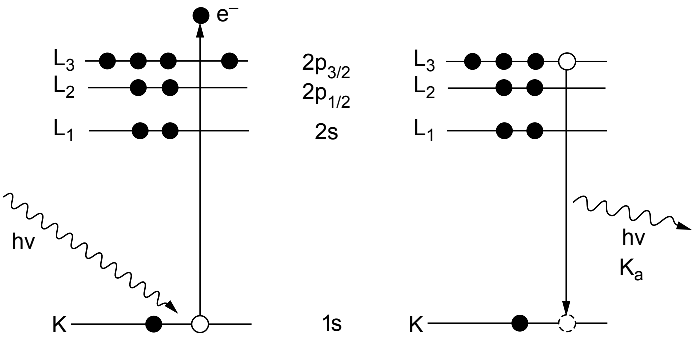

Figure 2.7: An incident X-ray ionizes the atom (left) such that recombination of an electron occurs (right), with emission of a characteristic X-ray (from[25]).

The energy of this photon, also called characteristic X-ray, is equal to the difference in energy between the 2 electron shells. As energy levels of electron shells are specific and different for all atoms, the emitted characteristic X-rays can be used to identify elements.

Several peaks in an XRF spectrum can correspond to one element since different X-rays will be emitted, depending on the original shell of the electron that is removed. These are grouped in the K- , L- and M-series, where the letter indicates the original shell of the removed electron. As a macroscopic sample consists of many atoms, lines of different series will be present with their relative intensity.

The detector measures the energy or wavelength of the fluorescent photons, emitted by the sample. The count rate can be plotted as a function of energy. As each element has its specific set of characteristic x-rays, the peaks in the count rate can be used to identify the elements, present in the sample. The magnitude of these peaks gives quantitative information. More atoms of a certain kind will result in higher peaks in the corresponding XRF spectrum.

A second approach for ionisation consists of bombarding the sample with a high energy electron or proton beam instead of an X-ray source. In this case, the technique is called energy dispersive X-ray spectroscopy (EDS or EDX). The result of the impact of the high energy particle beam is similar as for XRF. The sample will emit an X-ray spectrum, containing information with regard to the chemical composition of the sample.

2.5 X-ray photoelectron spectroscopy

X-ray photoelectric spectroscopy (XPS), also known as electron spectroscopy for chemical analysis (ESCA), measures elemental composition, chemical state and electronic state of the elements within a sample. In XPS, a sample is irradiated with ionizing X-rays, while detecting the electrons escaping from the material. In order to detect the emitted electrons, XPS requires vacuum conditions. The emitted electrons have low energies and corresponding small mean free path, such that the XPS technique is limited to measuring the top few nanometers of a sample surface. Since the surface of samples is often contaminated, for example by exposure to the atmosphere, it can be more interesting to measure the bulk material. Depth profiling is commonly done by sputtering the sample with ions such as argon, to remove the first atomic layers. The disadvantage of sputtering is that the composition of the sample can be changed by preferential sputtering of some elements, especially for transition metal oxides. Silversmit et al. reported that oxygen will be sputtered preferentially for vanadium oxides[26].

XPS is based on the photoelectron effect. A photon can transfer its energy to an electron such that the latter gains sufficient energy to break its bond with the atom. The atom gets ionized and the electron is emitted with a kinetic energy equal to the energy of the photon subtracted with the binding energy between atom and electron. In equation 2.4, $\hbar\omega$ is the energy of a photon with angular frequency ω, $E_k(e)$ and $E_B(e)$ are the kinetic and binding energy of the electron.

$$E_k(e) = \hbar\omega - E_B(e) \tag{2.4}$$

The kinetic energy of the electrons is measured by the detector and since the energy of the X-ray source is known, the binding energy of the electrons can be calculated. As $E_B(e)$ is element specific, XPS can be used to determine elemental composition of samples. Binding energies are also influenced by chemical composition and oxidation state. For example, electrons bound to the oxidation states V^{4+} and V^{5+} of vanadium will have slightly different binding energies[26], such that XPS can be used to obtain information regarding oxidation state and chemical composition.

2.6 Scanning electron microscopy

Scanning electron microscopy (SEM) is used to examine the morphology of solid state samples. A high energy electron beam produced by an electron source in the SEM is focused on a small spot on the surface of the sample by electromagnetic lenses, as shown in figure 2.8a. The electrons will interact with the matter as they hit the sample. Atoms can be ionized by collisions with the incident electrons, causing secondary electrons (SE) and characteristic X-rays to be emitted by the sample. These secondary electrons have low energies, compared to the energy of the incident electron. An incident electron can also be backscattered out of the sample by elastic collision with an atomic nucleus. Backscattered electrons (BSE) have high energies, comparable to the initial energy of the beam.

To create an image, the incident electron beam scans the surface of the sample in a raster while detecting the electrons coming out of the sample. The varieties in signal intensity of different locations are represented by varieties in pixel brightness. If BSE are detected, information regarding the elemental composition of the sample is obtained, since heavy elements result in more backscattered electrons than light elements. In contrary, detection of SE yields information with respect to the morphology. As SE have low energies, their mean free path through the material is very small (in the order of nanometer). Only secondary electrons emitted by the top layer can be detected. In figure 2.8b, the electron beam on the left hand side of the figure will result in the detection of many electrons. Accordingly, bulges of the surface will be visualised as bright spots, while dark spots are visualised if less electrons are detected, for example in a clove or crack of the surface.

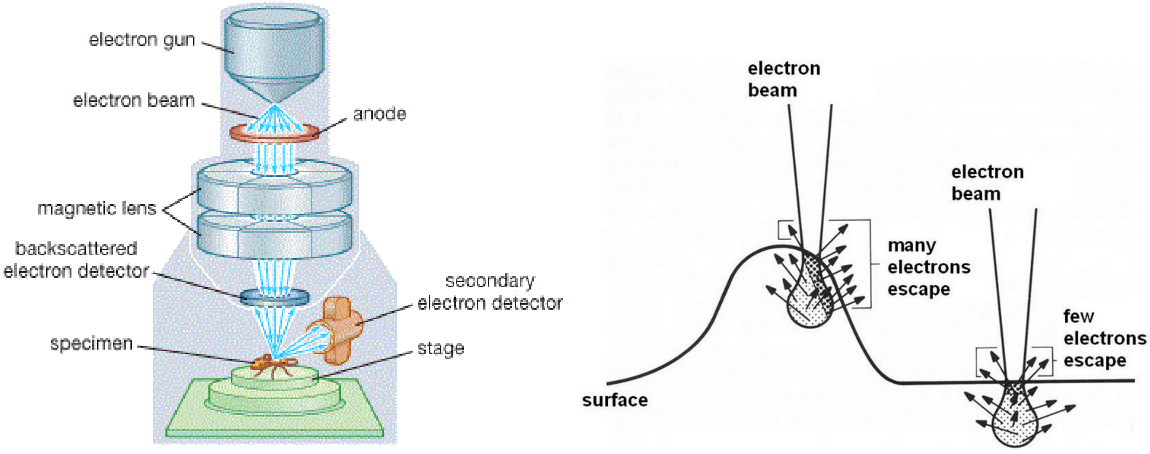

(a)

(b)

Figure 2.8: Schematic illustration of a SEM device (a) by Encyclopedia Brittanica, and surface visualization by detection of SE (b) (from[27]).

2.7 Atomic force microscopy

Atomic force microscopy (AFM) is a useful technique for obtaining images and topological information at nanometer resolution and can also be used to measure forces at nanoscale dimension[28]. The device uses a sharp probe, with tip radius between 5 and 20 nm, to scan the surface of a sample in a raster like fashion. The probe is usually made out of silicon (Si) or silicon nitride (Si_3N_4) and mounted on a cantilever. When the probe is moved with respect to the surface of the sample by a piezoelectric element, the distance between tip and surface will vary because of the topological structure of the surface. As this distance changes, so will the interatomic forces between tip and surface. The forces cause bending of the cantilever, detected by a laser focused on the back of the cantilever, reflected on a photo detector. The recorded signal closes the feedback loop, such that topological information is obtained. High resolution AFM is possible because of the extremely sensitive optical system and precise movements of the piezoelectric element. The sharpness of the tip is a crucial factor as well, regarding the resolution of this technique[29].

Three different operation modes exist for AFM imaging.

- The first possibility is to operate the AFM in '*contact mode*', also known as static or repulsive mode. The tip remains in contact with the sample and is dragged over its surface. Due to the close proximity of tip and surface, the interaction is repulsive because of the repelling electron clouds of surface and tip. The disadvantage of contact mode is the possible damage to the surface of the sample, caused by the tip.
- In '*non-contact mode*', the cantilever hovers above the sample at a certain frequency, which is influenced by the attractive forces between surface and tip. By measuring the shift in frequency with respect to the position of the tip, the topological structure of the sample can be measured.
- The last option is to operate the AFM in '*tapping mode*'. The cantilever is oscillated at a frequency close to its natural resonant frequency by an extra piezoelectric element. Afterwards, the tip is lowered until it starts to lightly tap the surface of the sample. The amplitude of the vibration will be affected by energy losses caused by the short contact of the tip and surface. The feedback loop adjusts the tip position such that a constant amplitude is obtained.

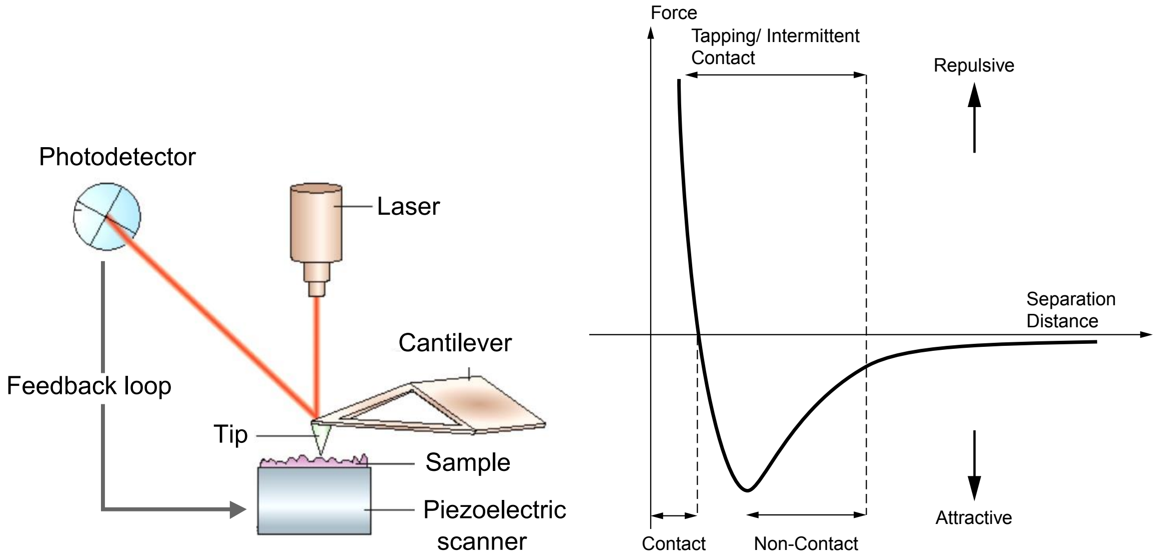

(a)

(b) Different operation modes of

Figure 2.9: Schematical illustration of an AFM device (a) (from[30]) and indication of the forces and distances in the different operation modes (b)(from[25]).

To quantify the roughness of a sample, the root mean square roughness (R_q) is most often presented. This value is calculated by[31]

$$R_q(N,M) = \sqrt{\frac{1}{NM}\sum_{x=1}^{N}\sum_{y=1}^{M}\Big(z(x,y) - \overline{z}(N,M)\Big)^2} \tag{2.5}$$

In this equation, N and M are the number of data points in x- and y-direction and z(x,y) is the altitude at coordinate (x,y). $\overline{z}$(N,M) is the average altitude in the region of interest. Thus, the root mean square value expresses the average deviations with respect to the average altitude. A high R_q-value corresponds with a rough topology.

2.8 Recapitulation of the used techniques

The techniques that were described in this chapter were all applied on thin films of vanadium oxide. The results will be discussed in the next chapter. Table 2.1 summarizes the experimental techniques and their specific purpose.

Table 2.1: Overview of the used techniques.

Technique	**Purpose**
ALD	Deposition of thin films
XRR	Measurement of film thickness
XRF and EDX	Determination of elemental composition
XRD	Identification of phase structure
XPS	Composition and chemical or oxidation state
SEM	Imaging of sample
AFM	Observation of surface roughness

3

Deposition and characterization of vanadium oxide thin films

3.1 Atomic layer deposition of vanadium oxide

The first experiments to deposit thin films of vanadium oxide with ALD were carried out by Badot et al.[32] The vanadium precursor was vanadyl triisoproproxide, $VO(OC_3H_7)_3$, which has a high vapour pressure. H_2O was used as second precursor. The growth rate saturated at 20 ng/cm^2/cycle, corresponding to approximately 10% of a monolayer per cycle. The deposited vanadium oxide films were amorphous and could be annealed to V_2O_5 at 400 °C.

Dagur et al.[33] used vanadyl acetylacetonate, $VO(acac)_2$, as vanadium precursor and O_2 as oxygen precursor. The depositions were carried out in the temperature range between 400 and 475 °C. As a result, a crystalline VO_2(M) layer was deposited. This was in contrast with the process of Badot et al. were amorphous layers were formed. The growth per cycle (GPC) of this process saturated at 2.4 Å/cycle, which is nearly equivalent to one monolayer of VO_2(M1). However, Blanquart et al.[34] stated that the acac ligands undergo thermal decomposition at temperatures between 400 and 475 °C, resulting in a reaction with oxygen which is otherwise inert under these conditions. As a consequence, the growth was of CVD-nature.

Tetrakis[ethylmethylamino]vanadium, $V(NEtMe)_4$, was first used as vanadium precursor by Rampelberg et al.[35], in combination with H_2O, O_3 and plasma enhanced (PE) O_2 as oxygen precursor. For the process with the O_3 precursor, Rampelberg obtained a growth rate of 0.76 Å/cycle of amorphous VO_2. The same processes were studied by Blanquart et al.[34]. For the H_2O process, a constant growth rate of 0.8 Å/cycle was observed between 125 °C and 250 °C. The growth per cycle of the O_3 process was significantly lower, ca. 0.3 Å/cycle. Finally, Premkumar et al.[36] examined the influence of precursor doses and temperature of the TEMAV and O_3 process, and stated that this process does not exhibit the characteristics of an ideal ALD process. The growth was dependent on temperature and gas pressures, indicating a possible CVD contribution. Cycles of TEMAV without O_3 pulse confirmed this hypothesis and showed a CVD contribution smaller than 10% and dependent on the substrate temperature.

Table 3.1: Summary of the reported ALD processes for deposition of vanadium oxide films.

Author	**Vanadium precursor**	**Oxygen precursor**	**Deposited Film**	**GPC (Å/cycle)**	**Temperature (°C)**
Badot et al.[32]	$VO(OC_3H_7)_3$	H_2O	am. VO_x	0.5	170
Dagur et al.[33]	$VO(acac)_2$	O_2	VO_2(M1)	2.4	400-475
Rampelberg et al.[35]	$V(NEtMe)_4$	O_3	am. VO_2	0.76	200
		PE O_2	V_2O_5	-	-
		H_2O	-	-	-
Blanquart et al.[34]	$V(NEtMe)_4$	H_2O	am. VO_x	0.80	125-200
		O_3	am. VO_x	0.34	125-200
Premkumar et al.[36]	$V(NEtMe)_4$	O_3	am. VO_2	1.4	150
Pemble et al.[37]	$VOCl_3$	H_2O	-	-	-
Willinger et al.[38]	V n-propoxide	CH_3COOH	V_2O_4	0.4	200

3.1.1 Experimental set-up

In this master's dissertation, two of the processes described by Rampelberg et al. were used to deposit thin films of vanadium oxide. In both cases, TEMAV was used as vanadium precursor. The oxygen precursor was either H_2O or O_3. For both processes, the recipe is schematically shown in figure 3.1.

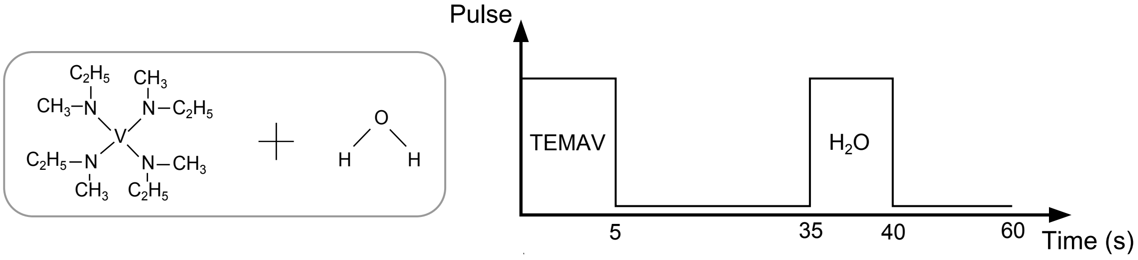

(a) TEMAV + H_2O

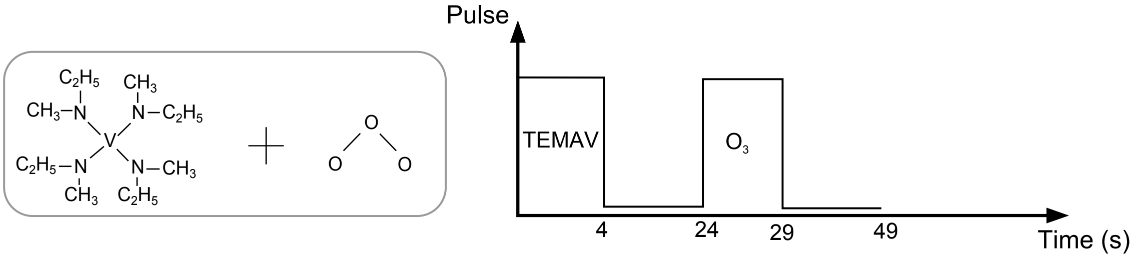

(b) TEMAV + O_3

Figure 3.1: Schematic illustration of standard recipes for both ALD processes.

A LabView program controlled the valves between the precursor bottles and the chamber, based on the predefined recipes. The TEMAV pulse was 5 seconds in the H_2O process and 4 seconds in the O_3 process. The pulses of the H_2O and O_3 precursors both lasted 5 seconds. The standard procedure for the H_2O process contained 400 cycles, while only 250 cycles were used for the O_3 process. Both resulted in an amorphous vanadium oxide film of approximately 20 to 30 nm.

For both processes, three substrates were examined, i.e. a SiO_2, TiN and Pt substrate. The SiO_2-substrate consisted of a Si wafer with a thermal oxidation layer of 100 nm. For the TiN substrate, a Si wafer was sputtered with 48 nm TiN. The Pt substrate was fabricated by sputtering 2 layers on a Si wafer: a layer of approximately 80 nm Pt on top of 40 nm TiN.

All ALD processes were carried out in an experimental high-vacuum ALD reactor, illustrated in figure 3.2. The walls of the reactor chamber were heated to 95 °C, to avoid condensation of the gases on the chamber walls. The TEMAV precursor bottle was heated to 70 °C and the tube connecting the precursor bottle with the chamber was heated to 100 °C. Heating of the connection tube proved to be critical to avoid condensation. The sample itself was heated to 150 °C. The base pressure in the chamber was 10^{-6} mbar. During the TEMAV, H_2O and O_3 pulses, the pressure was 6.10^{-3} mbar, $7,5.10^{-3}$ mbar and 2.10^{-1} mbar respectively. During the O_3 pulse, the valve to the vacuum pump was closed. In between pulses, sufficient time was available to allow the pressure to drop to approximately 1.10^{-5} mbar, in order to prevent the occurrence of CVD side-reactions. For the TEMAV pulse, Ar was used as carrier gas, to counter the effect of the low vapour pressure of TEMAV. The O_3 was produced from a pure flow of O_2 with an OzoneLabTM OL100, resulting in an O_3 concentration of 150 μg/ml.

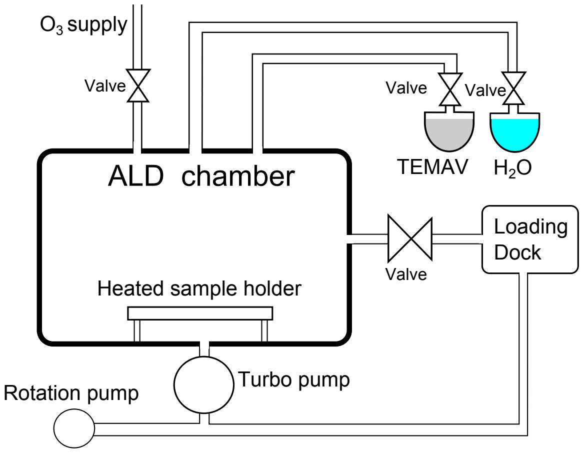

Figure 3.2: Schematical illustration of the experimental ALD chamber, used for deposition of vanadium oxide thin films.

3.2 X-ray reflectivity to measure film thickness

The XRR spectra were measured with a Bruker D8 Discover device using a Copper X-ray source, emitting Cu K radiation at 0,154 nm. The set-up is controlled by the software program XRD commander. To obtain the physical properties of the thin films, a simulated spectrum has to be matched with the experimental data. This fit was generated by the software program WinGixa. Figure 3.3 shows the measured data and the fit for an amorphous vanadium oxide film deposited with the H_2O and O_3 ALD processes.

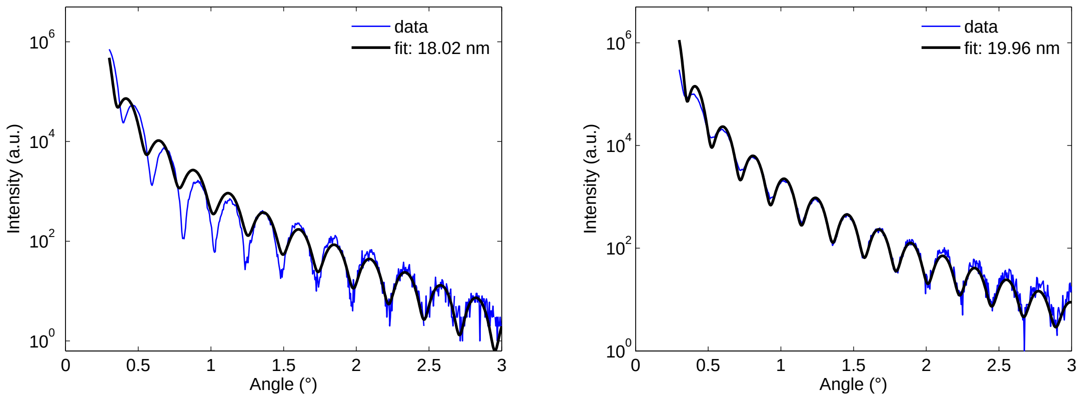

(a) H_2O process **(b)** O_3 process

Figure 3.3: The XRR spectrum of the amorphous vanadium oxide thin film, as deposited by the two ALD processes.

Table 3.2 gives the thickness, roughness and density of several amorphous vanadium oxide films deposited on a SiO_2 substrate, as obtained by XRR measurements. This data allows to calculate the growth per cycle of both processes.

Table 3.2: Results of XRR fits on thin films deposited on SiO_2 substrate.

	Thickness (nm)	**Roughness (nm)**	**Density (g/cm^3)**
Deposited with H_2O process			
400 cycles	17.09	0.458	5.87
400 cycles	18.02	0.307	3.14
400 cycles	17.83	0.446	3.68
400 cycles	22.28	0.497	4.20
400 cycles	26.29	0.403	3.49
400 cycles	14.88	0.665	3.82
Deposited with O_3 process			
250 cycles	23.32	0.247	5.75
250 cycles	19.97	0.262	3.76
250 cycles	28.74	0.251	5.61
250 cycles	27.02	0.389	3.96
125 cycles	12.68	0.311	3.03
500 cycles	50.06	0.451	3.18

The average values for the GPC are 0.67 Å/cycle for the H_2O process and 1.05 Å/cycle for the O_3 process. Rampelberg et al. reported a GPC of 0.76 Å/cycle for the process with O_3 precursor[35]. Furthermore, XRR indicates that the roughness of the films deposited by the H_2O process is slightly higher. With respect to the density, no conclusions can be made based on the XRR measurements, as the deviations from the average value are rather large.

The XRR technique does not give reliable results for the TiN- and Pt-substrate. Figure 3.4 shows the result of some fits on an amorphous vanadium oxide film, deposited with the O_3 process on the Pt substrate.

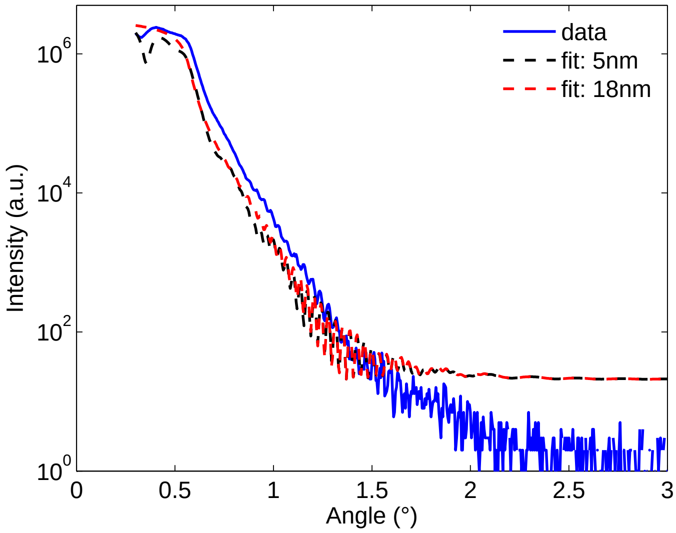

Figure 3.4: XRR measurement of a vanadium oxide film on Pt substrate and illustration of the difficulties to obtain the film thickness.

The two fitted curves with thickness of 5 nm and 18 nm coincide almost perfectly, implying that this technique does not allow to draw conclusions for the films on the Pt substrate. To obtain a measure of the film thickness for these depositions, other techniques were used, see paragraph 3.3.3 and 3.5.2.

The measured interference patterns for the TiN and Pt substrate are caused by reflected X-rays on respectively 3 and 4 layers. The presence of this multilayer structure complicates fitting of a theoretical spectrum to obtain the required parameters. On top of that, the roughness of the vanadium oxide films on TiN and Pt substrates is significantly higher compared to the SiO_2 substrate, obtained by AFM measurements, see paragraph 3.6. The high roughness causes another difficulty for applying XRR on the films deposited on TiN and Pt, since the use of XRR is limited to layers of low roughness.

3.3 X-ray fluorescence

3.3.1 XRF measurements on thin VO_x films

XRF is used to obtain quantative elemental analysis of the samples. The measurements were carried out with a Bruker ARTAX XRF detector. The samples were exposed to a molybdenum source (0.709Å = 17 keV) for 100 seconds. As an example, the measured spectrum of two amorphous thin films on a Pt substrate is given in figure 3.5.

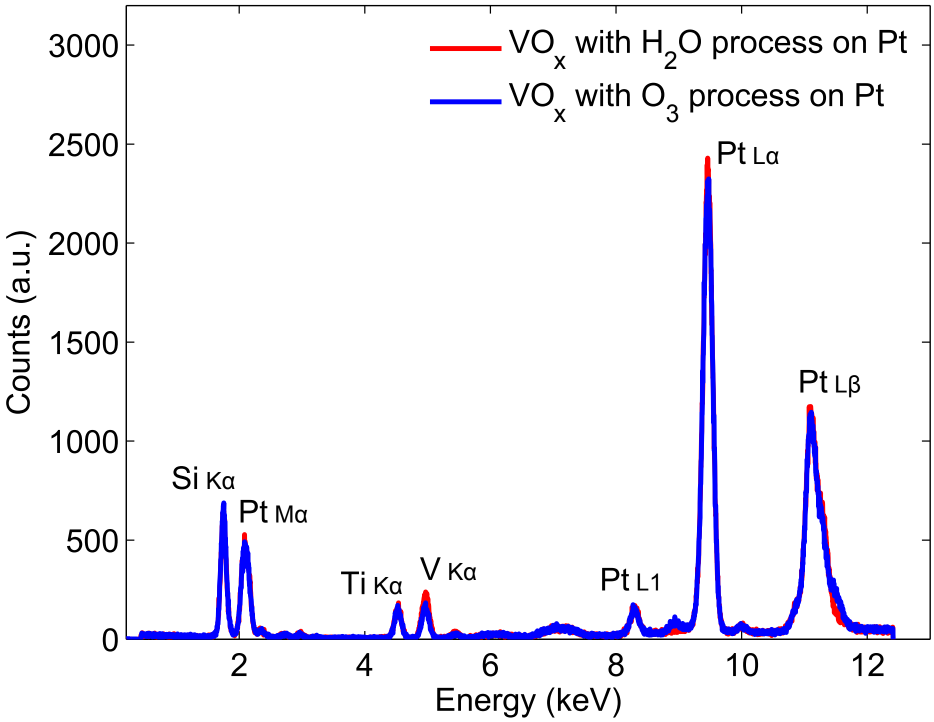

Figure 3.5: XRF spectra of amorphous thin films, deposited with the two ALD processes on a Pt substrate.

Identification of the peaks is performed by the ARTAX software program. Since the platinum substrate was formed by sequential sputtering of a TiN layer and a Pt layer on a silicon wafer, the XRF measurement contains peaks for Ti, Pt and Si. On top of that, a signal is obtained for vanadium, confirming the deposition of a vanadium oxide layer. Due to the technical limits of XRF, oxygen and nitrogen could not be observed. The characteristic X-rays of light elements have low energy and according low penetration and thus high absorption in air.

The vanadium signal of the layer deposited with the H_2O process is more intense, compared to the signal of the layer deposited with the O_3 process. Since both films have approximately equal thickness, this indicates a higher density of the film deposited with the H_2O process, as will be discussed in detail in paragraph 3.3.3.

3.3.2 XRF maps to analyze uniformity

XRF gives local quantitative information about the abundance of elements in the film, because of the small spot size of the incident beam ($\sim mm^2$). Thus, it can be used to map a thin film to determine the uniformity. An XRF map consists of a series of single XRF measurements on different places, allowing to determine the spatial distribution of the elements. In a completely homogeneous film, one would expect the peak intensities to be equal at all measured sites.

Figures 3.6a and 3.6b compare normalised XRF maps of the integrated intensity of the vanadium Kα peak of thin films deposited with the O_3 process on SiO_2 and Pt substrate. The thickness is very uniform on the SiO_2 substrate, it is however clearly not uniform on the Pt substrate. This could also be observed visually, as the color of the sample is influenced by the film thickness. Premkumar et al.[36] stated that the TEMAV with O_3 process did not exhibit the characteristics of a typical ALD process, i.a. because of the influence of the substrate. These XRF maps demonstrate the different behaviour of the process on SiO_2 and Pt substrate, as a pulse time of 4 seconds was insufficient to saturate the process for the Pt-substrate. The highest vanadium concentration was retrieved at the corner where the TEMAV precursor entered the reactor chamber, which is indicated on figure 3.6b. To resolve the conformity issues, the precursor pulses where prolonged. Figure 3.6c shows that a constant intensity of vanadium was measured such that the gradient in thickness was no longer present when longer precursor pulses were used. The standard O_3 process was changed thereafter from 4 s to 8 s pulses for both O_3 and TEMAV. Figure 3.6d shows the uniformity of a vanadium oxide thin film deposited with the H_2O process. This process showed to be uniform on all samples.

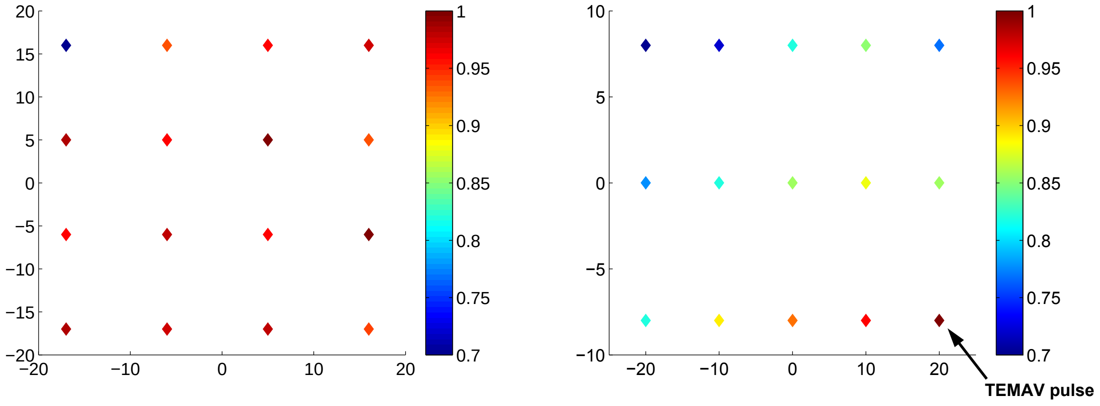

(a) SiO_2 - 4s O_3 process **(b)** Pt - 4s O_3 process

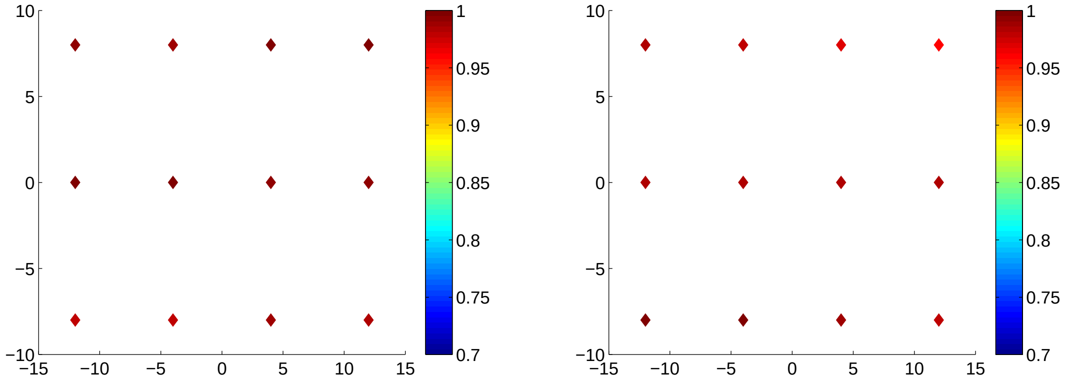

(c) Pt - 8s O_3 process **(d)** Pt - H_2O process

Figure 3.6: Normalized XRF map of the intensity of the vanadium Kα peak on different samples.

3.3.3 Relation XRR-XRF to determine the film thickness

When more vanadium atoms are incorporated in the film, a higher vanadium peak will be recorded in the XRF spectrum. As a consequence, the peak intensity of vanadium is directly related to the film thickness, since the density of the vanadium oxide is assumed constant throughout the entire film. This can be used to determine the film thickness for the vanadium oxide thin films on TiN and Pt substrates, as the XRR-technique was not applicable for these substrates as discussed before.

In order to obtain correct thickness information, a calibration is required. Since both XRR and XRF can be used on the SiO_2 substrate, these samples were used for calibration. The XRR measurements provide the exact film thickness, which can then be related to a number of counts in the XRF spectrum. All samples on SiO_2-substrate are shown in figure 3.7. A linear fit yields the following results, see equation 3.1.

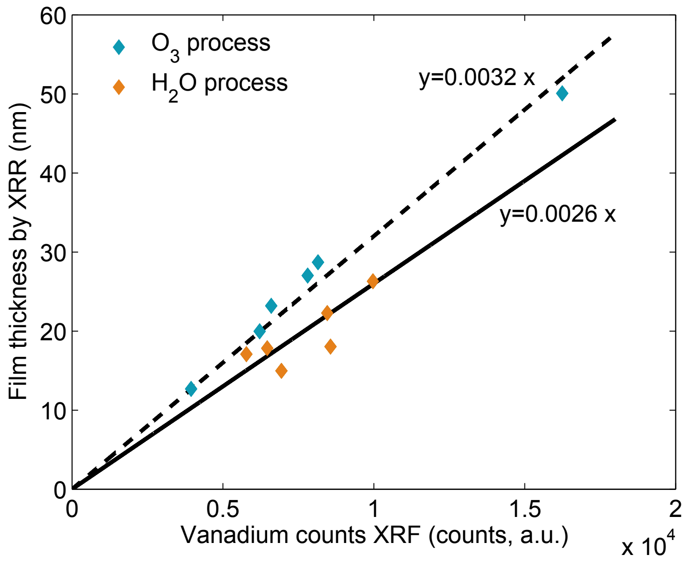

Figure 3.7: The relation between XRF counts and thickness determined by XRR, based on films deposited on the SiO_2 substrate with the 2 ALD processes.

$$\begin{cases} d = 0.0026 * \textit{V-counts} & H_2O \text{ process} \\ d = 0.0032 * \textit{V-counts} & O_3 \text{ process} \end{cases} \tag{3.1}$$

The chi squared test for the two fits yields 0.0211 and 0.1622, respectively. The obtained XRR-XRF relations were used to estimate the film thickness d of the deposited amorphous films on TiN and Pt substrate. The results are listed in table 3.3. A remark needs to be made on the energy of the characteristic X-rays of Pt, which is high enough to ionize vanadium atoms. Thus, the intensity of the vanadium peak will be enhanced slightly due to the presence of the platinum layer underneath. The magnitude of this effect can be examined by comparing the intensity of the Pt peak with and without amorphous vanadium oxide layer, since re-absorption of the Pt X-rays in the vanadium oxide films would induce a drop in the intensity of the Pt characteristic X-rays. However, since no distinctive difference could be observed between the Pt peak intensity of coated and uncoated Pt substrates, this effect will be neglected further.

The values in table 3.3 indicate that large fluctuations exist in the thickness of the deposited layers by both ALD processes. This could also be observed for the depositions on the SiO_2 substrate, see table 3.2. Since all temperatures, pulse lengths and pressures were identical between the different depositions, one would expect the film thickness to be more or less constant per process. A possible explanation for the deviations might be the presence of active groups on the chamber wall, due to previous ALD depositions with other materials.

Table 3.3: Vanadium counts, measured with XRF and calculated thickness with the XRR-XRF relation on TiN and Pt substrates.

	# V counts (a.u.)	**Estimated thickness (nm)**
TiN substrate		
H_2O process		
400 cycles	15591	38.97
O_3 process		
250 cycles	14776	47.28
250 cycles	13739	43.96
Pt substrate		
H_2O process		
400 cycles	6126	15.32
400 cycles	7558	18.89
400 cycles	9641	24.10
O_3 process		
125 cycles	5406	17.29
250 cycles	12280	39.30
250 cycles	11675	37.36
250 cycles	14220	45.50
250 cycles	9056	28.98
250 cycles	10802	34.57
250 cycles	8604	27.53
250 cycles	8182	26.18
500 cycles	20743	66.38

3.4 X-ray photoelectron spectroscopy

Silversmit et al. investigated the influence of the oxidation state of vanadium to the binding energy in an XPS spectrum[26]. The binding energy associated with the different oxidation states of vanadium are presented in table 3.4.

Table 3.4: XPS fit parameters for the V2p signal for different valence states of vanadium[26].

Core line	V^{5+} (eV)	V^{4+} (eV)	V^{3+} (eV)	$V^{2+/1+}$ (eV)
$V2p_{3/2}$	517.2	515.8	515.3	513.7
$V2p_{1/2}$	524.5	523.2	522.6	521.0

The amorphous layers deposited with the two ALD processes are examined with XPS. The binding energy of the carbon 1s peak (284.2 eV) was used as reference. The results of the XPS measurements of the V2p peaks and the O1s peak of both thin films are displayed in figure 3.8. The samples were not sputtered, as preferential sputtering of oxygen occurs.

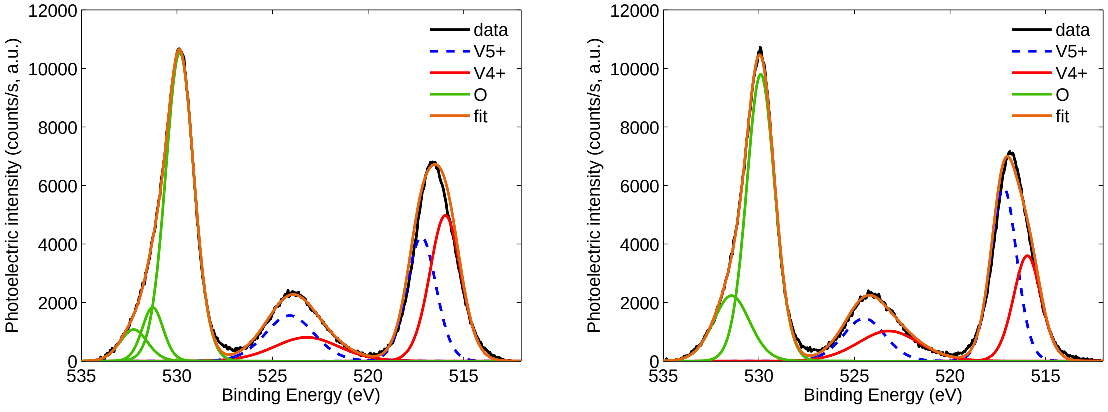

(a) H_2O **(b)** O_3

Figure 3.8: Background subtracted XPS measurements of amorphous vanadium oxide films, deposited with the two ALD processes on Pt.

The measured peaks for $2p_{3/2}$ and $2p_{1/2}$ can be decomposed into a V^{4+} and V^{5+} contribution, implying that the amorphous layers have a mixed oxidation state. This might explain the ability of the amorphous films to crystallize into different vanadium oxides upon annealing, depending on the amount of oxygen available in the atmosphere, as will be discussed in paragraph 3.7.2. All VO_x phases synthesised in this work, contain vanadium with valence state between 4+ and 5+. This indicates why post-deposition annealing never resulted in vanadium oxides from the Magnéli series, for example. Similar results were obtained by Blanquart et al. for as deposited amorphous layers with the TEMAV processes.[34].

Identification of the crystallized phases by means of fitting the V^{4+} and V^{5+} contributions involved too much uncertainty, such that no conclusions could be drawn from the ratio of the oxidation states.

3.5 Scanning electron microscopy

3.5.1 Surface morphology of VO_x thin films

SEM images of the as deposited amorphous films from the water and ozone based ALD processes are compared in figure 3.9. Both images show the sample with a magnification of 100.000. No clear differences can be observed. Both processes yield a uniform, closed layer. To get better quantitative information concerning the surface topology, AFM measurements are more accurate, see paragraph 3.6.

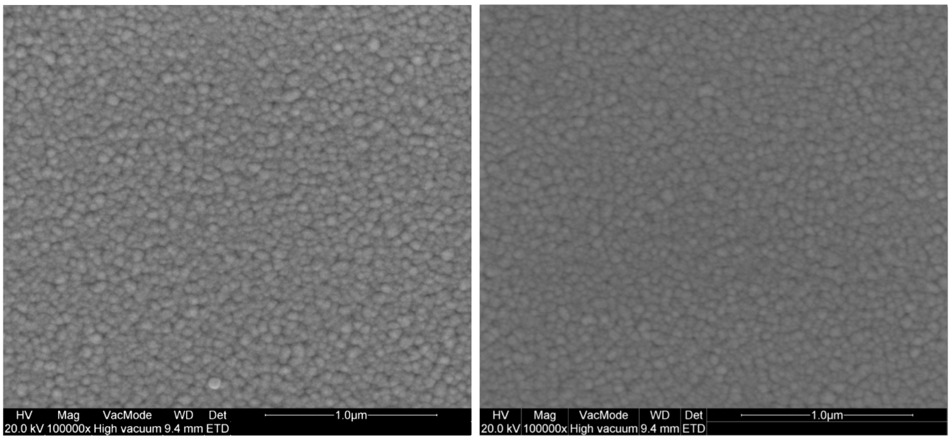

(a) H_2O **(b)** O_3

Figure 3.9: SEM images of the surface of as deposited amorphous films.

The amorphous thin films can be crystallized into different phase structures by thermal annealing, as will be discussed in section 3.7.2. As an example, thermal annealing in air at a temperature of 500 °C oxidizes the amorphous layer to V_2O_5. Figure 3.10 shows a SEM image of the surface of a V_2O_5 sample. The surface no longer appears to be smooth and uniform, since many cracks are visible on the sample surface. In the oxidation process, the amorphous layer has to expand to incorporate oxygen atoms, causing stresses inside the material, leading to the observed cracks. As a consequence, the layer might not be closed, meaning that platinum of the substrate is visible. Figure 3.10 seems to indicate this, the morphology of the surface of VO_x films will be further discussed based on AFM measurements.

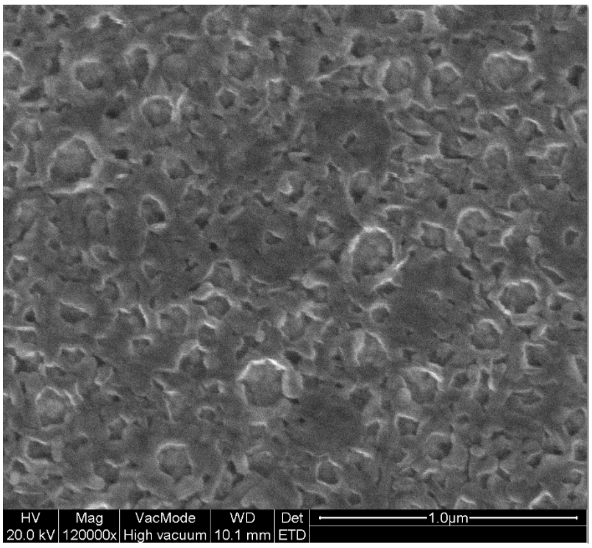

Figure 3.10: SEM image of the surface of V_2O_5.

3.5.2 Verification of layer thickness by cross SEM imaging

To determine the thickness of the thin films, two techniques were used. For SiO_2 samples, the XRR method was effective and reliable. For samples on TiN and Pt substrates, an empirical XRR-XRF relation was used. As this last method is slightly artificial and subject to some degree of error due to the fitting of the linear relations, it is definitely interesting to obtain a verification of these results. The images of figure 3.11 were obtained by cleaving the sample and looking at the cross section with the SEM (cross-SEM). Although detection of BSE is better suited for observation of different elements, the SEM operated in SE mode still allows identification of the various layers.

Both images show an amorphous layer on top of the Pt substrate, deposited with either the H_2O or the O_3 process. As mentioned before, the Pt substrate was formed by sequential sputtering of TiN and Pt on a Si wafer. The SEM images clearly show the 4 layers on top of each other: Si - TiN - Pt - VO_x. The thickness of the two samples, obtained by the XRR-XRF relation, was 18.89 nm (H2O) and 37.36(O3) respectively, demonstrating that the XRR-XRF relation provides rather accurate thickness estimations.

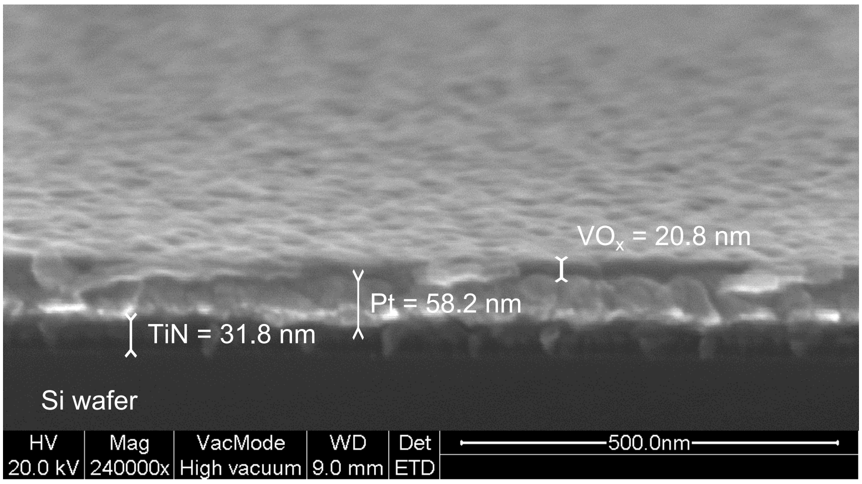

(a) H_2O process

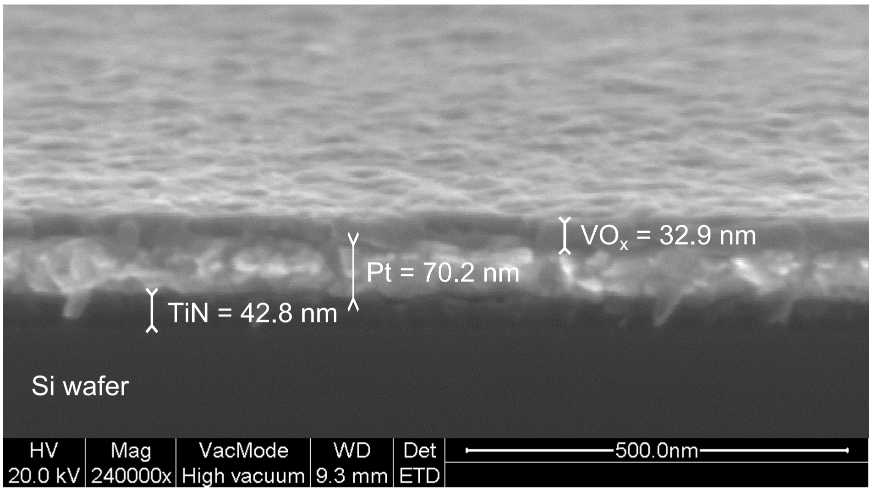

(b) O_3 process

Figure 3.11: Cross SEM images to measure the thickness of the as deposited amorphous vanadium oxide films.

3.6 Atomic force microscopy

The three substrates used in this work are examined with AFM. The device is operated in tapping mode and a Si tip is used with radius of approximately 10 nm. The AFM used in this work was a Bruker Dimension Edge.

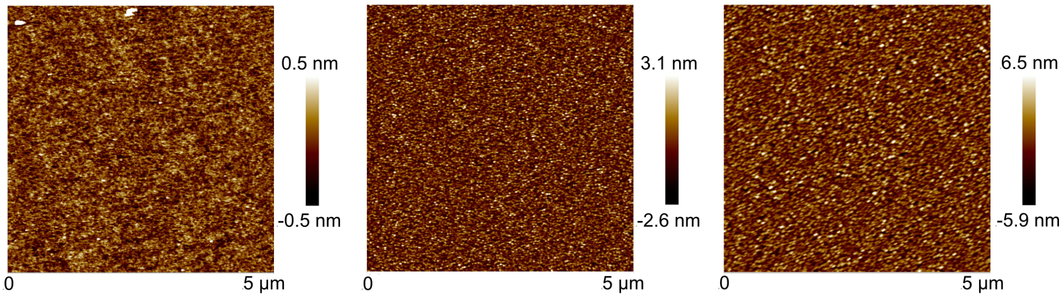

(a) SiO_2 substrate **(b)** TiN substrate **(c)** Pt substrate

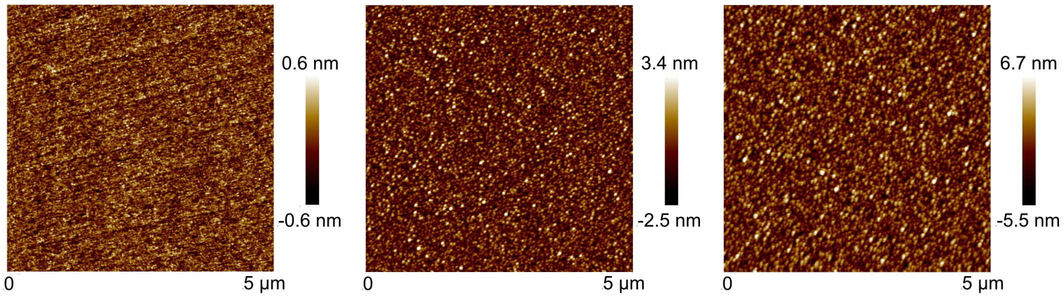

(d) SiO_2 + am. VO_x **(e)** TiN + am. VO_x **(f)** Pt + am. VO_x

Figure 3.12: AFM measurements of the three examined substrates (up) and amorphous layers deposited with the O_3 process on the three substrates (down).

The results of the measurements on the three substrates are displayed in figure 3.12. Considerate differences in roughness are observed. For the SiO_2 substrate, the morphology contains deviations of the order of Å while the roughness of the Pt substrate is approximately ten times larger. The titanium nitride substrate is situated in between SiO_2 and Pt with respect to roughness. Table 3.5 gives the R_q and z-range of the three substrates. AFM measurements are also performed on the vanadium oxide coated substrates, to measure the roughness of a layer deposited with the O_3 process. The results are presented as well in figure 3.12 and table 3.5.

Table 3.5: Comparison of roughness parameters of the three substrates considered in this work. The AFM results are given for both the bare substrates and for the as deposited amorphous layer, deposited by the O_3 process on the different substrates.

Bare substrates			**Vanadium oxide coated substrates**		
Sample	*R_q (nm)*	*z-range (nm)*	*Sample*	*R_q (nm)*	*z-range (nm)*
SiO_2	0.139	2.93	SiO_2 + am. VO_x	0.168	1.24
TiN	0.808	6.94	TiN + am. VO_x	0.818	6.25
Pt	1.75	13.3	Pt + am. VO_x	1.77	14.2

The roughness parameters of the amorphous vanadium oxide layers are comparable with the parameters of the bare substrates. The ALD process deposits a rather uniform layer and the existing features in the morphology of the substrate remain visible. As mentioned previously, the high roughness of the films on Pt and TiN substrates contributes to the error of determination of film thickness with XRR. Considering XRR is limited to films with roughness of approximately 10 Å, reported by Tiilikainen et al.[39].

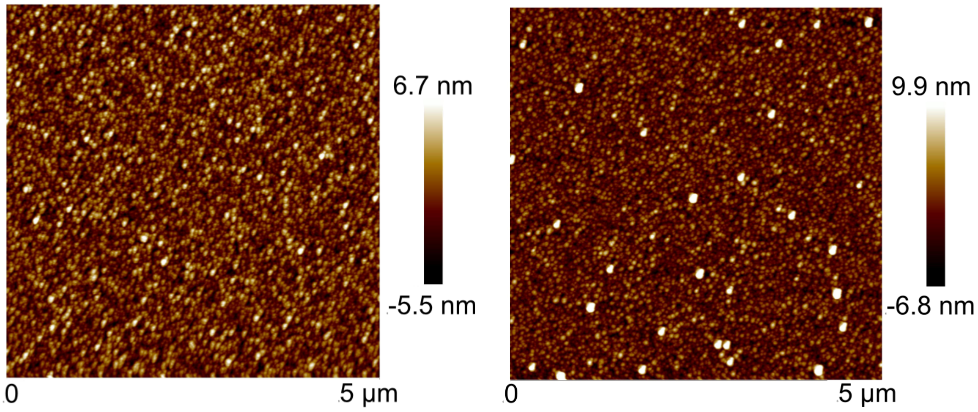

(a) O_3 process **(b)** H_2O process

Figure 3.13: AFM measurements of amorphous layers deposited on a Pt substrate with the H_2O and O_3 based processes.

Figure 3.13 compares the roughness of the amorphous vanadium oxide films, deposited with either H_2O or O_3 process on the platinum substrate. The R_q values of the amorphous films are 1.77 nm for the O_3 process and 1.95 nm for the H_2O process, indicating that the roughness of both films is comparable.

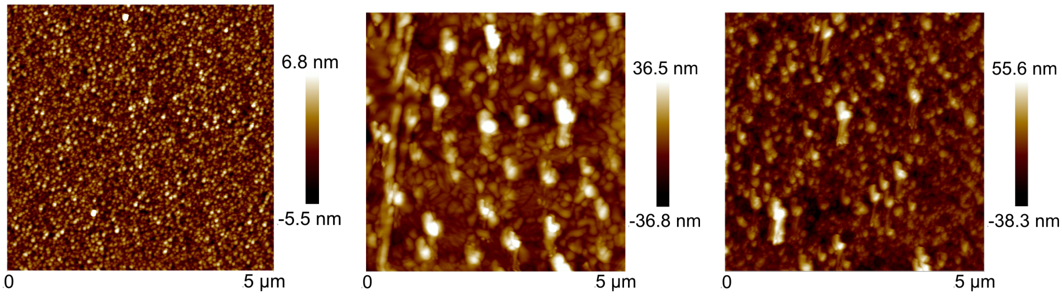

(a) VO_2(M1) **(b)** V_3O_7 **(c)** V_2O_5

Figure 3.14: AFM measurements of various vanadium oxides on Pt substrate.

Three distinct vanadium oxide phases are measured with AFM, more specifically VO_2(M1), V_3O_7 and V_2O_5, annealed from an amorphous vanadium oxide layer on the Pt substrate, as will be discussed in paragraph 3.8. Figure 3.14 illustrates that some remarkable differences exist in roughness between these three oxides. The R_q values and z-range of the three samples are listed in table 3.6.

Table 3.6: AFM obtained parameters indicating the roughness of three annealed vanadium oxide films on a Pt substrate.

Phase	R_q (nm)	z-range (nm)
VO_2(M1)	1.65	13.5
V_3O_7	3.45	18.7
V_2O_5	10.7	69.7

Annealing of VO2(M1) does not require absorption of oxygen, as the oxidation number of the vanadium oxide in the amorphous film was between +4 and +5, determined by XPS. Since Rampelberg et al. reported that the amorphous film deposited with the O_3 based ALD process was VO_2[35], it is reasonable to assume that the compositions of the films deposited in this work will be situated close to VO_2. The AFM measurements seem to confirm this expectation. The R_q value of the amorphous layer was equal to 1.95nm, which is approximately equal to the R_q of VO_2(M1). This is in contrast with the V_3O_7 and V_2O_5 samples. In the latter, absorption of oxygen is required, causing the lattice to expand such that stress is induced in the material. The AFM measurement of V_2O_5 indicates that the roughness of the layer is strongly modified upon absorption of oxygen. The R_q value increases with increasing amount of oxygen absorbed, based on the intermediate values for V_3O_7, see table 3.6. The z-range indicates that large variations in altitude are present for these oxides. As the thickness of the amorphous film was approximately 34 nm, the surface probably contains spots where the platinum is no longer covered with vanadium oxide, which was also indicated by SEM images in figure 3.10.

3.7 X-ray diffraction

The vanadium oxide thin films deposited by ALD were amorphous, which means the atoms are not organized into a crystal structure. Amorphous samples give no peaks in an XRD spectrum, because of the lack of positive interference by reflected waves at many parallel atomic layers. It is possible to change the crystallographic structure of a material by thermal annealing. The atoms of an amorphous layer can be (re-)organized in a lattice structure or a crystalline layer can be restructured in an energetically more favourable lattice, when enough energy is provided, for example by heating the sample or laser ablation[40].

3.7.1 Annealing of vanadium oxides

Various authors report phase transformations of vanadium oxides upon annealing. Bruckner et al. reported that V_2O_5 can be reduced to VO_2 by thermal annealing in a reducing atmosphere by means of the following sequential transitions: $V_2O_5 \longrightarrow V_3O_7 \longrightarrow V_4O_9 \longrightarrow V_6O_{13} \longrightarrow VO_2$[41]. Ningyi et al. confirms this reducing sequence, by demonstrating that some multiphase regions can be obtained before VO_2(M) is formed[42]. Sidorov et al. mentions that the reversed processes are possible by annealing in an oxidizing atmosphere, although no data is reported[43]. The following table summarises some reported annealing processes of vanadium oxides.

Table 3.7: Non-exhaustive overview of literature concerning annealing of vanadium oxides.

Author	**Transition**	**Temperature (°C)**	**Annealing time (min)**	**Atmosphere**
MacChesney et al.[44]	$V_2O_5 \longrightarrow VO_2(M)$	526	33	50% CO_2 50% CO
Chae et al.[45]	$V_2O_5 \longrightarrow VO_2(M)$	400	30	O_2
Sidorov et al.[43]	$V_2O_5 \longrightarrow VO_2$	200	960	H_2
Wang et al.[46]	$VO_2(B) \longrightarrow VO_2(M)$	450	60	Ar flow
Wang et al.[47]	$VO_2(B) \longrightarrow V_6O_{13}$	400-480	360	vacuum ($<9.10^{-4}$Pa)
Badot et al.[32]	am. $VO_x \longrightarrow V_2O_5$	400	30	air
Rampelberg et al.[48]	am. $VO_2 \longrightarrow VO_2(R)$	560-800	in-situ	<10 Pa O_2
	am$\cdot VO_2 \longrightarrow V_6O_{13}$	500-675	in-situ	35 Pa O_2
Premkumar et al.[36]	am. $VO_2 \longrightarrow V_2O_5$	500	5	120 Pa O_2
	am. $VO_2 \longrightarrow V_6O_{13}$	500	5	30 Pa O_2
	am. $VO_2 \longrightarrow VO_2$	500	5	11 Pa O_2
Blanquart et al.[34]	am. $VO_x \longrightarrow VO_2$	500	in-situ	N_2
	am. $VO_x \longrightarrow V_2O_5$	330	in-situ	air

The annealing processes summarised in table 3.7 indicate that the atmosphere determines if oxidation or reduction of the vanadium oxide will happen. Moreover, control of the partial pressure can shift the end result in an anneal[48][36]. Bruckner et al. stated that reduction of V_2O_5 passes through the phases of the V_nO_{2n+1} series before VO_2 is reached. Indications exist that this sequence will be present in the reversed direction[43] and although various authors have published one or more annealing procedures, no detailed overview is available.

3.7.2 Systematical annealing study by in-situ XRD

The *in-situ* XRD set-up allows to determine the phase structure by taking XRD measurements while heating the sample in a controlled ambient, see figure 3.15. In order to achieve this, the sample is placed on a heating stage in a leak tight chamber, containing 2 X-ray transparant windows of Kapton foil. This allows to take XRD measurements while heating the sample. The heat treatment allows phase transformation which can be stabilized by subsequent quenching to room temperature. The set-up is controlled by a LabView program and the XRD device used in this set-up was a Bruker D8 Discover, using Cu Kα radiation (0.154 nm) and point sensitive (i.e. linear) detector with 2θ range of 20°.

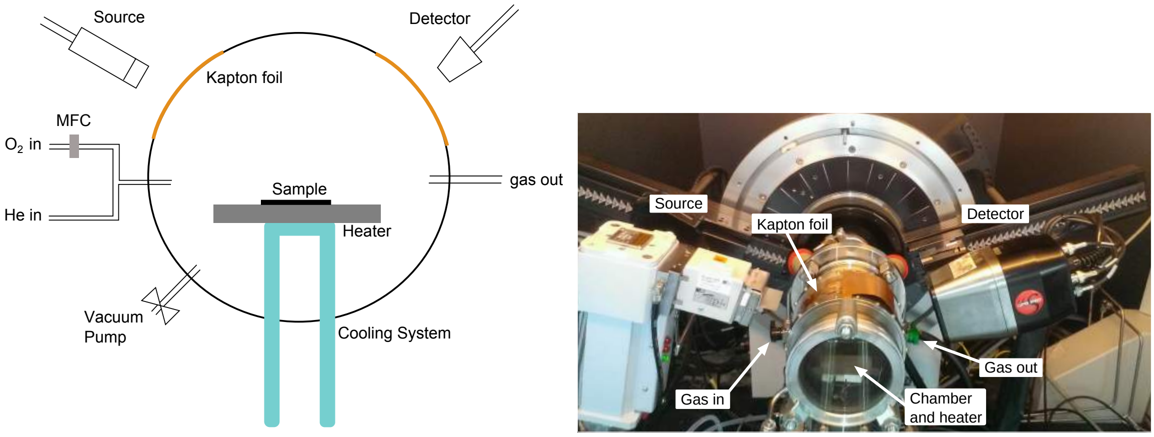

Figure 3.15: Systematical representation and photo of the in-situ XRD set-up.

A systematic study of the thin films, deposited with the 2 ALD processes on the three distinct substrates, was carried out with the in-situ XRD set-up. In this study, the atmosphere inside the chamber was tuned to investigate the influence of the oxygen partial pressure on the phase formation. The atmosphere was controlled by adjusting the flow of O_2, superimposed to a constant He flow. At first, the chamber was evacuated to low vacuum with a rotation pump until a base pressure of $5.10^{-2}\ mbar$ was reached, to eliminate possible contaminations from the chamber. Then a constant Helium flow of $2.7\ l/min$ was injected in the chamber and oxygen was added with a Mass Flow Controller (MFC) with a range of 1 to 50 cm^3/min (sccm, standard cubic centimeters per minute). As the bottle connected to the MFC only contained 10% O_2 and 90% N_2, in reality the flow O_2 was limited between 0.1 and 5 sccm. The partial pressure of oxygen is defined as the mole fraction of oxygen times the total pressure, $p_{O_2} = x_{O_2}.p_{tot}$. This yields for a flow of 0.1 sccm

$$p_{O_2} = \frac{0.1\ cm^3/min}{2700.1\ cm^3/min} p_{tot} = \frac{0.1}{2700.1} 10^5\ Pa = 3.7\ Pa \tag{3.2}$$

For the systematical study of phase formation, the temperature was increased linearly at a rate of 0.25 °C/s to 700 °C while the ambient was kept constant. Multiple anneals were performed in atmospheres containing variating oxygen content. An XRD spectrum was measured every 4s with $\theta_{detector} = 11.5°$ and $2\theta_{source} = 23°$, such that the most prominent XRD peaks of the various vanadium oxides were situated in the detection range.

Thin films deposited with the O_3-process on SiO_2

Figure 3.16 shows the in-situ XRD measurements of the amorphous vanadium oxide film, deposited with the ozone based ALD process on the SiO_2 substrate. The partial pressure of oxygen is indicated for all measurements.

Various vanadium oxide phases are formed, depending on the partial pressure of oxygen in the atmosphere. The phase diagram of the V-O system (figure 1.6) indicates that no transitions occur when VO_x phases with $2 \leqslant x \leqslant 2.5$ are heated up to 665 °C, except for the transition of VO_2(M1) to VO_2(R) at 67 °C. This is not in line with the results obtained in this study, where multiple transitions are observed. However, the phase diagram of the V-O system of figure 1.6 is obtained in a condensed system, signifying that no gaseous phase was present. In these experiments, the presence of the gaseous phase, and additionally the amount of oxygen, gives rise to completely different results.

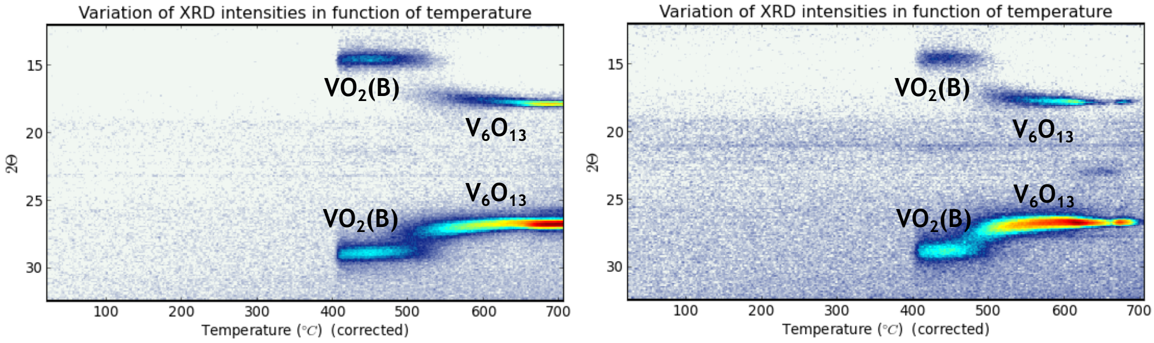

(a) 3.7 Pa **(b)** 7.4 Pa

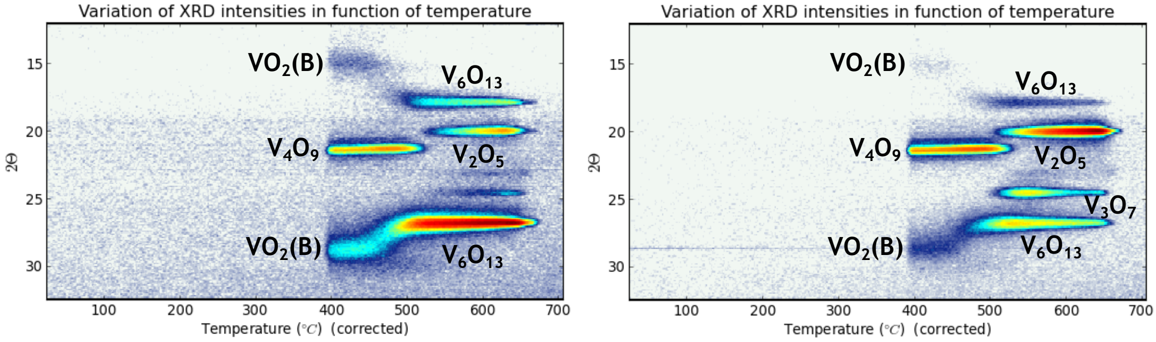

(c) 14.8 Pa **(d)** 29.6 Pa

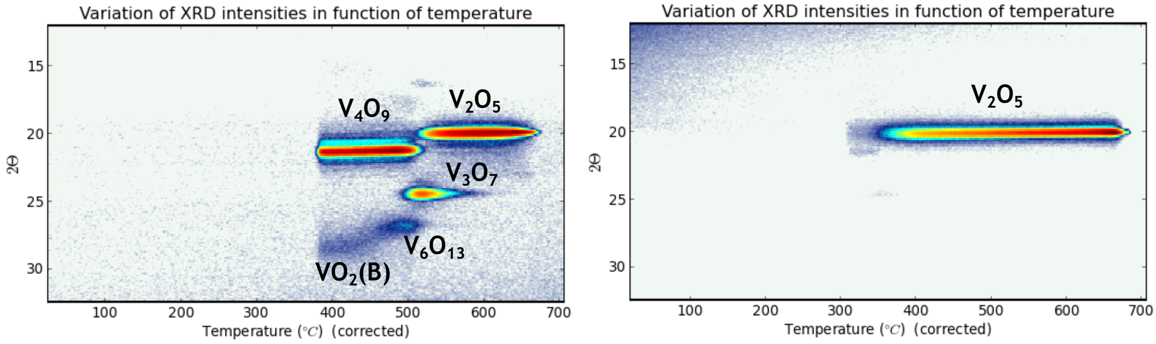

(e) 48.1 Pa **(f)** Air

Figure 3.16: Systematical study of phase formation by thermal annealing of amorphous vanadium oxide films with O_3 process on SiO_2 in atmosphere with controlled oxygen level.

In an atmosphere with the lowest oxygen concentration possible for this set-up (partial pressure ≈ 3.7 Pa), the amorphous film crystallizes to VO_2(B) at 400 °C and subsequent to V_6O_{13} at approximately 500 °C. In paragraph 1.2 was mentioned that VO_2(B) and V_6O_{13} contain many similarities[13]. The transition of the amorphous film to VO_2(B) and V_6O_{13} was observed by Rampelberg et al. for a thin film deposited with the same ALD process at slightly higher oxygen partial pressure[48].

If the partial pressure of oxygen is increased to 7.4 Pa, identical transitions are observed. Further increase of oxygen results in the formation of V_4O_9 and V_2O_5, both containing more oxygen than VO_2(B) and V_6O_{13} indicating that absorption of oxygen from the atmosphere is occurring. The peak of V_3O_7 around 25° is slightly visible as well and becomes more pronounced if the film is annealed in an atmosphere with oxygen partial pressure of 29.6 Pa. VO_2(B) and V_6O_{13}, formed at low concentrations of oxygen, are less visible for 29.6 Pa and their intensity decreases further for an 48.1 Pa of O_2. Annealing in air of the amorphous film resulted in formation of V_2O_5, observed as well by Blanquart et al.[34].

In paragraph 3.4 was described that the vanadium peak in the XPS spectrum of the amorphous film consisted of a mixture of vanadium 4+ and 5+. This indicates the ability to form the various vanadium oxide phases with oxidation number from 4+ to 5+ by absorption or emission of oxygen. In figure 3.16, all vanadium oxides with valence state from 4+ to 5+ are retrieved.

The observed crystallization can be compared with the Ellingham diagram of the V-O system, since an Ellingham diagram illustrates which phases are thermodynamically favourable for a certain temperature and ambient composition. The Ellingham diagram is limited to the 4 principal vanadium oxides, with oxidation state from +2 to +5, which are thermodynamically stable. Yamaguchi et al. published the Ellingham diagram of the V-O system, presented in figure 3.17. The details of the anneals, conducted in this work, have been superimposed in blue on the figure of Yamaguchi et al.

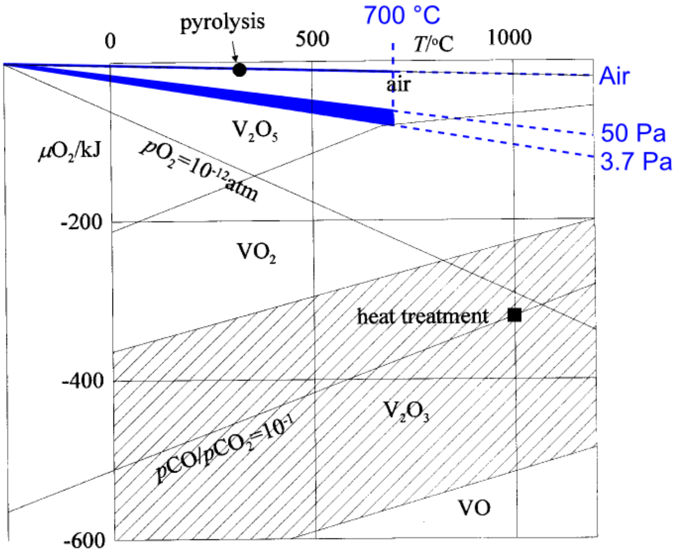

Figure 3.17: Ellingham diagram of the V-O system, from Yamaguchi et al.[49], adapted with data concerning the anneals conducted in this work (indicated in blue).

For the entire blue region, indicated in figure 3.17, V_2O_5 is retrieved as thermodynamically stable state. Since crystallization of many other oxides was observed, it can be concluded that the phase formation was limited by kinetics, rather than thermodynamics.

Thin films deposited with the H_2O-process on SiO_2

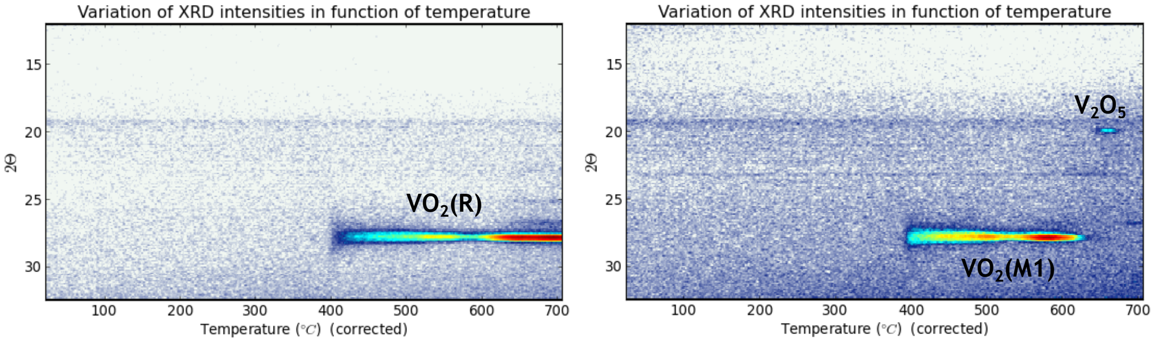

(a) 3.7 Pa **(b)** 7.4 Pa

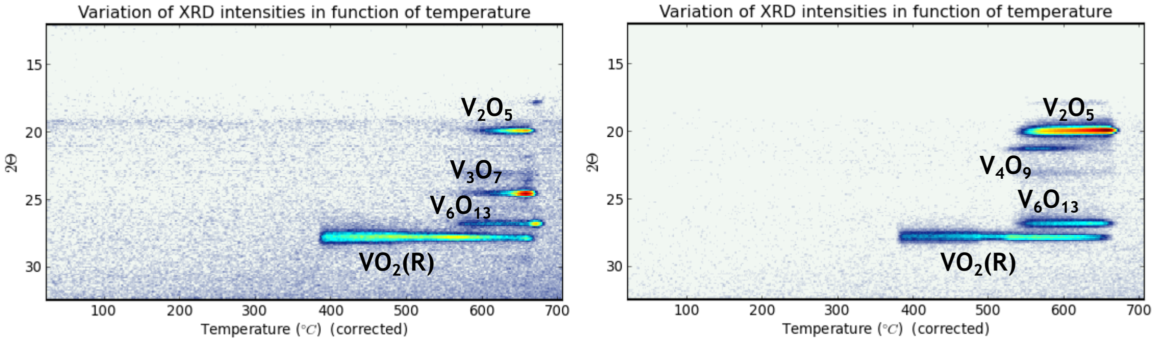

(c) 14.8 Pa **(d)** 29.6 Pa

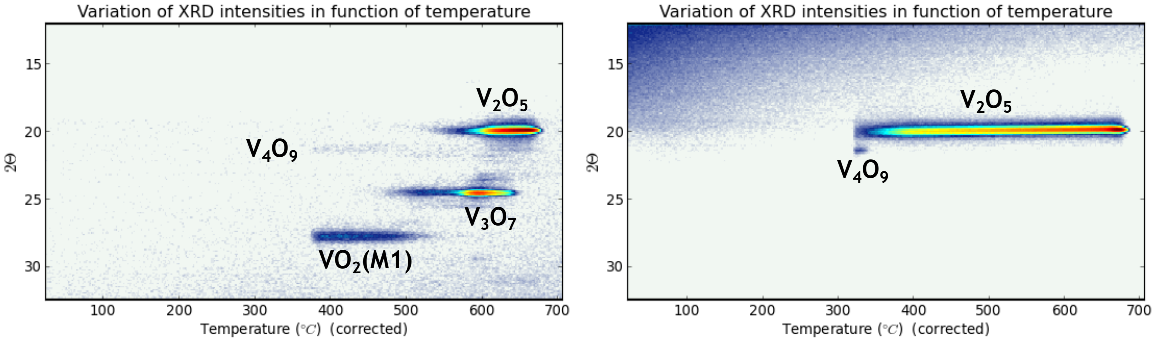

(e) 48.1 Pa **(f)** Air

Figure 3.18: Systematical study of phase formation by thermal annealing of amorphous vanadium oxide films with H_2O process on SiO_2 in atmosphere with controlled oxygen level.

A similar study is performed for the films deposited with the water based process on SiO_2, see figure 3.18. If the film is annealed in an atmosphere with partial pressure of oxygen $\leqslant$ 7.4 Pa, formation of rutile VO_2 is observed at 400 °C. The lower melting temperature at 7.4 Pa is caused by the formation of V_2O_5 at a temperature of approximately the melting temperature of V_2O_5. For higher concentration of oxygen (partial pressure of 14.8 Pa and 29.6 Pa), VO_2(R) transforms to a mixed phase region. The second peak of V_6O_{13}, visible in the measurements on the O_3-based film, is present with very weak intensity. For 48.1 Pa of O_2, more oxygen is present and as a result, the most oxygen-containing phases of the V_nO_{2n+1} series are formed. Annealing in air finally yields V_2O_5, as was the case for the films deposited with the O_3 ALD process. In general, it can be noted that some differences exist in results of annealing of the films deposited by the 2 considered processes. These differences are discussed in detail in the next paragraph.

A similar systematical study of annealing in variable oxygen concentration was performed for the vanadium oxide films deposited on TiN and Pt, with both the water and ozone based ALD process. The results of which are represented in the appendix. The formation of the various phases on those substrates will be discussed in detail in paragraph 3.8, where an overview of the phase formation is given.

Differences between the two ALD processes

The amorphous layers deposited by the H_2O and O_3 process do not behave identical under the same annealing conditions, even though they are both amorphous and grown with the same vanadium precursor, pointing to a difference in the films caused by the second precursor gas. Figure 3.19 compares anneals in an atmosphere with oxygen partial pressure of 3.7 Pa. The layer deposited with the H_2O process crystallizes into the VO_2(R) phase, while the layer of the O_3 process transforms to the VO_2(B) and afterwards to V_6O_{13}.

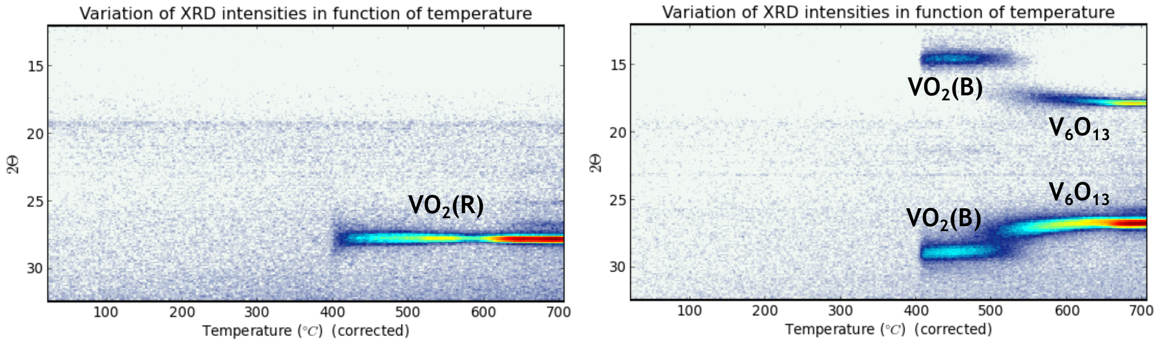

(a) H_2O process **(b)** O_3 process

Figure 3.19: Anneal of two amorphous vanadium oxide thin films, deposited with the 2 ALD processes, at 0.25 °/C in oxygen partial pressure of 3.7 Pa.

As VO_2(B) and VO_2(R) are different phases, they have different lattice structures, even though both consist of twice as much oxygen as vanadium. Both are based on an oxygen BCC lattice with vanadium in the octahedral sites[13], as discussed in paragraph 1.2. The different mutual orientation of the fourfold axis of the oxygen octahedra[13] translates to a difference in density between the two phases. VO_2(R) and VO_2(B) have a density of 4.67 and 4.031 g/cm^3, respectively. This information can be compared to the XRR-XRF relation for both processes deduced in figure 3.7. The layer deposited by the O_3 process is thicker when an equal intensity of vanadium counts is measured, compared to a layer of the H_2O process. This means less vanadium atoms are present per unit of film thickness, such that the density is lower. Therefore, it can be understood that the layers deposited with the O_3 process form VO_2(B) when annealed and layers from the H_2O process form VO_2(R). Identical results were noticed for the TiN and Pt substrate, these measurements will be discussed in paragraph 3.8.

In general, more phase formation is observed for the amorphous films deposited with the O_3 process. If one compares all oxides of the V_nO_{2n+1} series with respect to density, all oxides are situated between 3.3 g/cm^3 and 4.05 g/cm^3, except for VO_2(M1) (4.67 g/cm^3), which can be seen as a rough indication that VO_2(B) more closely resembles the other phases than VO_2(M1). A more convincing proof is found in the theoretical study of Katzke et al.[16], where VO_2(B) is described as the border of the series lock-in phases V_nO_{2n+1} and VO_2(M1) is regarded as the limit of the V_nO_{2n-1} series. Thus, VO_2(B) is more closely related to the other observed phases, explaining why more phase formation is observed for the amorphous films deposited with the ozone based ALD process.

Influence of film thickness

The thickness of the deposited film can have influence on the phase formation and structure upon annealing for some materials[50]. For the vanadium oxide thin films treated in this work, this is however not the case. In figure 3.20, the in-situ XRD measurements of 2 thin films in a partial pressure of 48.1 Pa oxygen is displayed. The first sample was deposited with 125 cycles of the O_3 ALD process, while the second sample was the result of 250 cycles of the same process. The two films give nearly identical in-situ XRD measurements. For both films, the same phases are formed at approximately the same temperature. Since the thickness of the film deposited with 125 cycles is lower, it results in broader peaks in the XRD spectrum. This effect was discovered by Scherrer in 1918[51].

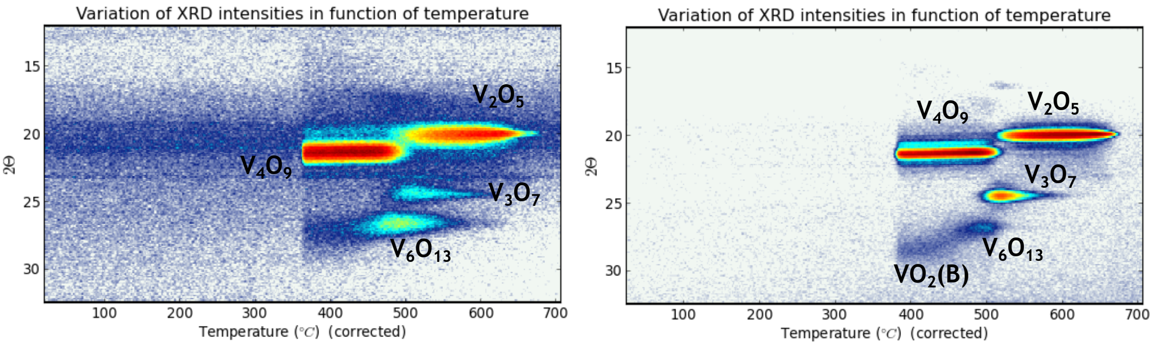

(a) 125 cycles: 12.68 nm **(b)** 250 cycles: 21.96 nm

Figure 3.20: Anneal at 0.25 °C/s in oxygen partial pressure of 48.1 Pa of two amorphous vanadium oxide thin films, deposited with the O_3 ALD processes with varying thickness.

3.7.3 Ex-situ XRD

The in-situ XRD measurements have a limited range, due to the linear detector spanning only a 20° window. In this case, the spectra were recorded between $2\theta = 13°$ and $2\theta = 32°$. To verify if peaks outside of this region were missed, an ex-situ measurement of all phases between $2\theta = 10°$

and $2\theta = 70°$ was conducted. However, no extra peaks outside of the region investigated by the in-situ XRD were recorded, except for a peak with minor intensity for V_6O_{13} at 46°. This means identification of the phases had to be performed by matching the position of only one or two peaks with the database, which provided an extra difficulty. Figure 3.21 shows an ex-situ XRD measurement for all the phases on SiO_2 substrate. A y-offset is given to the different phases for better visualization. The database files used for identification of the phases are given in the legend.

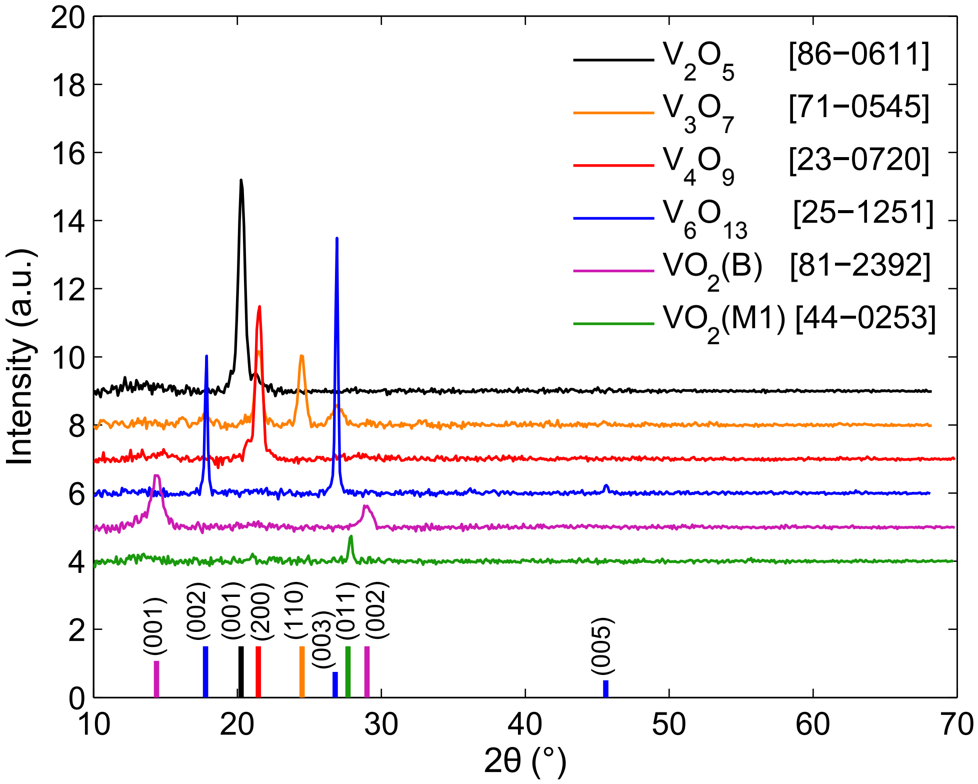

Figure 3.21: Ex-situ XRD measurements of all VO_x phases on SiO_2 substrate

Six oxides were encountered in the annealing process of the vanadium oxide films on SiO_2 ·, i.e. VO_2(R) (transforms to VO_2(M1) at 67 °C), VO_2(B), V_2O_5, V_3O_7, V_4O_9 and V_6O_{13}. V_3O_7 could only be reached in a mixed phase region for the SiO_2 substrate, see figure 3.21.

3.8 Summary of experimentally obtained vanadium oxide phases

An overview of the systematic study of the annealing of amorphous films as deposited with the two ALD processes is presented for the different substrates. Figures 3.22, 3.23, 3.25, 3.26, 3.28 and 3.29 illustrate the phases present while annealing the samples with a constant rate of 0.25 °C/s. These figures should not be interpreted as phase diagrams, as some phases are metastable. They can be interpreted as ‘formation diagrams’, since they give an overview of the observed phase formations of these films. Annealing for a long time at a given temperature might cause the layer to oxidize further. The figures were based on measurements with oxygen partial pressure of 3.7 Pa, 7.4 Pa, 14.8 Pa, 29.6 Pa & 48.1 Pa and in air, which contains a partial pressure of $21{,}2.10^3$ Pa oxygen. These measurements are indicated as dotted lines on the figures. The indicated transitions between certain 'phase domains' are therefore not exact. When one phase occurred at 14.8 Pa which was not present at 7.4 Pa, a discrete boundary was introduced around 10 Pa. This boundary must not be interpreted very strictly, but as a simplification of the change between two measurements. On the other hand, data on the x-axis is continuous, as the in-situ XRD set-up allows to constantly measure the phase structure as a function of temperature in a constant atmosphere.

3.8.1 Silicon dioxide substrate

As discussed in paragraph 3.7.2, the films deposited by the H_2O process crystallize to VO_2(R) while the O_3 process gives films that crystallize to VO_2(B) for low oxygen concentration in the ambient, as a consequence of the higher density of the films deposited by the H_2O process. The V_6O_{13} phase contains only slightly more oxygen than VO_2 and has a comparable lattice to VO_2(B), as discussed in 1.2. This phase can only be reached in pure form for low oxygen partial pressures for films deposited by the ozone process. For higher pressures, mixed phase regions occur, starting at 400 °C for the ozone based process and from higher temperatures for films deposited by the water based process. The composition and relative intensity of the different phases in a mixed phase region is affected by the oxygen concentration in the atmosphere. Annealing in pure air yields V_2O_5 for the films of both processes. When the partial pressure of oxygen is higher, formation of V_2O_5 becomes even more favourable thermodynamically, as can be seen in figure 3.17. Melting of V_2O_5 was observed at approximately 680 °C.

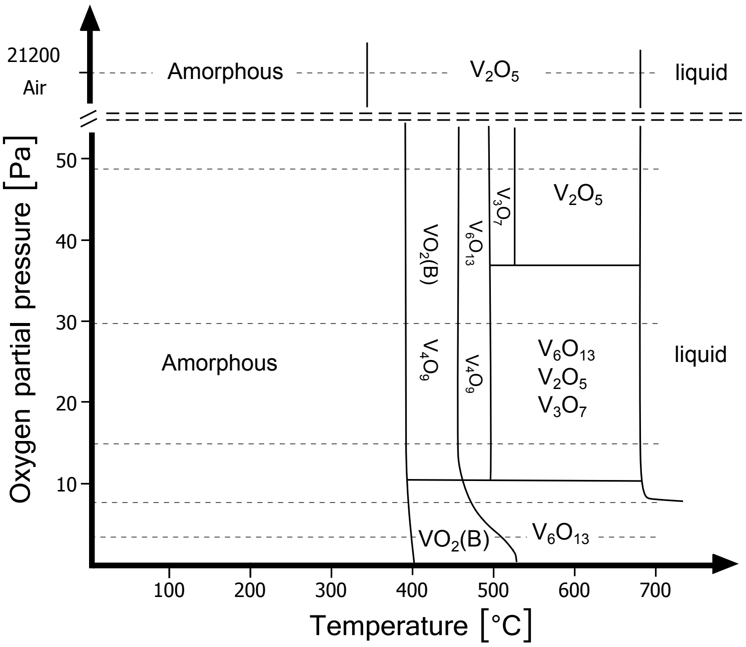

Figure 3.22: Formation diagram of amorphous films deposited with the **O_3 process** on a **SiO_2 substrate**, based on six in-situ XRD measurements. The value of the partial pressure for these measurements is indicated by the dotted lines.

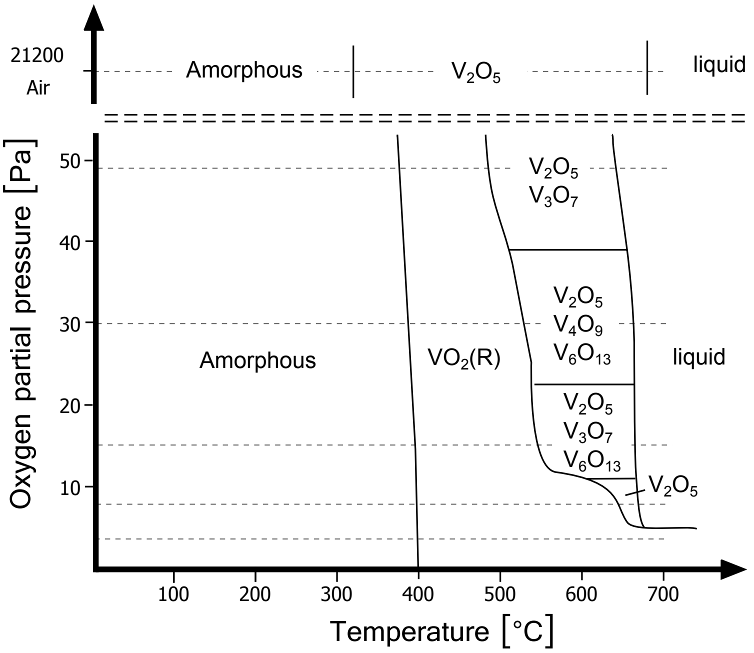

Figure 3.23: Formation diagram of amorphous films deposited with the **H_2O process** on a **SiO_2 substrate**, based on six in-situ XRD measurements. The value of the partial pressure for these measurements is indicated by the dotted lines.

3.8.2 Titanium nitride substrate

The formation diagrams of the SiO_2 based films were much richer than for the TiN or Pt based films. The mixed phase regions were not observed for oxygen partial pressure below 50 Pa as was the case for the films deposited on the SiO_2 surface, illustrating that the substrate has an influence on the deposited film. A possible explanation can be found in the oxygen concentration of the SiO_2 substrate. The oxygen already present in SiO_2 can be an extra oxygen source for further oxidation of the VO_2 layer, while the TiN substrate shows the opposite behaviour. For higher temperatures, the titanium starts to oxidize by formation of anatase[1] and rutile TiO_2. This means oxygen atoms diffuse from the VO_x film into the TiN layer where TiO_2 is formed. The XRD peak caused by TiO_2(R) is situated very close to VO_2(R). The matching peak locations of the two phases is caused by the affinity of their lattices (note that both oxides consist of an identical rutile structure and that V and Ti are situated next to each other in Mendeleev's table). When TiO_2(R) is formed in the proximity of VO_2(R), a gradual change in the peak location of VO_2(R) is observed, see figure 3.24, which could indicate that TiO_2(R) and VO_2(R) form a mixed state containing both vanadium and titanium atoms in a rutile lattice. If the formation of TiO_2(R) happens when another vanadium oxide phases is formed, the TiO_2(R) can force the vanadium oxide to form a rutile lattice as well, such that VO_2(R) is formed. This happens for instance in figure 3.25. Because of the influence on the crystal structure of the vanadium oxide and the possible phase mixing, the region where formation of TiO_2(R) was observed is cross hatched in the formation diagrams. Based on several in-situ XRD measurements (e.g. figures A.1d, A.2f and A.3a), crystallization of TiO_2(R) occurred at approximately 600 °C.

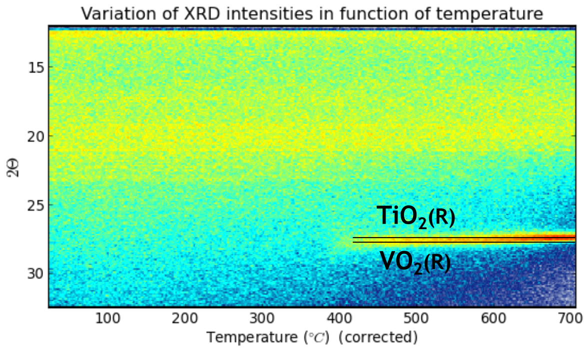

Figure 3.24: Illustration of the shifting of the peak situated at VO_2(R) and TiO_2(R).

---

[1] formation of anatase TiO_2 (TiO_2(A)) is not indicated on the formation diagrams, see Appendix

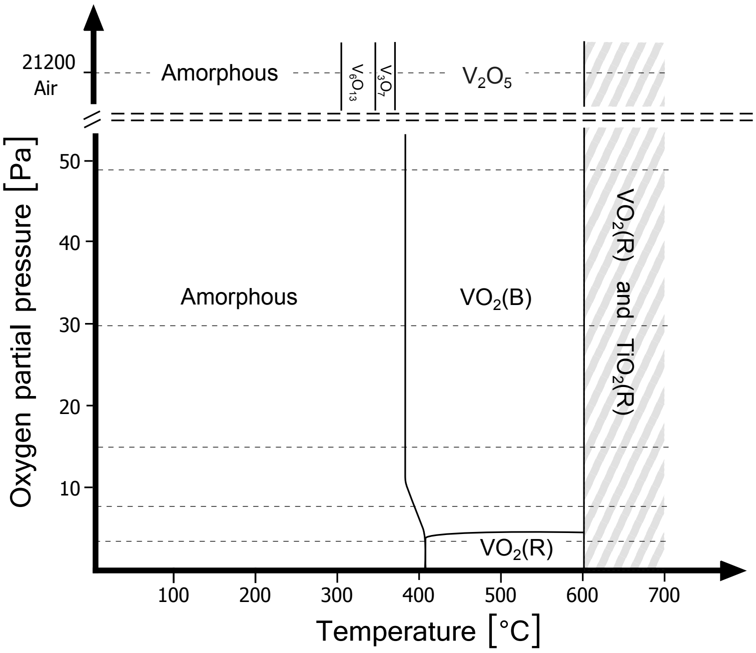

Figure 3.25: Formation diagram of amorphous films deposited with the **O_3 process** on a **TiN substrate**, based on six in-situ XRD measurements. The value of the partial pressure for these measurements is indicated by the dotted lines.

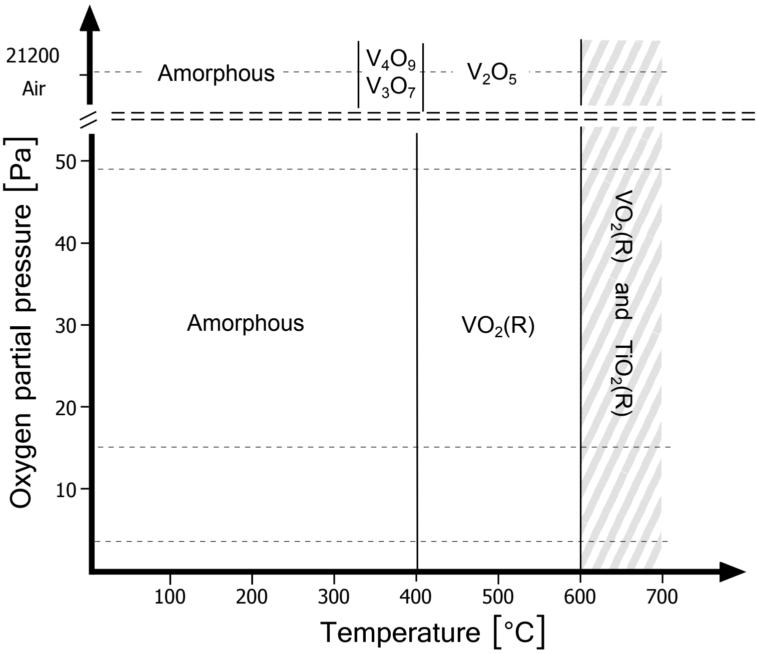

Figure 3.26: Formation diagram of amorphous films deposited with the **H_2O process** on a **TiN substrate**, based on four in-situ XRD measurements. The value of the partial pressure for these measurements is indicated by the dotted lines.

The amorphous films form VO_2(B) and VO_2(R) (which transforms to VO_2(M1) when cooling down) for atmospheres with low concentration of oxygen. By analogy with the films on the SiO_2

substrate, VO_2(B) is formed if the O_3 process was used and VO_2(R) is formed by films deposited with the H_2O process. Furthermore, V_2O_5 is observed for both processes if the films are annealed in air. Formation of V_2O_5 is preceded by metastable states, i.e. V_6O_{13} and V_3O_7 for the films deposited with the O_3 process and V_4O_9 in the other case.

Figure 3.27 shows the formation of anatase TiO_2 and rutile TiO_2, which cause a peak at 25.28° and 27.45°. The presented in-situ XRD measurement was obtained from a TiN sample without vanadium oxide film. The formation of the two TiO_2 oxides happens at higher temperatures than for the samples coated with amorphous vanadium oxide, indicating that the absorption of oxygen into the TiN lattice is improved by the presence of the vanadium oxide layer. In this study, oxidation of the TiN layer is highly unwanted, because TiO_2 is not conducting and the TiN and Pt substrates were meant as possible electronic back-contacts for electrochemical measurements. To avoid problems with TiO_2, the Pt substrate was used for testing of VO_x films as electrode material, which will be discussed in detail in chapter 5.

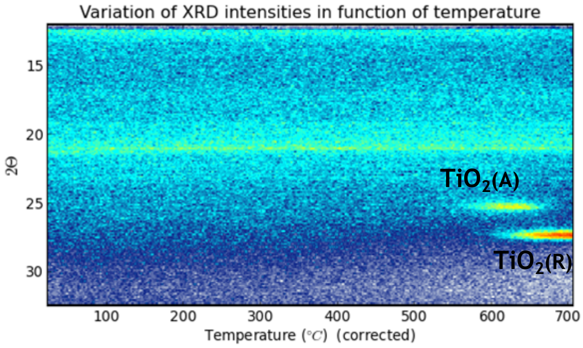

Figure 3.27: Oxidation of the titanium in the TiN substrate to TiO_2(A) and TiO_2(R).

3.8.3 Platinum substrate

The platinum substrate consists of a sputtered platinum layer on top of a TiN layer. Although the titanium was not in direct contact with the vanadium oxide layer, because of the presence of the Pt layer in between, oxidation of the titanium was yet again observed. Thus, oxygen atoms must diffuse through the platinum film. Schmiedl et al. investigated whether or not this is possible and concluded that oxygen diffusion was indeed observed, more specifically by grain boundary diffusion[52]. In figures 3.28 and 3.29, the regions were TiO_2(R) is formed are cross hatched.

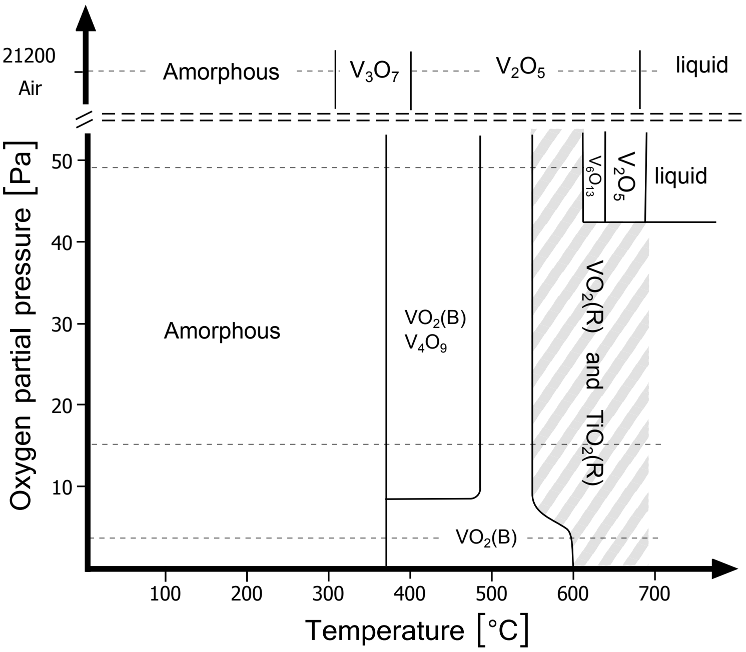

Figure 3.28: Formation diagram of amorphous films deposited with the **O_3 process** on a **Pt substrate**, based on four in-situ XRD measurements. The value of the partial pressure for these measurements is indicated by the dotted lines.

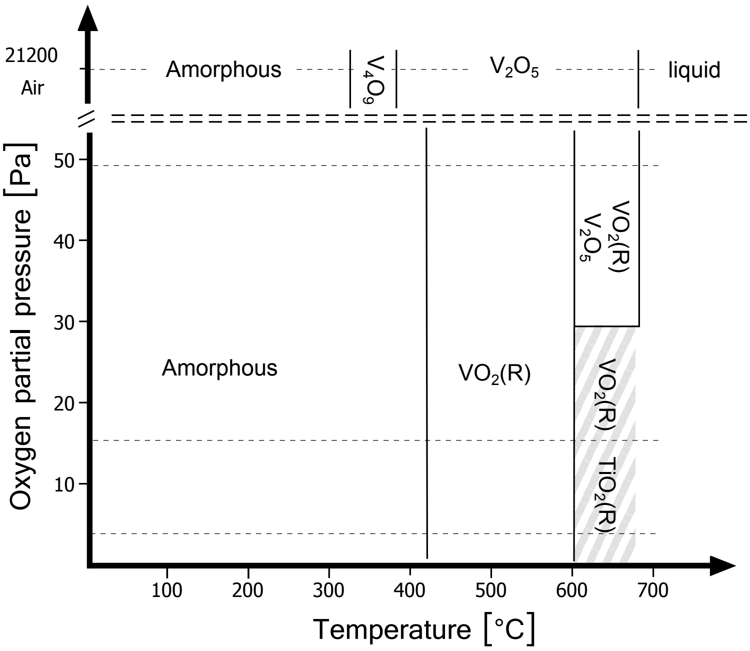

Figure 3.29: Formation diagram of amorphous films deposited with the **H_2O process** on a **Pt substrate**, based on four in-situ XRD measurements. The value of the partial pressure for these measurements is indicated by the dotted lines.

The formation diagrams of the amorphous films on a Pt substrate contain some similarities with the formation diagrams of the films on the other substrates. Once more, VO_2(B) and VO_2(R) are formed by anneals in low oxygen concentration of films deposited with the O_3 and H_2O process, respectively. This is observed for all substrates and is caused by the structure (and density) of the as deposited films. Furthermore, V_2O_5 is formed in air, preceded by the metastable phases V_3O_7 and V_4O_9.

Samples with Pt substrate were used for the electrochemical testing of the various vanadium oxides, as will be described in chapter 5. The annealing procedures listed in table 3.8 were used to form the distinct phases.

The $VO_2(M_1)$ phase is formed by transition of a VO_2(R) lattice at 67 °C. The small V_6O_{13} region observed in figure 3.28 could not be reached easily, instead V_3O_7 was formed. However, one sample of V_6O_{13} could be formed by annealing at 3.7 Pa oxygen partial pressure and 600 °C. The V_6O_{13} phase formed out of VO_2(B), as happens for samples on SiO_2 substrate.

Table 3.8: The required temperature of anneal and partial pressure of oxygen in the atmosphere for formation of the different phase structures are listed. The ALD process, used for deposition of the amorphous layer is mentioned per VO_x.

Phase	ALD process	Oxygen partial pressure (Pa)	Temperature (°C)
VO_2(M1)	H_2O	18.5	500
VO_2(B)	O_3	3.6	420
V_2O_5	O_3	$21.2*10^3$ (air)	500
V_3O_7	O_3	48	560
V_4O_9	H_2O	$21.2*10^3$ (air)	355
V_6O_{13}	O_3	3.6	550

3.9 Conclusion

Two ALD processes were used for deposition of vanadium oxide thin films, using TEMAV and H_2O or O_3 as precursors. XRR was used to determine the film thickness, with success for samples deposited on SiO_2. However, XRR was not applicable for layers on Pt and TiN, because of the increased roughness (obtained by AFM) and multilayer structure. Thus, an alternative approach was required to determine the film thickness on these substrates. Therefore, a relation between XRR thickness and XRF counts was obtained from the samples on SiO_2. Based on this relation, estimations were obtained for thin films on Pt and TiN, which were verified by cross SEM images, indicating that the XRR-XRF relation yielded reasonable results.

AFM measurements revealed the differences in roughness between the SiO2 and Pt/TiN substrates, as mentioned. The roughness of the amorphous films of the two ALD processes was comparable. An interesting increase in roughness was observed for annealed phases containing more oxygen with respect to vanadium. The roughness of VO_2(M1) was small compared to V_3O_7 and V_2O_5, which could be explained by the expansion required for absorption of oxygen.

The oxidation state of the amorphous films was examined with XPS, resulting in a composition of V^{4+} and V^{5+}. The in-situ XRD measurements on the amorphous films allowed formation of 6 different phases, all of which had an oxidation state between V^{4+} and V^{5+}. As a result could be concluded that the oxidation state of the amorphous film limits the phase formation upon annealing.

A systematical annealing study was performed for the amorphous films on the three substrates with temperature and oxygen content in the ambient as parameters. This resulted in 6 formation diagrams. Some general conclusions could be drawn.

- First of all, an increased oxygen content in the atmosphere leads to crystallization of phases with higher oxygen to vanadium ratio, illustrating that oxygen from the atmosphere was absorbed into the film. This is also proved by several authors describing anneals in reducing atmospheres where the reversed reactions were observed.
- A second conclusion was that the two processes did not behave identical upon annealing. A distinct density (quantified by XRF counts per unit thickness) could explain the preferable formation of VO_2(R) and VO_2(B).
- The third observation was the different outcome of identical anneals on the different substrates. An explanation was found in the distinct behaviour of the substrate with respect to oxygen. SiO_2 could deliver oxygen to the vanadium, acting as a secondary oxygen source. TiN absorbed oxygen, since formation of TiO_2(A) and TiO_2(R) was recorded. Pt behaved intermediate, although some diffusion of oxygen through platinum was observed, resulting in the formation of TiO_2.

4

Fundamentals of electrochemistry

4.1 Introduction to electrochemistry

Electrochemistry studies the relation between chemical changes and electron transfer. The chemical reactions take place at the interface between an electrode and an electrolyte. Electrodes can be solid (eg. lithium ion batteries[53]), liquid (eg. carbon ionic liquid[54]) or gaseous (eg. lithium - air batteries[55], fuel cells[56]). The electrolyte is a medium required for transfer of ions between the electrodes and is most often liquid[5]. Solid electrolytes are heavily researched to solve some key issues with safety and stability[57].

Chemical reactions with electron transfer between compounds are called reduction-oxidation (redox) reactions. In electrochemistry, the reduction and oxidation reaction are separated spatially and the electron transfer between the two half-reactions happens by means of an external circuit[58]. On the one hand, a chemical redox reaction can be used to generate electron transfer and thus electrical energy, this happens in a galvanic cell. A commercial battery consists of one or more galvanic cells, connected in series or parallel. On the other hand, electrical energy can be applied to induce a chemical reaction in the case of an electrolytic cell. This process is called electrolysis and is used for example on industrial scale to produce metals in pure form[59].

4.1.1 Electrochemical cells

An electrochemical cell consists of three main components[58]: two electrodes where the reactions occur, and an electrolyte to transfer the ions between the electrodes. The two electrodes are called the cathode and the anode, where respectively the reduction and oxidation reaction take place. In the reduction reaction, uptake of electrons is present and the oxidation state is raised. On the other hand, the oxidation reaction is associated with loss of electrons and lowering of the oxidation state. An example of an electrochemical cell with copper and zinc electrodes is shown in figure 4.1. Both electrodes are in contact with an electrolyte, which is electronically insulating, and are separated by a salt bridge or ion permeable sheet. This way, electrons are forced to pass through the external circuit, but electric neutrality and charge balance is ensured by transport of ions.

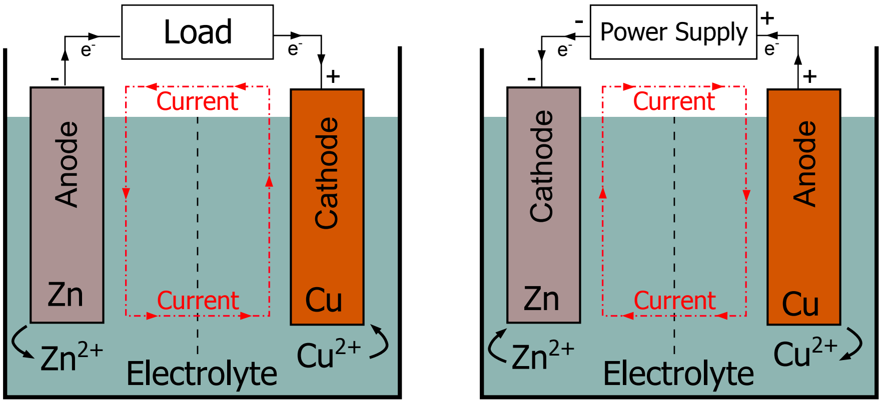

(a) Discharge **(b)** Charge

Figure 4.1: Schematical representation of the operation of an electrochemical cell in discharge and charge mode.

Discharging and charging of an electrochemical cell

As an example, consider the galvanic cell with zinc and copper electrodes of figure 4.1. It is energetically more favourable for the copper electrode to reduce and for the zinc electrode to oxidize. However, for these reactions to occur, electron exchange is needed. Because the electrolyte is electrically insulating, the electrons must pass through the external circuit as mentioned previously. By applying an external load, the circuit is closed such that the reactions can take place. The cell starts to discharge. Electrons flow from the anode to the cathode, such that current flows through the load. The two reactions are[58]:

$$\begin{cases} \text{Cathode:}\ \text{Reduction} = & \mathrm{Cu^{2+}(aq) + 2\,e^- \longrightarrow Cu(s)} \\ \text{Anode:}\quad \text{Oxidation} = & \mathrm{Zn(s) \longrightarrow Zn^{2+}(aq) + 2\,e^-} \end{cases} \tag{4.1}$$

As the electrons flow from anode to cathode, the anode is the negative pole of the battery and the cathode is the positive pole. The overall reaction can be written as

$$\mathrm{Zn(s) + Cu^{2+}(aq) \longrightarrow Zn^{2+}(aq) + Cu(s)} \tag{4.2}$$

In a rechargeable battery, the reaction can be inverted by applying an external power supply. This causes the potential inside the battery to be shifted, so that it is energetically more favourable for the inverse reactions to happen. The battery is charged and the two half-cell reactions become

$$\begin{cases} \text{Cathode:}\ \text{Reduction} = & \mathrm{Zn^{2+}(aq) + 2\,e^- \longrightarrow Zn(s)} \\ \text{Anode:}\quad \text{Oxidation} = & \mathrm{Cu(s) \longrightarrow Cu^{2}(aq)^{+} + 2\,e^-} \end{cases} \tag{4.3}$$

The material that undergoes oxidation in the discharging mode will be reduced when the cell is charged and vice versa, rendering the process reversible.

The current corresponding with transfer of charges as a result of an electrochemical reaction is called faradaic current. Non-faradaic current is the background current associated with movement of electrolyte ions, reorientation of solvent dipoles, adsorption at the interface, charging of the double layer, etc. This current is not caused by redox reactions. The presence of non-faradaic currents is often small enough or of no importance for the functionality of the electrochemical cell. In these cases, the non-faradaic component of the current can be neglected and one assumes that the total amount of current is caused by chemical reactions.

Fuel cells

A fuel cell is a galvanic cell where the active material is not a part of the cell, as is the case for batteries[56]. In a fuel cell, the active materials, which undergo oxidation and reduction, are fed to the electrodes when energy production is required. Chemical energy is irreversibly transformed to electrical energy in fuel cells, in contrast to the reversible transformation in a rechargeable battery, as for the Cu/Zn example discussed above. The active materials of fuel cells are generally liquids or gases. A lot of research is carried out for development of electric vehicles with fuel cell technology, often with H_2 as fuel.

4.1.2 Electrochemical potential

The cell potential of an electrochemical cell is the difference between the potential of both electrodes[60]. Since two electrodes are needed to measure the potential of a cell, the potential of a single electrode cannot be defined independently. Therefore, reference electrodes are used. The potential of the standard hydrogen electrode (SHE, as discussed in paragraph 4.1.2) is defined as zero for all temperatures. This allows to determine a specific value for the relative potential of other electrodes with respect to the SHE, i.e. the standard electrode potential (E°) in standard conditions. An electrode is at standard conditions when all solutes have a concentration of 1 mol/l and gases are at a pressure of 1 atm[61]. Once the standard electrode potentials of the two electrodes are known, the cell potential is determined by

$$\Delta\phi^\circ = E^\circ{}_{cathode} - E^\circ{}_{anode} \tag{4.4}$$

Thus, by measuring the cell potential of a cell in standard conditions with SHE as the anode, one can determine E° of the cathode. Values of E° are tabulated for many electrodes, usually determined at 25 °C. The standard cell potential is related to the change in the standard free enthalpy of the reaction, $\Delta_r G^\circ$[61].

$$\Delta\phi^\circ = -\frac{\Delta_r G^\circ}{nF} \tag{4.5}$$

In this equation, n is the number of electrons transferred in the cell reaction and F is the constant of Faraday. When the system is not in standard conditions, equation 4.5 remains valid

$$\Delta\phi = -\frac{\Delta_r G}{nF} \tag{4.6}$$

The Gibb's free energy of the reaction ($\Delta_r G$) is related to the standard free enthalpy according to equation 4.7, where Q is the reaction quotient, R is the universal gas constant and T is the temperature.

$$\Delta_r G = \Delta_r G^\circ + RT \ln Q \tag{4.7}$$

This allows to express the cell potential of an electrochemical cell which is not in standard conditions in terms of the standard cell potential and Q. This equation is known as the Nernst equation[61].

$$\Delta\phi = \Delta\phi^{\circ} - \frac{RT}{nF}\ln Q \tag{4.8}$$

Reference electrodes

In literature, different kind of reference electrodes are used. Next to the SHE, the most frequently used are the Ag/AgCl electrode and the Standard Calomel Electrode (SCE)[62]. In lithium-ion battery applications, Li/Li^+ is often used to directly evaluate the potential for lithium insertion/extraction reactions. The standard electrode potential for Li/Li^+ is -3.040V vs SHE, corresponding to -3.257V vs. Ag/AgCl[63].

Standard hydrogen electrode

As mentioned before, the standard electrode potential E° of SHE is declared to be zero at all temperatures. The half-cell reaction is:

$$2\,H^+(aq) + 2\,e^- \rightleftharpoons H_2(g) \tag{4.9}$$

For this reaction, hydrogen gas is bubbled through an acidic solution containing a platinum electrode. The pressure of the hydrogen gas is 1 bar and the activity of the ions is unity. However, as this electrode is inconvenient to use, other reference electrodes are not uncommon.

Saturated calomel electrode

The saturated calomel electrode (SCE) is based on the reaction between mercury (Hg) and calomel (Hg_2Cl_2). The half-cell reaction is

$$Hg_2Cl_2(s) + 2\,e^- \rightleftharpoons 2\,Hg(l) + 2\,Cl^-(aq) \tag{4.10}$$

The potential of this electrode is determined by the activity of the Cl^- ions in the solution. When the concentration of Cl^- is fixed by the solubility of KCl, one speaks of the saturated calomel electrode. The electrode potential of SCE at 25 °C is 0.244 V[63].

Ag/AgCl

A silver chloride electrode is often used as reference electrode. The overall reaction can be written as

$$AgCl(s) + e^- \longrightarrow Ag(s) + Cl^- \tag{4.11}$$

The electrode potential is dependent on the activity of the Cl^-, as was the case for the SCE. In a solution of 1 mol/kg KCl, the standard electrode potential E° of Ag/AgCl is 0.235 V[63]. The Nernst equation yields E° for different activities of Cl^-.

4.1.3 Battery characteristics

The main characteristics used in battery research are listed below.

Capacity

The capacity of a battery expresses the amount of charge that can be produced or stored by the battery. The charge is calculated by integrating the current with respect to time. The capacity of a battery is usually expressed in coulomb (C = A.s) or ampere-hour (A.h), where one ampere hour equals the charge delivered by a current of 1 A during 1 h, which is 3600 Coulomb. The capacity of a battery is often dependent on the discharge current. A larger current will correspond with a lower capacity due to blocking effects of a fully charged top-layer and diffusion limits[5].The degree of correlation between capacity and current density is expressed by the 'rate capability'. Materials with good rate capability show almost no loss of capacity when the current increases. The capacity of an electrode of a Li-ion battery, which is determined by the amount of lithium ions that can be inserted in the electrode (see 4.2) is often expressed in terms of the gravimetric capacity. This is the capacity per unit mass, expressed in Ah/g. In thin-film battery research, the volumetric capacity (capacity per volume, Ah/l) or area capacity (capacity per unit of surface area, Ah/cm^2) are most often used.

Cell Potential

The cell potential of a battery is the potential of the electrochemical cell, as explained in-depth above. When multiple galvanic cells are connected in series, the cell potential of the entire battery is the sum of the individual potentials.

Stored energy

The energy stored in a battery is given by the capacity times the cell potential, $E = Q.V$ and is expressed in watt-hours (W.h). The specific energy or gravimetric energy density is defined as the energy per unit mass and is expressed in Wh/kg. The volumetric energy density expresses the energy stored by a battery in comparison to its volume and is expressed in Wh/l.

Charge rate

The charge rate (C) of the charging or discharging current gives information about the time required to fully charge or discharge the battery. A C-rate of 1C signifies that it takes 1 hour to charge the battery to full capacity. For 2C, the battery can be charged twice during one hour. As an example, a battery with a capacity of 1.5 Ah will charge at 1C under a current of 1.5 A or at 2C under a current of 3 A.

Cycle life

The cycle life of a battery is defined as the number of cycles before the capacity fades to a certain percentage of the original capacity. 80% is often used as threshold to describe the cycle life.

Shelf life

The shelf life of a battery is governed by self-discharge reactions, which occur in most batteries. Shelf life is typically expressed in % capacity loss per month.

4.2 The lithium-ion battery

Rechargeable lithium ion batteries use a reversible insertion and extraction of lithium ions into the 2 electrode materials[53]. Lithium has a very high energy density, which makes it one of the most interesting materials for battery applications. The high mobility and small size of the lithium ions ensure that they can diffuse through most materials relatively easy.

4.2.1 Lithium-ion battery electrodes

In commercial batteries, the anode often consists of graphite[64]. This material has a good energy density and low cost. Lithium Titanate (LTO), hard carbon and TiN/Cobalt alloys are investigated as alternative anode material[53], mostly for increasing cell capacity and cycle life. The cathode material is in most cases a transition metal oxide, such as $LiCoO_2$ (commercially used[65]), $LiMn_2O_4$ or $LiFePO_4$[66].

Table 4.1: Specific capacity and work potential of commercially used electrode materials, data from[3,67,68].

Material	Work potential (V vs. Li/Li^{+}+)	Specific capacity (mAh/g)
Anode		
Graphite	0.2	372
Silicon	0.5	4200
Cathode		
$LiCoO_2$	3.9	140
$LiNi_{0.8}Co_{0.15}Al_{0.05}O_2$ (NCA)	3.8	180-200
$LiNi_{1/3}Co_{1/3}Mn_{1/3}O_2$ (NMC)	3.8	160-170
$LiMn_2O_5$ (LMO)	4.1	100-120
$LiFePO_4$ (LFP)	3.45	150-170

Energy is produced by the flow of lithium ions through the cell, which is accompanied by a flow of electrons in the external circuit. Figure 4.2 displays a schematical representation of a Li-ion battery with carbon anode and $LiCoO_2$ cathode[5]. If this cell is discharging, Li ions are extracted from the graphite and intercalate into the $LiCoO_2$. If the cell is being charged, the reversed process occurs. The two half-cell reactions of this Li-ion battery are[5]:

$$\begin{aligned} LiCoO_2 &\rightleftharpoons Li_{1-x}CoO_2 + xLi^{+} + xe^{-} \\ xLi^{+} + xe^{-} + C_6 &\rightleftharpoons Li_xC_6 \end{aligned} \tag{4.12}$$

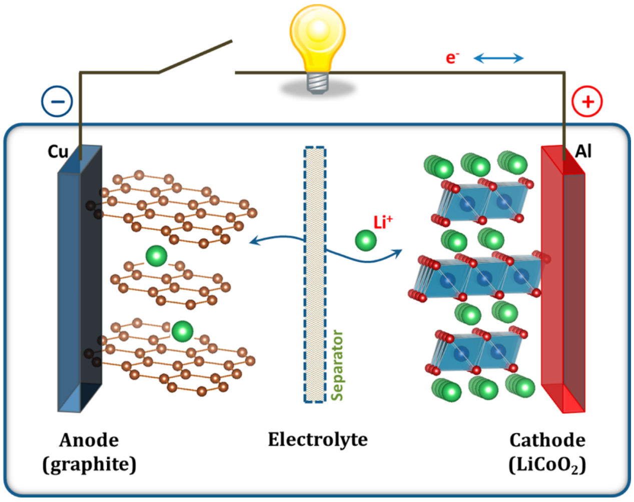

Figure 4.2: Illustration of the working principles of a lithium-ion battery (from[5]).

The open-circuit voltage V_{oc} of a lithium cell is given by the difference of the lithium chemical potential of cathode and anode[53].

$$V_{oc} = \frac{\mu_{Li(c)} - \mu_{Li(a)}}{F} \tag{4.13}$$

In this equation, $\mu_{Li(c)}$ and $\mu_{Li(a)}$ represent the chemical potentials involved and F is the constant of Faraday. The V_{oc} of the cell is influenced by the energy involved in both lithium and electron transfer.

4.2.2 The electrolyte of lithium-ion batteries

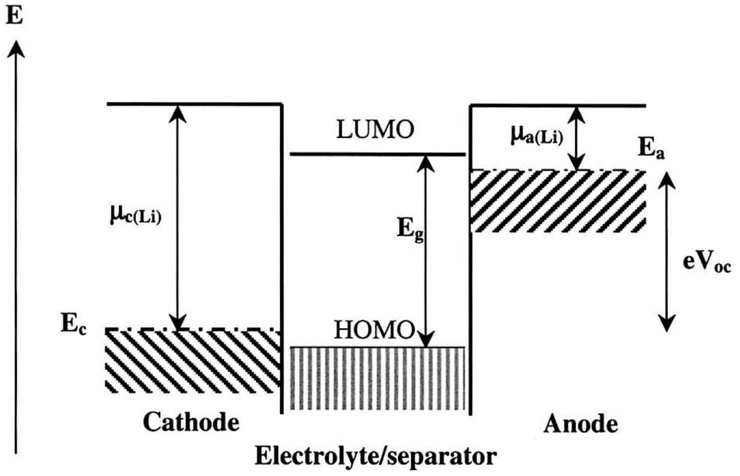

Figure 4.3: Schematic energy diagram of a lithium-ion battery at open circuit (from[53]).

The electrolyte is electronically insulating and simultaneously acts as a good ion conductor. To avoid unwanted side reactions of the electrolyte, the redox energies of cathode (E_c) and anode

(E_a) should lie within the electronic band gap of the electrolyte, defined by the difference between highest occupied molecular orbital (HOMO) and lowest unoccupied molecular orbital (LUMO). If this were not the case, electrons could flow between electrolyte and electrode. This is unwanted, since electrons should pass through the external circuit for battery applications. As a consequence, the cell voltage of the Li-ion battery is limited by the electrolyte. Luckily, multiple electrolytes have been developed for these types of applications, each with a respective stability window. Proper choice of electrolyte for the application at hand is of utmost importance.

4.2.3 Solid electrolyte interface

The solid electrolyte interface (SEI) is a passivating layer that is often formed on the surface of the electrode. Formation of SEI films has been associated with the decomposition of electrolyte components, both solvents and salts, as well as with unwanted side reactions with the electrodes. These degradation products react with Li^+ ions, which leads to the growth of lithium containing structures on top of the electrodes, such as Li_2O, LiF, Li_2CO_3, RCO_2Li, etc.[69]. Formation of the SEI layer consumes lithium ions, hence is responsible for an irreversible loss of capacity. The SEI layer has a small electronic conductivity and high ionic conductivity[70], though some lithium ions will be trapped in the layer when passing through. As a result, the SEI is less ideal than a real solid electrolyte.

In most Li-ion batteries, a graphite anode is being used because of the high capacity(372 mAh/g[3]), good cyclability and low potential. However, some disadvantages exist for graphite anodes. The graphite surface is catalytic for the decomposition of the electrolyte. Additionally, the decomposed electrolyte parts have the tendency to intercalate into the graphite, such that less Li ions can be stored and the graphite electrode is put under stress. Both negative effects on the performance of the battery are countered by the formation of a passivating SEI film on top of the graphite anode, which stabilizes the battery operation[71]. The SEI layer on cathode surfaces is less studied and hard to detect, but some reports indicate that a SEI layer must be present on cathode surfaces[72–74]. Finally, two negative effects of extreme temperatures of lithium-ion batteries can also be explained by the SEI. The reduced efficiency of batteries for low temperatures can be explained by low ionic conductivity through the SEI, while the lowered efficiency at high temperatures can be explained by the instability of the SEI[75].

4.3 Methods for electrochemical analysis

In electrochemistry, a chemical reaction, such as the intercalation of lithium into the lattice of an electrode is accompanied by electron transport through an external circuit. As a result, the external circuit can be controlled or measured to obtain information regarding the chemical reactions that are occurring. Three basic approaches are possible[76].

1. Measure the potential while controlling the current (galvanostatic technique)
2. Measure the current while controlling the potential (voltammetric technique)

3. Measuring the impedance by means of the response to an imposed signal at different frequencies

Although only three approaches exist, numerous electrochemical techniques are being used. The most important techniques are[62]:

- Potentiometry: methods without externally imposed potential
- Conductometry: methods based on measuring the electric conductivity
- Coulometry: methods for determination of amount of material consumed by measuring charge
- Voltammetry: methods based on the influence of applied potential on current
- Electrogravimetry: methods based on weight differences caused by electrochemical processes

The procedures applied on the vanadium oxide thin films will be discussed in detail in the following paragraphs.

4.3.1 Voltammetric methods

Methods based on control of the potential and measurement of the current are called voltammetric methods. Several types exist:

Linear sweep voltammetry

In linear sweep voltammetry, the applied potential is varied at a constant rate while the current is measured. A peak in the measured current at a given potential indicates the presence of an electrochemical reaction. Such a reaction starts at a given potential. When the potential is further increased, the driving force for the reaction gets stronger and the current increases. The current decreases again when the reaction is completed.

Cyclic Voltammetry

Cyclic voltammetry (CV) is strongly related to linear sweep voltammetry, as the potential is controlled externally and changes at a constant rate in both techniques. In cyclic voltammetry, the potential is varied back and forth in a linear way between two boundaries[77], see figure 4.4. Data from CV measurements is often presented in a current vs. potential plot, also called a cyclic voltammogram. If the sample undergoes a redox-reaction, an anodic and cathodic current peak will be measured. The anodic and cathodic peak are separated, according to equation 4.14, where n is the number of electrons transferred[62].

$$\Delta E_p = E_{pc} - E_{pa} = \frac{59 \pm 2mV}{n} \tag{4.14}$$

Multiple CV sweeps give an indication regarding the reversibility of the reaction. In reversible systems, the peak intensities and locations should be constant. Furthermore, the total charge related with the electrochemical reaction can be calculated by integration of the current as a function of time. Since the applied voltage is linearly dependent on time, the total charge is also proportional to the area under the current peaks in a cyclic voltammogram.

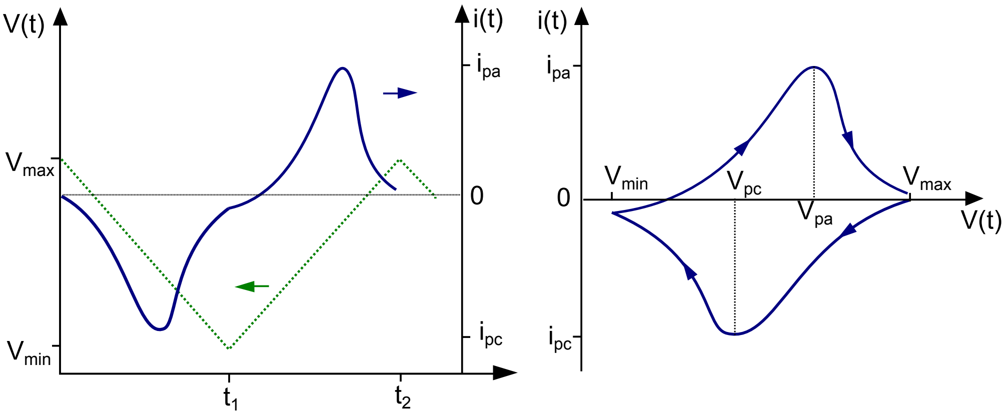

(a) **(b)**

Figure 4.4: In cyclic voltammetry, the potential (green) is applied and the current (blue) is measured (left), the result is often presented by means of a voltammogram (right).

4.3.2 Coulometric methods

In coulometric analysis, the total charge is measured to quantify the reaction in the cell under consideration[62]. For Li-ion battery applications, the total charge of a measurement yields information concerning the amount of intercalated lithium ions and thus the capacity of the battery. One distinguishes ‘controlled-potential coulometry’ and ‘controlled-current coulometry’, where respectively the change in potential (dV/dt) or the current remains constant. In this work, controlled-current coulometry was used. Techniques where current is constant over time are called galvanostatic techniques.

Galvanostatic charge/discharge

In galvanostatic charge/discharge (CD) analysis, a constant current is applied and the resulting potential is measured. When the current is applied, the potential quickly shifts to the value corresponding with the electrochemical reaction (such as intercalation of lithium ions). During the reaction, the potential remains approximately at this value. When this specific reaction finishes, because one of the products is fully depleted, the voltage will further rise or fall, depending on the sign of the applied current. The potential vs. time curve can be described by[62].

$$E = E_{\tau/4} + \frac{RT}{nF} \ln \frac{\tau^{1/2} - t1/2}{t^{(}1/2)} \tag{4.15}$$

In this equation, τ is the transition time of the reaction.

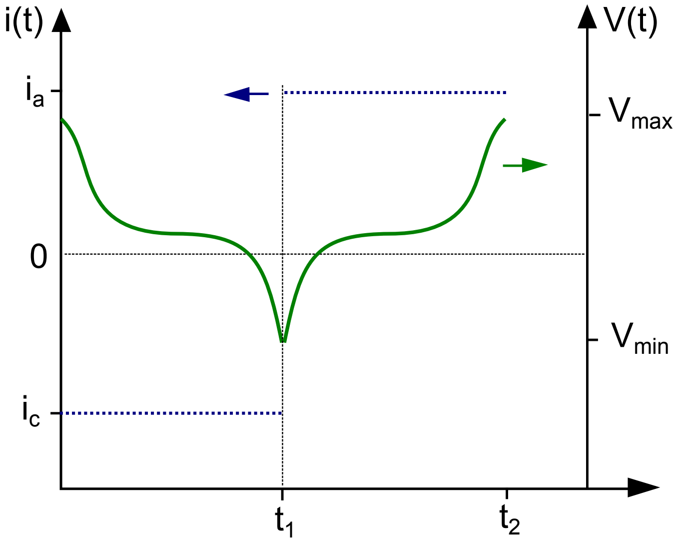

Figure 4.5: In a galvanostatic charge/discharge, a constant current is applied (blue) and the resulting potential is measured (green). If a transition occurs, a plateau is observed at the characteristic potential of the transition.

A galvanostatic charge/discharge measurement provides information regarding cell or electrode capacity and characteristic potential of the associated electrochemical reactions. The capacity is calculated by means of integrating the current over time until the reaction is finished or reaches a certain cut-off potential. As a constant current is applied during a CD measurement, the capacity is proportional to the required time. The characteristic potential of the electrochemical reactions can be identified by plateaus in the potential vs. time plot, as previously explained and visualised in figure 4.5. In a LIB, the insertion of lithium ions in an electrode host is the cathodic reaction. Thus by applying a negative current (until $t=t_1$ in figure 4.5), the battery is charged. The capacity associated with this reaction is the lithiation capacity of the electrode. A comparison between the capacity of lithiation and delithiation provides information about the coulombic efficiency of the electrode, namely the percentage of material left behind in the electrode or consumed by side reactions. The coulombic efficiency (η_c) is calculated with equation 4.16 where Q_{out} and Q_{in} are the capacities of the discharge and charge cycle[64].

$$\eta_c(\%) = \frac{Q_{out}}{Q_{in}} * 100 \tag{4.16}$$

Cyclability testing

In order to test the cyclability, several consecutive galvanostatic charge/discharge measurements are carried out at a fixed current and associated C-rate. The evolution of the total lithiation and delithiation capacity with regard to the number of cycles gives information concerning the cyclability behaviour of the cell.

4.3.3 Electric impedance spectroscopy

Electric impedance spectroscopy (EIS) is based on the measurement of the current response induced by a variable potential, consisting of a small AC signal superimposed to a DC-voltage[78]. More specifically, the influence of the frequency of the AC perturbation is examined. The applied potential can be decomposed as

$$E = E_{DC} + E_m \sin(\omega t) \tag{4.17}$$

Where $\omega = 2\pi\nu$ is the frequency of the perturbation imposed to the off-set potential (E_{DC}). The amplitude of the perturbation is E_m. The resulting current will be

$$I = I_{DC} + I_m \sin(\omega t + \phi) \tag{4.18}$$

The phase shift ϕ between potential and current contains physical meaning. For example, ϕ of a ideal resistor is equal to 0, while ϕ of a capacitor is $\pi/2$. Usually, current (I) and potential (E) will be described by phasors and the relation between these two phasors is described by the complex impedance (Z), which can be decomposed into a real (Z_R) and imaginary part (Z_I).

$$Z = \frac{E}{I} = Z_R + jZ_I \tag{4.19}$$

The results of an EIS experiment are usually presented in a Nyquist plot, where the real and imaginary part of the impedance are indicated for each frequency. The acquired data is fitted to an electric circuit, in which the components have physical meaning. The frequency response of the different components can be related to the time-scale of the physical processes. Thus, EIS allows to separate processes occurring at different time-scale. Since this technique was not used in this work, it is only discussed briefly. A more thorough discussion on this can be found in[78].

4.4 Experimental set-up for electrochemical measurements

The electrochemical measurements carried out in this work were performed with 2 Autolab potentiostat/galvanostat devices, manufactured by Metrohm, i.e. PGSTAT302N and PGSTAT204. Both were controlled by the software program 'Nova 1.10.4'. The Autolab devices control current or potential when they operate in galvanostatic or potentiostatic mode, respectively. The devices are connected to the sample under investigation with (maximum) 5 electrodes: working electrode (WE), counter electrode (CE), reference electrode (RE), sense electrode (S), ground connection[79].

- WE: electrode on which reaction of interest is occurring.
- CE: electrode used to close the current circuit. This electrode does not participate in the reaction.
- RE: has a stable and well known electrode potential and is used as point of reference to control and measure the potential in the cell.
- S: Only used in four-electrode set-up when the potential difference in a well defined interface needs to be measured. In other connection modes, the sense electrode is connected to the WE.

4.4.1 Connection modes of the Autolab devices

Different ways exist to connect the Autolab device to the electrochemical cell. One distinguishes two-electrode, three-electrode and four-electrode set-up.

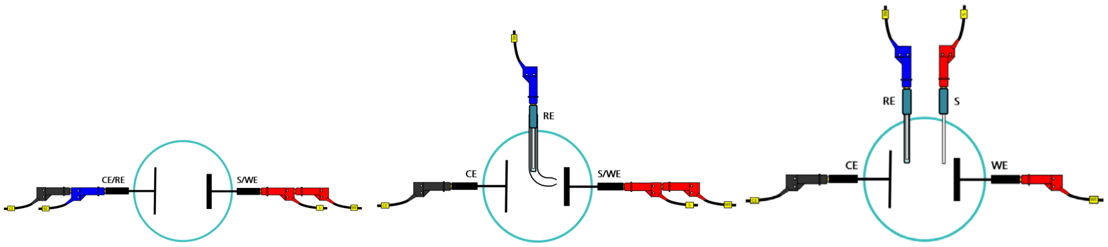

(a) 2 electrodes **(b)** 3 electrodes **(c)** 4 electrodes

Figure 4.6: Representation of different connection modes of the Autolab devices with 2, 3 and 4 electrodes (from[79]).

The two-electrode set-up is used when the behaviour of the entire cell is under investigation. In this case, the WE and the S are joined together and connected to one electrode of the electrochemical cell. The other electrode is connected with the RE and CE, see figure 4.6a. This allows measurement of current through and potential over the entire cell, such that influences of both electrodes and electrolyte are taken into account.

In the three-electrode set-up, the focus is on the processes concerning one electrode. The WE and S are connected to the electrode under investigation. The CE is connected to the second electrode of the electrochemical cell. The RE is separated from the CE, see figure 4.6b. In practice, the electrochemical cell has a third electrode, which is spatially close to the WE by means of a Luggin cappilary, such that the potential drop over the electrolyte is excluded from the measurement. The third electrode lies outside of the current path, as current flows from WE/S to CE, in order to allow precise potential measurements. When examining the application of VO_x thin films as electrodes for Li-ion batteries, the focus is clearlyte on the working electrode alone. Effects of electrolyte and reference electrode are not of interest. Therefore, the three-electrode set-up is used in this work.

The four-electrode set-up is used when one is specifically interested in a given interface. In this case, S is separated from WE.

4.4.2 Preparation of the electrochemical test cell

In the next chapter, the behaviour of the various vanadium oxides as electrode material for lithium-ion batteries is discussed. To measure the samples, a PTFE (teflon) test cell is used, schematically illustrated in figure 4.7.

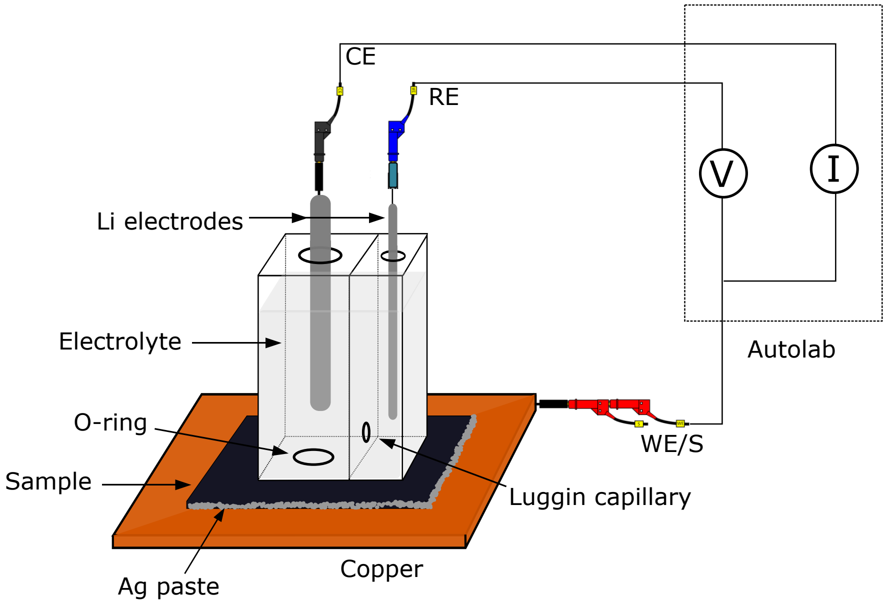

Figure 4.7: Schematic illustration of the electrochemical test cell, used for examining vanadium oxide thin films as electrode material for Li-ion batteries.

To assemble the electrochemical test cell, the following steps are performed:

1. The sample is placed on a conductive copper sheet
2. The edges of the sample are coated with a conductive silver paste. The examined thin films were deposited on top of a conducting layer during deposition, i.e. the platinum-substrate. The silver paste at the edges guarantees an electronically conducting path between the thin film and the copper sheet underneath.
3. The teflon body of the cell is tightly screwed on top of the copper sheet and sample. A rubber O-ring assures that the connection is leak-tight. The area of the sample under investigation is 0.9503 cm^2.
4. The cell is placed in an argon-filled glovebox ($H_2O < 1$ ppm; $O_2 < 1$ ppm), since the lithium electrodes and the electrolyte solvents are very sensitive to oxygen and water.
5. The teflon body is filled with electrolyte, more specifically 1M $LiClO_4$ in PC solvent, 99% pure from io-li-tec.
6. Two lithium electrodes, 99,9 % lithium ribbon from Sigma-Aldrich, are partially submerged into the electrolyte.
7. The electrodes of the Autolab device are connected with the cell. The WE/S is contacted with the copper sheet. The CE and RE are each connected with a separate lithium electrode, according to the tree-electrode set-up.

4.4.3 Standard testing procedures

Three standard procedures were carried out on all vanadium oxides.

- Cyclic Voltammetry, as a first indication of occurring reactions and their characteristic potential and capacity, as well as a first indication of the reversibility of the reactions within the region of interest.

- Galvanostatic charge/discharge to investigate the total charge/discharge capacity and voltage profiles at different C-rates, more specifically at currents of 1C, 2C, 5C, 20C and 50C. Determination of the required current densities for these C-rates was based on estimations of the capacity, obtained from the CV measurements. The actual C-rates of the CD measurements will be slightly different, since the capacity estimations obtained from CV are slightly inaccurate.
- Cyclability test: 50 cycles of galvanostatic charge/discharge at a C-rate of approximately 2C to test the reversibility of the processes. A C-rate of 2C was chosen so that the experiments would not outlast the limited amount of time available for this work. 50 cycles at 2C adds up to a little over 2 days per experiment. However, one has to take into account that, at a C-rate of 2C, the cell is not charged to its total capacity (as will be shown from the galvanostatic charge/discharge experiments), thus not straining the electrodes to the limits of their capabilities. Nevertheless, this will give a clear indication of their cycling capabilities, especially in a comparative study like this.

5 Thin vanadium oxide films as electrode for lithium-ion batteries

Thin films of amorphous vanadium oxide were deposited using ALD on Pt, TiN and SiO_2 substrates. Annealing of these thin films in an atmosphere with controlled oxygen partial pressure allowed formation of 6 different phases: VO_2(B), VO_2(R) (transforms to VO_2(M1) at 67 °C), V_2O_5, V_3O_7, V_4O_9 and V_6O_{13}. These six oxides are investigated with regard to application in lithium-ion batteries. For this application, a conductive layer is required underneath the VO_x film for efficient current collection, because of the low conductivity of vanadium oxide. Therefore, the films deposited on the Pt substrate will be treated in this chapter.

Earlier studies showed that vanadium oxides showed promise as cathode material in LIB. The next paragraph contains a summary of these studies.

5.1 Literature concerning vanadium oxides as electrode

Vanadium oxides have been investigated intensively as cathode material for LIB, since they combine the advantages of low cost, abundance and easy synthesis[9]. In addition, some vanadium oxides are known to have a higher energy density than typical commercial cathode materials[80].

The oxides with general formula V_nO_{2n+1} are related to each other since they are all shear structures derived from a hypothetical VO_3 with the ReO3 structure[17]. Characteristic for the entire series is the presence of distorted VO_6 octahedra, which result in promising electrochemical capacities[66]. The shear structure of VO_2(B) contains one dimensional monotunnels, in which lithium ions can be inserted. Apart from VO_2(B), V_2O_5 and V_6O_{13} were studied thoroughly. Few reports are available for V_3O_7, V_4O_9 and VO_2(M1). Christian et al. describes that cells with V_3O_7 and V_4O_9 cathodes were synthesised, but showed poor rechargeability[81].

Disadvantages of most vanadium oxides for application as cathode are low conductivity and capacity loss upon cycling[9]. The poor cycling behaviour could be caused by abrupt volume changes upon intercalation of lithium[82].

5.1.1 The $Li_xV_2O_5$ system

V_2O_5 is the most widely studied vanadium oxide for the purpose of intercalation host in LIB. Unlike other vanadium oxides, some theoretical studies exist regarding the deformation of the lattice structure of V_2O_5 upon insertion of lithium. Whittingham was the first to study the transformation of the V_2O_5 lattice at room temperature[83]. He concluded that reversibility was optimized when no chemical bonds are broken. Murphy et al.[84] and Dickens et al.[85] simultaneously performed a general study of the $Li_xV_2O_5$system ($0 \leqslant x \leqslant 1$). As their studies indicated that V_2O_5 could be very promising for rechargeable lithium ion batteries, a lot of research was devoted to the $Li_xV_2O_5$ system. Delmas et al. published an overview of the structure modifications induced in the V_2O_5 lattice by intercalation of lithium ions[11].

Different phases in the $Li_xV_2O_5$ system

Depending on the amount of lithium inserted into V_2O_5, five domains were distinguished at room temperature[86].

- α-LiV_2O_5 = $Li_xV_2O_5$ with $x \leqslant 0.01$
- ϵ-LiV_2O_5 = $Li_xV_2O_5$ with $0.35 \leqslant x \leqslant 0.7$
- δ-LiV_2O_5 = $Li_xV_2O_5$ with $0.9 \leqslant x \leqslant 1$
- γ-LiV_2O_5 = $Li_xV_2O_5$ with $x \leqslant 2$
- ω-LiV_2O_5 = $Li_xV_2O_5$ with $x \leqslant 3$

For lithium intercalation between 0.01 and 0.35 Li per V_2O_5, the α and ϵ phases coexist. A similar region exists for coexistence of ϵ-LiV_2O_5 and δ-LiV_2O_5 for x-values between 0.70 and 0.90 of $Li_xV_2O_5$. The structure of δ-LiV_2O_5 has been determined by neutron diffraction and is displayed in figure 5.1.

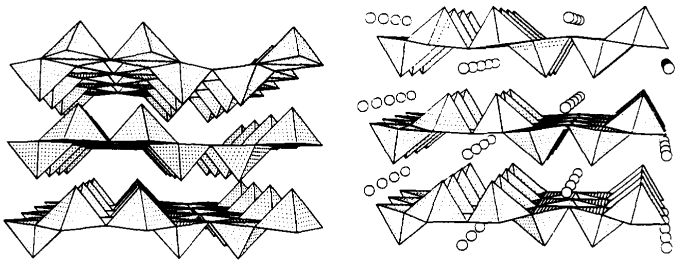

(a) V_2O_5 **(b)** δ-LiV_2O_5

Figure 5.1: The structure of V_2O_5 and δ-LiV_2O_5 containing 1 Lithium per V_2O_5 (from[11]).

The α and ϵ phases are similar to δ-V_2O_5, but those structures are slightly less deformed compared to δ-V_2O_5 as they possess a lower amount of intercalated lithium. Figure 5.1 illustrates that the formation of δ-LiV_2O_5 does not require breaking of chemical bonds. Therefore, the transitions α-ϵ and ϵ-δ are fully reversible, as a consequence V_2O_5 can be cycled in the α-ϵ-δ region without loss of capacity. The reactions α-ϵ and ϵ-δ occur at -0.14 and -0.29 vs. Ag^+/Ag[86], corresponding to 3.69 and 3.54 V vs. Li/Li^+ (the potential of Ag^+/Ag is 3.83 V vs. Li/Li^+). The characteristic pyramids in the α-ϵ-δ structure are oriented in an up-up-down-down fashion, see figure 5.1.

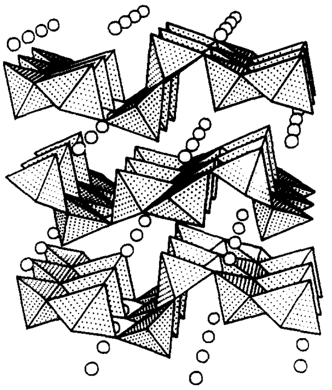

Figure 5.2: Illustration of the deformed lattice of γ-V_2O_5 (from[11]).

When a lower potential is applied, the driving force of lithium intercalation is strong enough to break chemical bonds in the V_2O_5 lattice. The orientation of the characteristic pyramids changes to up-down-up-down, see figure 5.2. This allows more lithium ions to be absorbed into the lattice, up to 2 lithium ions per V_2O_5, resulting in formation of γ-LiV_2O_5. As breaking of bonds is required, the δ-γ transition is not reversible. The γ-phase is formed at -1.30 V vs. Ag^+/Ag or 2.53 V vs. Li/Li^+[86].

The final phase in the $Li_xV_2O_5$-system is obtained when the potential is lowered below 2V vs. Li/Li+. The irreversible ω-$Li_xV_2O_5$ structure is formed. During the first charge, 3 lithium ions are intercalated. Afterwards, this structure allows cycling between $Li_{0.40}V_2O_5$ and $Li_{2.65}V_2O_5$[87]. Figure 5.3 illustrates all transitions in the $Li_xV_2O_5$-system.

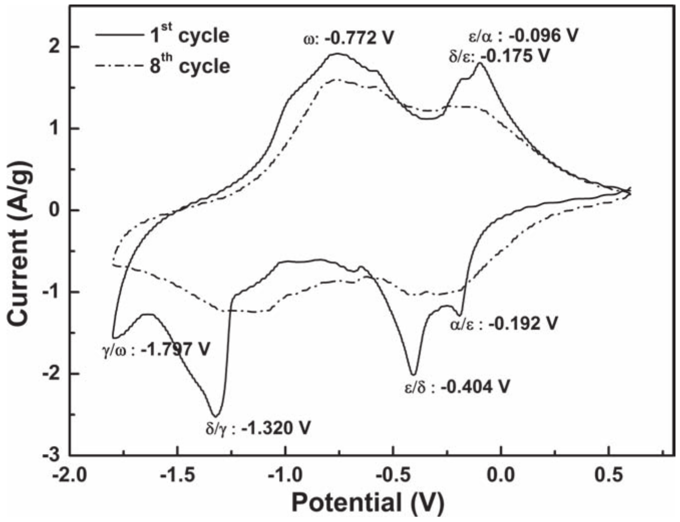

Figure 5.3: Example of a cyclic voltammetry measurement on V_2O_5, demonstrating the different phases in the $Li_xV_2O_5$-system, with potential given vs. Ag^+/Ag (from[86]).

For this work, three options for V_2O_5 as electrode in rechargeable lithium-ion batteries will be considered. The first option consists of charging and discharging within the reversible α-ϵ-δ-phases, with intercalation of up to 1 lithium per V_2O_5. Other options are the irreversible transitions to γ-

or ω-LiV_2O_5, with consecutive cycling within those phases. These three options will be investigated further on the thin vanadium films in paragraph 5.2.2.

5.1.2 Research concerning other VO_x as electrode material

The influence of lithium insertion on the lattices of the other vanadium oxides that are treated in this work have not been subject to in depth research as V_2O_5. As a consequence, no detailed information with respect to the modifications of the lattice structure are available. However, several experimental studies have been carried out for VO_2(B), V_6O_{13} and $V_3O_7 \cdot H_2O$.

V_6O_{13} was the second of the vanadium oxides to be studied as lithium intercalation host for battery applications by Murphy et al. in 1979[88]. They also investigated non-stoichiometric V_6O_{13+y}[89]. The conclusion of this research was that both V_6O_{13} and V_6O_{13+y} are very promising for use as electrode in LIB. West et al.[90] discovered that the insertion of non-stoichiometric V_6O_{13+y} was restricted to the number of electronic sites and mentions a volume expansion upon lithiation of 10% for V_6O_{13+y}. For V_6O_{13}, a volume expansion of 15%[91] is reported and a quite severe capacity loss was observed during the first few cycles[18]. Because of this, the interest in V_6O_{13} has decreased in the last decades and not much studies have been performed lately. A CV measurement of V_6O_{13} can be seen in figure 5.4.

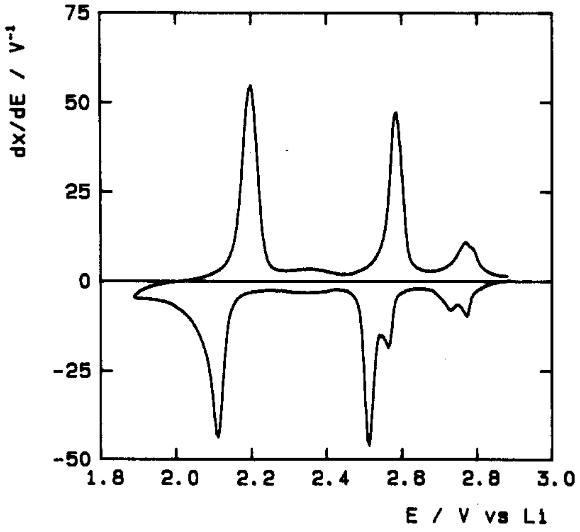

Figure 5.4: Cyclic voltammetry measurement on V_6O_{13}, performed by West et al.[18].

Recent studies regarding vanadium oxides focus on nanostructures of VO_2(B) and $V_3O_7 \cdot H_2O$, although the most stable oxide V_2O_5, remains popular for investigation. Various methods have been discovered for synthesis of nanostructured materials of VO_2(B) and $V_3O_7 \cdot H_2O$. An example of a hydrothermal method, used by Ganganagappa et al. is based on a reaction between V_2O_5 and quinol[92].

$$V_2O_5 + C_6H_6O_2 + H_2O \longrightarrow 2VO_2(B) + C_6H_4O_2 + 2H_2O \tag{5.1}$$

VO_2(B) is formed after a hydrothermal treatment at 180 ° C for 1 day. Several similar processes exist, allowing easy synthesis of vanadium oxide structures. Manthiram et al. reports that the method of synthesis influences the capacity of VO_2(B)[17]. By reduction in a solution, nanocrystalline VO_2(B) can be obtained, containing monodimensional tunnels in which 0.9 Li/V can be absorbed (290mAh/g). For thermally prepared VO2(B), the insertion is limited to 0.5 Li/V (161 mAh/g).

The oxidation/reduction peak of VO_2(B) can be found at approximately 2.6 V vs. Li/Li^+. For $V_3O_7 \cdot H_2O$, the electrochemical reaction occurs around 3.7 V vs. Li/Li^+. The result of a CV measurement on VO_2(B) and $V_3O_7 \cdot H_2O$ is displayed in figure 5.5. Both electrodes demonstrate good cyclability behaviour.

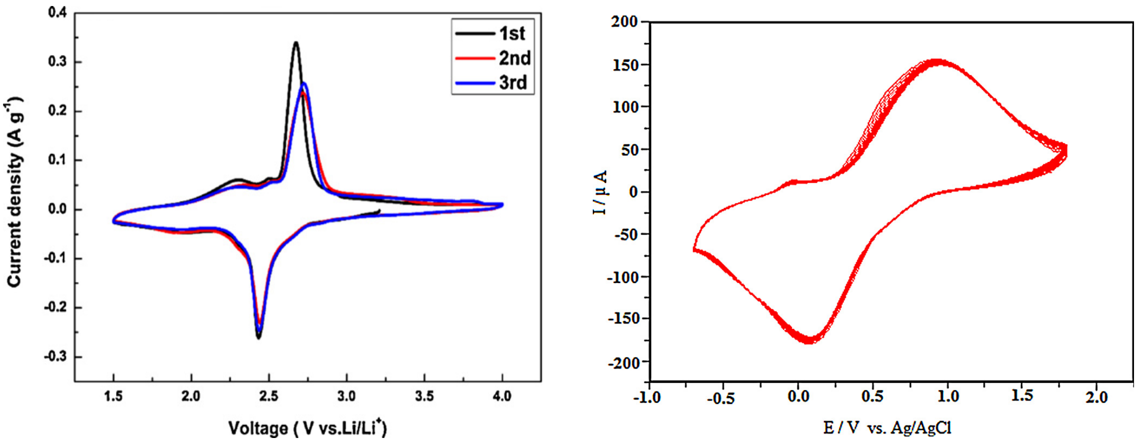

(a) VO_2(B) **(b)** V_3O_7

Figure 5.5: Example of CV measurement on VO_2(B) (left, from[93]) and $V_3O_7 \cdot H_2O$ (right, from[94]) nanostructured electrodes.

5.1.3 Comparison of capacity of vanadium oxide electrodes

Table 5.1: Non-exhaustive overview of literature concerning vanadium oxides as LIB electrode, the cycle number for the gravimetric capacity is indicated between brackets if multiple values were reported.

Authors	**Working electrode**	**Electro-lyte**	**Gravimetric capacity (mAh/g)**	**Deposition technique**	**Structure design**	**charge rate**
Pan et al.[95]	V_2O_5	$LiPF_6$	267	Solvoth. method	Micro flowers	-
Leger et al.[87]	80% V_2O_5 7.5% graphite 7.5% AB	$LiClO_4$	310	Sol-gel		C/20
Liu et al.[86]	V_2O_5	$LiClO_4$	402 (1^{st}) 240 (180^{th})	Cath. dep. sol-gel		1.3 C
Chou et al.[80]	V_2O_5	$LiNTf_2$	430 (1^{st}) 270 (50^{th})	Hydroth. method	Nano ribbons	2 C

Armstrong et al.[96]	75% VO_2(B) 18% CB 7.5% binder	$LiPF_6$ LiBOBO	265	Chemical method	Nano-wires	50 mA/g
Zhao et al.[93]	80% VO_2(B), 15% AB 5% PVDF	$LiPF_6$	218 (1^{st}) 152 (100^{th})	Hydroth. method	Nano-belts	50 mA/g
Rui et al.[97]	70% VO_2(B) 20% CB 10% PVDF	$LiPF_6$	160	One-pot synthesis	Nano-belts	200 mA/g
Gangana-gappa et al.[92]	70% VO_2(B) 20% AB 10% PVDF	$LiPF_6$	171 (1^{st}) 108 (47^{th})	Hydroth. method	Nano-rods	0.1 mA/g
Rahman et al.[98]	VO_2(B) on CNT	$LiPF_6$	177	Hydroth. process	MW-CNT	1C
Milosevic et al.[99]	85% VO_2(B) 10% CB 5% PVDF	$LiNO_3$	184	Solovoth. method	Snow-flake particles	-
Gao et al.[100]	$V_3O_7 \cdot H_2O$	$LiClO_4$	403 (1^{st}) 211 (30^{th})	Hydroth. route	Nano belts	20 mA/g
Qiao et al.[101]	60% $V_3O_7 \cdot H_2O$ 20% AB 20% teflon	$LiClO_4$	253 (1^{st}) 228 (50^{th})	Hydroth. treatment	Nano-belts	30 mA/g
Saidi et al.[102]	V_6O_{13}	$LiPF_6$	310	Thermal decomp.	-	0.25 mA/cm^2

Table 5.1 contains a non-exhaustive overview of experiments on vanadium oxides as electrode material. However, one must be careful to directly compare capacities between experiments, as the value of the capacity depends on the applied charge/discharge current and the cycle number as well as the structure of the material. On top of that, the electrolyte can have an influence. Cohen et al. demonstrated that better results are obtained with $LiClO_4$ than with $LiPF_6$[103]. The latter can react with hydrogen by formation of HF, which is a strong acid and reacts with the electrode. In many cases, the working electrode does not consist purely of the material under investigation. This is because the conductivity of the vanadium oxide is too low. In such cases, VO_x is mixed with an electric conductor and a binder. For the conductor, graphite, acethylene black or other carbon containing materials are often used. As binder, PVDF is the most commonly used material. In table 5.1, acethylene black and carbon black are abbreviated as AB and CB.

Table 5.1 illustrates that much research has been carried out on V_2O_5 and VO_2(B). Recent studies are focused on nanostructured materials, often synthesised with hydrothermal methods. Research of nanostructured $V_3O_7 \cdot H_2O$ is carried out in several studies as well, though pure V_3O_7 is only mentioned rarely. No studies have been found were gravimetric capacity values are given for V_4O_9 and pure form V_3O_7.

Furthermore, the overview of table 5.1 shows that a considerate loss of capacity upon cycling is observed for the vanadium oxide electrodes. If the capacity of several cycles is given, a loss of 30% to 50% is found. An exception is the report of Qiao et al., where the loss in capacity is limited to 10% after 50 cycles.

5.2 Electrochemical properties of VO_x

Chapter 3 discussed the deposition of vanadium oxide films by a water and ozone based ALD process. Post-deposition annealing in an atmosphere with varying oxygen concentration lead to formation of 6 oxides. All 6 oxides will be tested by means of three standard electrochemical procedures to compare them as potential electrode material for lithium-ion batteries.

First, a cyclic voltammetry measurement is performed, with a scan rate of 10 mV/s. Ten cycles are carried out, in order to obtain some information regarding reversibility. The results of the CV measurement can be used to calculate the charge associated with the occurring electrochemical reactions. This allows to estimate the current required for a charge and discharge rate of 1C. The second procedure is a galvanostatic charge/discharge, at current rates of approximately 1C, 2C, 5C, 20C and 50C. The actual C-rate will be slightly different, since the CV estimates for the total charge are not entirely accurate. The third procedure tests the cyclability of the sample, by means of 50 cycles of galvanostatic charge/discharge at approximately 2C. The loss of capacity within the first few cycles is often important, therefore a new sample was synthesized for the cyclability experiment. The electrochemical methods are discussed in detail in paragraph 4.3.

In both the CD and cyclability experiments, a constant current is applied. The capacity, associated with the occurring reactions, is calculated by integrating the charge with respect to time. In this work, the gravimetric capacity and the capacity per surface area will be presented. To calculate the gravimetric capacity, the mass of the film is required. As the density of the different oxides is known and the surface of the sample under investigation is constant (determined by the test cell: 0.9503 cm^2), the mass can be calculated once the thickness of the film is known. For the amorphous films, the thickness is obtained by the XRR-XRF relation, as described in paragraph 3.3.3. However, when the film is annealed, volume expansion will take place because oxygen is absorbed. The volume expansion upon annealing is determined for a VO_2 film deposited by the O_3 process to V_2O_5 by cross SEM images. An expansion of 20% was observed. This estimation will be used for all V_2O_5 films and for V_3O_7, since no clear thickness could be determined by cross SEM on V_3O_7. For the other samples, the film thickness was obtained by cross SEM images.

5.2.1 As deposited amorphous vanadium oxide films

The as deposited amorphous layers are examined first. Figure 5.6 shows the results of CV measurements on the vanadium oxide thin films, deposited with the H_2O or O_3 process. The cyclic voltammograms of both films are not identical, which indicates that differences between the two films exist. The film deposited with the ozone based process contains a reduction peak at 2.40 V vs. Li/Li^+, which is not present in the film deposited by the H_2O process. The location of this peak is identical to the location of the reduction peak of VO_2(B), which will be discussed in paragraph 5.2.3. This indicates that the structure of the as deposited film by the O_3 process strongly resembles VO_2(B), such that the same interstitial locations are available, giving rise to a typical reduction peak at 2.5 V. This is not surprising as the amorphous films of the O_3 process tend to crystallize into VO_2(B) in an atmosphere with low oxygen content. As the H_2O based film does not show a peak at 2.5 V, its structure probably contains more differences with respect to VO_2(B), which could be expected as these films crystallize into VO_2(M1).

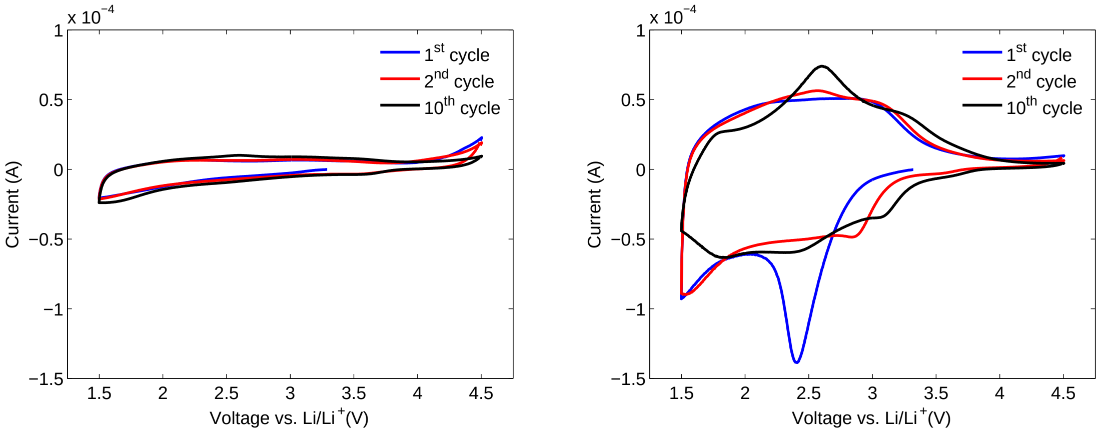

(a) H_2O **(b)** O_3

Figure 5.6: Cyclic Voltammetry (CV) of amorphous vanadium oxide thin film, deposited with H_2O and O_3 processes at a rate of 10 mV/s.

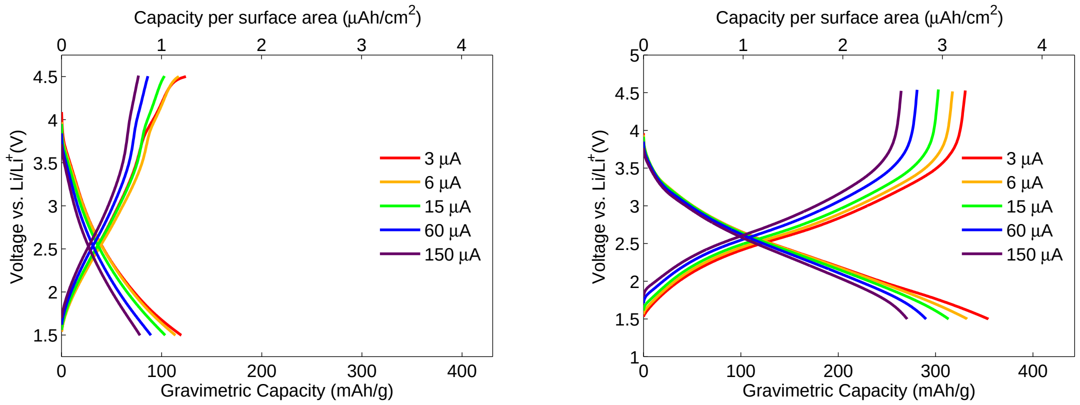

(a) H_2O: 3 μA = 2.70 C **(b)** O_3: 3 μA = 0.85 C

Figure 5.7: Galvanostatic charge/discharge (CD) measurement of amorphous vanadium oxide, deposited with H_2O and O_3 ALD processes. The C-rate corresponding with a current of 3 μA is given.

Another interesting fact is that the measured current is 4 times larger in the voltammogram of the O_3 based film. The CD measurements illustrate as well that more lithium can be intercalated in the thin film deposited by the O_3 process, see figure 5.7. In chapter 3 was discovered that the density of the films deposited by the O_3 process was lower than the density of the films deposited by the H_2O based process. The lower density signifies that the film contains more voids and interstitial spaces. Therefore, it can be understood that more lithium can be inserted in the film deposited by the O_3 based ALD process. Furthermore, figure 5.7 shows a decrease in capacity when the applied current increases. The C-rate for the lowest current is given, allowing to calculate the C-rate for the other current values.

The cyclability experiment of the amorphous film, deposited by the H_2O process, shows that the delithiation capacity is much lower than the lithiation capacity. This could indicate the presence of side-reactions, which contribute to the charging current but are not related to lithium intercalation in the vanadium oxide film. This will be further discussed in paragraph 5.2.4. The cyclability results of the O_3 based deposition are shown in figure 5.8b. The capacity remains quite stable during the first 10 cycles. Nevertheless, a decrease of approximately 24% in capacity is observed for the 50^{th} cycle.

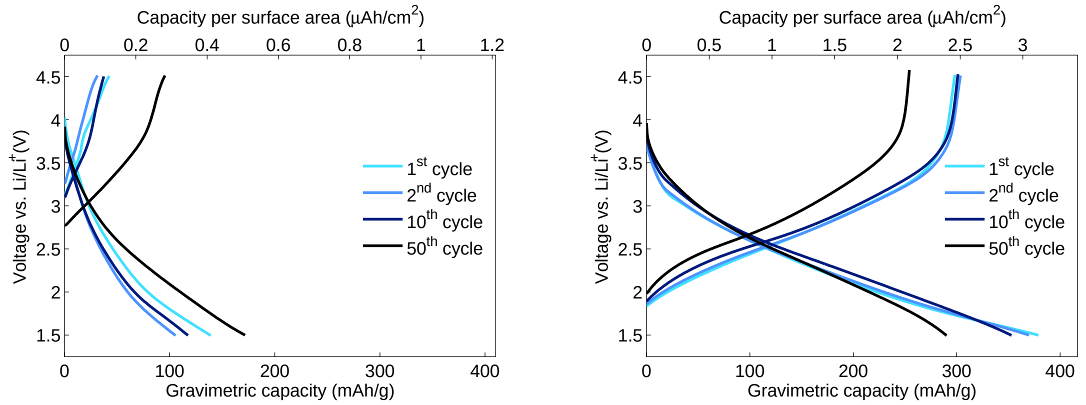

(a) H_2O: current 6 $\mu A = 4.50$ C **(b)** O_3: current 6 $\mu A = 1.56$ C

Figure 5.8: Cyclability testing of amorphous vanadium oxide, deposited with H_2O and O_3 ALD processes, at a current rate of 6 μA. The corresponding C-rate is given.

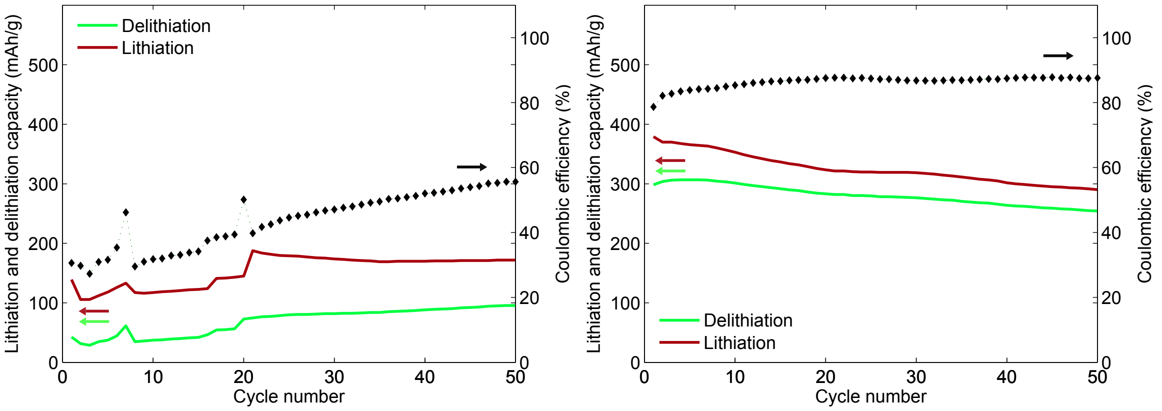

(a) H_2O: current 6 $\mu A = 4.50$ C **(b)** O_3: current 6 $\mu A = 1.56$ C

Figure 5.9: Coulombic efficiency and total lithiation and delithiation capacity of the cyclability experiment of amorphous vanadium oxide, deposited with H_2O and O_3 ALD processes, at a current rate of 6μA. The corresponding C-rate is given.

The lower capacity of the layer deposited with the H_2O process is clearly visible in figure 5.9, compared to the amorphous layer deposited with the O_3 process. Furthermore, a large discrepancy between lithiation and delithiation capacity is observed, resulting in a low coulombic efficiency. As mentioned previously, the total charge and discharge capacity are considerably higher for the amorphous vanadium oxide films deposited with the O_3-based process. The coulombic efficiency is higher as well, and remains stable at approximately 87%.

5.2.2 V_2O_5

V_2O_5 is the most studied vanadium oxide with respect to application as battery electrode and the $Li_xV_2O_5$ system contains three domains in which reversible battery operation is possible, which are the α-ϵ-δ, γ and ω regions. The V_2O_5 films will be tested in all 3 regions.

ω $Li_xV_2O_5$ with $0 \leqslant x \leqslant 3$

In the ω-$Li_xV_2O_5$ phase, three lithium ions are intercalated per V_2O_5. As this requires breaking of chemical bonds, the transitions are not entirely reversible, as can be seen in the voltammogram in figure 5.10a. The two reduction peaks that exist between 3 V and 3.5 V in the first cycle of the CV measurement are associated with the α-ϵ and ϵ-δ transitions. Cycling within these regions will be discussed in the next paragraph. The reduction peaks of 2.2 V indicates the transition to γ-LiV_2O_5, with intercalation of up to 2 lithium ions. The final peak at 1.7 V is caused by the transition to ω-LiV_2O_5. There is one broad oxidation peak visible, where the lithium ions are partly removed from the V_2O_5 lattice. According to Leger et al., V_2O_5 can be cycled reversibly between $Li_{0.40}V_2O_5$ and $Li_{2.60}V_2O_5$. As a result, a loss of capacity is observed after the first cycle, since insertion of 3 lithium ions is observed during the first charge.

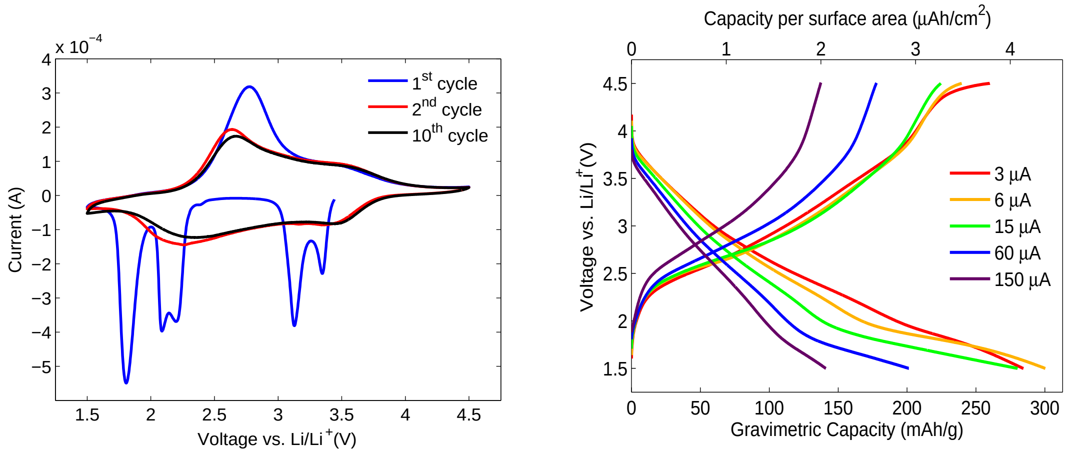

(a) CV at 10 mV/s

(b) CD: 3 μA = 0.70 C

Figure 5.10: CV and CD measurement of ω-LiV_2O_5

The CD measurement shows that less Li-ions intercalate into the structure, resulting in a loss of capacity, when the current density increases. The rate capability is not remarkably good for ω-LiV_2O_5 and was much better for the amorphous films, suggesting a slow diffusion in these samples.

Figure 5.11 shows the results of a cyclability test on ω-LiV_2O_5, where a constant current is applied and the potential varies between 1.5 V and 4 V vs. Li/Li$^+$. As mentioned previously, a new sample was prepared for the cyclability experiment, such that the plateaus of the transitions between α-ϵ, ϵ-δ, δ-γ and γ-ω are visible in the first cycle. Since the last transition is not reversible, these plateaus are not present during the 2^{nd} charge. A drop of capacity is observed after the first cycle, corresponding to intercalation of only 2.6 instead of 3 lithium ions per V_2O_5. The long plateau that emerges between 2 V and 1.5 V vs. Li/Li$^+$ during charging of the sample after a number of cycles is probably not caused by insertion of lithium in the ω-LiV_2O_5 lattice, otherwise a peak would be present in the voltammogram. Most likely, unwanted side-reactions are present and contribute to the current. This means that the actual capacity is significantly lower. The presence of side-reactions is also visible by the low coulombic efficiency and big difference between lithiation and delithiation capacity. The discharge capacity is not affected by side-reactions to the same degree, although a plateau-like shape is observed between 3.7 V and 4 V for the 50^{th} cycle, which might be caused by unwanted side-effects as well. Since the discharge capacity is less affected by side-reactions and is mainly caused by lithium extraction, one should focus on the delithiation curve to interpret the behaviour of ω-LiV_2O_5. The deliathiation curve indicates that a capacity of approximately 300 mAh/g can be obtained for ω-V_2O_5 and that the capacity decreases with the amount of cycles.

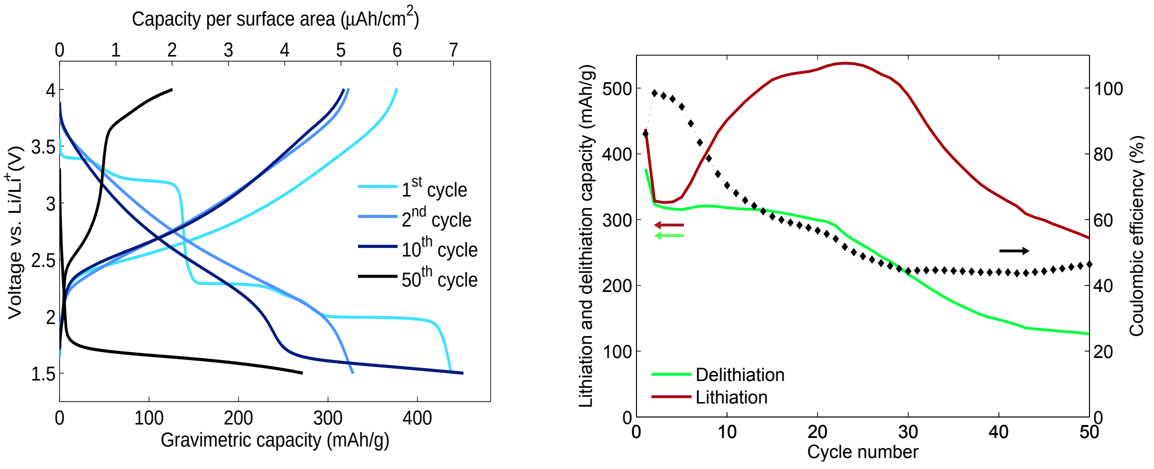

(a) Voltage vs. capacity

(b) Total capacity and efficiency per cycle

Figure 5.11: Cyclability testing of ω-LiV_2O_5 at a current 15 μA, corresponding to 2.0C.

α-ϵ-δ $Li_xV_2O_5$ with $0 \leqslant x \leqslant 1$

Figure 5.12a shows the cyclic voltammogram of a V_2O_5 film, cycled in the α-ϵ-δ phases, when the potential is sweeped between 2.9 V and 3.5 V vs. Li/Li$^+$. As mentioned in paragraph 5.1.1, these transitions are reversible as no breaking of bonds is required. The cyclic voltammogram illustrates the reversibility as 1^{st} and 10^{th} cycle coincide almost perfectly. The charge/discharge measurement on V_2O_5 α-ϵ-δ has well defined plateaus where the α-ϵ and ϵ-δ transitions occur. The rate capability of V_2O_5 α-ϵ-δ is remarkably good. This means that only a small loss of gravimetric capacity is observed when a higher current density is applied for charge and discharge.

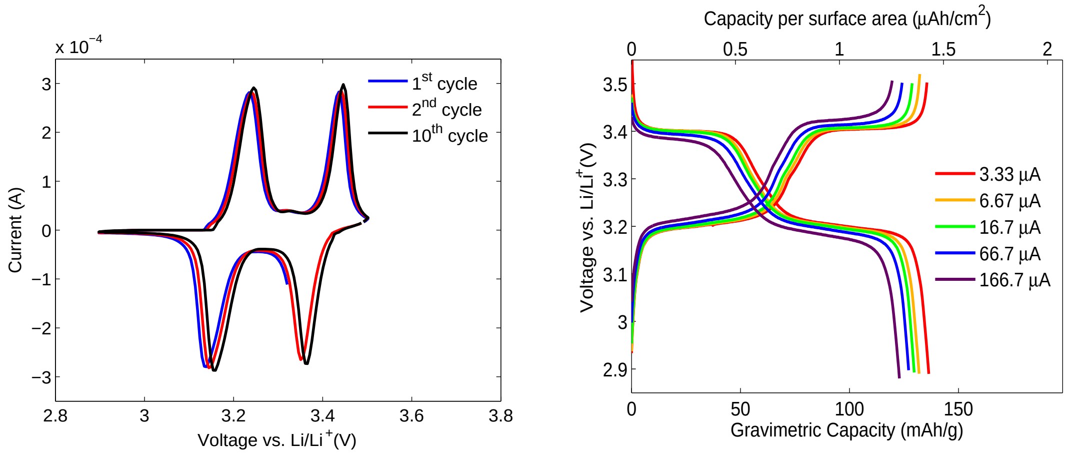

(a) CV at 10 mV/s

(b) CD: 3.33 μA = 0.72 C

Figure 5.12: CV and CD measurement of α-ϵ-δ LiV_2O_5.

The cyclability experiment reveals that α-ϵ-δ LiV_2O_5 barely suffers capacity loss because of cycling, which is very promising for battery applications. The total capacity of lithiation and delithiation remain approximately constant throughout cycling. On top of that, they coincide perfectly, yielding a coulombic efficiency of 100%. The discrete changes in coulombic efficiency, present in figure 5.13b are caused by a difference in runtime of the experiment. A difference of one time step between lithiation and delithiation results in an efficiency of 99.4%.

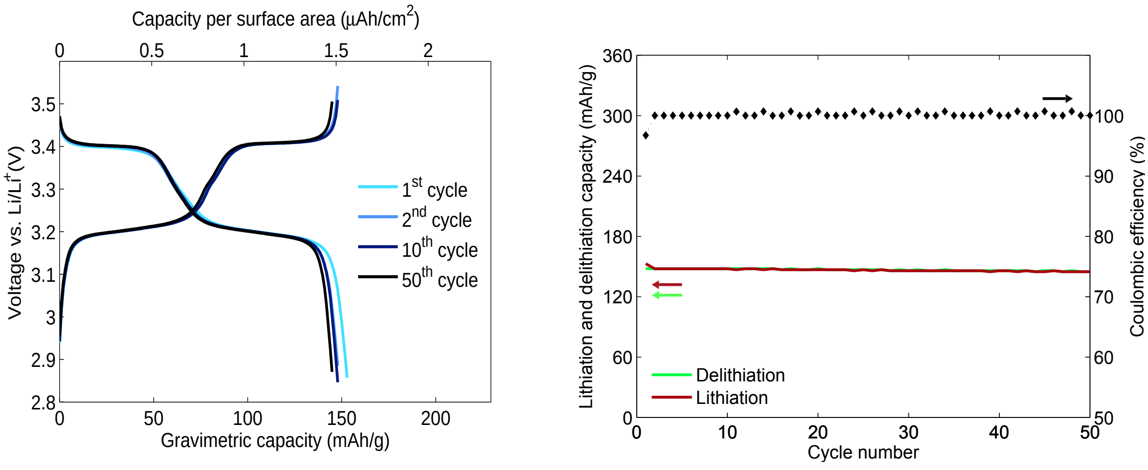

(a) Voltage vs. capacity

(b) Total capacity and efficiency per cycle

Figure 5.13: Cyclability testing of α-ϵ-δ-LiV_2O_5 at a current 10μA, corresponding to 6.30 C.

γ-$Li_xV_2O_5$ with $0 \leqslant x \leqslant 2$

The third option for reversible cycling of LiV_2O_5 is within the γ phase, reached when a potential of 2 V is applied. Figure 5.2 illustrated that the lattice of V_2O_5 needs to be deformed seriously for 2 lithium ions to intercalate per V_2O_5, which causes some irreversible damage to the lattice. However, the α-ϵ-δ oxidation and reduction peaks are still visible in the voltammogram, see figure 5.14a. Their intensity fades with the amount of cycles. In the CD measurements, figure 5.14b, the reduction peaks are visible for the lowest value of the current, which was the first cycle in these experiments. The gravimetric capacity decreases with increasing current, showing that the rate capability is not as good as for α-ϵ-δ LiV_2O_5. Nevertheless, a larger capacity is obtained, which was expected since 2 lithium ions are inserted instead of 1[86]. The theoretical capacity associated with insertion of a number of lithium ions will be compared with the experimentally obtained values in paragraph 5.4.

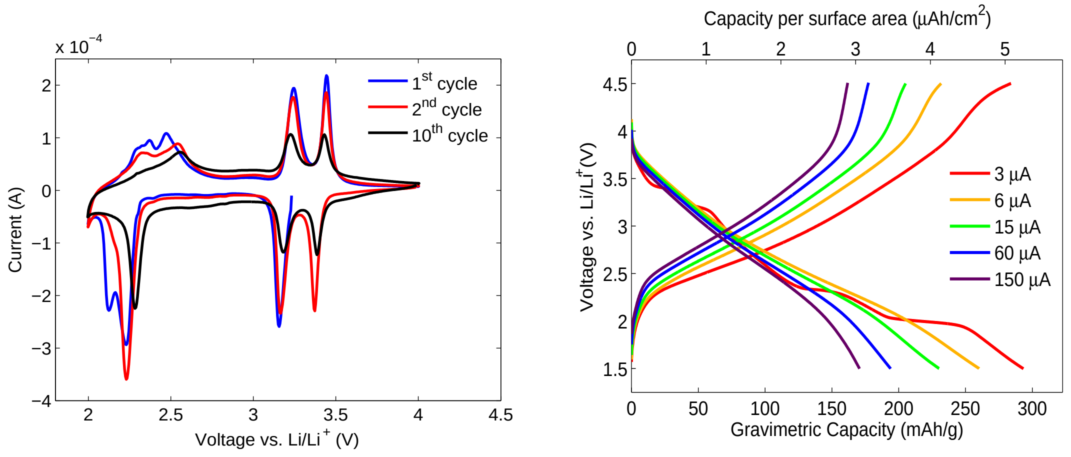

(a) CV at 10 mV/s

(b) CD: 3 μA = 0.58 C

Figure 5.14: CV and CD measurement of γ-LiV_2O_5.

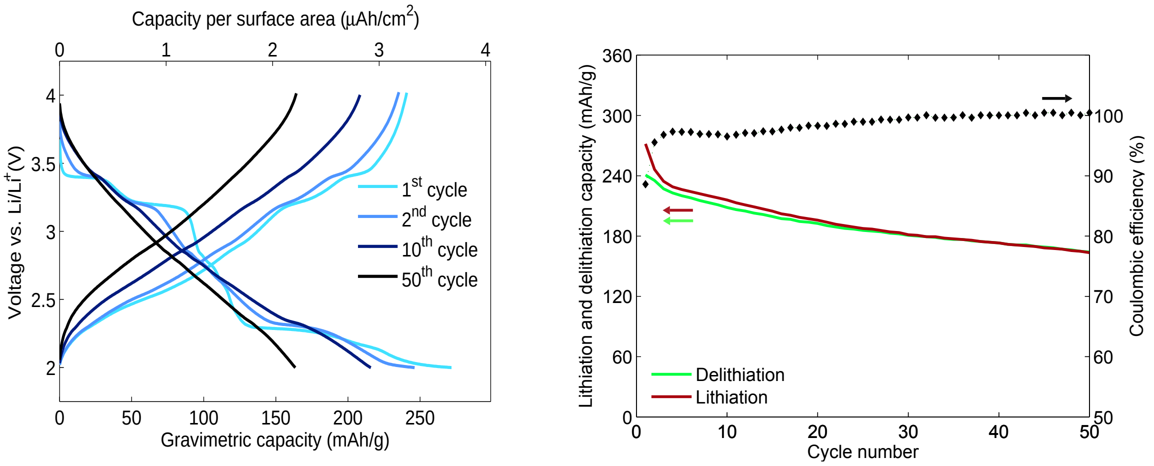

(a) Voltage vs. capacity

(b) Total capacity and efficiency per cycle

Figure 5.15: Cyclability testing of γ-LiV_2O_5 at a current 10 μA, corresponding to 2.57 C.

Figure 5.15 shows the results of the cyclability experiment on γ-LiV_2O_5. The capacity decreases with the number of cycles. After 50 cycles, the total capacity steadily decreased to approximately

60% of its original value. Figure 5.15b demonstrates that lithiation and delithiation capacity align when the number of cycles increases, such that the coulombic efficiency rises towards 100%.

Differences between V_2O_5 films annealed from H_2O- and O_3-based ALD

The amorphous vanadium oxide films, deposited by the H_2O and O_3 processes, behaved differently under electrochemical testing, as explained in paragraph 5.2.1. It is interesting to investigate whether or not the origin of the film still has an influence after crystallization. One would expect that this is not the case, since crystallized phases are fully determined by their lattice structure. All electrochemical tests performed on V_2O_5 samples, described in the previous paragraphs, were synthesised out of thin films deposited with the O_3 based ALD process. A V_2O_5 sample, annealed out of an amorphous film deposited with the H_2O process, is cycled in the α-ϵ-δ V_2O_5 phases to allow investigation of post-annealing differences between the two processes.

Figure 5.16 compares a CV measurement of α-ϵ-δ LiV_2O_5 thin films, deposited with H_2O and O_3 process, respectively. The measured spectra clearly overlap, indicating that the two films behave almost identical.

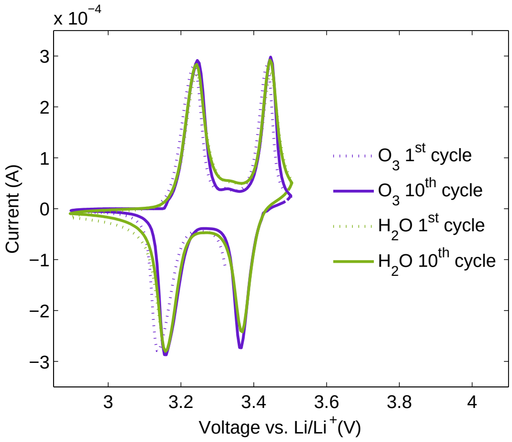

Figure 5.16: CV measurement of V_2O_5 thin films, annealed out of amorphous films deposited with H_2O and O_3 ALD processes.

The results of the CD measurement reveal an interesting aspect, see figure 5.17a. The films deposited with the H_2O-process correspond to higher capacity values, indicating that more lithium ions can be intercalated in the H_2O based films. As the mechanisms of intercalation are fully determined by the lattice and the V_2O_5 lattice of both films is identical , this seems highly unlikely. A possible explanation can be found in the volume expansion upon annealing of the amorphous films.

For the calculation of the gravimetric capacity, the film thickness is required in order to calculate the mass of the film, since the density of V_2O_5 is known. For both films of figure 5.17a, the thickness of the amorphous layer was multiplied by 1.20 to correct for the volume expansion upon annealing, since the VO_2 film expands when forming V_2O_5. This expansion of 20% was based on cross SEM images of the evolution of the thickness of an amorphous film (deposited by the O_3 process) when crystallizing into V_2O_5. The density of the V_2O_5 film is comparable to the density of the film deposited by the O_3 process, concluding that the volume expansion was only caused by the absorption of oxygen. However, the density of the layer deposited with the H_2O process was much higher than for the layer deposited with the O_3 process, see paragraph 3.3.3. And since the density of the O_3 based film was comparable to V_2O_5, this means that the film deposited by H_2O will undergo an additional expansion to obtain a lower density. As a consequence, the H_2O layer will suffer more volume expansion when it crystallizes to V_2O_5.

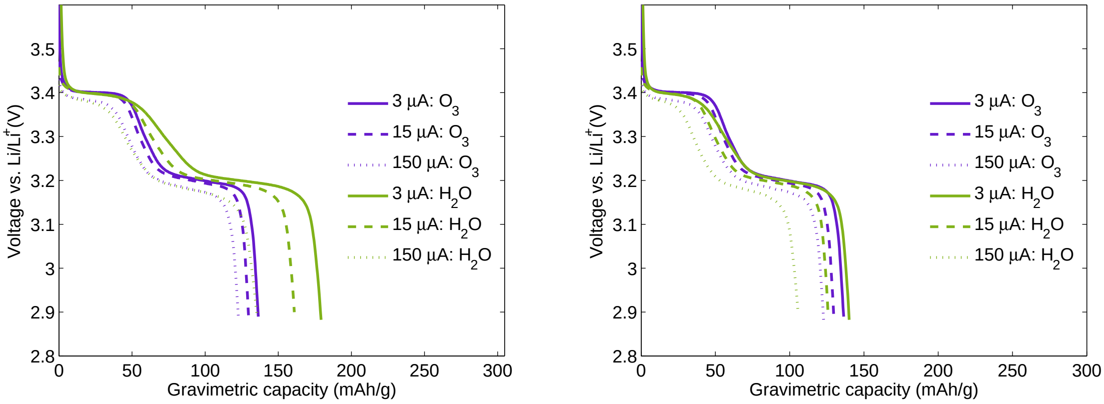

(a) Gravimetric capacity with thickness based on amorphous films

(b) Gravimetric capacity with corrected thickness for the H_2O deposited layer

Figure 5.17: CD measurement of V_2O_5 thin films, annealed out of amorphous films deposited with H_2O and O_3 ALD processes. The gravimetric capacity is calculated with the thickness of the amorphous film, increased by 20% for annealing(left) and with a corrected thickness to include volume expansion upon lowering the density of the H_2O based film(right).

The expansion can be estimated roughly by the difference in density of both films. From equation 3.1 is obtained that the density of the H_2O based film is 1.28 times the density of the film deposited with the O_3 process, such that the H_2O based film will have to expand 1.28 times more than the layer deposited by the O_3 proces upon formation of V_2O_5. If assumed that the volume expansion happens mainly perpendicular to the film surface, the thickness of the V_2O_5 film deposited with H_2O process will be $1.28 * 1.20$ times the thickness of the amorphous layer before annealing. As the corrected thickness is larger, the mass of the film will be larger as well. The result is a lower gravimetric capacity than the value obtained in figure 5.17a. Figure 5.17b contains the gravimetric capacity, calculated with the corrected thickness. The rough estimations and assumptions of the volume expansion give very good results. The capacity of both V_2O_5 films coincides for a current value of 3 μA.

For higher currents, the capacity of the film annealed from an amorphous H_2O based film deteriorates faster. A result which can be explained by greater damage induced in the V_2O_5 lattice because of the severe volume expansion.

This allows to draw general conclusions for other vanadium oxide films. When the samples are annealed out of an amorphous film deposited with the O_3 process, the thickness will increase by no more than 20% upon annealing, as the density of most vanadium oxide phases is comparable to the density of V_2O_5 and since the other oxides need to absorb less oxygen. If a film deposited with the H_2O process is annealed for the formation of a certain sample, more careful considerations with regard to film thickness are required.

5.2.3 VO_2(B)

The second most prominently researched vanadium oxide for application as electrode material is VO_2(B). Figure 5.18a contains the results of the CV measurement. A reduction and oxidation peak occur around 2.47 V and 2.70 V vs. Li/Li^+. The CV measurement shows good cycling behaviour of VO_2(B). The CD measurement contains well defined plateaus at approximately 2.6 V vs. Li/Li^+ where the lithium ions are inserted in or extracted from the electrode. The capacity is strongly dependent on the applied current, showing that the kinetic diffusion in these films is not optimal. For a current of 150 μA, only 56% of the capacity induced by 3 μA is retrieved.

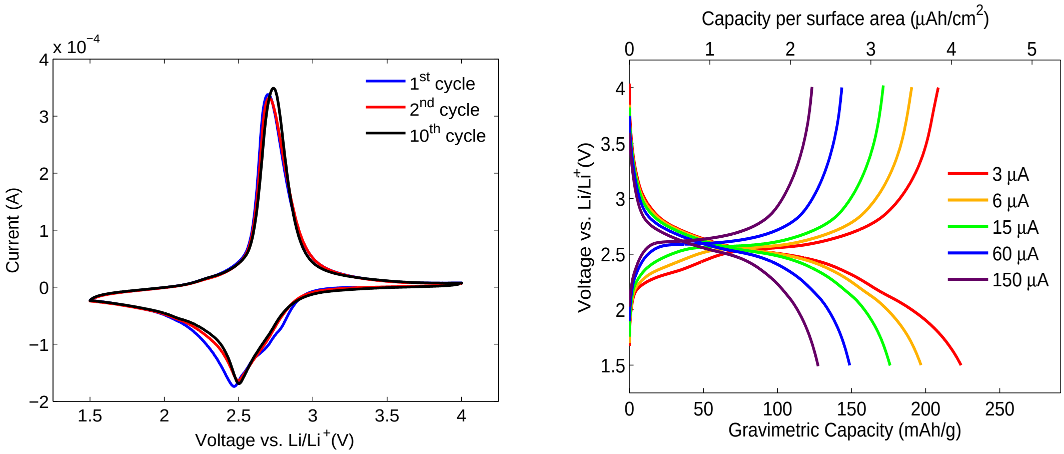

(a) CV at 10 mV/s

(b) CD: 3 μA = 0.70 C

Figure 5.18: CV and CD measurement of VO_2(B).

The cyclability experiment on the VO_2(B) electrode shows very promising cycling properties, see figure 5.19. The electrode suffered almost no loss of capacity after 50 cycles of galvanostatic charge/discharge at 2.48 C (current=10μA). Figure 5.19b illustrates an uncommon property of VO_2(B). After the first charge, not all lithium ions are extracted out of the lattice during the first discharge. Thus, the delithiation capacity of the first cycle is less than the lithiation capacity and the coulombic efficiency is only 85%. During the second cycle, a decrease in capacity is noted, which is the case for many materials. The interesting property of VO_2(B) is that the delithiation capacity increases with cycling, allowing the total lithiation capacity to restore slowly to the value of the initial charge. The coulombic efficiency rises and as a result, VO_2(B) can produce slightly more energy when discharged for the 50^{th} time than when discharged for the 1^{st} time.

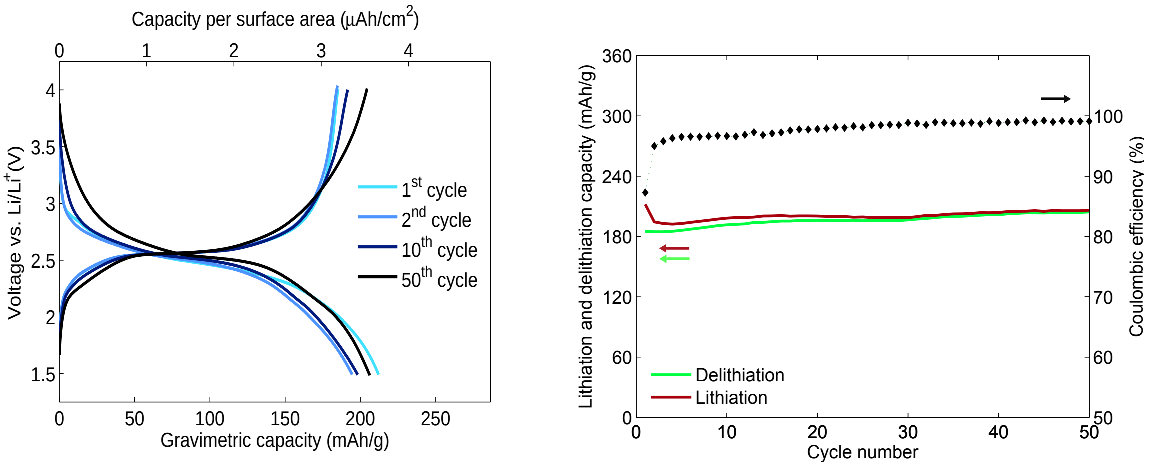

(a) Voltage vs. capacity **(b)** Total capacity and efficiency per cycle

Figure 5.19: Cyclability testing of VO_2(B) at a current 10 μA, corresponding to 2.48 C.

5.2.4 VO_2(M1)

Lithium intercalation in VO_2(M1) seems to be a complex process governed by various reduction/oxidation reactions, instead of one single reaction such as for VO_2(B), based on the voltammogram of figure 5.20a, containing 4 peaks in the first cycle and 3 in the following cycles.

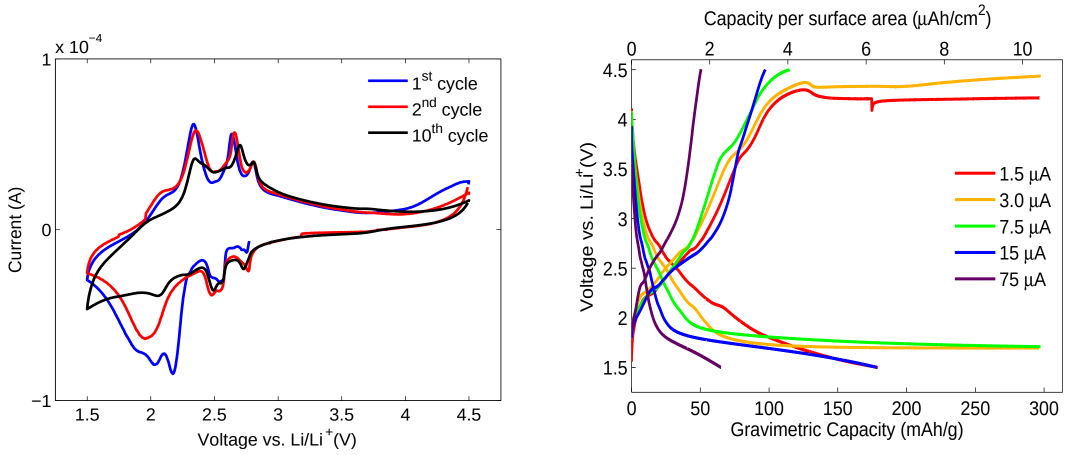

(a) CV at 10 mV/s **(b)** CD: 1.5 μA = 0.41 C

Figure 5.20: CV and CD measurement of VO_2(M1)

It should be noted that the current values obtained in the voltammogram are of the order of 5.10^{-5}A which is a factor 5 smaller than the current measured for the other vanadium oxides already discussed, which means that less Li^+ ions intercalate into VO_2(M1). VO_2(M1) has the highest density of all vanadium oxides discussed in this work. Its density is 15% larger than the density of VO_2(B) and 40% larger than V_2O_5. As the structure is more dense, less space in the lattice will be available for the small lithium ions to occupy.

Based on the CD measurement of VO_2(M1) at different charge rates, one would state that high capacity values are reached for the smaller currents, despite the expectations based on the CV measurement, see figure 5.20. In addition, the cycles at 1.5 μA, 3 μA and 7.5 μA were only stopped because a maximum time limit of 4 times the expected duration was reached and not because the cut-off potential of 4.5 V or 1.5 V vs. Li/Li^+ was obtained. This indicates that the plateaus at 4.2 V and 1.7 V vs. Li/Li^+ are not caused by intercalation of lithium into VO_2(M1), but are the result of unwanted side-reactions. To explain these plateaus, reactions with the substrate were investigated. A platinum substrate sample without thin film was tested with identical CV and CD procedures as applied on the vanadium oxides.

Electrochemical reactions with the platinum substrate

The CV and CD measurement on a non-coated Pt substrate sample are presented in figure 5.21. Comparison with figure 5.20b reveals the presence of identical plateaus around 4.2 V. The plateau at 1.7 V is also observed in the CD measurement of the Pt substrate and a corresponding reduction peak is noticed in the CV measurement, illustrating that the plateaus in the CD measurement of VO_2(M1) can definitely be explained as side-reactions with the substrate.

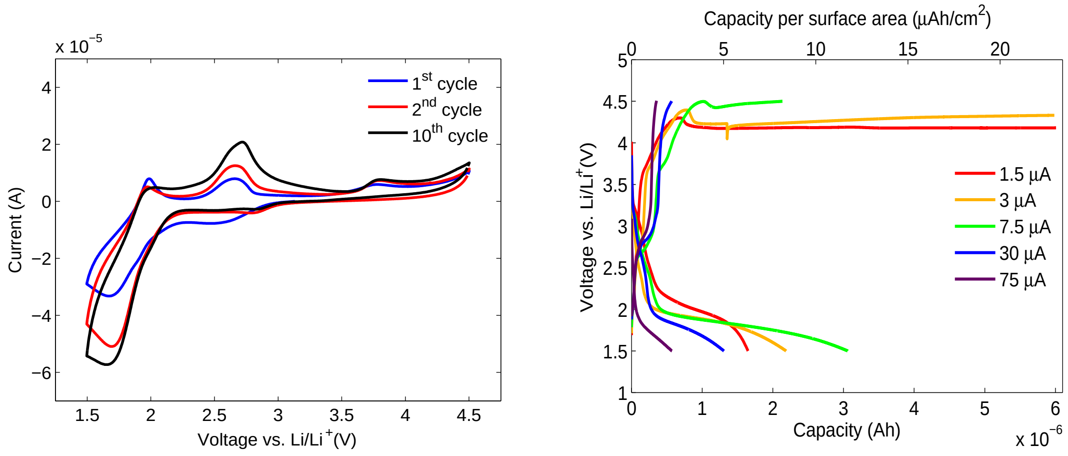

(a) CV at 10 mV/s

(b) CD: 1.5 μA = 0.91 C

Figure 5.21: CV and CD measurement of Pt-substrate to examine influence of side-reactions caused by platinum on the experiments on VO_x films

Standard electrode potentials of various electrodes can be found in literature. The potential of reactions with platinum and titanium are given, as the Pt substrate is formed by a sputtered Pt layer on top of a TiN layer, such that reactions with these 2 elements could be happening.

1. $Ti^{3+} + 3\,e^- \rightleftharpoons Ti(s)$ 1.67 V vs. Li/Li^+ [104]
2. $TiO(s) + 2\,H^+ + 2\,e^- \rightleftharpoons Ti(s) + H_2O$ 1.73 V vs. Li/Li^+ [105]
3. $Ti_2O_3(s) + 2\,H^+ + 2\,e^- \rightleftharpoons 2\,TiO(s) + 2\,H_2O$ 1.81 V vs. Li/Li^+ [105]
4. $TiO^{2+} + 2\,H^+ + 4\,e^- \rightleftharpoons Ti(s) + H_2O$ 2.18 V vs. Li/Li^+ [105]
5. $2\,TiO_2(s) + 2\,H^+ + 2\,e^- \rightleftharpoons Ti_2O_3(s) + H_2O$ 2.48 V vs. Li/Li^+ [105]
6. $PtCl_6{}^{2-} + 2\,e^- \rightleftharpoons PtCl_4{}^{2-} + 2\,Cl^-$ 3.77 V vs. Li/Li^+ [62]

7. $\mathrm{PtCl_4}^{2-} + 2\,\mathrm{e}^- \rightleftharpoons \mathrm{Pt(s)} + 4\,\mathrm{Cl}^-$ 3.80 V vs. $\mathrm{Li/Li^+}$[62]
8. $\mathrm{Pt}^{2+} + 2\,\mathrm{e}^- \rightleftharpoons \mathrm{Pt(s)}$ 4.23 V vs. $\mathrm{Li/Li^+}$[62]

The electrochemical cell consists of the two electrodes and the $LiClO_4$ electrolyte, such that no hydrogen is present under normal circumstances which makes reactions 2 to 5 unlikely to happen, unless minor traces of H are available. In that case, it was already established that the titanium of TiN can oxidize to TiO_2, see paragraph 3.8. Furthermore, the peak at approximately 1.7 V could be caused by reaction 1. An alternative explanation could be that this peak is associated with intercalation of Li into TiO_2, formed during annealing. Kavan et al. mentions the existence of an insertion reaction around 1.7 V vs. $\mathrm{Li/Li^+}$[106]. The peak at 4.2 V, visible in figure 5.21b, can be explained by reaction 8: $\mathrm{Pt}^{2+} + 2\,\mathrm{e}^- \rightleftharpoons \mathrm{Pt(s)}$. Reactions 6 and 7 are also occurring in some samples. The effect can be seen in the voltammogram of the Pt-substrate, but is for example as well noticeable in the cyclability experiment of V_6O_{13}. The required Cl^- ions are supplied by the electrolyte. To conclude, all peaks of the voltammogram in figure 5.21a can be explained, except for the peak at 2.5 V vs. $\mathrm{Li/Li^+}$, observed in the CV diagram.

Cyclability of VO_2(M1)

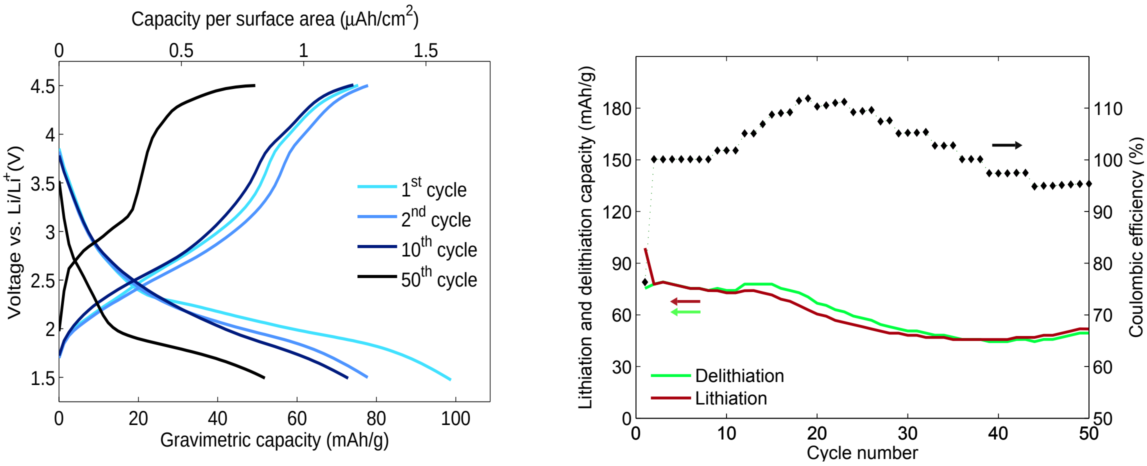

(a) Voltage vs. capacity **(b)** Total capacity and efficiency per cycle

Figure 5.22: Cyclability testing of VO_2(M1) at a current 10 μA, corresponding to 4.86 C.

Interpretation of the cyclability experiment on VO_2(M1) is not straightforward, since severe contributions of substrate-related side-reactions are present. In any case, the observed total capacity is rather low, such that VO_2(M1) is certainly not the best candidate for application as electrode for Li-ion batteries.

5.2.5 V_3O_7

In the first cycle of the voltammogram, V_3O_7 has 2 large reduction peaks. In the following cycles, a broad transition regime is observed without these pronounced peaks. As V_3O_7 is an element of the V_nO_{2n+1} series, it might be interesting to compare these peaks with VO_2 and V_2O_5. This will be discussed in detail in paragraph 5.3. The CD measurement of V_3O_7 shows very high capacity values for 3.33 μA and 6.67 μA, once again caused by reactions with the platinum substrate as previously discussed, more specific under the influence of the Ti.

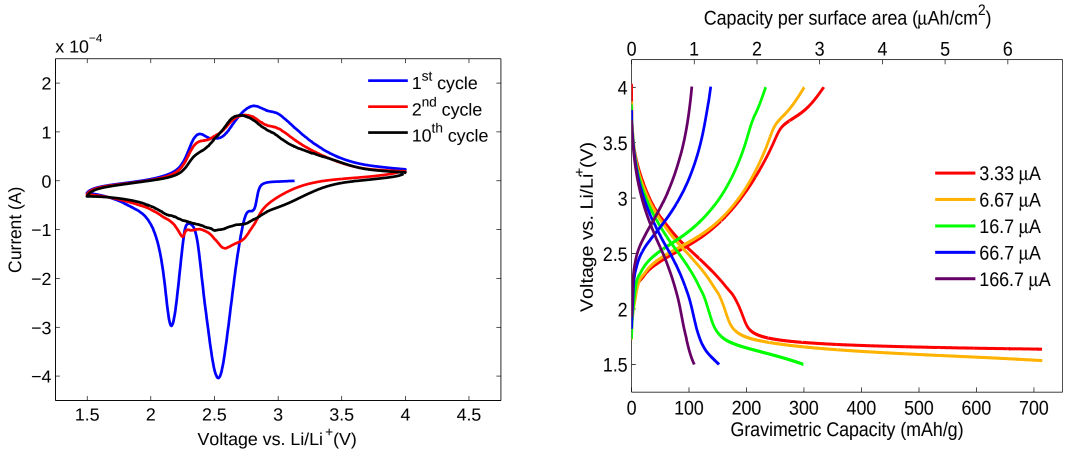

(a) CV at 10 mV/s **(b)** CD: 3.33 μA = 0.25 C

Figure 5.23: CV and CD measurement of V_3O_7.

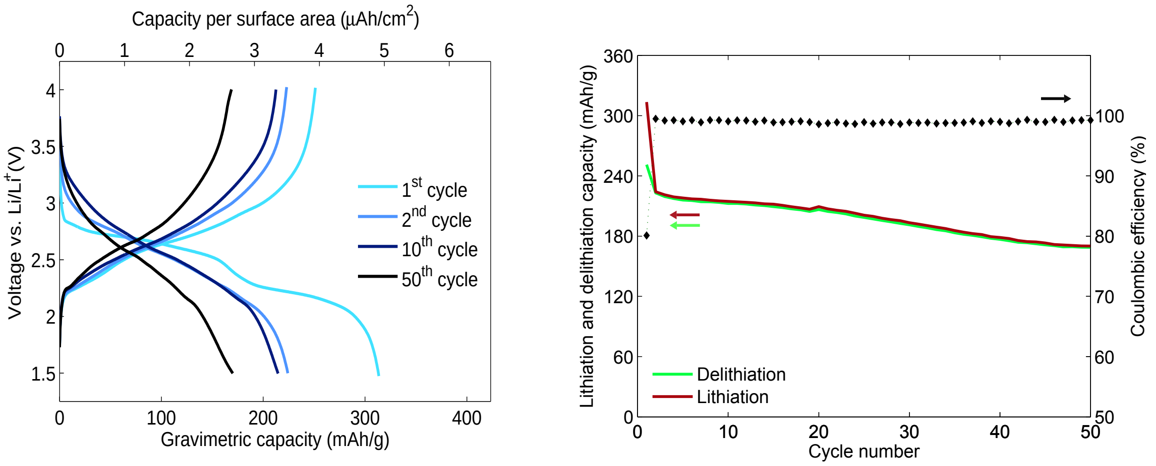

(a) Voltage vs. capacity **(b)** Total capacity and efficiency per cycle

Figure 5.24: Cyclability testing of V_3O_7 at a current 10 μA, corresponding to 2.76 C.

The sample used for the cyclability experiments did not suffer from unwanted side reactions with the platinum substrate. Figure 5.24a does not contain the plateaus at 1.7 V as was the case in figure 5.23b, although the current in the cyclability experiment was 10 μA, a value for which side reactions were observed in the CD measurement. The large peaks in the first cycle of the voltammogram allow intercalation of quite a lot of lithium and consequently a large capacity of 314 mAh/g, which corresponds to the large reduction peaks seen in the voltammogram, during the first cycle (figure 5.23a). The delithiation capacity is much lower, such that the coulombic efficiency of the first cycle is only 80%. Afterwards, there is a steady decrease observed in gravimetric capacity, while the efficiency remains stable at 99%. At the end of the 50^{th} cycle, 75% of the capacity of the 2^{nd} cycle is observed.

5.2.6 V_6O_{13}

The voltammogram of V_6O_{13} contains multiple peaks, with the most prominent oxidation and reduction peak around 2.5 V vs. Li/Li^+. Leroux et al. mentioned that the structures of V_6O_{13} and VO_2(B) are strongly related. The voltammogram of VO_2(B) and V_6O_{13} show striking similarities, more specifically because of the intense peak at 2.5 V vs. Li/Li^+. This will be further discussed in paragraph 5.3. The CD experiment on V_6O_{13} illustrates that the capacity is strongly dependent on the charge rate. For a current of 150 μA, the capacity is only 38% of the value obtained for a current of 3 μA.

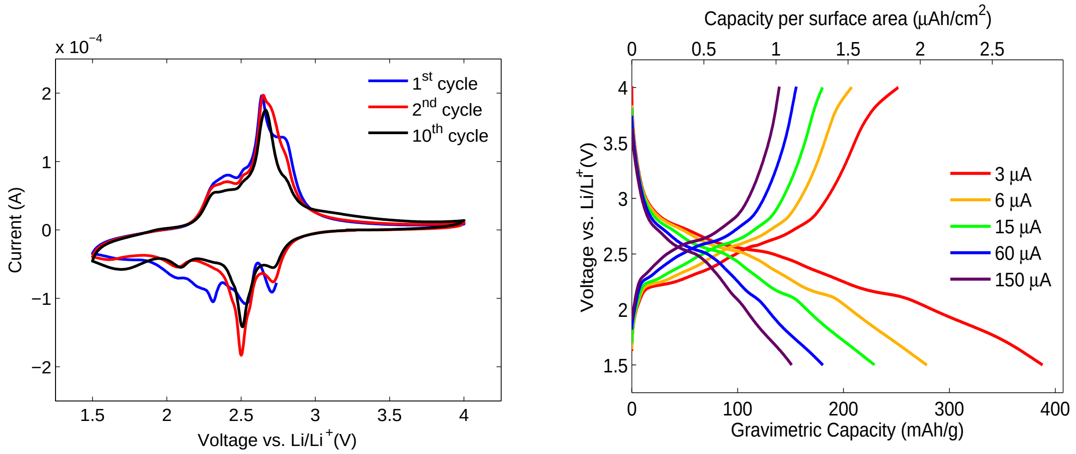

(a) CV at 10 mV/s

(b) CD: 3 μA = 0.72 C

Figure 5.25: CV and CD measurement on V_6O_{13}.

Annealing of the thin films to V_6O_{13} proved to be very difficult and only one sample could be synthesized, since it was hard to establish the low oxygen concentration in the in-situ XRD chamber. As a consequence, the cyclability experiment was performed on the sample that had already been tested in CV and CD measurements. These experiments might have caused some damage to the sample, as the cyclability measurement contains the unwanted side reactions once again. The typical plateau around 1.5 V is observed from the first cycle on. Figure 5.26b illustrates how high the capacity would be if the entire current could be explained by intercalation of lithium, this yields unrealistic high values. However, the actual capacity related to the lithium processes can be estimated by the delithiation capacity, which varies between 400 and 150 mAh/g, although the reactions with Pt and Cl^- contribute to the delithiation capacity as well, as seen by the plateau-like shape at 3.7 V in figure 5.26a.

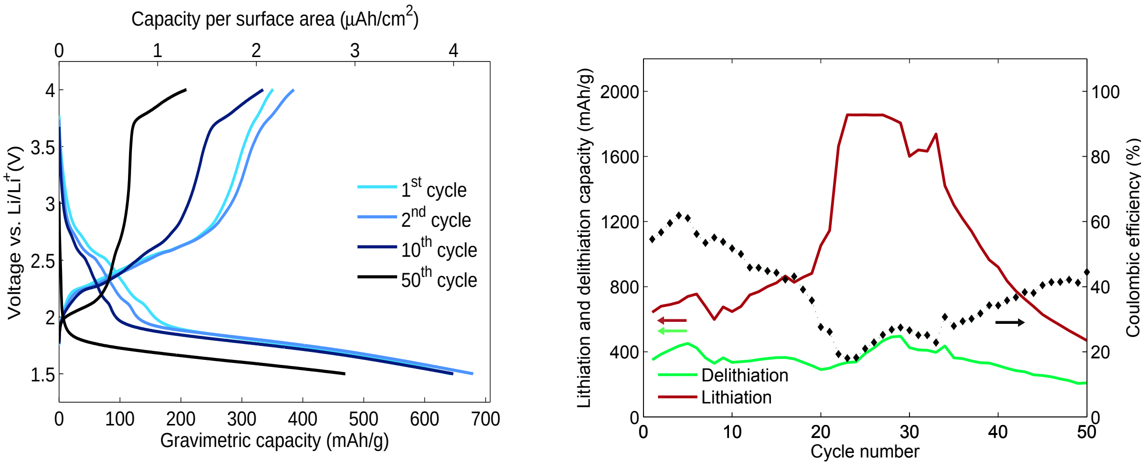

(a) Voltage vs. capacity **(b)** Total capacity and efficiency per cycle

Figure 5.26: Cyclability testing of V_6O_{13} at a current 10 μA, corresponding to 1.44 C.

5.2.7 V_4O_9

A reduction peak around 2.5 V vs. Li/Li$^+$ and a smaller peak around 2 V are observed in the V_4O_9 spectrum. The gravimetric capacity, measured by the CD experiment is extremely high and decreases with increasing current. The smooth shape of the curves and the absence of plateaus indicate that no side-reactions were present. For a current of 3 μA, the lithiation capacity reaches 536 mAh/g, which is the highest value obtained for all vanadium oxide films tested in this work. To exclude errors, the thickness of the V_4O_9 film was checked with cross-SEM, since an error in thickness would affect the weight of the layer, such that the calculated gravimetric capacity would be incorrect. The cross-SEM images confirmed the thickness of the layer, used for calculation of the gravimetric capacity. Thus the exceptional high value of 536 mAh/g is correct. V_4O_9 has the lowest density of all vanadium oxides examined in this work. This can be an indication that more interstitial spaces are available, such that V_4O_9 can host more lithium ions. Leroux et al.[13] described that the V_4O_9 lattice can be regarded as a VO_2(B) structure with ordered vacancies. Thus, this might indicate that the capability of VO_2(B) with respect to lithium incorporation can be enhanced by the extra vacancies, leading to the large capacity value observed.

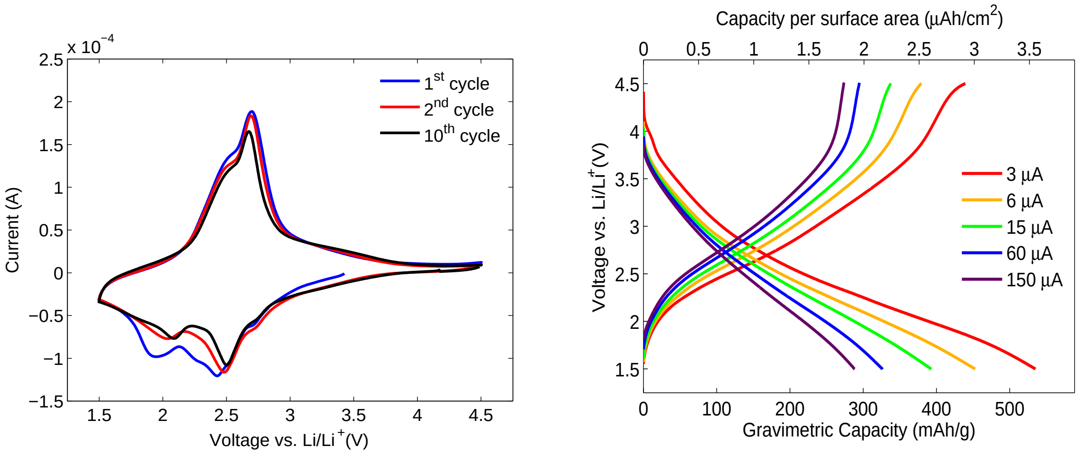

(a) CV at 10 mV/s

(b) CD: 3 μA = 0.72 C

Figure 5.27: CV and CD measurement of V_4O_9

Figure 5.28b clearly illustrates that the sample was damaged after 35 cycles in the cyclability experiment, allowing the side-reactions with the substrate to take place. The lithiation capacity skyrockets while the delithiation capacity remains approximately constant. During the first 35 cycles, the volumetric capacity decreased from 520 to 375 mAh/g while the efficiency remained constantly between 93 and 100%.

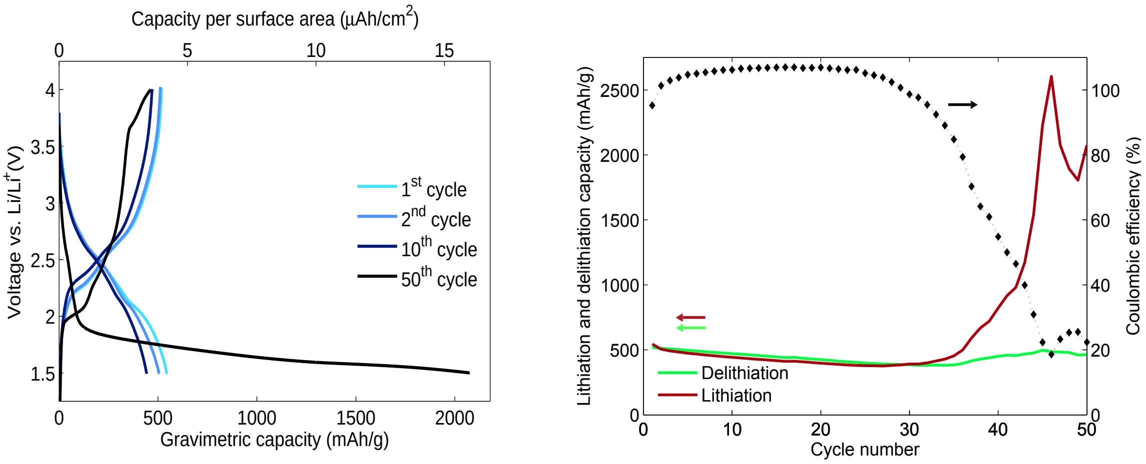

(a) Voltage vs. capacity

(b) Total capacity and efficiency per cycle

Figure 5.28: Cyclability testing of V_4O_9 at a current 10 μA, corresponding to 2.40 C.

5.3 Evaluation of the potential of various transitions

Table 5.2 gives an overview of all oxidation and reduction peaks, present in the voltammograms of the vanadium oxide thin films. Some clear similarities exist between the different vanadium oxides. For other systems, several authors have explained similarities between the potential of reactions in different species by similarities in the structures and associated mechanisms. Gorren et al. related similarities of various tetrahydropterins with the resemblance of their structure[107] and Hourani et al. explained matching CV peaks of Pt and Rh by similarities in their structures and surface behaviour[108]. A similar approach is used to explain the similarities between the potential of lithiation for the various vanadium oxides.

Table 5.2: Potential of lithiation and delithiation of the vanadium oxide thin films, obtained by cyclic voltammetry. The average potential and the reversibility of the transition is indicated.

VO_x	E_{Lith} (V vs. Li/Li$^+$)	E_{Delith} (V vs. Li/Li$^+$)	$E_{1/2}$ (V vs. Li/Li$^+$)	Reversible
V_2O_5 α-ϵ	3.36	3.45	3.41	Yes
V_2O_5 ϵ-δ	3.15	3.25	3.20	Yes
V_2O_5 δ-γ	**2.20**	2.54	2.39	Partially
	2.09			No
V_2O_5 γ-ω	1.81	2.78	2.30	No
V_2O_5 ω	2.23	2.61	2.42	Yes
VO_2(B)	2.47	2.70	2.59	Yes
V_4O_9	2.43	2.70	2.57	Yes
	1.95	2.52	2.24	Yes
V_3O_7	2.53	2.80	2.67	No
	2.16	2.38	2.27	No
V_6O_{13}	2.50	2.64	2.57	Yes
	2.71	2.79	2.75	No
	2.31			No
	2.06	2.41	2.24	No
VO_2(M1)	2.77	2.80	2.79	Yes
	2.48	2.65	2.57	Yes
	2.18	2.34	2.26	No
	2.03	2.11	2.07	No

In paragraph 1.2 was mentioned that the phases in the V_nO_{2n+1} series can be considered as a sequence of oxygen deficient FCC structures with ordered vacancies, formed out of a VO FCC parent structure[16]. Accordingly, the lattices of the phases of the V_nO_{2n+1} series are strongly related. Other authors agree that strong resemblance exist between some of these phases[13,17].

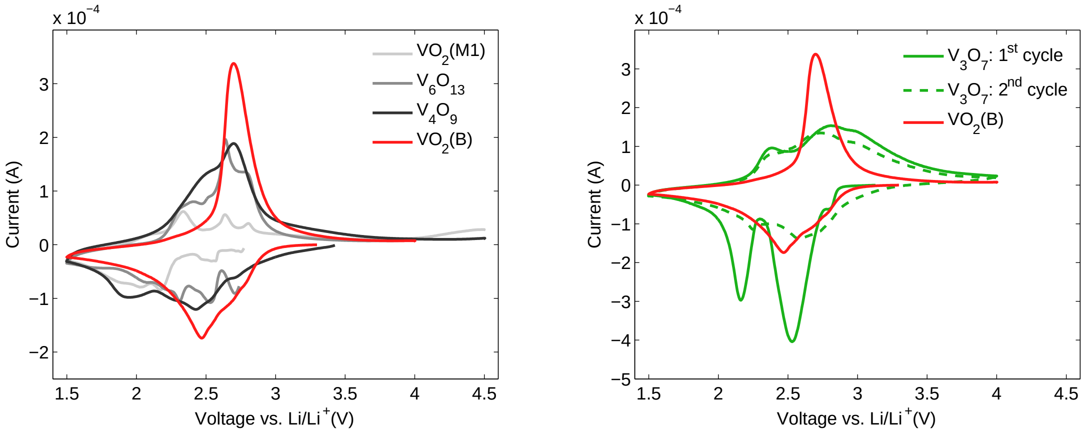

Figure 5.29: Correlation between the transformations of VO_2(B) and V_4O_9, V_6O_{13} and VO_2(M1) (left) and V_3O_7 (right).

Similarities in the lattices of certain phases should be visible in the position of the peaks associated with lithium intercalation. The average peak position of VO_2(B) is 2.59 V vs. Li/Li^+. For V_4O_9 and V_6O_{13}, a coinciding peak is retrieved, indicated in blue in table 5.2. Figure 5.29 illustrates that the main peaks of V_4O_9 and V_6O_{13} resemble the peak in VO_2(B). For VO_2(M1), the intensity of the peak is rather low, which might indicate that small VO_2(B) grains are present in the VO_2(M1) lattice, although this peak can also be related to a reaction induced by the substrate. In paragraph 5.2.4, a transition with small intensity at 2.5 V in the voltammogram of the substrate was left unexplained. It is unlikely that the peaks of V_6O_{13} and V_4O_9 are related to substrate effects, because of their higher intensity. The voltammogram of V_3O_7 indicates a transition at 2.5 V vs. Li/Li^+ as well, which is however not reversible and not retrieved to the same extent during the second cycle. A possible explanation might be that the peak at 2.27 V vs. Li/Li^+ is related to the irreversible transition in γ-V_2O_5.

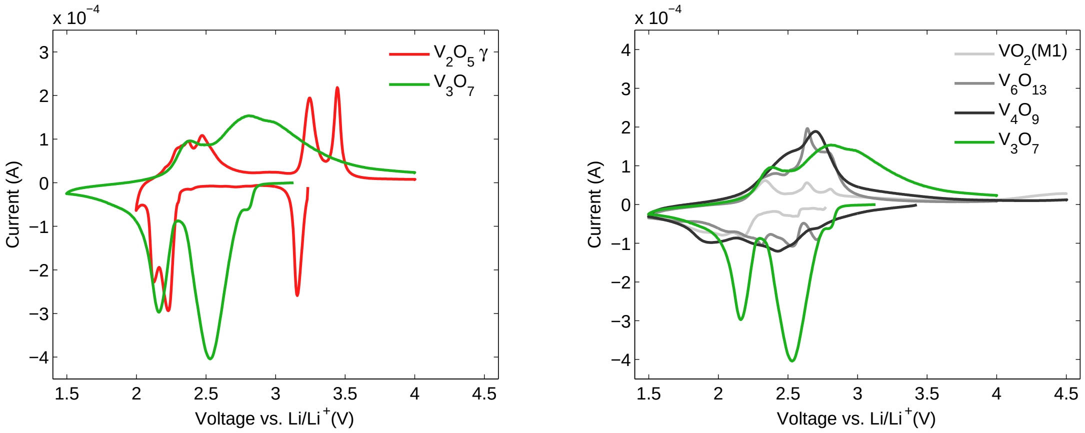

Figure 5.30: Correlation between the transformations of γ-V_2O_5 and V_3O_7, V_4O_9, V_6O_{13} and VO_2(M1).

If one would compare the vanadium oxides of the V_nO_{2n+1} series on the oxygen concentration, the V_3O_7 phase is closer related to V_2O_5 than V_4O_9 and V_6O_{13}. The transition with average potential of 2.27 V vs. Li/Li^+ in V_3O_7, could be caused by an interaction comparable to the transition to

γ-V_2O_5. Both peaks are irreversible and situated roughly at the same potential. The similarities between the transitions of V_3O_7 and γ-V_2O_5 are shown in figure 5.30. VO_2(M1), V_6O_{13} and V_4O_9 all contain a smaller peak with average potential around 2.27 V, indicated in orange in table 5.2.

Similarities in the voltammogram of the various vanadium oxides have been interpreted as indications of related structures and intercalation mechanisms. Figures 5.29 and 5.30 confirm that the phases of the V_nO_{2n+1} series are related to each other and that V_2O_5 and VO_2(B) are the borders of the series. V_3O_7 has the strongest resemblance with V_2O_5, due to the presence of the irreversible peak at 2.27 V vs. Li/Li$^+$ in V_3O_7 and γ-V_2O_5. At this potential, only a minor peak is observed for V_4O_9 and V_6O_{13}, while better resemblance at 2.5 V vs. Li/Li$^+$ is observed between these phases and VO_2(B), indicating a closer relation to VO_2(B).

5.4 Theoretical capacity

The experimental capacities can be compared with the theoretical capacity corresponding with intercalation of a number of lithium ions per unit cell. The theoretical capacity is calculated by dividing the charge of the inserted Li$^+$ ions by the mass of the vanadium oxide. Take for example V_2O_5, consisting of 2 vanadium and 5 oxygen atoms. The atomic mass of vanadium and oxygen are respectively 50,94 and 15,99 atomic mass units (amu), with 1 amu equal to $1,66.10^{-27}$kg. Thus, the mass of V_2O_5 is

$$m_{V_2O_5} = (2 * 50,9415 + 5 * 15,9999) * 1,66.10^{-27}\ kg = 3,02.10^{-25}\ kg \tag{5.2}$$

One lithium ion has a positive charge of 1,602.10^{-19} C or (1/3,6)*1,602.10^{-19} mAh. Therefore, the theoretical capacity, induced by intercalation of 3 lithium ions in V_2O_5 is

$$\text{Gravimetric Capacity}_{\omega-LiV_2O_5} = 3 * \frac{1}{3,6}\frac{1,602.10^{-19}}{3,02.10^{-22}}\ mAh/g = 442\ mAh/g \tag{5.3}$$

442 mAh/g is the theoretical capacity of ω-$Li_3V_2O_5$. The following table contains the theoretical capacities of intercalation of up to 8 lithium ions for the different vanadium oxides treated in this work.

Table 5.3: Theoretical capacity corresponding with insertion of up to 8 lithium ions in VO_x. Irrelevant values are displayed in gray. The highest experimentally obtained capacity value is presented in the last column.

	Theoretical capacity of inserted lithium ions (mAh/g)								
Phase	*1*	*2*	*3*	*4*	*5*	*6*	*7*	*8*	**Exp.(mAh/g)**
VO_2	323.1	646.2	969.3	1292.4	1615.5	1938.6	2261.7	2584.8	B: 230
									M1: -
V_2O_5	147.3	294.7	442.0	589.3	736.7	884.0	1031.3	1178.7	$\alpha\epsilon\delta$: 154
									γ: 272
									ω: 438
V_3O_7	101.1	202.3	303.5	404.8	505.9	607.1	708.3	809.5	310
V_4O_9	77.0	154.1	231.1	308.2	385.3	462.3	539.42	616.4	536
V_6O_{13}	52.1	104.3	156.5	208.6	260.8	313.0	365.2	417.3	388

If V_2O_5 is cycled in the α-ϵ-δ phases, 1 lithium ion per V_2O_5 is intercalated, corresponding to a theoretical capacity is 147,3 mAh/g. This is in good comparison to the experimental capacity since a value of 154 mAh/g is obtained in the cyclability measurements for a charge of 10 μA. The discrepancy is probably caused by a variation in the film thickness. For γ-V_2O_5, two lithium ions are intercalated. The theoretical capacity is 294.7 mAh. The experimental obtained gravimetric capacity of 272 mAh/g is comparable with the theoretical capacity. The last V_2O_5 phase, ω-V_2O_5, can host 3 lithium ions per V_2O_5. Consequently, its theoretical capacity is 442.0 mAh/g, which is of the same order of the first cycle in the cyclability experiment(438 mAh/g). Consecutive cycles only allow intercalation of 2.6 lithium ions, according to various authors. This decrease in capacity is observed in the following cycles of the cyclability experiment and in the capacity obtained with the CD experiment.

In the CD measurement of VO_2(B), a gravimetric capacity of approximately 230 mAh/g is reached, corresponding to 0.7 lithium ion per VO_2(B). Manthiram et al. mentioned that the number of lithium ions intercalated depends on the method of synthesis. A reduction process resulting in nanocrystalline VO_2(B) can host 0.9 lithium ions, while only 0.5 can be inserted for thermally prepared VO_2(B)[17]. The value obtained in this work is situated in between. VO_2(M1) can be neglected, as the capacity is quite low and it is doubtful if the measured capacity is caused by intercalation of lithium into the VO_2(M1) lattice. The capacity obtained in the cyclability experiment of V_3O_7 indicates that insertion of 3 lithium ions is possible, based on table 5.3. The gravimetric capacity reached at the end of the first charge was of the order of 310 mAh/g, which is slightly higher than the theoretical capacity but small deviations with respect to the mass of the film are possible.

The capacity obtained in the CD measurement on V_6O_{13} (388 mAh/g) indicates that 8 lithium ions can be intercalated in V_6O_{13} if the current density is sufficiently low, which is confirmed by other authors[18,89]. The highest gravimetric capacity is observed for V_4O_9, with a maximal value of 536 mAh/g at lithiation, which indicates that 7 lithium ions can be intercalated per V_4O_9. As mentioned before, the film thickness was double checked successfully with cross-SEM images, indicating that the value of 536 mAh/g is correct. However, as the delithiation capacity is smaller, not all 7 lithium ions can be removed out of the V_4O_9 lattice.

The experimentally obtained values for gravimetric capicity have been compared by theoretical values associated with intercalation of a number of lithium ions. For the phases where data was found in literature (V_2O_5, VO_2(B) and V_6O_{13}), confirmation between published and measured values was found.

5.5 Comparison of different phases

The various vanadium oxides are compared to each other regarding capacity, rate capability, cyclability and energy density upon lithium intercalation.

5.5.1 Capacity and rate capability

Figure 5.31 allows quick comparison of the data obtained by the CD measurements of all vanadium oxides. The total gravimetric capacity of the discharge is presented with respect to the current rate. The capacity of the charge cycle was in some cases substantially higher. Nevertheless, the discharge capacity is presented, because this value will limit the charge that can be delivered reversibly if the vanadium oxide would be used as an electrode in a lithium-ion battery. The values for VO_2(M1) according with 1.5 μA and 3 μA are not presented, since long plateaus were caused by side-reactions in those discharge cycles, such that the observed capacities were not reliable. The results are presented on a logarithmic current axis.

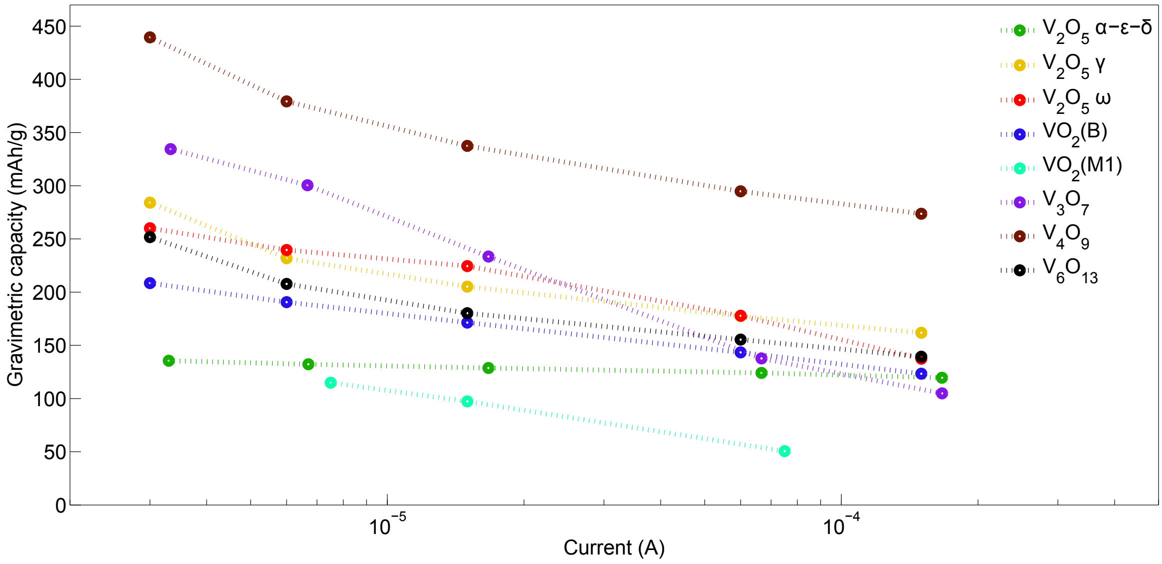

Figure 5.31: Gravimetric capacity of the discharge cycle versus applied current for the various vanadium oxide thin films.

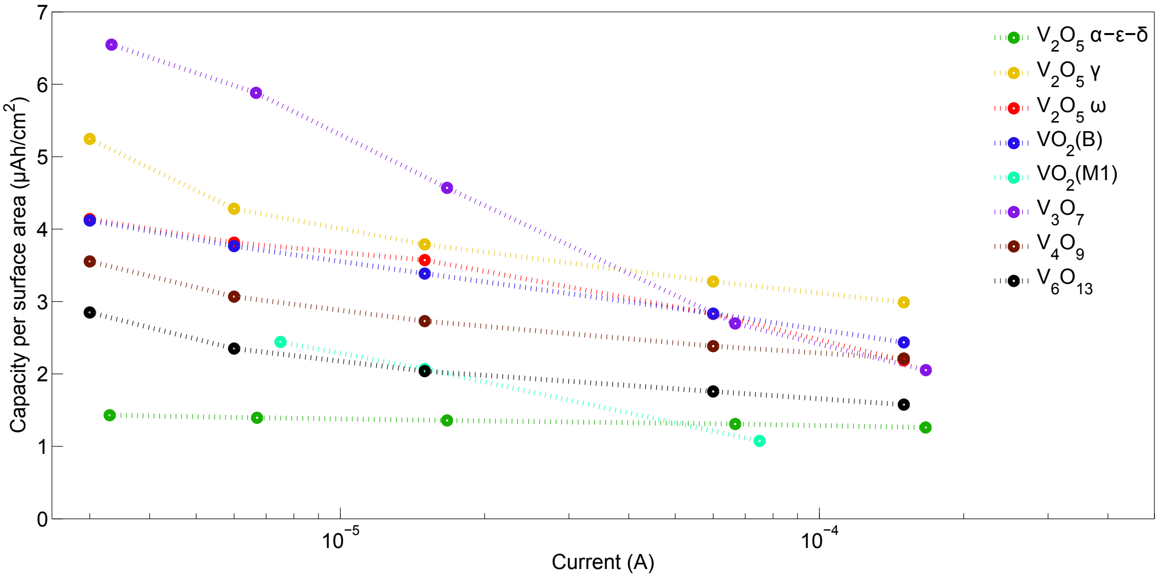

Figure 5.32: Capacity per surface area of the discharge cycle versus applied current for the various vanadium oxide thin films.

The gravimetric capacity is shown in figure 5.31, while the capacity per surface area is presented in figure 5.32. The differences between the two figures are caused by non equal thickness (up to factor 2) of the films and by changes in density between the various phases. Figure 5.32 is of interest for thin film battery research. However, comparison of the materials with respect to gravimetric capacity better allows to understand the differences between the distinct phases. The highest gravimetric capacity is obtained for V_4O_9, one of the less studied vanadium oxides. As mentioned before, V_4O_9 has the lowest density of all vanadium oxides and its structure is related to V_2O_5 and VO_2(B), with ordered vacancies. The capacity of V_4O_9 clearly decreases when the current is increased, such that only 60% of the initial capacity is measured for currents of 150μA.

For applications where very low C-rates are of interest, V_3O_7 can be a promising candidate as well. However, its capacity fades very fast when higher currents are applied, as it is the vanadium oxide with the worst rate capability (30% of capacity at 167 μA). A third interesting oxide with respect to capacity is V_2O_5, especially for cycling within the γ-phase, which has a better rate capability than the ω-phase. Advantages of V_2O_5 are the good stability of the oxide and the easy fabrication process.

With respect to rate capability, the best vanadium oxide is V_2O_5 when it's cycled in the α-ϵ-δ region. It is the only vanadium oxide thin film which barely suffers capacity loss when the current density is increased. However, it is also the vanadium oxide with almost the lowest capacity at low charge rates.

Table 4.1 contains the specific capacity of commercially used lithium-ion battery cathodes. Comparison of these values with the gravimetric capacities of the vanadium oxide thin films, reveals that the capacities obtained for the vanadium oxides are potentially interesting, especially the observed value for V_4O_9 is substantially higher. The experimentally obtained capacities can also be compared with table 5.1, containing a summary of other research concerning vanadium oxide as electrode material. One can conclude that similar results are obtained in this work. The lithiation capacity corresponding to V_4O_9 (536 mAh/g) is the highest value reported for vanadium oxides.

5.5.2 Capacity vs. density

The vanadium oxides with highest (V_4O_9) and lowest capacity (VO_2(M1)) correspond to the lowest and highest density among the investigated phases. Therefore, it was examined if an inversely proportional relation is present. The total capacity of the various vanadium oxides is presented in figure 5.33 with respect to the density. The α-ϵ-δ and γ phases are presented by smaller symbols, since these phases are formed by partial lithiation.

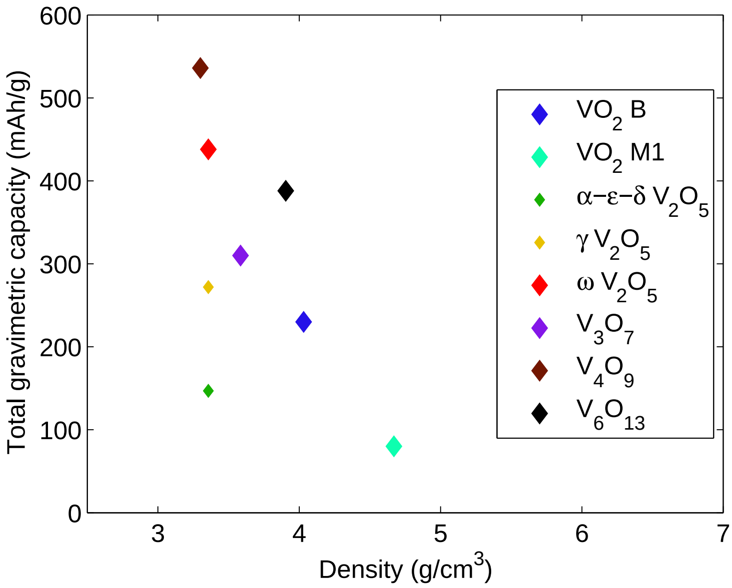

Figure 5.33: The total lithiation capacity at approximately 3 μA vs. the density of the different phases.

Figure 5.33 shows that a trend between density and total capacity can indeed be observed, if the non completely charged V_2O_5 phases are neglected. A likely explanation is that structures with lower density contain more voids and interstitial space, such that more lithium ions can be inserted. This relationship might be valid to some extent for other materials, and can be an indication on which materials might be interesting to examine.

5.5.3 Cyclability

The cyclability experiments investigate the decrease in capacity when multiple charge/discharge cycles are performed sequentially. The results of the different vanadium oxides are shown in figure 5.34. Since the cyclability experiment on V_6O_{13} did not provide realistic results, likely due to heavy side reactions, this measurement is omitted in figure 5.34. To allow comparison of the evolution of the capacity of different phases, the capacity is normalised with respect to the value of the first cycle, which is indicated in the legend.

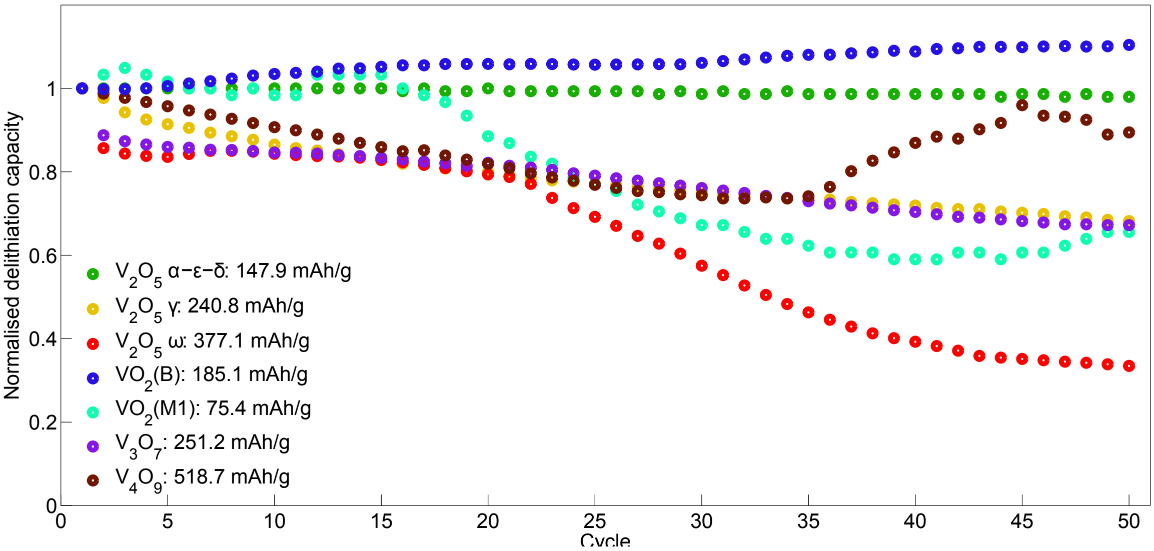

Figure 5.34: Evolution of the normalised delithiation capacity upon cycling. The delithiation capacity of the first discharge is given in the legend.

V_4O_9 clearly outperforms the other oxides in terms of capacity, but the cyclability experiment shows that the capacity of V_4O_9 fades constantly. After 30 cycles, a loss of 133 mAh/g (25.6%) is present. In the specific sample tested here, the lattice had suffered severe damaging after 30 cycles such that side reactions started to occur, causing an increase in delithiation capacity. The cycling behaviour of V_4O_9 should be further investigated to examine if the capacity stabilizes or if the decreasing trend remains present. Less deep charging of this material could, with the very high initial capacity in mind, improve the cyclability while still maintaining high capacity. However, this falls out of scope of this work, which was mainly aimed at screening the various oxides.

The remarkable behaviour upon cycling of ω-V_2O_5 and VO_2(M1) is also influenced by side-reactions. Furthermore, it can be noted that γ-V_2O_5, V_3O_7 and V_4O_9 display a comparable loss of capacity with respect to cycling. The cycle life of a battery is usually defined as the amount of cycles before a loss of capacity of 20% is observed. For the most vanadium oxides, the cycle life would be limited to 25 cycles.

Figure 5.34 shows that only VO_2(B) and α-ϵ-δ V_2O_5 behave well when cycled and that all other oxides suffer a significant decrease in capacity upon cycling. The capacity of α-ϵ-δ V_2O_5 remains constant while an increase is observed for VO_2(B) due to better efficiency. Since the electrodes of a lithium ion battery should be able to allow reversible intercalation of lithium ions for many cycles, VO_2(B) and α-ϵ-δ V_2O_5 can be regarded as most promising electrode materials. If these two phases are compared with respect to rate capability, an interesting conclusion can be made. Figure 5.31 illustrates that VO_2(B) has a higher capacity for lower currents, such as the 10 μA used in the cyclability experiments, but α-ϵ-δ V_2O_5 has a higher capacity for high currents, due to its very good rate capability. Thus, if low currents are required, one should consider VO_2(B) as best option, while α-ϵ-δ V_2O_5 is the best choice for applications with high currents.

5.5.4 Energy density

The capacity of a material gives information regarding how many lithium ions can be intercalated and how much charge can be generated when these ions are removed out of the lattice. To calculate the energy density, generated by this transition, one must multiply the capacity with the potential of the transition. For the three most interesting VO_x phases, the gravimetric energy density is given in the following table. For V_4O_9, a capacity of 400 mAh/g is used. It should be verified with further examination whether this is a stable capacity value, or whether the capacity will decrease further upon cycling.

Table 5.4: Gravimetric capacity and average transition potential of the most promising vanadium oxides and some commercially used cathode materials[3]. Multiplication of these two values results in the gravimetric energy density.

Phase	Gravimetric capacity (mAh/g)	Transition potential (V)	Gravimetric energy density (Wh/kg)
Experimental vanadium oxide films			
α-ϵ-δ V_2O_5	147	3.30	485
VO_2(B)	250	2.59	647
V_4O_9	400	2.57	1028
Commercially used cathodes			
$LiNi_{0.8}Co_{0.15}Al_{0.05}O_2$ (NCA)	180-200	3.8	760
$LiNi_{1/3}Co_{1/3}Mn_{1/3}O_2$ (NMC)	160-170	3.8	646
$LiFePO_4$ (LFP)	150-170	3.45	586

Comparison between the vanadium oxide thin films and some commercially used cathode materials indicates that the obtained gravimetric energy density is of the same order of magnitude. Certainly for V_4O_9, the energy density is promising and potentially interesting, though improvement of the cycling behaviour will be required.

The transition potential of α-ϵ-δV_2O_5 is 3.30 V vs. Li/Li^+. One of the main reasons for research in thin films as electrode for LIB is that faster surface reactions can enhance the behaviour of the LIB at higher currents, since the transitions in classic LIB's are diffusion limited at high current densities. Thus, the new technologies, based on nanostructured materials, could lead to batteries with higher specific power. With the Ragone plot of figure 1.1 in mind, a gravimetric energy density comparable to the commercially used cathodes, combined with an increased specific power, would be a step forward in LIB technology.

5.6 Characterization of the lithiated vanadium oxide films

5.6.1 Detecting lithium concentration with XPS

In the previous paragraph, the experimental capacity was compared with theoretical values associated with insertion of a number of lithium ions. However, if side-reactions are present, their contribution to the current can be interpreted incorrectly as related to lithium intercalation processes, thus resulting in a higher capacity value. To verify the experimentally obtained capacity, XPS is used to directly measure the lithium concentration for the various vanadium oxides.

In practice, measuring lithium with XPS is rather difficult, because of the low intensity of the X-rays emitted by lithium. The sensitivity factor for detecting lithium is equal to 0.0568. For comparison, the sensitivity for the detection of oxygen, vanadium and platinum is 2.93, 9.66 and 15.5. As a result, the lithium signal is barely detectable against the noise of the background. On top of that, the energy of the lithium 1s X-ray (≈ 55 eV) is situated close to the energy of the X-rays induced by the Pt 5p transition (≈ 51 eV) and Ti 3s transition (≈ 59 eV), causing a second difficulty.

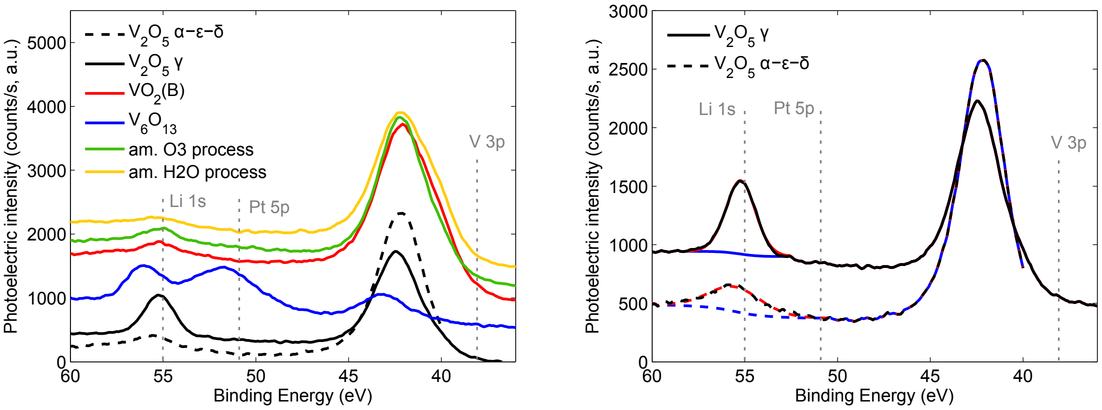

(a) XPS spectra of various vanadium oxides **(b)** Background and fit of the two V_2O_5 samples

Figure 5.35: Results of the XPS measurement, an y-offset is applied to the various spectra to enhance visibility.

Before the XPS spectra were obtained, the samples were charged at a charge rate of 1C. Figure 5.35 shows that the lithium signal is indeed hard to detect against the background for both amorphous layers, VO_2(B) and α-ϵ-δ V_2O_5. The γ-V_2O_5 and V_6O_{13} phases give rise to a more intense lithium peak, while a Pt signal was recorded as well for V_6O_{13}. Figure 5.35b shows the spectra for the two examined V_2O_5 samples in detail and contains the background (blue) and fitted curve (red) for determination of the lithium concentration.

Several studies have demonstrated that 1 lithium ion can be inserted in α-ϵ-δ V_2O_5, while the γ-phase allows insertion of 2 lithium ions, see paragraph 5.1.1. The XPS measurement confirms this ratio, as approximately twice as much lithium is measured for γ-V_2O_5. Since the gravimetric capacity of V_2O_5 is thoroughly studied, it can be used as reference to determine gravimetric capacity of the other phases.

Table 5.5: Intensity of the lithium peak, obtained by XPS. The value for α-ϵ-δ V_2O_5 is used as reference to determine the gravimetric capacity for the other oxides from the measured intensity of the XPS peak.

		Gravimetric capacity (mAh/g)	
Phase	**Li counts by XPS (a.u.)**	*XPS Estimation*	*Experimental value*
α-ϵ-δ V_2O_5	*reference = 0.113*	*reference = 147*	147
γ-V_2O_5	0.210	273	272
VO_2(B)	0.136	177	230
V_6O_{13}	0.124	161	388
am. VO_x by H_2O process	0.058	75	115
am. VO_x by O_3 process	0.142	185	380

Table 5.5 shows the number of counts observed by XPS measurements without sputtering. The estimations of the gravimetric capacity, based on the number of counts relative to α-ϵ-δ V_2O_5 give remarkably good results. The estimation for γ-V_2O_5 even coincides perfectly with the value obtained by the CD measurement (272). Although it should be noted that this is a coincidence, since the margin of error is very large for this method, because of the low sensitivity of lithium. However, the result for VO_2(B) indicates in the same direction as the experimentally obtained gravimetric capacity as well, though with larger deviation. A remark concerning the V_6O_{13} sample should be made. As only one V_6O_{13} sample was synthesised, the XPS measurement was carried out after the cyclability test, in which some serious side-reactions occurred. This might explain the larger discrepancy between experimentally obtained gravimetric capacity and the XPS-based estimation. For the amorphous layers, the difference between the estimations and the experimentally obtained values is quite large as well, though the ratio between the two films is retrieved.

The XPS measurements of VO_2(M1) and V_4O_9 are not included in table 5.5. The spectra of both samples is shown in figure 5.36, together with a sample of the Pt substrate, treated with the identical electrochemical procedure. The platinum 5p peak at 51 eV is observed for the three samples and due to its large intensity, detection of the lithium peak is not possible.

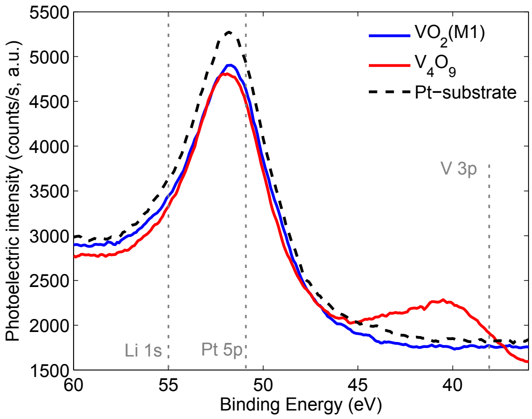

Figure 5.36: XPS measurement of vanadium oxides with high intensity platinum peak, hindering detection of lithium.

As a concluding remark, the only two samples in which the platinum peak was observed to this extent are samples annealed out of an amorphous film deposited with the H_2O process. In paragraph 5.2.2, was mentioned that the amorphous film deposited by the H_2O process needed to expand more upon formation of V_2O_5. Thus, a possible explanation could be that these two films suffered stresses upon expansion, inducing cracks in the surface of the film such that the platinum layer underneath became visible. However, AFM measurements on VO_2(M1) did not confirm this hypothesis, as the measured roughness of VO_2(M1) was low. Further understanding of the origin of the platinum peak was obtained by the XRD measurements and will be discussed in paragraph 5.6.3

The relative intensity of lithium counts by XPS measurement can be used to determine a rough estimation of the gravimetric capacity, by relative comparison of different phases. The obtained values should not be regarded as exact, since the margin of error is considerably large for this method, due to the low number of lithium counts.

5.6.2 Atomic Force Microscopy

Atomic force measurements of two lithiated samples are presented in figure 5.37. The root mean square roughness is given for both measurements. Comparison with the R_q values of a non-lithiated VO_2(M1) and V_2O_5 samples show that the roughness has slightly increased for the the VO_2(M1) sample and decreased for the V_2O_5 sample (see table 3.6). For the z-range, the identical evolution is observed. The z-range was respectively 21.4 nm (VO_2(M1)) and 31.2 nm(α-ϵ-δ V_2O_5). The white dots in figure 5.37a reveal the presence of some debris on the surface of the sample, these regions were excluded for the determination of the roughness.

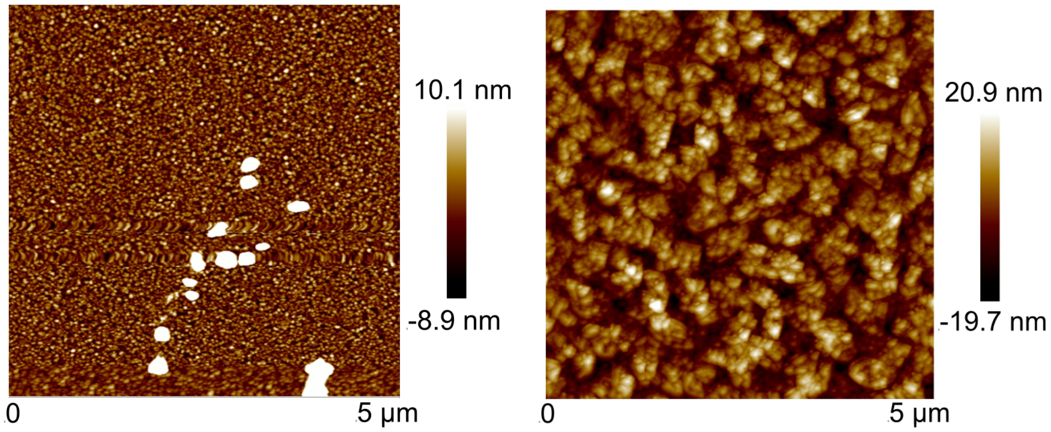

(a) VO_2(M1): R_q= 2.67 nm **(b)** α-ϵ-δ $Li_xV_2O_5$: R_q= 5.89 nm

Figure 5.37: AFM measurements on two lithiated vanadium oxides.

The evolution of the roughness upon lithiation can be understood intuitively by the expansion of the lattice upon intercalation of lithium. Expansion of the smooth VO_2(M1) surface increases the roughness. On contrary, the surface of V_2O_5 was rough prior to lithiation, such that expansion in all directions was possible instead of only in the z-direction, as for VO_2(M1). This results in a slightly more smooth surface, decreasing the R_q.

5.6.3 X-ray diffraction

Various lithiated vanadium oxide samples have been examined with XRD, see figure 5.38. All samples show a peak with low intensity at 27.3°, which can be associated to TiO_2(R). Since this peak was visible during the in-situ XRD anneals to obtain the various phases, prior to the electrochemical testing, it is not caused by side-reactions in the electrochemical cell. The depicted XRD spectra are limited to $2\theta = 35°$, because no peaks related to vanadium oxide were observed for larger values of 2θ.

Furthermore, figure 5.38 indicates that the vanadium oxide peaks visible before lithiation have disappeared, except for δ-LiV_2O_5. The δ-LiV_2O_5 phase, allowing reversible insertion of 1 lithium ion, still displays the peak at 20.2°, caused by reflection at the (001) plane of V_2O_5. In paragraph 5.1.1 was mentioned than no breaking of bonds is required such that the V_2O_5-lattice barely deforms when transformed to δ-V_2O_5. This could explain why the XRD peak of V_2O_5 is still visible after insertion of 1 lithium ion.

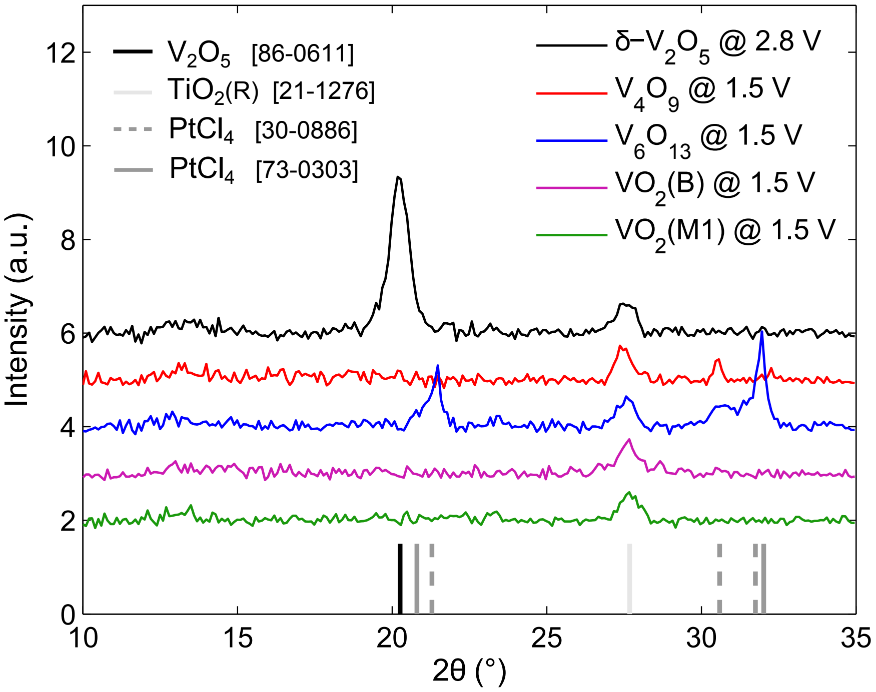

Figure 5.38: Ex-situ XRD measurement of various lithiated vanadium oxide samples.

The other vanadium oxides showed less ideal behaviour with respect to cycling, which possibly indicates that some deformation of the lattice is happening when lithium is intercalated. As a result, the long order structure is disturbed, causing the peaks in the XRD spectrum to disappear. An exception was VO_2(B), which behaved well upon cycling. However, the characteristic peaks of VO_2(B) (at 14.3°and 29.0°) have not been observed either.

For V_6O_{13}, two intense peaks have emerged at $2\theta = 21.5°$ and 32.0°, and a smaller one at 30.5°. As mentioned in paragraph 5.2.6, only one V_6O_{13} sample could be synthesised. Therefore, both the CD and cyclability experiment, in which heavy side-reactions were visible, were carried out on this sample. This XRD spectrum was measured after the cyclability experiment, such that side-reactions could be responsible for the occurring peaks at 21.5° and 32°. The database files of TiO, TiO_2, Ti_2O_3 and $PtCl_6$ (all discussed in par. 5.2.4) did not show agreement with the measured peaks. However, certain tabulated values for $PtCl_4$ did coincide with the measured peaks, see figure 5.38, where 2 database files for $PtCl_4$ are presented. A possible explanation is that Pt^{2+} ions were formed at approximately 4.2 V, which subsequently reacted with Cl^- ions of the electrolyte to $PtCl_4{}^{2-}$. A part of the $PtCl_4{}^{2-}$ was probably deposited on top of the vanadium oxide layer in crystalline form, giving rise to the measured peaks. The peak at 30.5° is also observed for V_4O_9, indicating that some side-reactions must have been present for the V_4O_9 sample too.

The observation of $PtCl_4$ on the surface of the V_6O_{13} and V_4O_9 samples brings new understanding concerning the XPS results. For these samples, a platinum peak was observed, which can now be interpreted as caused by $PtCl_4$. Thus, no cracks have to be present to obtain the Pt signal, which is in line with the smoothness of the surface obtained by AFM. By the same reasoning, $PtCl_4$ should be present on the surface of VO_2(M1) as well, although no sign of $PtCl_4$ was retrieved with XRD.

5.6.4 Cross-SEM images for volume expansion

Transition metal oxide electrodes often suffer large volume expansion due to lithium intercalation[109], and these drastic volume changes lead to decreased cycling life of the electrode[64]. With respect to vanadium oxides, several authors mention that large volume expansion is occurring[9,17,109], although numerical data is hard to obtain. Zhao et al. mentions that large volumetric changes are occurring for V_2O_5, while VO_2 is subject to a smaller degree of expansion[93]. As volume expansion can have a negative effect on the performance of the electrode, it is interesting to compare the different VO_x on this subject.

In order to obtain an expansion coefficient upon absorption of lithium, cross SEM images of several vanadium oxide samples were taken before and after lithiation. However, it is not straightforward to get clear images on this scale with the SEM. As a consequence, only 2 of the tested samples give clear results for both the pure and the lithiated sample, i.e. an amorphous film deposited with the O_3 process and a VO_2(B) sample. Figures 5.39 and 5.40 show the images, obtained by cross SEM, allowing determination of the film thickness.

The thickness of these 4 samples is summarized in table 5.6. The thickness expands with 26.5% and 33.3% for the two examined thin films, confirming that large expansion is occurring for vanadium oxide samples. Since the thickness of the films fluctuates, the obtained value for the volume expansion coefficient varies as well. Therefore, the expansion coefficients should not be regarded as exact values but merely as an indication of the order of magnitude of the expansion. The magnitude of expansion of both samples is comparable, which is not surprising as the amorphous film deposited with the O_3 process showed similarities with the VO_2(B) phase, as described in paragraph 5.2.1.

Table 5.6: The thickness of 2 samples, before and after lithiation and the obtained thickness expansion, with values obtained from cross SEM images.

Phase	cross-SEM thickness pure sample (nm)	cross-SEM thickness lithiated sample (nm)	Volume expansion upon lithiation (%)
VO_2(B)	46.5	58.8	26.5
amorphous layer (ALD O_3 process)	29.4	39.2	33.3

It would be interesting to examine all vanadium oxides to investigate if the volume expansion is of the same order. Thicker films could be used, such that qualitative cross SEM images can be obtained more easily and such that the relative error of the expansion coefficient is smaller. Limiting the expansion when lithium ions intercalate the structure, could result in better cycling behaviour[82].

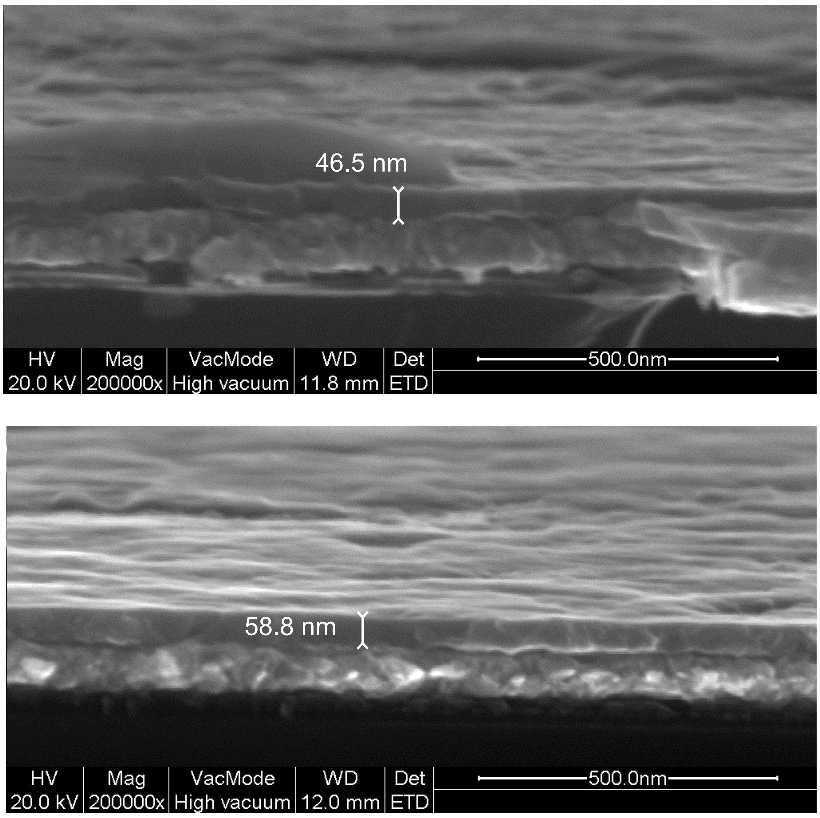

Figure 5.39: Cross SEM images of a VO_2(B) thin film before (up) and after (down) lithiation.

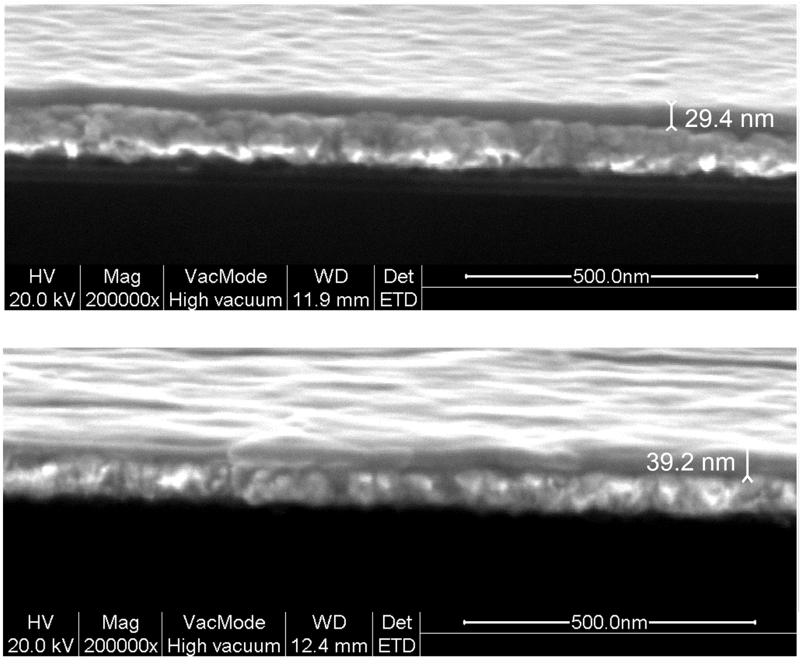

Figure 5.40: Cross SEM images of an amorphous sample, deposited with O_3 process, before (up) and after (down) lithiation.

5.7 Conclusion

Two ALD processes (H_2O-based and O_3-based) were used to deposit amorphous thin films of vanadium oxide. Post-deposition annealing in an atmosphere with controlled oxygen partial pressure allowed formation of six different phases on a Pt substrate, i.e. VO_2(B), VO_2(M1), V_2O_5, V_3O_7, V_4O_9 and V_6O_{13}. These six phases were examined by means of identical electrochemical procedures (CV, CD and cyclability) to investigate possible application as electrode for lithium ion batteries.

The cyclic voltammetry measurements granted information of the transition potential of the lithium intercalation processes. Accordance between several phases was observed, which could be explained by similarities in the lattices of the different vanadium oxides, confirming the theory that the V_nO_{2n+1} phases are related.

The charge/discharge measurements of the various phases allowed calculation of the capacity of the different electrodes and their dependence on the current density. The highest capacity was observed for V_4O_9 (536 mAh/g). V_2O_5, V_3O_7 and V_6O_{13} all yielded a lithiation capacity between 300 and 400 mAh/g for low currents. The capacity could be compared by theoretical values, associated with insertion of a certain number of lithium ions. The experimentally obtained results were in line with values reported in literature. Unwanted side-reactions were present for some samples, which could be related to several reactions with the substrate. Furthermore, information with respect to the rate capability was obtained from the CD measurements at different current rates. Except for V_2O_5, cycled in the α-ϵ-δ phases, all oxides suffered a considerate loss of capacity when higher currents were applied. Moreover, the loss of capacity was of the same order for most oxides (except V_3O_7). Although the capacity of α-ϵ-δ V_2O_5 is lower than nearly all other vanadium oxides, the very good rate capability makes it one of the most promising materials when higher currents are applied. The limits of this electrode were not yet reached and can be further examined. A last observation from the CD measurements was that the capacity is approximately inversely proportional to the density.

For application in LIB, the cycling behaviour of the electrode is crucial. The cyclability experiments showed that only 2 of the examined vanadium oxides don't suffer capacity loss upon cycling, i.e. VO_2(B) and α-ϵ-δ V_2O_5. If low charge and discharge currents are required, VO_2(B) should be considered, due to its larger initial capacity. However, because of the good rate capability, the capacity of α-ϵ-δ V_2O_5 exceeds VO_2(B) for higher currents, making it the most interesting of the different oxides when higher currents are required.

Finally, several lithiated samples were characterised by XPS, AFM, XRD and SEM. XPS was performed to directly measure the lithium concentration. Because of the high degree of error, caused by the low sensitivity for detection of lithium, no absolute quantified results could be obtained. However, by relative comparison of the lithium signal between the various phases, rough estimates of the capacity could be obtained. XPS further indicated that Pt was present on the surface for some samples. By XRD measurements, this could be interpreted as $PtCl_4^{2-}$, caused by side-reactions in the electrochemical cell. Various lithiated samples were examined with cross SEM to quantify the volume expansion upon lithiation, yet only two samples resulted in good measurements because of the difficulties associated with imaging layers of approximately 20 nm. These two samples indicated that the volume expansion was of the order of 25% to 30%. Decreasing the volume expansion upon lithiation could lead to enhanced cycling behaviour, such that this topic definitely deserves to be studied more in-depth in future research.

6

Vanadium oxide coated nanopillars as electrode material

Downsizing the electrodes to thin films causes a decrease in capacity since less material is available for insertion of lithium. To counter this decrease, thin films can be applied on three dimensional substrates with large surface area. In this work, the 2 ALD processes are applied for the deposition of a vanadium oxide film on silicon nanopillars. These coated nanopillars can then be used as electrode material for lithium ion batteries, thus combining the advantages of the fast mechanisms of lithium intercalation in thin films with obtaining a larger capacity because of the enhanced surface area.

6.1 ALD of vanadium oxide on nanopillars

SEM images of the nanopillars used in this work, are presented in figure 6.1. The nanopillars consist of silicon with thermally grown SiO_2. The width of the pillars is 1.749 μm on top and 3.080 μm at the bottom and the length is 55.3 μm. The pillars are oriented in lines with equal spacing to the closest two neighbours. Figure 6.1 illustrates that a surface element of 5.37 μm by 5.37 μm contains one nanopillar. Hence, the surface factor, i.e. the increase in surface by the presence of the pillar, can be estimated by:

$$\text{Surface factor} = \frac{x^2 + 2\pi \bar{r} h}{x^2} = \frac{5.37^2 + 2\pi * 1.21 * 55.3}{5.37^2} = 15.55 \qquad (6.1)$$

Where $\bar{r}$ is the average of the radius along the length of the pillar and h is the height of the nanopillar. The surface factor indicates that the total surface is 15.55 times larger than the surface of a flat substrate with equal dimensions.

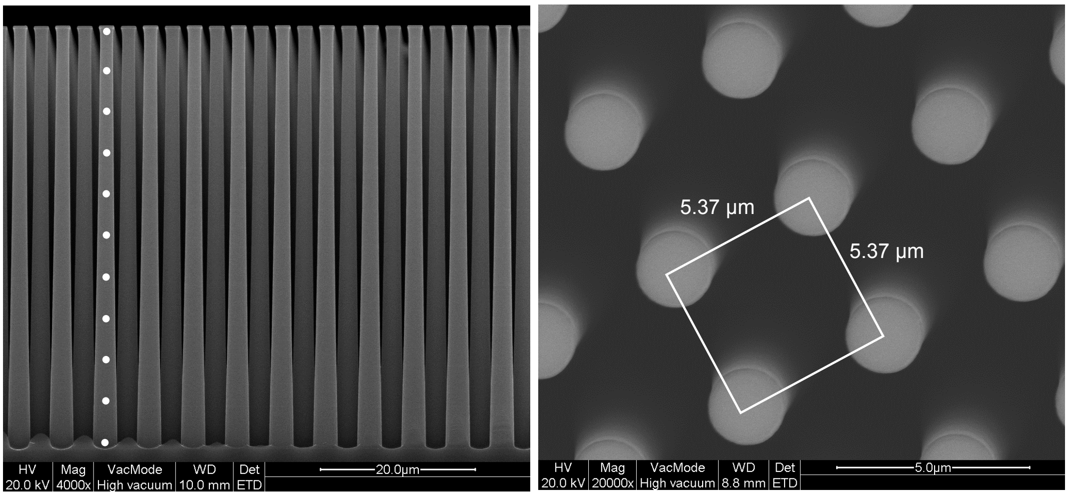

(a) cross SEM: Frontal view

(b) SEM: Top view

Figure 6.1: SEM images of the Si nanopillars, the white dots indicate points at which an EDX measurement is carried out.

Both the ozone and water based ALD processes were used to deposit a vanadium oxide thin film on the surface of the nanopillars. The advantage of ALD is that this technique allows deposition of a uniform layer on 3 dimensional structures if the precursor exposures are high enough. This is in contrast to other techniques, such as CVD, PVD and sol-gel. For these processes, deposition of a uniform film on 3D substrates is limited or not possible, see figure 2.2. To verify the uniformity of the deposited thin films, EDX measurements are performed.

6.2 Test of conformity layer with EDX

EDX analysis gives information regarding the elemental composition of a sample. In this case, the coated nanopillar is visualised with the SEM, allowing careful positioning on the nanopillar of the electron source for the EDX measurement. Thus, the EDX spectrum and corresponding elemental composition of a specific point along the nanopillar can be measured. By performing a single measurement every 5 μm, a composition profile can be determined and the conformity of the layer can be checked. In figure 6.1, the locations at which an EDX measurement was performed are indicated by a white dot. For one EDX measurement, the sample is bombarded for 50 seconds with 20 keV electrons.

The electrons have high energy and penetrate the sample, such that the elemental composition up to a given depth is measured. Because the nanopillar is conical, its cross section is larger at the bottom than at the top. This means that the silicon signal will be larger at the bottom. As a result, it is not possible to use the silicon signal to determine the atom percentage of vanadium measured. However, the evolution of the raw vanadium signal can be examined with respect to the depth along the nanopillar.

6.2.1 Comparison of the H_2O and O_3 processes

Figure 6.2 shows the evolution of the number of vanadium counts along the length of one nanopillar, measured with EDX. The total number of vanadium counts is higher for the film deposited with the H_2O process, which is not surprising since it is established that the density of the H_2O film is higher than the density of the amorphous film deposited with the O_3 process, such that the H_2O process requires more vanadium atoms for a layer of equal thickness. Furthermore, it is clear that the vanadium oxide layer is not uniform and that the thickness is lower at the bottom of the pillar. Apparently, insufficient time was available for the precursor gases to penetrate the gaps between the nanopillars and for the growth to saturate. The evolution of the vanadium counts on the film deposited by the O_3 process shows that a rather uniform layer is present until a depth of 20 μm is reached, afterwards the thickness starts to decrease.

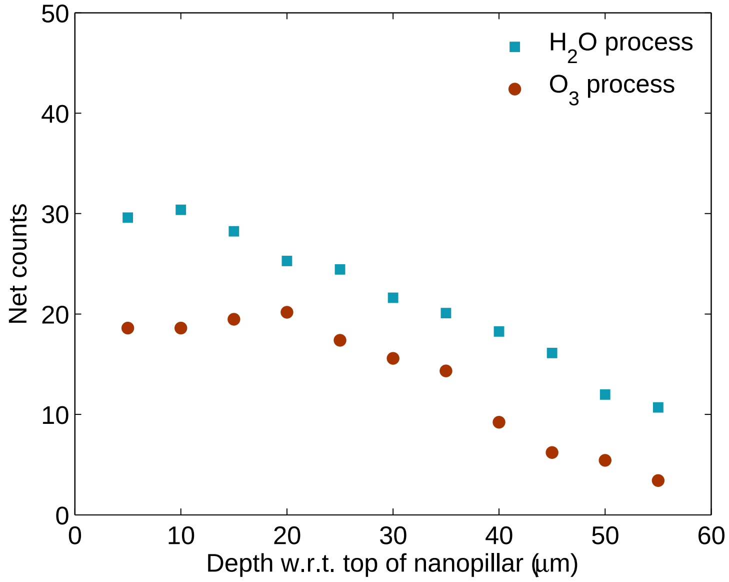

Figure 6.2: Evolution of the vanadium signal, measured with EDX, along the length of one nanopillar. The conformity of amorphous layers deposited with the two ALD processes is examined.

6.2.2 Prolongating the precursor pulses to increase conformity

The conformity of the layer deposited with the H_2O process was further examined. More specific, longer pulses were applied in order to increase the conformity of the deposited film. The standard length of both TEMAV and H_2O pulses was 5 seconds for the H_2O process, which was increased to 10 seconds for both precursors. In addition, the vacuum pump was closed during the pulses, while it operated constantly during pulses in the standard setting of the ALD process. As a consequence of these two measures, more precursor molecules were present in the reaction chamber and more time was allowed to penetrate into the gaps between the pillars and interact with the lower regions on the sample. The result on the conformity is displayed in figure 6.3.

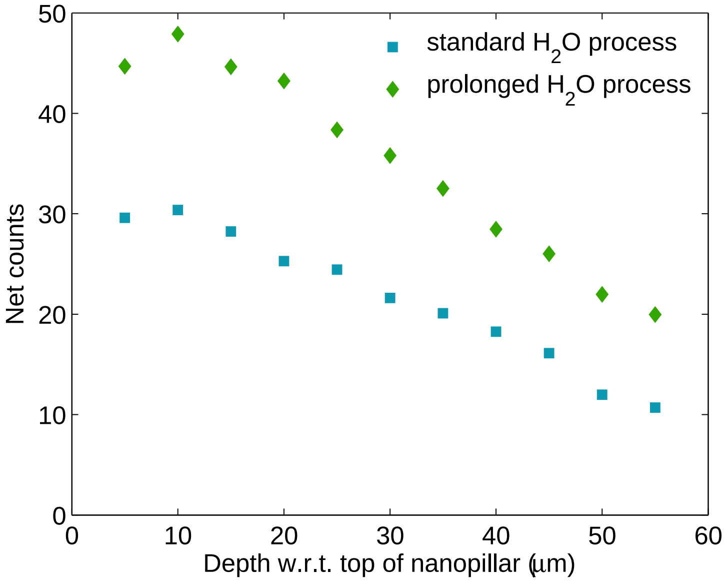

Figure 6.3: Evolution of the vanadium signal, measured with EDX, along the length of one nanopillar. The influence of longer precursor exposure on the conformity of the thin film is investigated.

More vanadium counts are recorded along the entire profile of the nanopillar. The increase on the top of the pillar indicates that the growth was not saturated on the top either previously. A result that is not surprising, since the total surface of the nanopillars is 15.55 times larger than the surface of a flat sample. The available precursor molecules must be spread over the larger surface, such that the density of molecules available on top is insufficient to saturate the growth. Figure 6.3 also illustrates that a rather uniform layer is deposited within the first 20 μm below the top, afterwards a decrease in film thickness is observed. Further increase of the precursor pulses would result in a more uniform layer. Nevertheless, this is not pursued in this work. The prolonged ALD process already required 16 hours to complete. As a concluding remark on this matter, it was shown on other samples that the shape of the pillars has an effect to some extent on the shape of the EDX spectrum. However, no clear relation was found so far.

6.2.3 A platinum coated nanopillar for current collection

If the nanopillar with thin vanadium oxide film is tested as electrode material, lithium ions are inserted into the material, resulting in a current. As both the silicon and the vanadium oxide are not sufficiently conducting, an extra conducting layer should be applied underneath the vanadium oxide thin film. The material used as current collector in this case is a platinum layer, exactly as for the films on flat surfaces. The platinum layer is deposited on the entire surface of the nanopillars by an ALD process, as reported by Dendooven et al.[110]. The conformity of this platinum layer is not crucial, although it is important that the entire surface is covered. Otherwise, the current generated by a part of the surface cannot be extracted.

The ALD process, described by Dendooven et al., used (Methylcyclopentadienyl)trimethylplatinum ($MeCpPtMe_3$) and ozone as precursor gases[110]. The nanopillars were heated to 200 °C. A pulse of 10 seconds was applied for $MeCpPtMe_3$ while the vacuum pump was closed, followed by 10 seconds of additional exposure. For the O_3 precursor, a pulse of 8 seconds was followed by 5 seconds of additional exposure. This allowed the pressure to rise to 8.10^{-1} mbar and 1 mbar for the platinum-precursor and ozone, respectively. 200 cycles were performed, resulting in the deposition of a platinum layer of several nanometer on the surface of the nanopillars. Afterwards, the prolonged H_2O process was applied for the deposition of a vanadium oxide film on top of the platinum layer.

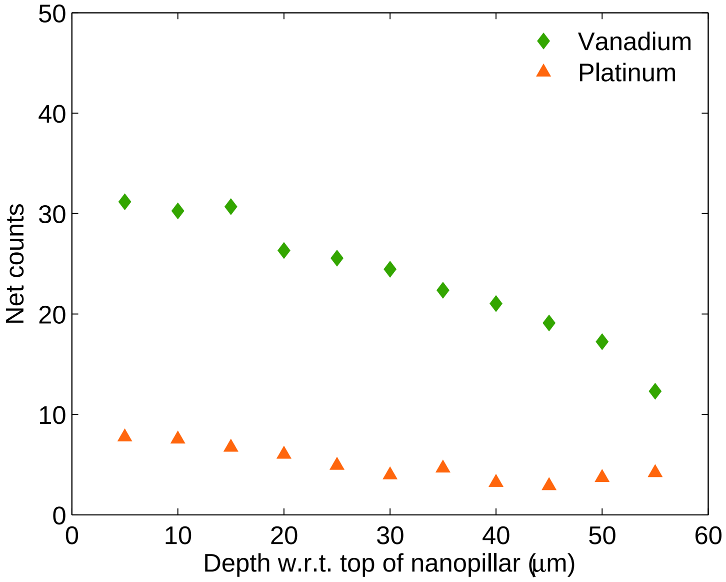

Figure 6.4: Evolution of the V and Pt signals, measured with EDX, along the length of one nanopillar.

The platinum and vanadium concentration are measured with EDX along the depth of the nanopillar. Figure 6.4 shows that the conformity of the Pt-layer is rather good. Most important is that a platinum signal is recorded on the entire length of the pillar, such that the current path is closed and that lithium insertion over the entire surface can contribute to the current.

6.3 Electrochemical testing of V_2O_5 coated nanopillars

In the previous chapter was concluded that V_2O_5 (more specifically the α-ϵ-δ phases) and VO_2(B) are the most promising vanadium oxides for applications in lithium ion batteries. In this study, the vanadium oxide film deposited on the nanopillars was annealed to V_2O_5, which was performed by heating the sample to 500 °C in pure air. The temperature was raised at a rate of 2 °C/s to 300 °C and further by 1 °C/s to 500 °C. When this temperature was reached, it was kept at 500 °C for 3 minutes, allowing all vanadium oxide to crystallize into V_2O_5. Afterwards, an ex-situ XRD measurement was carried out, of which the measured spectrum is displayed in figure 6.5.

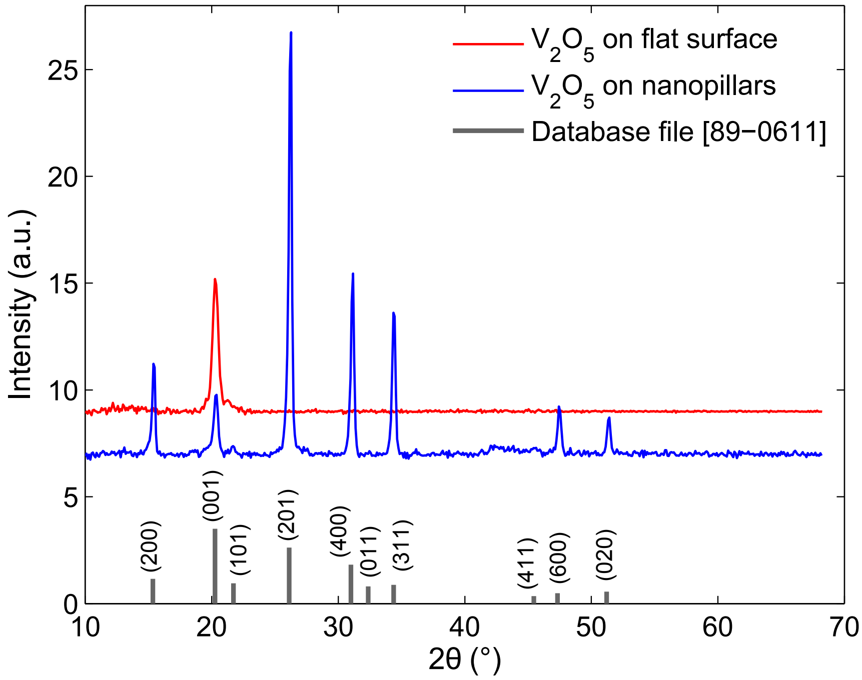

Figure 6.5: Ex-situ XRD measurement of V_2O_5 layer on the surface of nanopillars and on a flat substrate. The database file used for identification of the peaks is given, as well as the (hkl) values of the planes responsible for the given peak.

The spectrum of the XRD measurement of the V_2O_5 coated nanopillar is compared with the spectrum of V_2O_5 on a flat surface. A y-offset is imposed to both spectra to enhance the visibility. For the layer on the flat surface, only one peak is present, at approximately $2\theta = 20°$. In contrast, the V_2O_5 on the surface of the nanopillar yields many peaks in the XRD spectrum. The difference is caused by the orientation of the atomic layers with respect to the incident X-ray beam. When a flat substrate is used, only the atomic spacing perpendicular to the substrate can be measured. All atomic layers of V_2O_5 are aligned and only one peak is retrieved. The same principles result in many peaks for the coated nanopillar, as the surface of the nanopillar has planes with both horizontal and vertical orientation. Thus, for the V_2O_5 on top of the nanopillar, interatomic distances of different orientations are measured.

Electrochemical behaviour of the nanopillars with V_2O_5 thin film

The standard procedures of chapter 5 are carried out on the nanopillar with V_2O_5 thin film. The V_2O_5 layer is examined in the α-ϵ-δ phases, where one lithium ion can be inserted reversibly per V_2O_5. The cyclic voltammetry experiment was carried out at a rate of 0.001 V/s, which is a factor 10 lower than for the flat surfaces to prevent severe potential differences between anodic and cathodic peak induced by high currents, see equation 4.14. Figure 6.6a contains the voltammogram of the coated nanopillar. The expected peaks are observed and all cycles coincide perfectly, indicating good reversibility of the process.

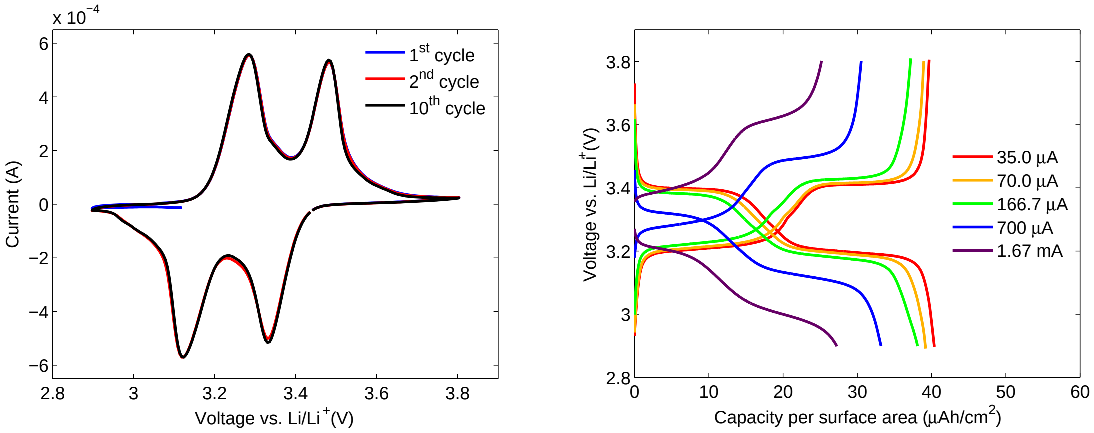

(a) CV at 1 mV/s **(b)** CD

Figure 6.6: CV and CD measurement of α-ϵ-δ V_2O_5 on the surface of nanopillars

A galvanostatic charge/discharge is performed at different C-rates to analyze the influence of the charge rate on the capacity. The results are shown in figure 6.6b. The capacity per surface area must be interpreted as surface area of the test cell instead of surface of the V_2O_5 film. Because of the shape of the nanopillars, the latter is substantially higher than the surface of the test cell. The V_2O_5 coated nanopillar shows a good rate capability for currents up to 166.7 μA. A capacity value of 40.38 μAh/g is obtained. The capacity of the V_2O_5 film with equal amount of ALD cycles was 1.42 μAh/g, which means a capacity increase with a factor 28.4 is observed. As the surface of the nanopillars was approximately 15.55 times the surface of the flat film, one would expect the increase in capacity to be 15.55. However, for the deposition of the film on the nanopillars, the procedure of the ALD process was adjusted. The exposure time to both precursors was doubled and the valve to the vacuum pump was closed during the precursor pulses. The capacity increase in the CD measurement indicates that the modifications of the ALD process lead to the deposition of a layer with increased thickness.

Figure 6.6b further indicates that a drop in capacity was observed when a current of 700 μA was used, which corresponds to a C-rate of 21.81 C. The decrease of capacity with respect to the applied charge rate of the V_2O_5 film on the surface of the nanopillars is compared with a V_2O_5 film on a flat Pt surface.

Table 6.1: Comparison of capacity decrease under influence of increasing current for α-ϵ-δ V_2O_5 films on flat surface and nanopillars

α-ϵ-δ V_2O_5 on flat substrate			**α-ϵ-δ V_2O_5 on surface nanopillars**		
Current (μA)	*C-rate*	*Relative capacity w.r.t. 3.33 μA (%)*	*Current (μA)*	*C-rate*	*Relative capacity w.r.t. 35 μA (%)*
3.33	2.40	100	35.0	0.90	100
6.67	4.93	96.7	70.0	1.84	97.1
16.7	12.63	95.1	166.7	4.61	94.4
66.7	52.17	93.2	700.0	24.82	82.2
166.7	133.33	90.1	1666.7	63.15	67.4

In the case of the α-ϵ-δ V_2O_5 film on the surface of the nanopillars, the capacity decreases faster with increasing charge rate. This could be caused by limited lithium supply by the electrolyte. Due to the narrow gaps, less electrolyte is available per surface area. When the charge rate increases, the supply of lithium by the electrolyte could be too slow, resulting in a decrease of capacity. An alternative explanation could be that the increased thickness (caused by the prolonged precursor exposure) reaches the critical thickness for slower diffusion mechanisms to influence the lithium insertion process at high current rates. This could be investigated by coating a flat surface with a thin film by the prolonged ALD process, to evaluate which explanation is legitimate.

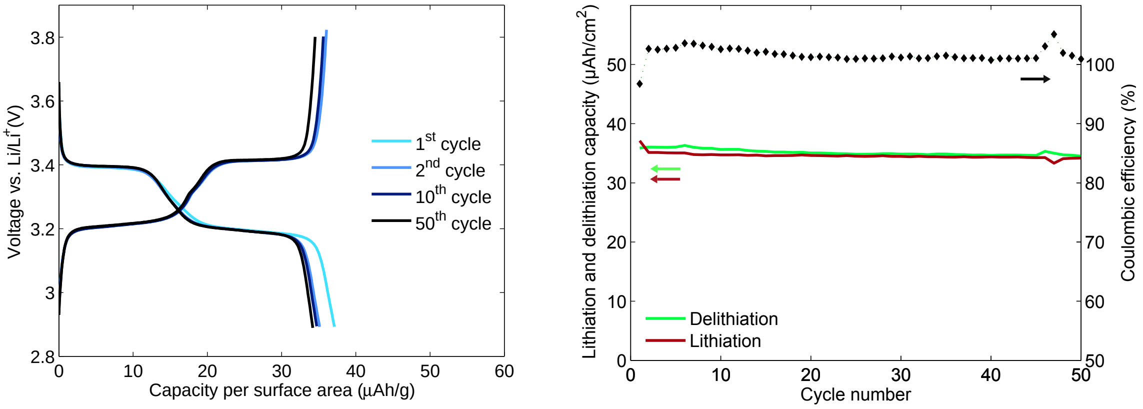

(a) Voltage vs. capacity

(b) Total capacity and efficiency per cycle

Figure 6.7: Cyclability testing of Si nanopillars, coated with α-ϵ-δ V_2O_5 at a current of 70 μA, corresponding to 1.94 C.

A cyclability experiment is performed on the nanopillars with α-ϵ-δ V_2O_5 film. Figure 6.7a shows the excellent cyclability behaviour of the sample. A small loss in capacity is observed after the first cycle. The coulombic efficiency remains constantly higher than 95%.

6.4 Conclusion

The aim of this work was to investigate thin films of vanadium oxide for application as lithium ion battery electrode. The main advantage of reducing the size of the electrode to a thin film is that faster surface kinetics govern the intercalation process, which is diffusion limited in traditional electrodes. To increase the total capacity, three dimensional structures with enhanced surface area were used. Since a certain level of conformity of the film thickness on the 3D substrate was desired, ALD processes were applied for the deposition of the vanadium oxide film.

Silicon nanopillars were coated with vanadium oxide by 2 processes, more specifically a water and ozone based ALD process, both using TEMAV as vanadium precursor. The conformity of the thin films was investigated by means of EDX measurements along the length of one nanopillar. As a decreased signal was measured on the bottom of the pillars, the exposure of the precursors was increased, illustrating that this leads to better results. Afterwards, the silicon nanopillars were prepared for electrochemical testing by coating them with Pt, required for current collection, before deposition of the vanadium oxide.

In chapter 5 was established that α-ϵ-δ V_2O_5 and VO_2(B) are most promising among the various vanadium oxides, for applications in LIB. As α-ϵ-δ V_2O_5 has a better rate capability and easier synthesis, the films on the nanopillars were crystallised to α-ϵ-δ V_2O_5 by annealing in air at 500°C. Electrochemical testing revealed that a lower rate capability is observed on three dimensional substrates, compared to the flat substrate. Limited supply of lithium ions by the electrolyte could be a plausible explanation, though further testing is required. Finally, a cyclability experiment indicated that barely any capacity loss occurs upon cycling, confirming the promising behaviour of the α-ϵ-δ V_2O_5 layer on three dimensional substrates.

To conclude, atomic layer deposition was succesfully applied in this work for synthesis of electrodes on the surface of nanostructures. Future research can investigate if these nanostructured electrodes can lead to enhanced cycling behaviour and increased power density, such that nanostructured electrodes could eventually lead to the next generation of lithium-ion batteries. Furthermore, research of ALD for lithium-ion batteries can also examine the possibilities of deposition of ultrathin multifunctional coatings to modify existing electrodes to boost their performance.

A

Systematical study of annealing of vanadium oxide films

Three substrates and two processes were used for deposition of vanadium oxide films. The results of the annealing study of the thin films on SiO_2 are discussed in 3.7.2. The results for TiN and Pt substrates are presented below.

Thin film deposited with H_2O-process on TiN

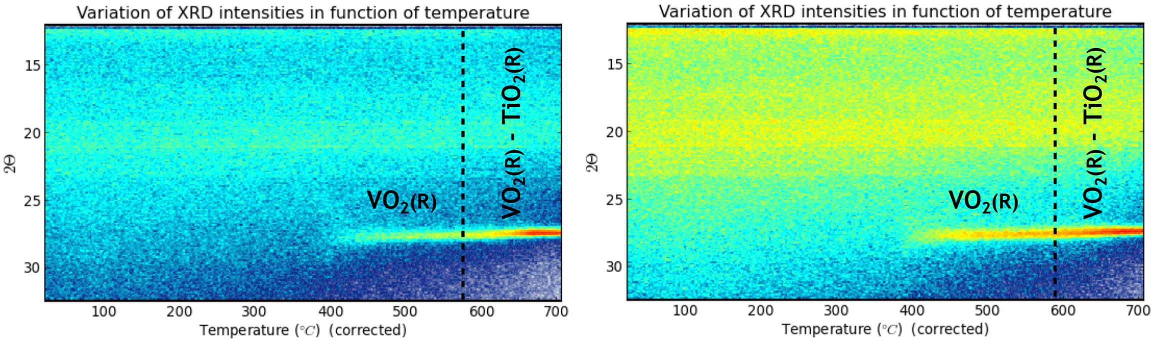

(a) 3.7 Pa **(b)** 14.8 Pa

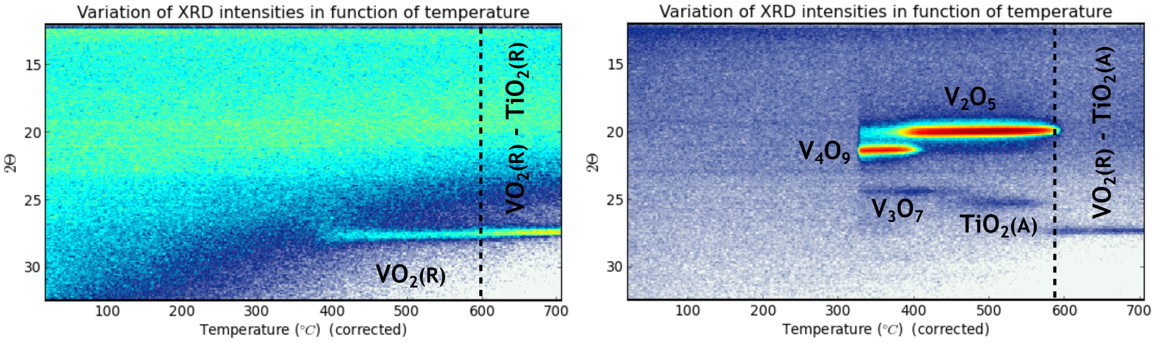

(c) 48.1 Pa **(d)** Air

Figure A.1: Systematical study of phase formation by thermal annealing of amorphous vanadium oxide films with H_2O process on TiN-substrate in atmosphere with controlled oxygen level.

Thin film deposited with O_3-process on TiN

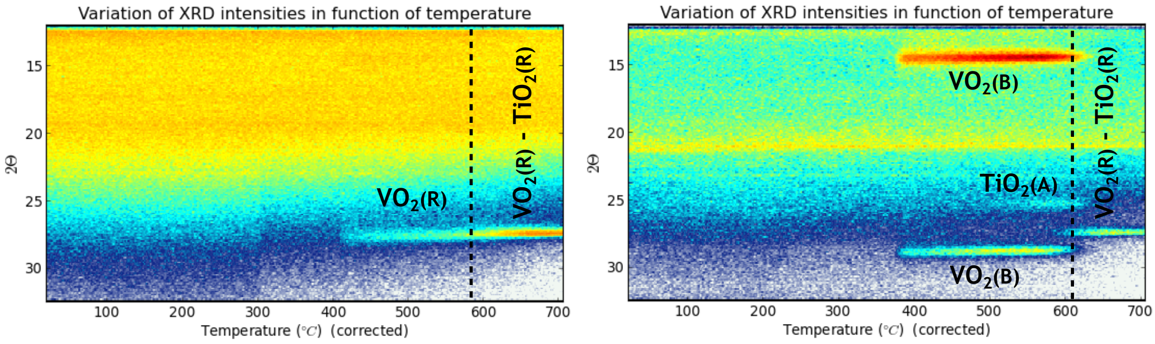

(a) 3.7 Pa

(b) 7.4 Pa

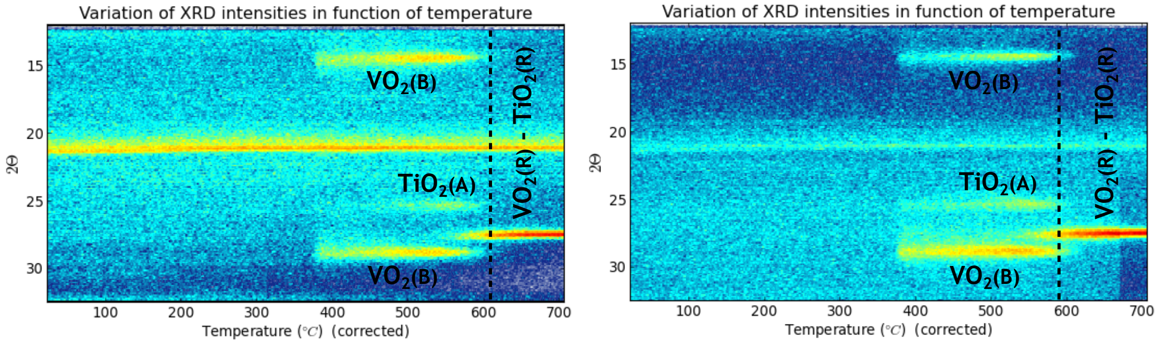

(c) 14.8 Pa

(d) 29.6 Pa

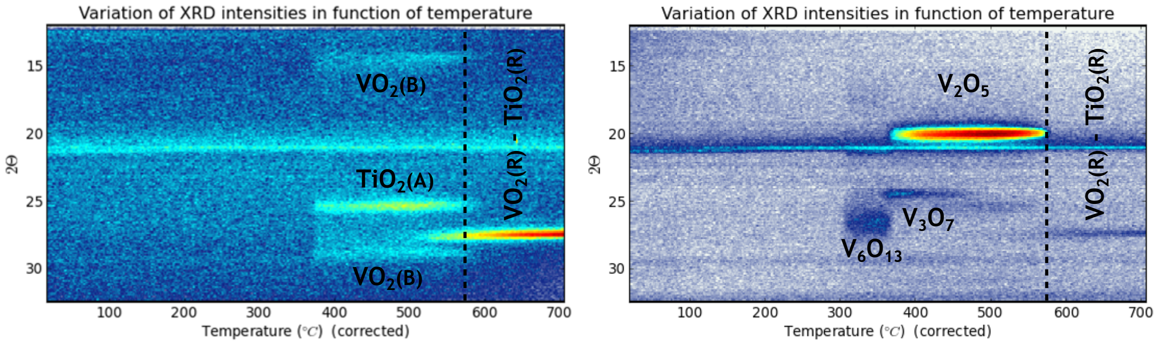

(e) 48.1 Pa

(f) Air

Figure A.2: Systematical study of phase formation by thermal annealing of amorphous vanadium oxide films with O_3 process on TiN-substrate in atmosphere with controlled oxygen level.

Thin film deposited with O_3-process on Pt

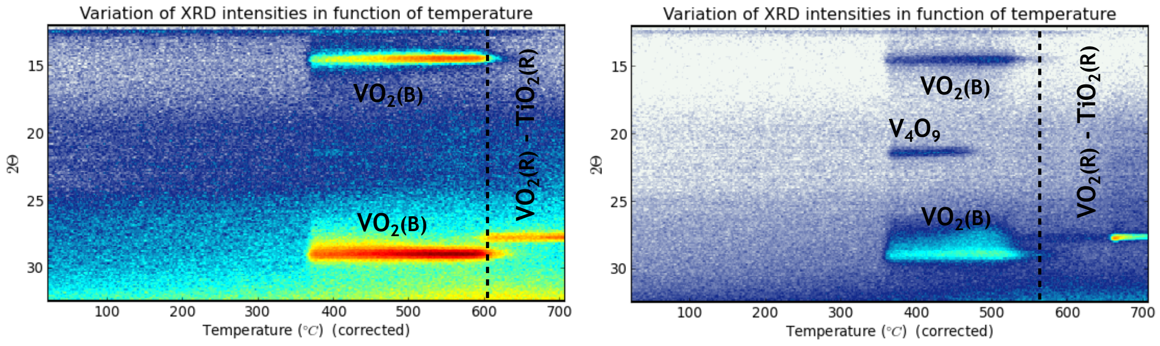

(a) 3.7 Pa **(b)** 14.8 Pa

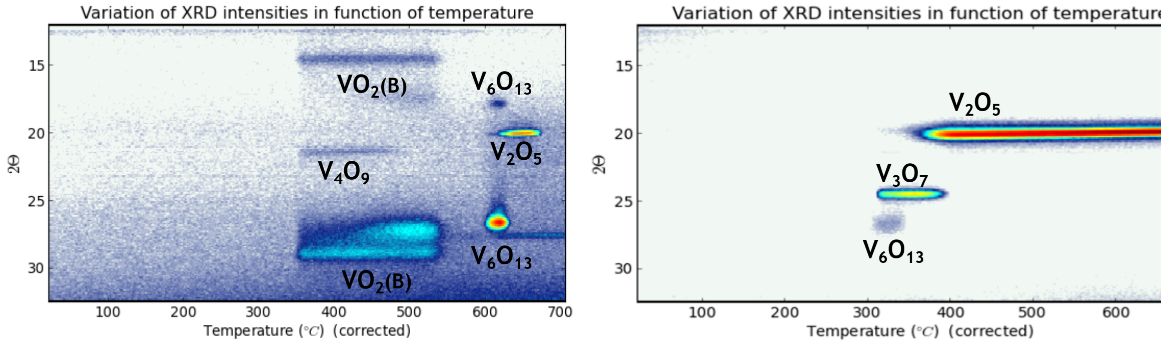

(c) 48.1 Pa **(d)** Air

Figure A.3: Systematical study of phase formation by thermal annealing of amorphous vanadium oxide films with O_3 process on Pt-substrate in atmosphere with controlled oxygen level. An unidentified background signal at $2\theta=21°$ was observed.

Thin film deposited with H_2O-process on Pt

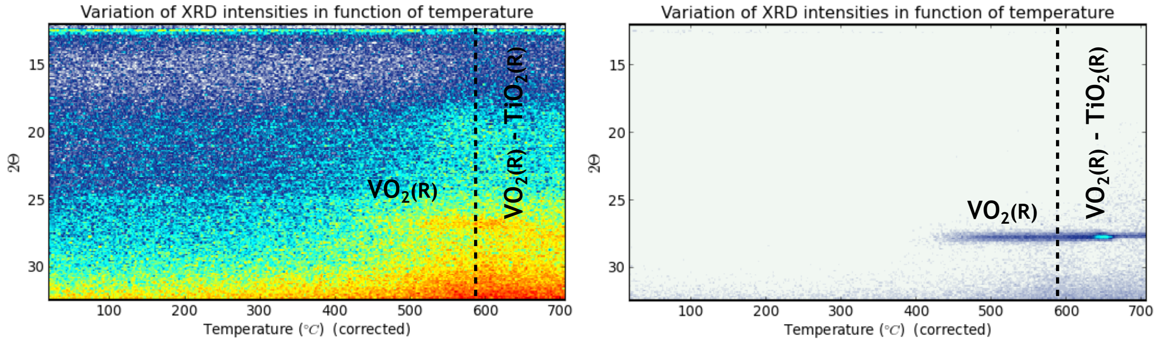

(a) 3.7 Pa **(b)** 14.8 Pa

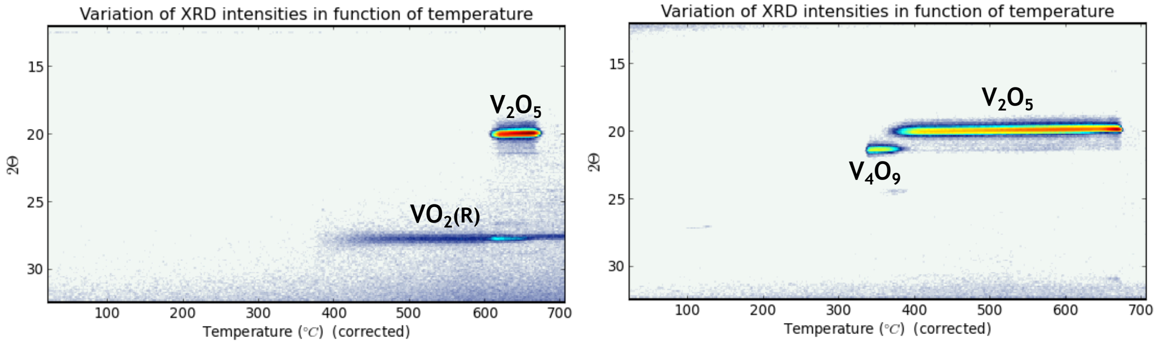

(c) 48.1 Pa **(d)** Air

Figure A.4: Systematical study of phase formation by thermal annealing of amorphous vanadium oxide films with H_2O process on Pt-substrate in atmosphere with controlled oxygen level.

Bibliography

[1] J. Sousanis, "Wardsauto, the information center for and about the global auto industry." `http://wardsauto.com/ar/world_vehicle_population_110815`, aug 15 2011. World vehicle population.

[2] "Fast Facts, U.S. Transportation Sector Greenhouse Gas Emissions 1990-2011." `http://www.epa.gov/otaq/climate/documents/420f13033a.pdf`. EPA, United States Environment Protection Agency.

[3] M. M. Doeff, *Batteries for Sustainability: selected entries from the encyclopedia of sustainability science and technology*. Springer, 2013.

[4] D. Linden and T. B. Reddy, *Handbook of Batteries*. McGraw-Hill, 2002.

[5] J. B. Goodenough and K.-S. Park, "The Li-ion Rechargeable Battery: A Perspective," *Journal of the American Chemical Society*, vol. 135, pp. 1167–1176, 2013.

[6] J. Jiang, Y. Li, J. Liu, X. Huang, C. Yuan, and X. W. D. Lou, "Recent Advances in Metal Oxide-based Electrode Architecture Design for Electrochemical Energy Storage," *Advanced Materials*, vol. 24, no. 38, pp. 5166–5180, 2012.

[7] X. Meng, X.-Q. Yang, and X. Sun, "Emerging Applications of Atomic Layer Deposition for Lithium-Ion Battery Studies," *Advanced Materials*, vol. 24, no. 27, pp. 3589–3615, 2012.

[8] M. Green, E. Fielder, B. Scrosati, M. Wachtler, and J. S. Moreno, "Structured Silicon Anodes for Lithium Battery Applications," *Electrochem. Solid-State Letters*, vol. 6, no. 5, pp. 75–79, 2003.

[9] M. C. Rao, "Vanadium Pentoxide Cathode Material for Fabrication of All Solid State Lithium-Ion Batteries - A Case Study," *Research Journal of Recent Sciences*, vol. 2, no. 3, pp. 67–73, 2013.

[10] B. Stegemann, M. Klemm, S. Horn, and M. Woydt, "Switching adhesion forces by crossing the metal-insulator transition in Magnéli-type vanadium oxide crystals," *Beilstein Journal of Nanotechnology*, vol. 2, pp. 59–65, 2011.

[11] C. Delmas, H. Cognac-Auradou, J. Cocciantelli, M. Menetrier, and J. Doumerc, "The $Li_xV_2O_5$ system: An overview of the structure modifications induced by the lithium intercalation," *Solid State Ionics*, vol. 69, no. 3, pp. 257–264, 1994.

[12] L. Fan, Y. Wu, C. Si, C. Zou, Z. Qi, L. Li, G. Pan, and Z. Wu, “Oxygen pressure dependent VO_2 crystal film preparation and the interfacial epitaxial growth study ,” *Thin Solid Films*, vol. 520, no. 19, pp. 6124 – 6129, 2012.

[13] C. Leroux, G. Nihoul, and G. Van Tendeloo, “From VO_2(B) to VO_2(R): Theoretical structures of VO_2 polymorphs and in situ electron microscopy,” *Phys. Rev. B*, vol. 57, pp. 5111–5121, Mar 1998.

[14] G.-H. Liu, X.-Y. Deng, and R. Wen, “Electronic and optical properties of monoclinic and rutile vanadium dioxide,” *Journal of Materials Science*, vol. 45, no. 12, pp. 3270–3275, 2010.

[15] H. Guo, K. Chen, Y. Oh, K. Wang, C. Dejoie, S. A. Syed Asif, O. L. Warren, Z. W. Shan, J. Wu, and A. M. Minor, “Mechanics and Dynamics of the Strain-Induced M1-M2 Structural Phase Transition in Individual VO_2 Nanowires,” *Nano Letters*, vol. 11, no. 8, pp. 3207–3213, 2011.

[16] H. Katzke, P. Toledano, and W. Depmeier, “Theory of morphotropic transformations in vanadium oxides,” *Phys. Rev. B*, vol. 68, p. 024109, Jul 2003.

[17] A. Manthiram and J. Kim, “Low Temperature Synthesis of Insertion Oxides for Lithium Batteries,” *Chemistry of Materials*, vol. 10, no. 10, pp. 2895–2909, 1998.

[18] K. West, B. Zachau-Christiansen, T. Jacobsen, and S. Atlung, “V_6O_{13} As cathode material for lithium cells,” *Journal of Power Sources*, vol. 14, no. 1, pp. 235–245, 1985.

[19] H. A. Wriedt, “The (O-V) Oxygen-Vanadium System,” *Bulletin of Alloy Phase Diagrams*, vol. 10, no. 3, p. 271, 1989.

[20] M. Putkonen, “Atomic Layer Deposition: Future trends in ALD research.” `https://noppa.aalto.fi/noppa/kurssi/s-69.4114/luennot/S-69_4114_ald_basics_and_future_trends.pdf`. Aalto University Scool of science and technology.

[21] B. Fultz and J. Howe, “Tranmission Electron Microscopy and Diffractometry of Materials,” *Graduate Texts in Physics*, pp. 1–58, 2013.

[22] M. Yasaka, “X-ray thin-film measurement techniques: X-ray reflectivity measurement,” *The Rigaku Journal*, vol. 26, no. 2, pp. 1–9, 2010.

[23] M. Birkholz, P. F. Fewster, and C. Genzel, *Thin Film Analysis by X-Ray Scattering*. Wiley-VCH, 2006.

[24] H. Kiessig, “Untersuchungen zur Totalreflexion von Röntgenstrahlen,” *Annalen der Physik*, vol. 402, no. 6, pp. 715–168, 1931.

[25] T. L. Alford, L. C. Feldman, and J. W. Mayer, *Fundamentals of Nanoscale Film Analysis*. Springer, 2007.

[26] G. Silversmit, D. Depla, H. Poelman, G. B. Marin, and R. D. Gryse, "Determination of the V2p XPS binding energies for different vanadium oxidation states (V^{5+} to V^{0+})," *Journal of Electron Spectroscopy and Related Phenomena*, vol. 135, no. 2, pp. 167 – 175, 2004.

[27] "SEM: Imaging with Secondary Electrons." `http://www.microscopy.ethz.ch/se.htm`. ETH, Swiss Federal Institute of Technology Zurich.

[28] H.-J. Butt, B. Cappella, and M. Kappl, "Force measurements with the atomic force microscope: Technique, interpretation and applications," *Surface Science Reports*, vol. 59, no. 1, pp. 1 – 152, 2005.

[29] N. Jalili and K. Laxminarayana, "A review of atomic force microscopy imaging systems: application to molecular metrology and biological sciences," *Mechatronics*, vol. 14, no. 8, pp. 907 – 945, 2004.

[30] "Geobacter." `http://www.geobacter.org/Nanowires`. University of Massachusetts Amherst.

[31] M. Raposo, Q. Ferreira, and P. a. Ribeiro, "A Guide for Atomic Force Microscopy Analysis of Soft- Condensed Matter," *Modern Research and Educational Topics in Microscopy*, pp. 758–769, 2007.

[32] J. C. Badot, S. Ribes, E. B. Yousfi, V. Vivier, J. P. Pereira-Ramos, N. Baffier, and D. Lincot, "Atomic Layer Epitaxy of Vanadium Oxide Thin Films and Electrochemical Behavior in Presence of Lithium Ions," *Electrochemical and Solid-State Letters*, vol. 3, no. 10, pp. 485–488, 2000.

[33] P. Dagur, A. U. Mane, and S. Shivashankar, "Thin films of VO_2 on glass by atomic layer deposition: microstructure and electrical properties," *Journal of Crystal Growth*, vol. 275, pp. 1223–1228, 2005.

[34] T. Blanquart, J. Niinisto, M. Gavagnin, V. Longo, M. Heikkila, E. Puukilainen, V. R. Pallem, C. Dussarat, M. Ritala, and M. Leskela, "Atomic layer deposition and characterization of vanadium oxide thin films," *RSC Advances*, vol. 3, pp. 1179–1185, 2013.

[35] G. Rampelberg, M. Schaekers, K. Martens, Q. Xie, D. Deduytsche, B. D. Schutter, N. Blasco, J. Kittl, and C. Detavernier, "Semiconductor-metal transition in thin VO_2 films grown by ozone based atomic layer deposition," *Applied Physics Letters*, vol. 98, pp. 162902–162904, 2011.

[36] P. A. Premkumar, M. Toeller, I. P. Radu, C. Adelmann, M. Schaekers, J. Meersschaut, T. Conard, and S. V. Elshocht, "Process study and characterization of VO_2 thin films synthesized by ALD using TEMAV and O3 precursors," *ECS Journal of Solid State Science and Technology*, vol. 1, no. 4, pp. 169–174, 2012.

[37] M. Pemble, I. Povey, and F. Chalvet, "Developments in the Understanding of ALD Processes and Applications of ALD in Critical Technologies," *ECS Trans.*, vol. 11, no. 7, pp. 155–166, 2007.

[38] M.-G. Willinger, G. Neri, E. Rauwel, A. Bonavita, G. Micali, and N. Pinna, "Vanadium Oxide Sensing Layer Grown on Carbon Nanotubes by a New Atomic Layer Deposition Process," *Nano Letters*, vol. 8, no. 12, pp. 4201–4204, 2008.

[39] J. Tiilikainen, J.-M. Tilli, V. Bosund, M. Mattila, T. Hakkarainen, J. Sormunen, and H. Lipsanen, "Accuracy in x-ray reflectivity analysis," *Journal of Physics D: Applied Physics*, vol. 40, no. 23, p. 7497, 2007.

[40] C. M. Hastings, "Synthesis of VO_2 Nanostructures for Infrared Modulation Applications," master's dissertation, University of Zululand, November 2009.

[41] W. Bruckner, H. Oppermann, and W. Reichelt, "Vanadium oxide: synthesis, properties, application," *In Berlin: Akad.-Verl.*, vol. 12, pp. 252–255, 1983.

[42] Y. Ningyi, L. Jinhua, and L. Chenglu, "Valence reduction process from sol-gel V_2O_5 to VO_2 thin films," *Applied Surface Science*, vol. 191, no. 1, pp. 176 – 180, 2002.

[43] A. Sidorov, O. P. Vinogradova, I. E. Obyknovennaya, and T. A. Khrushchova, "Synthesis and optical properties of vanadium dioxide nanoparticles in nanoporous glasses," *Technical Physics Letters*, vol. 33, pp. 581–582, 2007.

[44] J. B. MacChesney, J. F. Potter, and H. J. Guggenheim, "Preparation and Properties of Vanadium Dioxide Films," *J. Electrochem. Soc.: Solid State Science*, vol. 115, no. 1, pp. 52–55, 1968.

[45] B.-G. Chae, H.-T. Kim, S.-J. Yun, B.-J. Kim, Y.-W. Lee, D. Youn, and K.-Y. Kang, "Highly Oriented VO_2 Thin Films Prepared by Sol-Gel Deposition," *Electrochemical and Solid-State Letters*, vol. 9, no. 1, pp. 12–14, 2006.

[46] H. Wang, X. Yi, and S. Chen, "Low temperature fabrication of vanadium oxide films for uncooled bolometric detectors," *Infrared Physics and Technology*, vol. 47, no. 3, pp. 273 – 277, 2006.

[47] X. Wang, H. Li, Y. Fei, X. Wang, Y. Xiong, Y. Nie, and K. Feng, "XRD and Raman study of vanadium oxide thin films deposited on fused silica substrates by RF magnetron sputtering," *Applied Surface Science*, vol. 177, no. 1, pp. 8 – 14, 2001.

[48] G. Rampelberg, D. Deduytsche, B. D. Schutter, P. A. Premkumar, M. Toeller, M. Schaekers, K. Martens, I. Radu, and C. Detavernier, "Crystallization and semiconductor-metal switching behavior of thin VO_2 layers grown by atomic layer deposition," *Thin Solid Films*, vol. 550, no. 0, pp. 59 – 64, 2014.

[49] I. Yamaguchi, T. Manabe, T. Kumagai, W. Kondo, and S. Mizuta, "Preparation of epitaxial V_2O_3 films on C-, A- and R-planes of α-Al_2O_3 substrates by coating-pyrolysis process," *Thin Solid Films*, vol. 366, no. 1-2, pp. 294 – 301, 2000.

[50] K. Govatsi, A. Chrissanthopoulos, V. Dracopoulos, and S. N. Yannopoulos, “The influence of Au film thickness and annealing conditions on the VLS-assisted growth of ZnO nanostructures,” *Nanotechnology*, vol. 25, no. 21, pp. 10–12, 2014.

[51] P. Scherrer, “Bestimmung der Große und der inneren Struktur von Kolloidteilchen mittels Rontgenstrahlen,” *Nachrichten von der Gesellschaft der Wissenschaften zu Gottingen, Mathematisch-Physikalische Klasse*, vol. 1918, pp. 98–100, 1918.

[52] R. Schmiedl, V. Demuth, P. Lahnor, H. Godehardt, Y. Bodschwinna, C. Harder, L. Hammer, H.-P. Strunk, M. Schulz, and K. Heinz, “Oxygen diffusion through thin Pt films on Si(100),” *Applied Physics A*, vol. 62, no. 3, pp. 223–230, 1996.

[53] G.-A. Nazri and G. Pistoia, *Lithium Batteries, Science and Technology*. Springer, 2003.

[54] A. Safavi, N. Maleki, O. Moradlou, and F. Tajabadi, “Simultaneous determination of dopamine, ascorbic acid, and uric acid using carbon ionic liquid electrode,” *Analytical Biochemistry*, vol. 359, no. 2, pp. 224 – 229, 2006.

[55] T. Zhang and N. Imanishi, “Lithium-air batteries,” in *Nanoscale Technology for Advanced Lithium Batteries* (T. Osaka and Z. Ogumi, eds.), Nanostructure Science and Technology, pp. 227–241, Springer New York, 2014.

[56] L. Carrette, K. A. Friedrich, and U. Stimming, “Fuel Cells - Fundamentals and Applications,” *Fuel Cells*, vol. 1, no. 1, pp. 5–39, 2001.

[57] R. Komiya, A. Hayashi, H. Morimoto, M. Tatsumisago, and T. Minami, “Solid state lithium secondary batteries using an amorphous solid electrolyte in the system (100-x)$(0.6Li_2S \cdot 0.4SiS_2) \cdot xLi_4SiO_4$ obtained by mechanochemical synthesis,” *Solid State Ionics*, vol. 140, no. 1, pp. 83 – 87, 2001.

[58] V. S. Bagotsky, *Fundamentals of electrochemistry, second edition*. Wiley, 2006.

[59] M. Jha, V. Kumar, and R. Singh, “Review of hydrometallurgical recovery of zinc from industrial wastes,” *Resources, Conservation and Recycling*, vol. 33, no. 1, pp. 1 – 22, 2001.

[60] Z. Hens, *Fysische Chemie*. Academia Press, 2013.

[61] M. Paunovic, *Fundamentals of electrochemical deposition*. Wiley-Interscience, 2006.

[62] A. J. Bard and L. R. Faulkner, *Electrochemical Methods, Fundamentals and Applications*. John Wiley and sons inc., 2001.

[63] P. C. Hayes and S. H. Algie, *Process Principles in Minerals and Materials Production*. Hayes Publishing, 1993.

[64] M. Yoshio, R. J. Brodd, and A. Kozawa, *Litium-Ion Batteries, Science and Technologies*. Springer, 2009.

[65] R. Ruffo, C. Wessells, R. A. Huggins, and Y. Cui, "Electrochemical behavior of $LiCoO_2$ as aqueous lithium-ion battery electrodes," *Electrochemistry Communications*, vol. 11, no. 2, pp. 247 – 249, 2009.

[66] M. S. Whittingham, "Lithium Batteries and Cathode Materials," *Chemical Reviews*, vol. 104, no. 10, pp. 4271–4302, 2004.

[67] I. R. Mattson, "Stability of the Graphite Electrode for Li-ion Batteries," master's dissertation, Norwegian University of Science and Technology, Trondheim, July 2013.

[68] H. Wu, G. Zheng, N. Liu, T. J. Carney, Y. Yang, and Y. Cui, "Engineering Empty Space between Si Nanoparticles for Lithium-Ion Battery Anodes," *Nano Letters*, vol. 12, no. 2, pp. 904–909, 2012.

[69] S. Zhang, M. S. Ding, K. Xu, J. Allen, and T. R. Jow, "Understanding Solid Electrolyte Interface Film Formation on Graphite Electrodes," *Electrochemical and Solid-State Letters*, vol. 4, no. 12, pp. 206–208, 2001.

[70] Y. Ein-Eli, "A New Perspective on the Formation and Structure of the Solid Electrolyte Interface at the Graphite Anode of Li-Ion Cells," *Electrochemical and Solid-State Letters*, vol. 2, no. 5, pp. 212–214, 1999.

[71] S. S. Zhang, K. Xu, and T. R. Jow, "EIS study on the formation of solid electrolyte interface in Li-ion battery," *Electrochimica Acta*, vol. 51, pp. 1636–1640, 2006.

[72] M. Balasubramanian, H. S. Lee, X. Q. Yang, A. R. Moodenbaugh, J. McBreen, D. A. Fischer, and Z. Fu, "Formation of SEI on Cycled Lithium-Ion Battery Cathodes, Soft X-Ray Absorption Study," *Electrochemical and Solid-State Letters*, vol. 5, no. 1, pp. 22–25, 2002.

[73] Y. Wang, X. Guo, S. Greenbaum, J. Liu, and K. Amine, "Solid Electrolyte Interphase Formation on Lithium-Ion Electrodes: A Li Nuclear Magnetic Resonance Study," *Electrochemical and Solid-State Letters*, vol. 4, no. 6, pp. 68–70, 2001.

[74] D. Ostrovskii, F. Ronci, B. Scrosati, and P. Jacobsson, "A FTIR and Raman study of spontaneaous reactions occuring at the $LiNiCoO_2$ electrode/non-aqueous electrolyte interface," *Journal of Power Sources*, vol. 94, no. 2, pp. 183–188, 2001.

[75] P. B. Balbuena and Y. Wang, *Lithium-Ion Batteries, Solid-Electrolyte Interphase*. Imperial College Press, 2004.

[76] D. Harvey, "Analytical Chemistry 2.0." pp. 667-781.

[77] "Application Note E-4: A Review of Techniques for Electrochemical Analysis." `http://goals.usim.edu.my/moodle/pluginfile.php/118191/mod_resource/content/1/Review%20Techniques%20for%20Electrochemical%20Analysis.pdf`. Princeton Applied Research.

[78] J. Oudenhoven, “Deposition and Characterization of Thin Films for 3D Lithium-ion Micro-Batteries,” phd thesis, Technische Universiteit Eindhoven, November 2011.

[79] “Basic overview of the working principle of a potentiostat/galvanostat (PGSTAT) - Electrochemical cell setup.” `http://www.ecochemie.nl/download/Applicationnotes/Autolab_Application_Note_EC08.pdf`. Autolab Application Note EC08, Metrohm Autolab B.V.

[80] S.-L. Chou, J.-Z. Wang, J.-Z. Sun, D. Wexler, M. Forsyth, H.-K. Liu, D. R. MacFarlane, and S.-X. Dou, “High Capacity, Safety, and Enhanced Cyclability of Lithium Metal Battery Using a V_2O_5 Nanomaterial Cathode and Room Temperature Ionic Liquid Electrolyte,” *Chemistry of Materials*, vol. 20, no. 22, pp. 7044–7051, 2008.

[81] P. A. Christian, D. W. Murphy, F. J. DiSalvo, and J. N. Carides, “Vanadium Oxide Cathode Materials for Secondary Lithium Cells,” *J. Electrochem. Soc.*, vol. 126, no. 3, pp. 497–499, 1979.

[82] K. West, B. Zachau-Christiansen, M. Ostergard, and T. Jacobsen, “Vanadium oxides as electrode materials for rechargeable lithium cells,” *Journal of Power Sources*, vol. 20, no. 1, pp. 165 – 172, 1987. 3rd International Meeting on Lithium Batteries.

[83] M. S. Whittingham, “The role of ternery phases in cathode reactions,” *Journal of Electrochemical Society*, vol. 123, no. 3, pp. 315–320, 1976.

[84] D. W. Murphy, P. A. Christian, F. J. DiSalvo, and J. V. Waszczak, “Lithium incorporation by vanadium pentoxide,” *Inorganic Chemistry*, vol. 18, no. 10, pp. 2800–2803, 1979.

[85] P. Dickens, S. French, A. Hight, and M. Pye, “Phase relationships in the ambient temperature $Li_xV_2O_5$ system,” *Materials Research Bulletin*, vol. 14, no. 10, pp. 1295 – 1299, 1979.

[86] Y. Liu, M. Clark, Q. Zhang, D. Yu, D. Liu, J. Liu, and G. Cao, “V_2O_5 Nano-Electrodes with High Power and Energy Densities for Thin Film Li-Ion Batteries,” *Advanced Energy Materials*, vol. 1, no. 2, pp. 194–202, 2011.

[87] C. Leger, S. Bach, P. Soudan, and J.-P. Pereira-Ramos, “Structural and Electrochemical Properties of ω-$Li_xV_2O_5$ as rechargeable chatodic material for lithium batteries,” *Journal of the electrochemical society*, vol. 152, no. 1, pp. 236–241, 2005.

[88] D. W. Murphy, P. A. Christian, F. J. DiSalvo, and J. V. Waszczak, “Lithium incorporation by vanadium pentoxide,” *Inorganic Chemistry*, vol. 18, no. 10, pp. 2800–2803, 1979.

[89] D. W. Murphy, P. A. Christian, F. J. DiSalvo, J. N. Carides, and J. V. Waszczak, “Lithium Incorporation by V_6O_{13} and related vanadium (+4,+5) oxide cathode materials,” *Journal Electrochem. Soc.*, vol. 128, no. 10, pp. 2053–2060, 1981.

[90] K. West, B. Zachau-Christiansen, and T. Jacobsen, “Electrochemical properties of non-stoichiometric V_6O_{13},” *Electrochimica Acta*, vol. 28, no. 12, pp. 1829–1833, 1983.

[91] B. Steele, G. Lagos, P. Spurdens, C. Forsyth, and A. Foord, "Behaviour of $Li_xV_6O_{13}$ and Li_xTiS_2 composite electrodes incorporating polyethylene oxide based electrolytes," *Solid State Ionics*, vol. 9, no. 1, pp. 391 – 398, 1983.

[92] N. Ganganagappa and A. Siddaramanna, "One step synthesis of monoclinic VO_2(B) bundles of nanorods: Cathode for Li ion battery," *Materials Characterization*, vol. 68, no. 0, pp. 58–62, 2012.

[93] Q. Zhao, L. Jiao, W. Peng, H. Gao, J. Yang, Q. Wang, H. Du, L. Li, Z. Qi, Y. Si, Y. Wang, and H. Yuan, "Facile synthesis of VO_2(B)/carbon nanobelts with high capacity and good cyclability," *Journal of Power Sources*, vol. 199, no. 0, pp. 350 – 354, 2012.

[94] I. Mjejri, N. Etteyeb, and F. Sediri, "Hydrothermal synthesis of mesoporous rod-like nanocrystalline vanadium oxide hydrate $V_3O_7 \cdot H_2O$ from hydroquinone and V_2O_5 ," *Materials Research Bulletin*, vol. 48, no. 9, pp. 3335 – 3341, 2013.

[95] A. Pan, H. B. Wu, L. Yu, T. Zhu, and X. W. D. Lou, "Synthesis of Hierarchical Three-Dimensional Vanadium Oxide Microstructures as High-Capacity Cathode Materials for Lithium-Ion Batteries," *ACS Applied Materials and Interfaces*, vol. 4, no. 8, pp. 3874–3879, 2012.

[96] G. Armstrong, J. Canales, A. R. Armstrong, and P. G. Bruce, "The synthesis and lithium intercalation electrochemistry of VO_2(B) ultra-thin nanowires," *Journal of Power Sources*, vol. 178, no. 2, pp. 723 – 728, 2008.

[97] X. Rui, D. Sim, C. Xu, W. Liu, H. Tan, K. Wong, H. H. Hng, T. M. Lim, and Q. Yan, "One-pot synthesis of carbon-coated VO_2(B) nanobelts for high-rate lithium storage," *RSC Adv.*, vol. 2, pp. 1174–1180, 2012.

[98] M. Rahman, J.-Z. Wang, N. H. Idris, Z. Chen, and H. Liu, "Enhanced lithium storage in a VO_2(B)-multiwall carbon nanotube microsheet composite prepared via an in situ hydrothermal process," *Electrochimica Acta*, vol. 56, no. 2, pp. 693 – 699, 2010.

[99] S. Milosevic, I. Stojkovic, S. Kurko, J. G. Novakovic, and N. Cvjeticanin, "The simple one-step solvothermal synthesis of nanostructurated VO_2(B)," *Ceramics International*, vol. 38, no. 3, pp. 2313 – 2317, 2012.

[100] S. Gao, Z. Chen, M. Wei, K. Wei, and H. Zhou, "Single crystal nanobelts of $V_3O_7 \cdot H_2O$: A lithium intercalation host with a large capacity," *Electrochimica Acta*, vol. 54, no. 3, pp. 1115 – 1118, 2009.

[101] H. Qiao, X. Zhu, Z. Zheng, L. Liu, and L. Zhang, "Synthesis of $V_3O_7 \cdot H_2O$ nanobelts as cathode materials for lithium-ion batteries," *Electrochemistry Communications*, vol. 8, no. 1, pp. 21 – 26, 2006.

[102] M. Saidi, R. Koksbang, E. Saidi, H. Shi, and J. Barker, "Rocking-chair batteries based on $LiMn_2O_4$ and V_6O_{13}," *Journal of Power Sources*, vol. 68, no. 2, pp. 726–729, 1997. Proceedings of the Eighth International Meeting on Lithium Batteries.

[103] Y. S. Cohen and D. Aurbach, “Surface films phenomena on vanadium-pentoxide cathodes for Li and Li-ion batteries: in situ AFM imaging,” *Electrochemistry Communications*, vol. 6, no. 6, pp. 536 – 542, 2004.

[104] G. Aylward and T. Findlay, *SI Chemical Data, 6th edition*. John Wiley and Sons, Australia, 2008.

[105] Y. Katayama and B. Friedrich, “Electrochemical Reduction of Titanium Dioxide Thin Film in LiCl-KCl-$CaCl_2$ Eutectic Melt,” 2004. 206th Meeting of the Electrochemical Society Inc., Honolulu.

[106] L.Kavan, M. Gratzel, J. Rathousky, and A. Zukalb, “Nanocrystalline TiO_2(Anatase) Electrodes: Surface Morphology, Adsorption and Electrochemical Properties,” *J. Electrochem. Soc.*, vol. 143, no. 2, pp. 394–400, 1996.

[107] A. C. Gorren, A. J. Kungl, K. Schmidt, E. R. Werner, and B. Mayer, “Electrochemistry of pterin cofactors and inhibitors of nitric oxide synthase,” *Nitric Oxide*, vol. 5, no. 2, pp. 176 – 186, 2001.

[108] M. Hourani and A. Wieckowski, “Single crystal electrochemistry of rhodium: Anion effects and order/disorder transitions of clean and silver coated Rh (111) surfaces,” *Journal of Electroanalytical Chemistry and Interfacial Electrochemistry*, vol. 244, no. 1, pp. 147 – 161, 1988.

[109] J. H. Song, H. J. Park, K. J. Kim, Y. N. Jo, J.-S. Kim, Y. U. Jeong, and Y. J. Kim, “Electrochemical characteristics of lithium vanadate, $Li_{1+x}VO_2$, new anode materials for lithium ion batteries,” *Journal of Power Sources*, vol. 195, no. 18, pp. 6157 – 6161, 2010. Selected Papers Presented at 4th International Conference on Polymer Batteries and Fuel Cells.

[110] J. Dendooven, R. K. Ramachandran, K. Devloo-Casier, G. Rampelberg, M. Filez, H. Poelman, G. B. Marin, E. Fonda, and C. Detavernier, “Low-Temperature Atomic Layer Deposition of Platinum Using (Methylcyclopentadienyl)trimethylplatinum and Ozone,” *The Journal of Physical Chemistry C*, vol. 117, no. 40, pp. 20557–20561, 2013.